LIGHT-TRIGGERED UNIDIRECTIONAL MOLECULAR ROTORS: THEORETICAL INVESTIGATIONS ON CONFORMATIONAL DYNAMICS AND LASER CONTROL

Dissertation

zur Erlangung des akademischen Grades doctor rerum naturalium

(Dr. rer. nat.)

seit 1558

vorgelegt dem Rat der Chemisch-Geowissenschaftlichen Fakultät der Friedrich-Schiller-Universität Jena

von Guillermo Pérez Hernández
geboren am 07.07.1982 in Santa Cruz de Tenerife

Gutachter:
1. .....
2. .....
3. .....

Tag der öffentlichen Verteidigung:
01.12.2010

Abstract - English

Two light-triggered molecular motors based on chiral overcrowded alkenes have been studied in the electronic ground state: a second-generation motor (**2**) and a redesigned motor (**3**). A semiempirical Monte-Carlo-type of conformational search has been implemented to find local minima in the ground state PESs of **2** and **3**, which then have been reoptimized by *ab-initio* calculations. While in **3** only the four isomers of the rotary cycle are found, new isomers have been found in the case of **2**, leading to different reaction pathways for the thermal helix-inversion. TSs for all the possible thermal conversions have been also computed. The obtained E_a values are in excellent agreement with those reported in the literature.

The simple model BCH (core unit of many motors) has been studied from a quantum chemical and quantum dynamical point of view. The controversial nature of BCH's electronic transitions has been investigated using high-level *ab-initio* multiconfigurational and perturbational methods, including the development of a basis set specific to the problem at hand. The first two excited states of B_u-symmetry ($(\pi, 3s)$-Rydberg and (π, π^*), respectively) are resolved at the MS-CASPT2-level of theory, providing vertical transition energies and oscillator strengths matching the experimental values. In addition, the origin of the (π, π^*)-band is computed, yielding an energy value well below the FC-value of the $(\pi, 3s_R)$-maximum, explaining this band's unexpected intensity.

Finally, a one-dimensional PES along BCH's torsional coordinate has been computed at the MS-CASPT2-level of theory, and quantum dynamical simulations have been carried out. These have focused on the obtainment of control laser fields that are able to trigger unidirectionality even in the symmetric PES (as opposed to **2** and **3** system). Optimal control strategies as well as the intuitive IR+UV-scheme both succeeded in achieving sustained, unidirectional torsional motion of BCH in the excited state.

Abstract - Deutsch

Zwei lichtinduzierte, auf chiralen überladenen Alkenen basierende molekulare Motoren wurden im Grundzustand betrachtet: Motor **2** (der sog. zweiten Generation solcher Motoren angehörend) und ein weiterentwickelter Motor **3**. Eine semiempirsche Monte-Carlo-Konformer-Suche wurde programmiert, um alle möglichen Konformere der Potentialenergiefläche des Grundzustandes zu finden, und um sie abschließend mit *ab-initio*-Methoden weiter zu optimieren. Desweiteren wurden Übergangszustände berechnet. Im Fall des Motors **2** wurden drei neue Isomere gefunden. Ein neuer Zwischenschritt in der thermischen Helizitätsinversion wurde postuliert. Alle erhaltenen Aktivierungsbarrieren entsprechen in sehr guter Übereinstimmung den experimentellen Werten.

Das einfache Alken BCH wurde als Modellsystem für quantenchemische und quantendynamische Berechnungen gewählt. Die kontrovers diskutierten elektronischen Übergänge wurden gründlich anhand quantenchemischen *ab-initio*-Methoden untersucht. Teil der Untersuchung war die Optimierung eines spezifischen Basissatzes. Die ersten zwei angeregten Zustände wurden als $(\pi, 3s_R)$-Rydberg und (π, π^*) von der MS-CASPT2-Methode bestimmt. Die erhaltenen vertikalen Anregungsenergien und Oszillatorstärken stimmen sehr gut mit experimentellen Werten überein. Progressionen entlang der Scheren- und Streck-Schwingungen des *anti*-(π, π^*)-Übergangs tragen zum Profil der (π, π^*)-Bande bei, und erklären somit die scheinbar hohe Intensität der Rydberg-Bande.

Dieselbe MS-CASPT2-Methode wurde eingesetzt, um eindimensionale Potentialenergiekurven entlang BCH's Torsionskoordinate zu berechnen. Diese Kurven wurden für die Simulation lichtinduzierte Rotation verwendet. Sowohl *Optimal Control-Theory* als die intuitive IR+UV-Strategie erwiesen sich als erfolgreich in der Auslösung unidirektioneller Torsion.

Preface

The present dissertation comprises the work performed under the DFG-project *Coherent control and coherent spectroscopies in complex systems*[1]. The project has focused on the theoretical characterization and manipulation of light-triggered, biologically inspired molecular motors. The results obtained during the course of this project are presented fully in the corresponding articles, which have been published in international scientific journals. A fourth publication is currently in preparation. A summary of the published results can be found in Sections 3.1 to 3.3, which can be read independently from the original articles, provided in Section 3.5 as facsimiles. Two additional articles[2], closely related to the presented work, have been published as a result of the supervision of the diploma-thesis from Dipl. Chem. M. Aßmann. Additionally, several programs have been developed from scratch, either to implement existing methodologies or for other purposes concerning this work. These programs are included in the appendix with a brief description.

[1]The Deutsche Forschungsgemeinschaft is gratefully acknowledged for financial support.
[2]See items 8 and 5 in the publication list.

Contents

List of Figures

List of Tables

List of Articles

Nomenclature

In order to keep the abbreviations and the symbols consistent in the whole Thesis, the used nomenclature differs in some items from that used in Articles 3.5.1 to 3.5.3.

$\Psi(\vec{r},t)$	Total molecular wavefunction
$\psi_n(\vec{r})$	n-th eigenfunction solution to the molecular TISE (stationary state)
E_n	n-th energy eigenvalue solution to the molecular TISE
$\Psi_n(\vec{r},t)$	n-th time-dependent eigenfunction solution to the molecular TDSE
$\Psi(\vec{r},t)$	Time-dependent wavepacket solution to the molecular TDSE
C_n	Time-dependent expasion coefficient of $\Psi_n(\vec{r},t)$ in the wavepacket $\Psi(\vec{r},t)$
$\varphi_e(\vec{r}_e;\{\vec{R}_N\})$	Time-independent electronic wavefunction
$\psi_N(\vec{R}_N)$	Time-independent nuclear wavefunction
$\hat{H}_e(\vec{r}_e;\{\vec{R}_N\})$	Time-independent electronic Hamiltonian
$\varphi_e^i(\vec{r}_e;\{\vec{R}_N\})$	i-th electronic eigenfunction solution to the electronic TISE
ε^i	i-th energy eigenvalue solution to the electronic TISE
$\hat{H}_N(\vec{R}_N)$	Time-independent nuclear Hamiltonian
$\psi_N^\nu(\vec{R}_N)$	ν-th nuclear eigenfunction solution to the vibrational nuclear TISE
E^ν	ν-th energy eigenvalue solution to the vibrational nuclear TISE
$\hat{V}(\beta)$	Potential energy operator in β
ψ_ν	ν-th torsional eigenfunction
E_ν	ν-th torsional eigenvalue
$\{\phi_l\}$	Particle-in-a-ring basis functions
$\mathbf{H}$	Time-independent torsional Hamilton operator in matrix form
$\hat{V}(\beta)$	Potential energy operator in β-space
$\hat{T}(\beta)$	Kinetic energy operator in β-space
H_{lm}	Matrix element of the torsional Hamiltonian in the l-th row and the m-th column

V_{lm}	Matrix element of the potential energy operator n in the l-th row and the m-th column
T_{lm}	Matrix element of the kinetic energy operator in the l-th row and the m-th column
g	Index of the discretized position or momentum space
N_g	Total number of grid-points
β_g	g-th element of the localized basis set of δ-functions in position space
$U_{l\nu}$	Coefficient of the basis element l in the nu-th torsional eigenfunction
$\psi_{g\nu}$	Amplitude of the ν-th torsional eigenfunction at the grid-point g of the β-space
$\mathbf{H}(\beta, t)$	Time-dependent torsional Hamilton operator in matrix form defined in β-space
$\psi_1(\beta, t)$	Time-dependent population in the ground electronic state defined in β-space
$\psi_2(\beta, t)$	Time-dependent population in the first excited electronic state defined in β-space
$\hat{\mu}(\beta)$	Dipole moment operator defined in β-space
$\hat{W}(\beta, t)$	Time-dependent field-dipole coupling operator
$\vec{\epsilon}(t)$	Oscillating external electromagnetic field
$\mathbf{W}(\beta, t)$	Time-dependent matrix operator for the field-dipole interaction expressed in β-space
$V_{11}(\beta)$	PES for the ground electronic state along the β-coordinate
$V_{22}(\beta)$	PES for the first excited electronic state along the β-coordinate
τ	Index for the discretized time variable
N_t	Total number of timesteps
$\mathbf{H}_\tau(\beta)$	Time-dependent torsional Hamiltonian matrix at the τ-th instant defined in β-space
$\mathbf{V}_\tau(\beta)$	Time-dependent potential energy matrix in β-space at the τ-th instant
p_g	g-th element of the localized basis set of δ-functions in momentum space
$\psi_1^p(\tau)$	Component of the torsional wavefunction for the ground electronic state in momentum space at the τ-th instant
$\psi_2^p(\tau)$	Component of the torsional wavefunction for the first excited electronic state in momentum space at the τ-th instant

$\psi_1^\beta(\tau)$	Component of the torsional wavefunction for the ground electronic state in β-space at the τ-th instant
$\psi_2^\beta(\tau)$	Component of the torsional wavefunction for the ground electronic state in β-space at the τ-th instant
Ψ_p	Total torsional wavefunction in momentum space
Ψ_β	Total torsional wavefunction in position space
$\mathbf{T}_g$	Kinetic energy matrix for the g-th point of momentum space
$\mathbf{V}_{g\tau}$	Potential energy matrix for the g-th point of position space at the τ-th instant
$\Psi_i(\beta)$	Initial wavefunction in the ground electronic state for the OCT-calculations
$\Psi_f(\beta)$	Target wavefunction in the first excited electronic state for the OCT-calculations
Ψ_{BW}^k	k-th backwardly propagated torsional wavefunction
Ψ_{FW}^{k+1}	k-th forwardly propagated torsional wavefunction
$\vec{\epsilon}_g(t)$	Guess laser-field for the OCT-algorithm
α_0	Penalty function for the OCT-algorithm
$\vec{\epsilon}_k(t)$	Laser field for the k-th iteration of the OCT-algorithm
Q	DOF to be randomized
Q_0	Randomized DOF
N_G	Number of geometries of the pseudo-random method
$\mathcal{R}$	Random number
ω	Weighting parameter of the pseudo-random method
I	Interval of the type of DOF
E_a	Energy of activation
ω^{syn}	Torsional frequency of *syn*-BCH
ω^{anti}	Torsional frequency of *anti*-BCH
$\hbar$	Planck's constant h over 2π
N_{el}	Number of electrons
$\chi_j(\vec{r}_{ei})$	j-th spin-orbital depending only on the coordinates of the i-th electron (with spin-state)
$\Theta_j(\vec{r}_{ei})$	j-th spatial orbital depending only on the coordinates of the i-th electron

$\overline{\alpha}, \overline{\beta}$	Spin-state eigenfunctions
$\|\varphi_{HF}\rangle$	HF Slater-determinant
κ_{kj}	Expansion coefficient for the k-th atomic orbital for the j-th spatial orbital
$\theta_k(\vec{r}_{ei})$	k-the atomic orbital depending only on the coordinates of the i-th electron
N_B	Number of basis functions in an electronic structure calculation
$\hat{H}^0(\vec{r}_e)$	HF-electronic Hamiltonian
ε_{HF}^i	HF-energy eigenvalue for the i-th electronic state
κ_{kj}^{HF}	HF-optimized expansion coefficient for the k-th atomic orbital for the j-th spatial orbital
E_{corr}	Correlation energy
$\|\varphi_a^d\rangle$	Singly excited CSF
$\|\varphi_{ab}^{de}\rangle$	Doubly excited CSF
$\|\varphi_{abc}^{def}\rangle$	Triply excited CSF
$\|\varphi_{FCI}\rangle$	FCI vector
$\varepsilon_0^{(2)}$	Second order perturbatively corrected electronic energy for the ground electronic state
$\|\varphi_j^{(0)}\rangle$	j-th unperturbed Slater-determinant constructed by excitation of the ground state HF-Slater-determinant
ρ	Electron density
ρ_0	True ground state electron density
ρ_{TR}	Trial ρ
$\varepsilon_{DFT}[\rho]$	Energy functional
$T[\rho]$	Kinetic part of $\varepsilon_{DFT}[\rho]$
$J[\rho]$	Coulomb part of $\varepsilon_{DFT}[\rho]$
$\varepsilon_{eN}[\rho]$	Electron-nuclei interaction part of $\varepsilon_{DFT}[\rho]$
$\varepsilon_{xc}[\rho]$	Exchange-correlation part of $\varepsilon_{DFT}[\rho]$

Acronyms - General

^{1}HNMR	Proton nuclear magnetic resonance
AFC	Adaptative feedback control
ATP	Adenosin Triphosphate

CD	Circular dichroism
cw	continuous wave
DMS	Dipole moment surface
DOF	Degree of freedom
F0, F1	Rotary sub-units of the ATP-Synthase complex
FFT	Fast FT
FFT^{+1}	Forward-FFT from β-space to p-space
FFT^{-1}	Backward-FFT from p-space to β-space
FT	Fourier transform
FWHM	Full width at half maximum
IR	Infrared
IR+UV	Infrared + Ultraviolet
IRC	Intrinsic reaction coordinate
IVR	Internal vibrational redistribution
OCT	Optimal Control Theory
PES	Potential energy surface
PSB11	Protonated Schiff-base of 11-*cis*-retinal
PSS	Photostationary state
SE	Schrödinger Equation
SO	Split-Operator
TDSE	Time-dependent SE
TISE	Time-independent SE
TRK	Tannor-Rice-Kosloff
TS	Transition state
UV	Ultraviolet

Acronyms - Quantum Chemistry

ANO	Atomic natural orbital
ANO-L-R	ANO-Large basis set with optimized Rydberg components
AO	Atomic orbital

AS	Active space
B3LYP	Becke's three-parameter hybrid $\varepsilon_{xc}[\rho]$ using the Lee-Yang-Parr (LYP) correlation part
CAS	Complete active space
CASPT2	CAS Perturbation Theory to second order
CASSCF	Complete active space SCF
CI	Configuration interaction
CIS	CI singles
CISD	CI singles and doubles
CSF	Configuration state function
DFT	Density Functional Theory
FCI	Full CI
HF	Hartree-Fock
HK	Hohenberg-Kohn
KS	Kohn-Sham
LCAO	Linear combination of atomic orbitals
MCSCF	Multiconfigurational SCF
MO	Molecular orbital
MP2	Møller-Plesset second order perturbation theory
MS-CASPT2	Multi-state-CASPT2
PMCAS-CI	Perturbatively-modified CAS-CI
RASSCF	Restricted active space SCF
RHF	Restricted Hartree-Fock
RI	Resolution of the identity
ROHF	Restricted open-shell Hartree-Fock
SA-CASSCF	State-averaged CASSCF
SCF	Self consistent field
TDDFT	Time-dependent DFT
TZVP	Triple-zeta valence polarized

Units

°C	grad celsius
eV	electron volt
fs	femtosecond (10^{-15} s)
GVm^{-1}	gigavolt per meter
kcal/mol	kilocalorie per mol
nm	Nanometer
ps	picosecond (10^{-12} s)
rad	radian

Variables

$\vec{r}$	Molecular (nuclear and electronic) coordinates
β	Torsional coordinate, continuous
$\overline{r_{ei}}$	Electronic coordinates of the i-th electron (including the spin-state)
$\vec{r}_e$	Electronic coordinates (spin-free)
$\vec{R}_N$	Nuclear coordinates (spin-free)
$\vec{r}_{ei}$	Electronic coordinates of the i-th electron (without the spin-state)
p	Torsional momentum variable
t	Continuous time variable
t_τ	τ-th value of the discretized time

1. Introduction

The motivation of the present THESIS centers on four main ideas:

- Many fundamental aspects of biological processes rely on a machine-like function of large biomolecules.
- Inspired by biological machines as well as by regular, man-made machines, nanotechnology has produced a considerable amount of microscopic devices, among which rotatory motors represent an attractive candidate for study.
- Purely quantum phenomena play a decisive role both in biological and nano-sized machines.
- Quantum phenomena can be steered with external laser fields.

These concepts are nowadays accepted paradigms in life-sciences and chemical physics. The following introduction is articulated around them, because it is at the intersection of these four fields where the dream of every chemist becomes more accessible: the understanding and the control of matter and its transformations. The work presented here aims at providing some theoretical insight into how the combination of clever (nano)-synthesis and sophisticated laser control strategies can shape the chemistry of the future.

1.1. Biological Molecular Machines

Machine. At first glance, nothing seems less related to *life* than the word *machine.* Many instances of popular culture account for this antagonic concepts: from science-fiction novels, to films, to videogames. Even in music one often finds that there is an opposition between that which is *live* and that which comes out of *machines.* Indeed, the *Oxford's Advanced Dictionary* accounts for this *man vs machine* antagonism by using the following example in the corresponding entry for *machine*:

> (OFTEN DISAPPROVING) *a person who acts automatically, without allowing their feelings to show or to affect their work.*

Thus, the word *machine* can be even used in a negative context, where the presence of feelings is underlined as an attribute of being a living organism and not a *machine.* But, is

this interpretation entirely true? If one had consulted, for instance, the *Merriam-Webster Dictionary*, the situation would be somewhat different, since there, the second entry for *machine* (**2a**) reads:

> *a living organism or one of its functional systems.*

There is little room left for doubt in this definition. According to it, any living organism (or any of its functioning sub-systems) can be described as a machine. The first dictionary definition is, of course, correct, but the latter comprises better the framework of life-sciences nowadays: living organisms, humans included, are machines, and consist of even smaller machines. As a matter of fact, in the history of life-sciences, when discoveries have lead to a change of paradigm, they have also been illustrated, directly or indirectly, through comparison of the living object of study with a machine: a machines with mechanisms that help understand how life works.

Prominent examples of key biomolecules that base their functionality in machine-like properties are Adenosin Triphosphate ATP-Synthase and the retinal chromophore. The ATP-Synthase biomolecular system regulates the energy storage and flow in the cell. Its catalytic activity is based on a motor-like behavior, and it relies upon the rotary motion, a central aspect in the present Thesis. The retinal chromophore is responsible for the primary event in the vision process. The cascade of reactions that leads to the stimulation of the optic nerve is initiated with an ultrafast conformational change triggered by light. The example of retinal is chosen not because of a rotatory behavior, but rather because it is based upon a concept central to the present Thesis: the light-triggered isomerization of a double bond.

1.1.1. The ATP-Synthase enzyme

The most ubiquitous example of a rotatory molecular system in biology is ATP-Synthase, an enzyme present in all living systems.[1] It is responsible for manufacturing ATP, the cell's preferred form for energy storage. ATP-Synthase exploits a flux of protons through a membrane (following a chemical gradient) to fuel a mechanical rotatory motion. This rotation lastly catalyzes the ATP synthesis. The chemical gradient itself can be generated by respiration or photoreaction. In Fig. 1.1 the ATP-Synthase protein is shown coupled to photosynthesis. These two reactions define the way in which living organisms exchange energy and matter with their environments.

At a cellular level, ATP-Synthase can be located in thylakoid membranes of chloroplasts (plant cells), the inner membranes of mitochondria (animal cells), and plasma membranes (bacteria). At a molecular level, ATP-Synthase consists of many sub-units, the most important of which are the rotatory motors F0 and F1. Indeed, very often ATP-Synthase is designated F1-F0-ATP-Synthase. A simplified scheme of the enzyme with F0, F1, and

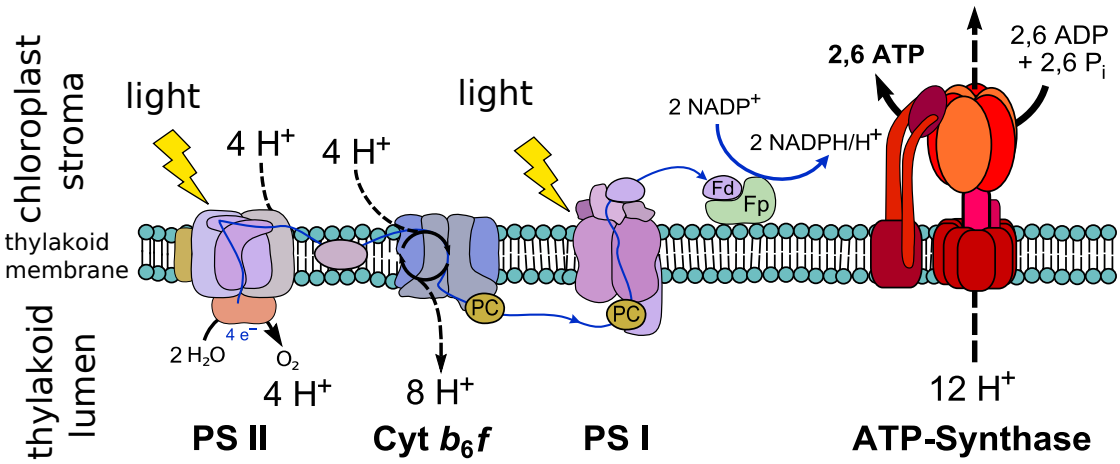

Figure 1.1.: Schematic representation of the ATP-Synthase enzyme coupled to photosynthesis in the thylakoid membrane. PSI and PSII are photosystems one and two, respectively. Cyt b_6f is the cytochrome b_6f complex. PC is plastocyanine and Fd and Fp are the enzymes ferrodoxin and ferrodoxin-NADP reductase, respectively.

their common axle γ is presented in Fig. 1.2. F0 is inserted in the membrane spanning from one side to the other, whereas the F1 motor protrudes to the outer side of the membrane. The two motors operate with different energy sources and in opposite directions: F0 uses the transmembrane chemical gradient to rotate in one direction, and F1 fuels its motion by hydrolyzing ATP molecules. Because the rotations are performed in opposite directions and the two motors share a common shaft (the γ-sub-unit), the rotation of one motor hinders the other. Under normal cellular conditions (physiological conditions), F0 is the motor with larger *torque*. The transmembrane proton gradient ($\Delta\mu H^+$) *fuels* the rotation in F0 so that it reverses the rotation of F1, thereby driving it to synthesize ATP from ADP and inorganic phosphate (P_i). When the conditions are those of ATP abundance, F1 starts hydrolyzing ATP and its *torque* can drive F0 backwards, turning it into an ion pump that moves protons across the membrane against the chemical gradient.[2–5]

Thus, the rotational catalysis accomplished by what was *the world's smallest rotary motor* in 1997[6] relies to a significant extent upon a mechanical property: the rigidity of the γ shaft connecting the two F1 and F0 rotors. The fact that chemical functionality at the molecular level (in this case, catalysis) can be achieved through somewhat mechanical properties has been summarized already by Francis Crick in the context of the DNA structure: *If you want to understand function, study structure.*[7] However, the fact that this principle is exploited by life itself to the point of creating machine-like devices has further inspired nanotechnology to an extent that will be reviewed in the next sections. Now, the retinal chromophore in the context of the vision process is presented as another example that provides valuable insight for the present work.

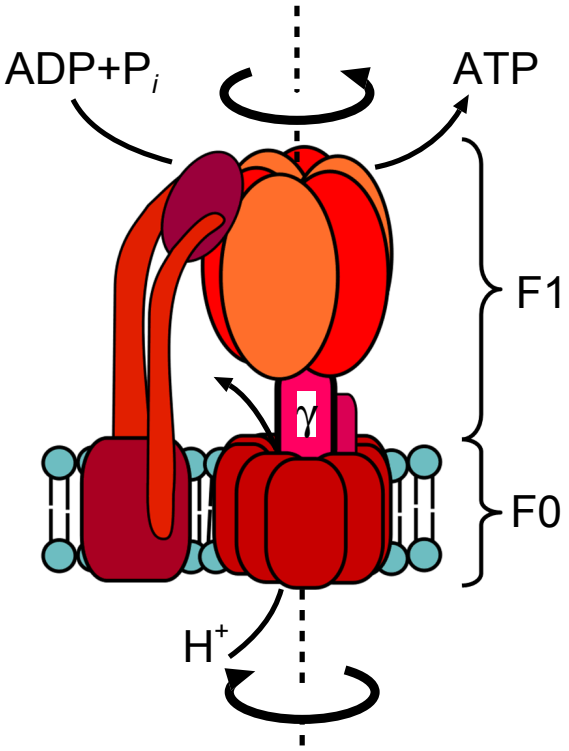

Figure 1.2.: Schematic representation of the ATP-Synthase enzyme, highlighting the two rotatory motors F0 and F1 and the shaft γ by which they are joined. The two opposed rotatory motions are represented with the circular arrows centered along the γ axle.

1.1.2. The retinal chromophore in rhodopsin

The visual phototransduction process is the process by which light stimuli are converted by photoreceptor cells of the retina (cones and rods) into electrical signals that finally stimulate the optic nerve.

The process starts with the absorption of a photon by a light-absorbing molecule (chromophore) bound to a G-protein coupled receptor, called the opsin protein. The chromophore (in its photoactive state) is 11-*cis*-retinal (an aldehyde of vitamin A), and when coupled to the opsin, the whole system is called rhodopsin. A schematic view of rhodopsin, which spans across the cellular membrane is shown in Fig. 1.3. In the opsin environment, the chromophore is actually the protonated Schiff-base of 11-*cis*-retinal (PSB11), covalently bound to the protein through the Lys296 residue.

PSB11 in the opsin environment (or models thereof) has been subject of numerous studies (over 10 000 according to Ref. 9), and is somewhat of a textbook example for a case in which a cascade of chemical reactions involving different timescales and size domains are highly correlated.

Of particular relevance for the present Thesis is the primary step of that cascade: the

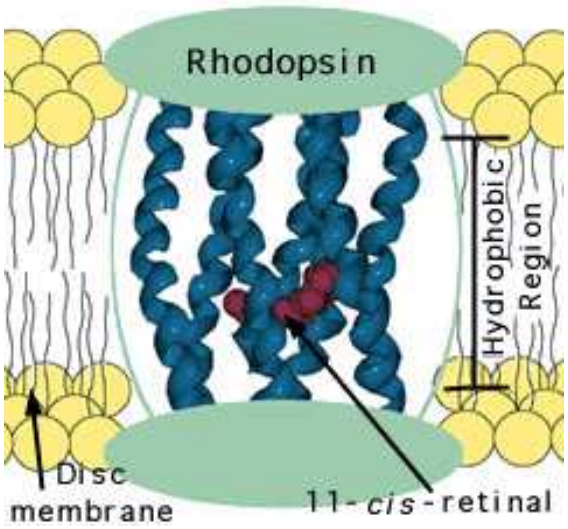

Figure 1.3.: Rhodpsin in the cellular membrane, containing the photoactive 11-*cis*-retinal (PSB11) as a chromophore in the binding site (dark red). Adapted from Ref. 8.

photoinduced isomerization of 11-*cis*-retinal inside of the protein binding pocket, as shown in Fig. 1.4. This rearrangement initiates the overall vision process because the isomerized

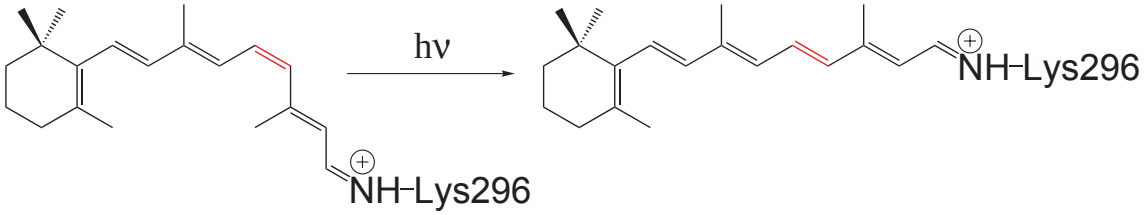

Figure 1.4.: Light-triggered *cis-trans*-isomerization at the 11-*cis*-bond in the protontated Schiff base of retinal (PSB11) to an all-*trans* configuration. The 11-12 double bond is marked in red.

chromophore no longer fits inside the binding site in the rhodopsin environment. The opsin structure is then forced to undergo a structural transformation to metarhodopsin II, which in turn is no longer stable and splits into the opsin and the all-*trans*-retinal. Then, a cascade of enzyme-catalyzed reactions follows, leading to the closure of cellular ion-channels in the membrane and finally to hyperpolarization, which ultimately propagates and stimulates the optic nerve.

Whereas the total duration of the vision process extends to the milisecond regime, the *cis-trans*-isomerization takes place at an ultrafast timescale of ∼200 fs (1 fs = $1{\cdot}10^{-15}$ s) after the absorption of a photon,[10] making it one of *the fastest chemical reaction known that involves nuclear motion*, according to Ref. 11. Various aspects of this fact are noteworthy for the present introduction. First of all, the reaction is triggered through light-

matter interaction (i.e., light is used as energy source for a structural change). Secondly, the involved time- and size-domains (∼200 fs and one double bond, respectively) situate the event in the realm of quantum phenomena. Indeed, the photochemically excited chromophore deactivates radiationlessly via a nonadiabatic transition to the ground state, i.e., through a conical intersection,[12,13] which is a pure quantum phenomenon. Finally, the *cis-trans* isomerization of the retinal chromophore (also in the bacteriorhodopsin protein) has also been the subject of laser control studies, experimentally[14–16] and theoretically,[17–20] thus bringing forward the third idea discussed in the introduction (developed fully in Section 1.3.6). A schematic view of the first hundreds of femtoseconds of the events in the vision process is given in Fig. 1.5

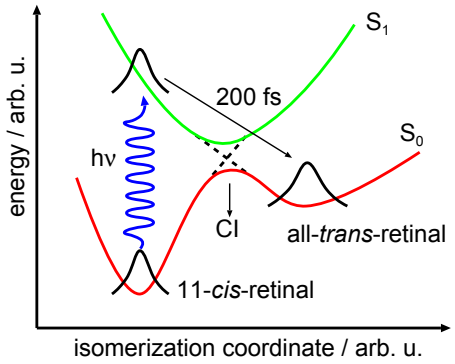

Figure 1.5.: Schematic energy diagram of the light-triggered *cis-trans*-isomerization of 11-*cis*-retinal along the reaction coordinate. S_0 and S_1 are the adiabatic electronic potential energy curves for the ground and first excited electronic state, respectively. The region with dashed curves represents the crossing of the diabatic curves, i.e., the conical intersection (CI) between the two potentials. Ultrafast, radiationless decay to the all-*trans*-retinal in the ground state is complete already after 200 fs. Adapted from Ref. 21.

The discovery of an ultrafast, nonadiabatic process in vision's primary event represented a paradigm-shift for visual photochemistry,[10] because it ruled out vibrational relaxation in the excited state, proposing an unprecedented speed of the isomerization.[22] Furthermore, it was shown[22] that the relaxation occurs in a coherent way, meaning that a vibrational wavepacket is created with specific phase and amplitude relations, another pure quantum phenomenon.

1.2. Nanoscale Molecular Motors

Apart from the previously discussed biological inspiration for molecular machines, everyday life also provides scientists with inspiration on how molecular devices may be envisioned. In the last two decades, scientists have produced molecular devices that mimic the macroscopic behavior of motors, shuttles, elevators, switches, muscles, linear motors

and many other devices. Among these devices, a variety of possibilities exists on how they can be constructed, operated, and monitored. Several comprehensive monographs exist, edited to a great extent by the leading authors of the field, see Refs. 23–27. A more recent (2007) comprehensive review by Kay, Leigh, and Zerbetto[28] provides further detailed insight into many examples of the aforementioned devices. Because, among these molecular devices, this THESIS focuses on rotary molecular motors (and a very particular sub-class within them), the following paragraphs are devoted to providing some background and to outlining the features of these particular devices: light-triggered molecular rotary motors.

1.2.1. Why rotary motors? Why light-triggered?

Venturi and coworkers[26] summarize five points when characterizing (and thus, designing) molecular machines, also applicable to normal-scale machines:

i) the kind of energy input,

ii) the manner in which their operation can be monitored,

iii) the possibility to repeat the operation at will, i.e., the feasibility of a cyclic process,

iv) the timescale needed to complete one cycle, and

v) the performed function.

Points i)-v) contain the main reasons why light-driven artificial rotary motors might be considered advantageous, specially those driven by a *cis-trans*-isomerization. Starting with item i), light represents one of the most convenient possible sources of energy. Contrary to other possible sources (such as the proton gradient difference addressed before), light can be generated far away from the sample and transported safely without much energy-loss from the source to the sample. Also, light can be switched on and off easily and rapidly, even with non-laser sources. In addition, for the case of *cis-trans*-isomerizations, using light as a source of energy does not produce unwanted byproducts (the equivalent to the CO_2+H_2O in combustion engines), thus operating on the sample in a less invasive manner. Moving on to item ii) (monitoring), light can be used both as energy source and as *readout* tool through spectroscopy. That is, not only does one initiate the reaction with light, but light can also monitor its own effects. To a great extent, that is how the particular class of rotors that will be treated afterwards are monitored. There is little to be said about item iii), since clearly rotary motors are the best candidates for cyclic processes. Item iv) is also adressed by *cis-trans*-isomerizations, since, as has been pointed out before, this process occurs in the ultrafast regime. In the particular cases that will follow, efforts to accelerate rotation rates are focused on other parts of the rotation. Lastly, one arrives at item v), function. Useful devices need to perform some kind of function of practical interest,

specially those intended to have some application in nanotechnology (the importance of light-driven, *cis-trans*-reactions in nature has already been addressed, *vide supra*). It has been shown experimentally that, when anchored to a surface, the class of light-driven *cis-trans*-rotors studied in this work can rotate nanoscopic objects. This capability fulfills two almost mandatory requirements for nanotechnology applications: the performance of physical work and the anchorage of the device to solid surfaces.

The use of photons as a source of energy becomes even more advantageous if laser technology enters the discussion (as it will, later on). Nowadays, laser sources are capable of tuning laser beams in many different ways, providing a variety of pulse lengths, frequencies, intensities, phase relationships, and sequences, which result ideal in dealing with different samples. In addition, when coupled to control setups (both experimentally and theoretically), lasers become a very powerful tool, since they can successfully activate non-trivial and non-intuitive pathways for achieving the rotation (see Section 1.3.)

1.2.2. Nomenclature

So far, the terms motor, rotor, and rotary motor have been used indistinctly, and indeed many authors do not make a distinction between them. However, a rotor is merely capable of performing rotary motion, whereas a motor has to be able to perform useful work. Thus, the term *rotary motor*, underlines a) the rotary nature of the performed motion and b) the ability to extract some work from that motion. Following that convention, the F1 and F0 systems in ATP-synthase are rotary motors, since the work performed by one of them is used to block the other. An even more pictorial example exists: hybrid F1-ATP-synthase-based motors can rotate nickel nano-rods attached to the rotator if fueled by increasing the ATP concentration.[29,30]

The class of light-triggered molecular machines studied in this work are capable of similar perfomances, such as rotating bulky substituents attached to their rotator[1] or even larger nanoscale objects,[31] thus earning the title of rotary motors. However, in most of the experimental instances they act strictly as rotors, because usually the focus of the experiments is a characterization of the stages of the rotation cycle and an optimization of its speed, rather than the use of the produced work. Nevertheless, even in those instances they are still addressed by the authors as rotary motors or, simply, motors. Thus, the same term *motors* shall be adopted from now on in the present Thesis, implying the rotary nature of the motion.

1.2.3. Molecular motors based on overcrowded alkenes

Functionalized overcrowded alkenes are a class of molecular motors successfully exploited by Feringa and coworkers since the early 1990s. The motors have evolved parallel to

[1] The more common word *rotor* is avoided because it can also refer to the whole molecule.

another class of closely related, also overcrowded alkene-based, class of light-triggered molecular devices: the chiroptical molecular switches.[25,32,33]

The word *overcrowded* addresses the fact that in these molecules some intramolecular distances between nonbonded atoms are smaller than the sum of the corresponding van der Waals radii, giving rise to significant steric hindrances. In the case of polycyclic aromatic *enes*, these overcrowdings distort the aromatic plane, so that the adopted conformation results in helicity (axial chirality), in the whole molecule as well as in some parts of it. The specific interplay between these steric factors results in an asymmetric potential that allows for the unidirectionality and irreversibility of some steps in the overall rotation of the motor. In addition to the steric hindrances, the motors base their functionality upon the *cis-trans*-bistability provided by a central olefinic bond, the only bond in the whole structure able to undergo such an isomerization, which is key when considering this class of molecules as molecular switches. A further key feature of the motors is the existence of at least one chiral center, where a methyl group is covalently bonded. Further functionalizations of the overcrowded alkenes will be addressed later.

How the unidirectional rotation arises and how asymmetries play a role in it is illustrated with the example of the unidirectional motor that was first published in 1999[34] by Feringa and coworkers. The motor **1** is presented in Fig. 1.6 and now it is referred to as a *first-generation motor*.

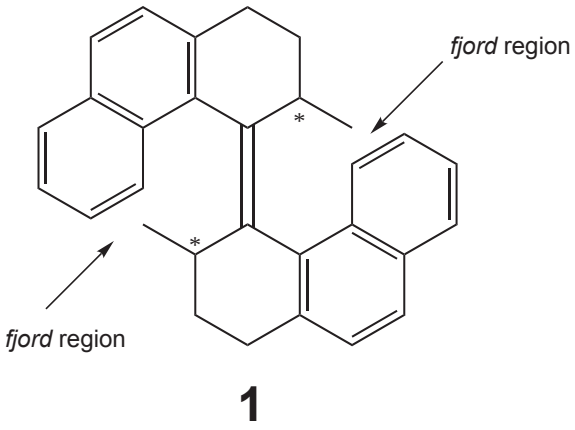

Figure 1.6.: (3*R*,3'*R*)-trans-1,1',2,2',3,3',4,4'-octahydro-3 ,3'-dimethyl-4,4'-biphenanthrylidene, the first reported light-driven unidirectional motor based on overcrowded alkenes.[34] The regions where distances between nonbonded atoms are small are referred to as *fjord* regions. The asterisks mark the chiral carbon atoms.

In **1**, both halves of the molecule are identical, thus no actual difference between stator and rotator exists. However, the lower half will be addressed as stator, and the upper as rotator, a convention that will be used throughout the complete text. Furthermore, and as mentioned above, not only does the central double bond possess helicity due to

its distortion, but also each separate half can adopt axial chirality P (*plus*, right handed) or M (*minus*, left-handed). Indeed, because $M \leftrightarrow P$ inversions occur as the motor rotates, the rotation can be monitored through the change in the optical activity of the sample using circular dichroism (CD) techniques.

A schematic representation of the cycle is presented in Fig. 1.7a, whereas the corresponding chemical structures at each stage are presented in Fig. 1.7b. The upper left corner will

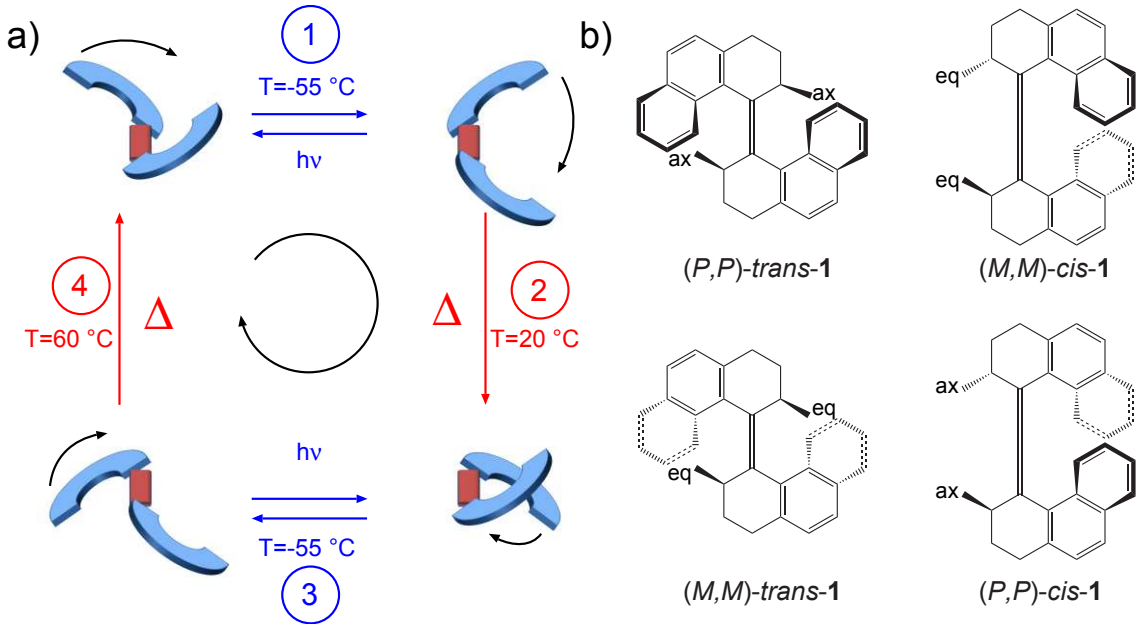

Figure 1.7.: a) Schematic representation of the four stages of the rotary cycle of the first unidirectional motor based on overcrowded alkenes. The bent arrows refer to the motion of the rotator (blue, in the background) with respect to the stator (also blue, in the foreground). The red bar is the axle of rotation. b) Equivalent structures for the four stages (adapted from Ref. 34).

be considered the starting point of the cycle in the following paragraphs: (*P*,*P*)-*trans*-**1**. From there, the rotation is initiated photochemically in step ①. Irradiation with a wavelength of $\lambda_{irr} \geq 280$ nm triggers the isomerization of the central double bond, resulting in (*M*,*M*)-*cis*-**1**. Apart from the *trans*→*cis* reaction, the helicity also switches from (*P*,*P*) to (*M*,*M*). Furthermore, the methyl groups change their orientation from axial to equatorial. Step ① is performed at low temperatures, because at room temperature, the thermal energy kT would be enough to further induce the next step.

In order to monitor the reaction, step ① is followed via ^{1}HNMR and CD spectrospy. Due to the equatorial→axial change of the methyl group, the protons in β of the stereogenic carbons (cf. Fig. 1.6) shift upfield, while the helicity change is monitored through the inversion of the CD spectrum around 217 nm.

Step ① is a reversible photoreaction, where irradiation at a different wavelength ($\lambda_{irr} \geq$ 380 nm) reverts the photoproduct to the reactant. Hence, one can speak of a photoequi-

librium in step ①, with different degrees of displacements to the photoproduct depending on each motor.[35–37] The product obtained once that the equilibrium is reached is the photostationary state (*PSS*). For the case of **1**, the PSS after step ① consists of 95% photoproduct.

On the contrary, step ② is irreversible at room temperature. A quantitative axial→equatorial and (*M*,*M*)→(*P*,*P*) conversion (monitored through ^{1}HNMR and CD) leads to (*P*,*P*)-*trans*-**1**. This pair of *cis*-isomers connected by step ② (or generally connected by thermal steps) are usually referred to as *unstable* and *stable*, given the facility and the irreversibility with which the former fully converts into the latter. After this thermal step has taken place, one can consider the overall rotation to be complete up to 50%. Step ③ is equivalent to step ① and is thus carried out at low temperatures, to allow for the experimental detection of the resulting PSS before it further evolves. In the case of step ③, the PSS consists of, to a high degree (90%), the unstable *trans*-isomer, as was the case of step ①.

Lastly, in step ④, conversion of unstable-*trans* to stable-*trans* is achieved by warming the sample, this time to a temperature of 60°C. Only the stable (*P*,*P*)-*trans*-**1** is observed in the CD and ^{1}HNMR spectra, accounting for the complete conversion. Thus, by irreversibly (at 60°C) reverting to the initial isomer, rotation of the motor can be considered complete.

Figure 1.8 depicts the various effects contributing to the unidirectionality at each stage of the rotary cycle. As previously mentioned, the potentials need to be asymmetric. In the overcrowded alkenes, that asymmetry is built-in through the appropiate steric interplay in the *fjord*-region between the naphtalene moieties and the methyl group.

In contrast, in a non-distorted, non-hindered olefinic bond, *cis*-*trans*-photoisomerization occurs symmetrically via the negative *and* the positive torsion coordinate pathway, with equal results for both pathways, given the periodicity of the potential (see Fig. 1.9).

Two factors differentiate **1** from the ideal ethylene shown in Fig. 1.9. First of all, the *cis*-**1** and *trans*-**1** isomers absorb at different wavelengths, assuring that a continuous irradiation at $\lambda_{irr} \geq 280$ nm interacts with the reactant only, and not with the photoproduct. That is to say, irrespective of the branching ratio, once the motor relaxes back to the ground state (circled regions in Fig. 1.9), the fraction of population that reverts to the reactant will be continously *pumped out* of the reactant side of the potential, so that yields higher that 50% can be achieved in the photoequilibrium. Second, the maximum in the excited state potential at the Franck-Condon region is displaced with respect to the minimum of the ground state potential, so that, upon vertical excitation, the positive direction of torsion (that of the overall rotation) is favoured over the other, negative direction. The fact that the photoreaction is reversible by no means hinders the motor's rotation, because irradiation is performed controlling the λ_{irr}. All these asymmetric features are

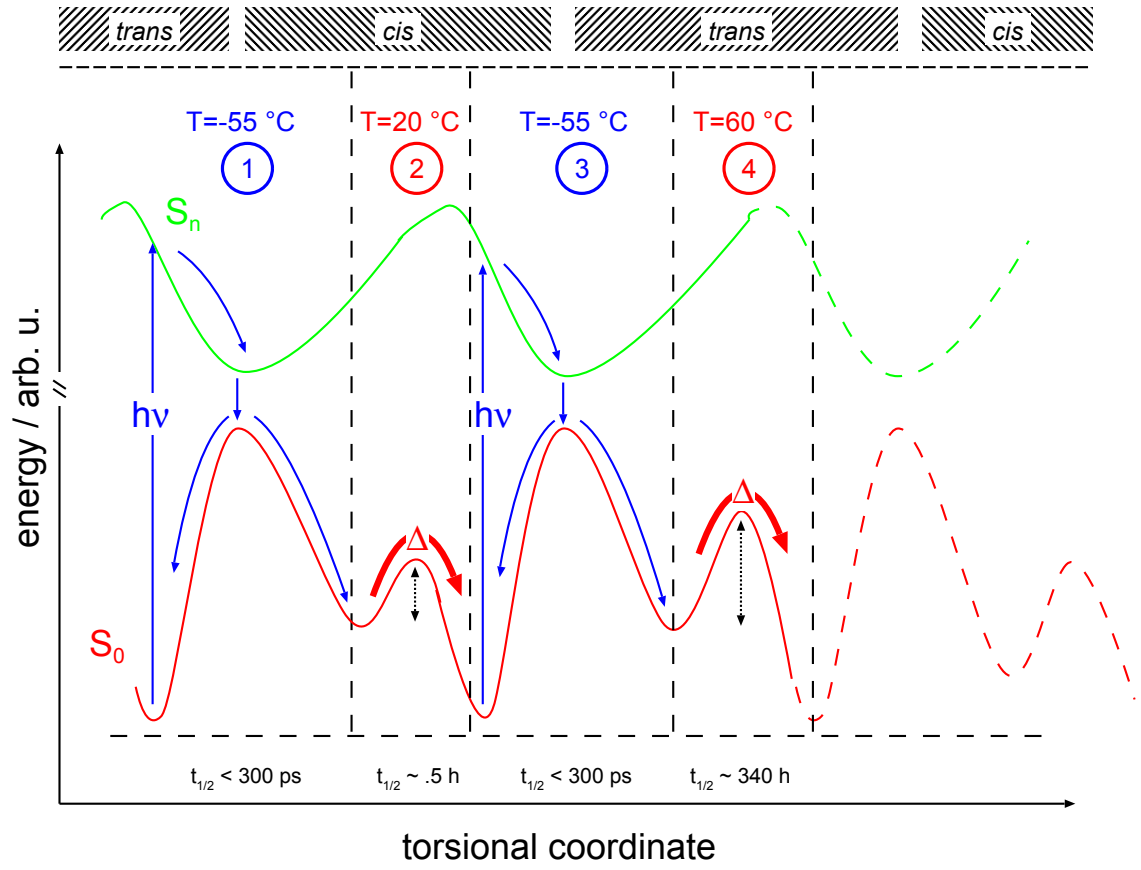

Figure 1.8.: Cyclic energy profile along the rotational coordinate of the motor **1**. The red and green curves represent the ground and excited state potential energy surfaces, respectively. The vertical dashed lines divide the torsion into the steps ①, ②, ③, and ④ (cf. Fig. 1.7a). The bars at the top indicate if the motor is on the *cis*- or the *trans*-isomer. The half-times of each step are written at the bottom. Arrows marked with $h\nu$ are photoinduced transitions, whereas arrows marked with Δ are the thermally induced helicity inversions, with the corresponding activation energies E_a in dotted arrows.

implemented in the form of the potentials in Fig. 1.8 for the steps ① and ③.

Considering the thermal steps ② and ④, the unidirectionality is assured through other means. In these cases, the large difference in stability (ca. 10 kcal/mol[34]) between the stable and unstable isomers alone suffices for the practical irreversibility of the reaction under thermodynamic conditions,

Even if the back reaction is made possible through heat, most of the population will find itself in the most stable isomer. That is, the directionality of the thermal step does not depend on the shape of the potential, but rather on a large enough energy-difference between product and reactant.

Indeed, given the fact that the motors are exploiting thermal fluctuations for their unidirectional rotation, they can be considered hybrid molecular Brownian ratchets, where

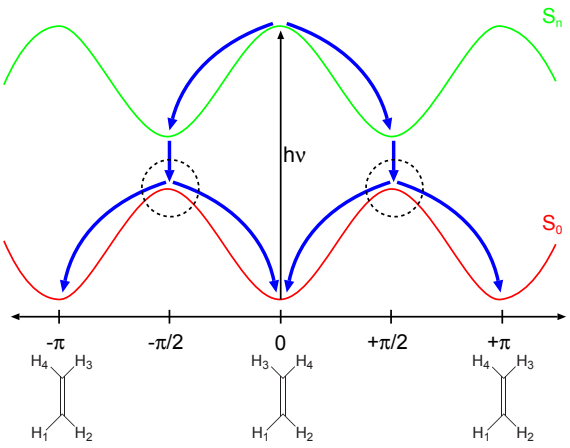

Figure 1.9.: Ideal photoisomerization of a double bond. The positions at which branching occurs are circled. When exciting to the S_n, both directions are equally probable. When relaxing to the S_0, the situation is analogous.

the intrinsic randomness of the thermal energy input is used to move the system in a particular direction (see Ref. 38 and references therein for a characterization of Brownian dynamics in the context of molecular motors).

The rotary cycle's efficiency can be addressed in terms different from its unidirectionality: speed is another crucial element when characterizing these molecular devices. Whereas the *cis-trans*-isomerization of overcrowded alkenes occurs in less than 300 ps,[39] the thermal steps take much longer times, so that ② and ④ are the rate-limiting steps for the whole rotation process. While ② has a half-time $t_{1/2}$ of about 30 min, $t_{1/2}$ equals 440 hours[2] for ④. Thus, in the cycle ①→②→③→④→①, the helicity inversion of unstable-*trans-1* (step ④) determines the overall speed. Because these helicity-inversion reactions are unimolecular, half-times are determined only by the reaction rate k,

$$t_{1/2} = \frac{ln2}{k}. \tag{1.1}$$

This rate can be expressed, in the simplest approach, by the Arrhenius equation[40] as:

$$k = Ae^{-\frac{E_a}{RT}}, \tag{1.2}$$

where A is the pre-exponential factor and R the ideal gas constant. Thus, for a given temperature T, the activation energies E_a of the involved transition states will define the speed of the motor.

Since the rate of rotation is thus ultimately determined by the magnitude E_a ($\Delta G^{\ddagger}$ with the enthalpic and entropic corrections), the subsequent efforts towards acceleration have

[2] at 20°C, see Ref. 37.

focused on decreasing the value of E_a for the thermal steps (cf. Fig. 1.8), and various approaches with different degrees of success have been attempted. In some cases, the unstable isomer was destabilized even more by attaching bulkier substituents.[41] Other strategies have aimed at reducing E_a via stabilization of the transition state, by reducing the rings fused to the axle from six-membered to five-membered rings. These approaches could indeed accelerate *one* of the helix inversions, but slowed the other one. Larger synthetic changes were carried out upon the overcrowded alkenes, giving rise to the *second-generation molecular motors*.[35] A representative member of this new class of motors is shown in Fig. 1.10

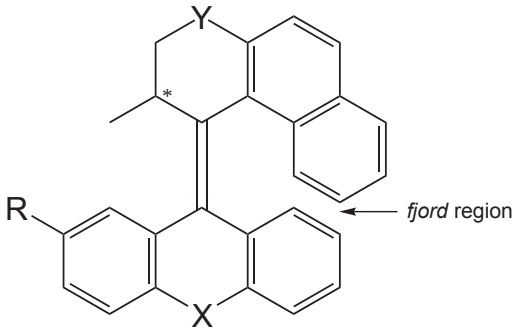

Figure 1.10.: Second-generation molecular motor.[35] The stator has been exchanged for a symmetric tricyclic moiety (cf. Fig. 1.6) that can be further functionalized, and there is only one chiral atom, marked with an asterisk.

The most distinctive feature of these motors is the symmetric lower half, making stator and rotator no longer equivalent. Also, substitutions at the positions X and Y (called *bridging* atoms) allow for different ring sizes while keeping the number of atoms constant. If the substituent R is a Hydrogen atom, the stator is totally symmetric, eliminating the chemical difference between the *cis* and the *trans* species. Even if R≠H, the two thermal helicity inversions (equivalent to steps ② and ④) are very similar in their activation barriers, reducing the complexity of accelerating the overall rotation. In addition, from a synthetic point of view, different rotator and stator allows for an easier functionalization. This functionalization has been successfully exploited in the cases where second-generation motors have been anchored to solid surfaces. Second-generation motors have been fixed, and operated on gold nanoparticles,[42] gold surfaces,[43] and quartz surfaces.[44] Not all of the newly envisioned motors achieved an acceleration of the rotation, for instance, when X = Y = S and R = H; $t_{1/2} \sim 200$ h. Nevertheless, the fastest second-generation motor (X = C, Y = CH_2, and R = H) reduced the half-time of the first motor by three orders of magnitude (a factor of ~ 660) to $t_{1/2} \sim 40$ min.

A further remarkable acceleration of second-generation motors was accomplished by further reducing both rings bonded with the axle to five-membered rings,[45] giving rise to

the fluorenyl based motors. Although further exploration of the substituents was needed to optimize the rotation speed, half-times finally could be reduced to the millisecond regime when a bulky *tert*-butyl substituent was used in R. The subsequent destabilization of the unstable isomers was such that E_a dropped down to ∼16 kcal/mol (from values typically between 25-35 kcal/mol[37]), resulting in $t_{1/2} \sim 6 \cdot 10^{-3}$ seconds, a half-time suggesting that the motor could perform 44 rotations per second.[37] Finally, with $t_{1/2}$ having been reduced to the microsecond domain, the benchmark for rotation speeds now lies in the MHz regime.[46,47]

1.3. Laser Control of Chemical Reactions

The drive behind a chemist's activity is not only the will to understand matter and its transformations, but also to *control*, to the highest degree of specificity, their outcome. Over centuries, tools at hand to do so have increasingly gained in complexity, from simple variation of macroscopic variables such as concentration, pressure or temperature, to the addition of sophisticated (and expensive) catalysts or cleverly conceived synthetic routes.

As was pointed out in Section 1.2.1, light is a particularly handy reactant, and as such it is also a useful tool when trying to steer a chemical process.[48] The extent to which control can be achieved is proportional to the extent to which the light acting upon the system can be manipulated. The development of laser technologies has provided experimentalists and theoreticians with a chemical reactant that can be tailored in almost every aspect. For molecular processes, the femtosecond regime results particularly attractive (see for instance Refs. 49 and 50), and thus a variety of approaches on how to use it to control chemical processes exist.

A brief overview of some laser control strategies follows. Only the approaches most relevant to this work have been selected, either because of the important concepts they introduce or because they have been directly used in this Thesis. Reference monographs for these and other laser control strategies are Refs. 51 and 52. The recent review (2010) in Ref. 53 provides a wider, more comprehensive perspective on the current state of the field.

1.3.1. The chemical intuition: mode-selective chemistry

The most intuitive approach on how to use laser light to manipulate chemical reactions is usually called the mode-selective approach. The goal is to selectively break a specific bond in a polyatomic molecule. The idea is that one identifies the frequency of that particular bond stretching, tunes the laser to that frequency and irradiates until the bond breaks. Although this intuitive approach can work under favorable circumstances,[54] mode-selective chemistry is not a broadly applicable approach.[55] The energy stored locally in a particular

bond can quickly redistribute among the other available modes of the molecule in a process called internal vibrational relaxation (IVR), what can be considered as the molecule just increasing its internal temperature. This approach is considered only effective in the cases were the control target can be achieved before IVR takes place, usually in the range of a few picoseconds (1 ps $\sim 1 \cdot 10^{-12}$ s). A graphic representation of this phenomenon is given in Fig. 1.11.

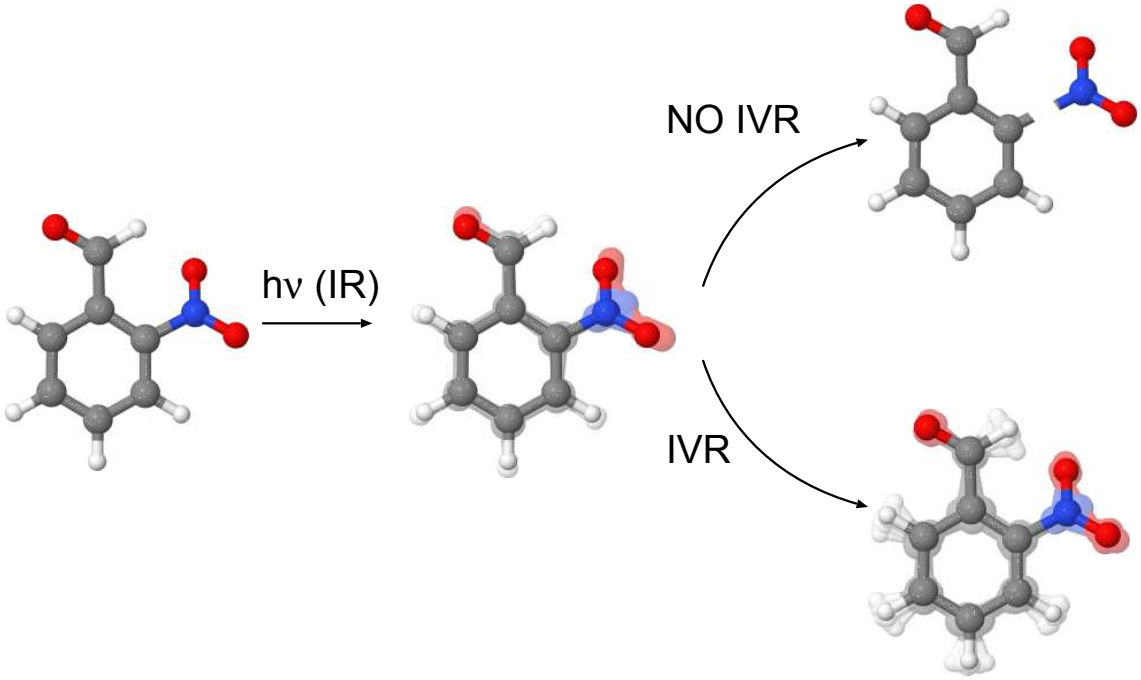

Figure 1.11.: Schematic representation of the mode-selective chemistry on the example of *ortho*-nitrobenzahldehyde molecule. In most cases, IVR is unavoidable and the energy *pumped* into a particular bond (the C−NO_2-bond) redistributes among other available modes.

1.3.2. The wave nature of matter: The Brumer-Shapiro approach

In contrast to the previous approach, Brumer and Shapiro[51] proposed and coined the term *coherent control of reactions*, which bases upon the quantum nature of molecules, in particular on the wave-matter duality. The essence of this approach is the manipulation of constructive and destructive quantum interferences that arise when the desired final state can be reached through degenerate pathways. This type of control is often viewed as an extension of the traditional double-slit experiment to show wave interferences. As will be shown in short, one of the key parameters in the control scheme is the phase information.

The context of photoinduced dissociation is used to briefly illustrate this principle, where

the control is aimed at manipulating the branching ratio of a given photoreaction, say

$$\mathrm{AB} + \mathrm{C} \xleftarrow{\mathrm{h}\nu} \mathrm{ABC} \xrightarrow{\mathrm{h}\nu} \mathrm{A} + \mathrm{BC}. \tag{1.3}$$

In the *bichromatic control*[51] approach, two continuous wave (cw) lasers of frequencies ω_1 and ω_2, with parallel polarization vectors, act upon a starting state $|\Psi(t=0)\rangle$:

$$|\Psi(t=0)\rangle = a_1 |E_1\rangle + a_2 |E_2\rangle \tag{1.4}$$

which is a superposition of two eigenstates $|E_1\rangle$ and $|E_2\rangle$, with the complex coefficients a_1 and a_2. How the superposition of states is prepared is of less importance at this point, as long as the phase relation between a_1 and a_2 is conserved, i.e., phase coherence exists. The frequencies ω_1 and ω_2 are tuned to match the difference between eigenenergies E_1 and E_2. These energy relationships are summarized in Fig. 1.12.

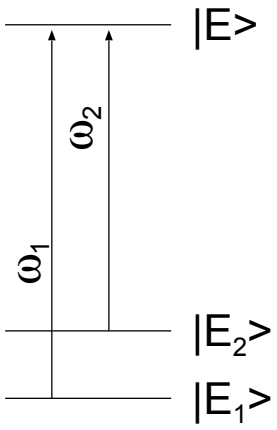

Figure 1.12.: Photodissociation of a superposition of two eigenstates via cw laser excitation with frequencies ω_1 and ω_2. $|E\rangle$ are the degenerated states of the continuum from which photodissociation can occur towards one or the other photoproducts.

Brumer and Shapiro arrive at an expression (Ref. 51 and references therein) for the branching ratio of the photoproducts (cf. Eq. (1.3)) in which the interacting laser-fields act via the interference terms between the two degenerated, indistinguishable photodissociation routes. These interference terms are governed by the relative phase relationship between the two lasers and the two initial coefficients a_1 and a_2, as well as by the intensities of the incident lasers. In order to map their influence, they collect these factors into two control variables, $\Delta\theta$ and s, for the phase difference and the relative intensities of the lasers, respectively, and then plot them vs. the yield of $\mathrm{CH_3} + \mathrm{I}$ in the following example:[56]

$$\mathrm{CH_3} + \mathrm{I}^* \xleftarrow{\mathrm{h}\nu} \mathrm{CH_3I} \xrightarrow{\mathrm{h}\nu} \mathrm{CH_3} + \mathrm{I} \tag{1.5}$$

The yield of $CH_3 + I$ vs. $\Delta\theta$ and s is shown in Fig. 1.13. As can be seen, yields can

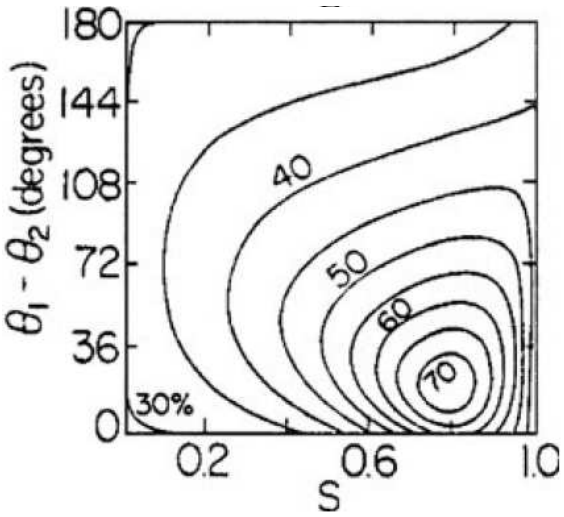

Figure 1.13.: Contour plot of $\Delta\theta$ (relative phase) and s (relative intensities) for the photodissociation of CH_3I. Adapted from 56.

be steered between 30 and 70% in this example, accounting for a considerable amount of control.

The bichromatic approach was simplified when the need for a superposition of states as the initial state was eliminated[57] in the *one vs. three photon interference* approach. The indistinguishable, degenerated pathways that are mandatory for the interference to occur are provided through two photoexcitation pathways: a one-photon pathway, with an associated frequency ω_1 and a three-photon pathway, with a frequency $\omega_3 = 3\omega_1$, as is shown in Fig. 1.14. This control scheme has been implemented successfully in various

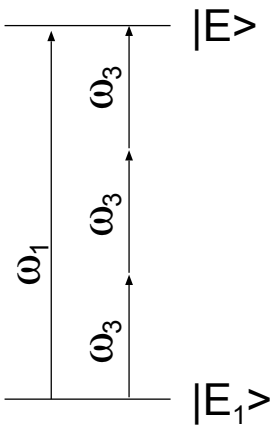

Figure 1.14.: One-photon vs. three-photon photodissociation scheme. As opposed to Fig. 1.12, no initial superposition of states is needed to create the interference.

experiments, for example by Gordon and coworkers[58–60] in modulating the branching ratio of the photoreaction:

$$HI^+ + e^- \longleftarrow HI \longrightarrow H + I. \tag{1.6}$$

1.3.3. Pulse-timing: the Tannor-Rice-Kosloff approach

The central idea behind the Tannor-Rice-Kosloff (TRK)[52,61–63] approach is to use a sequence of laser pulses whose relative delay is controlled to steer the time evolution of a wavepacket. This approach is also often called the *pump-dump* approach.

As opposed to the quantum interference approach of Section 1.3.2, the TRK-control is performed in the time-domain rather than through phase manipulation, although a version of it can be generated from the multiple path-interference of the quantum-interference scheme.[52] Basically, the *pump-dump* approach relies upon the topology of the excited state potential energy surface and the temporal evolution of a wavepacket on it.

Consider again a photoreaction of the type of Eq. (1.3). In the ground electronic state, different energy barriers need to be passed to access the exit channels AB + C and A + BC. In the TRK-scheme, contrary to the previous approach, excitation is not performed with a cw laser, but rather with a pulsed laser carrying a given bandwidth of frequencies. Upon excitation with such a pulse (the *pump*-pulse), a wavepacket is created in the excited state. Depending on the form of that potential, the wavepacket will evolve on it, ideally finding itself at times over the exit channel AB+C and at other times over the channel A+BC. An appropriate radiative de-excitation with the *dump*-pulse can place the wavepacket back on each of these channels selectively, thus steering the outcome of the reaction. An schematic representation of the *pump-dump* approach is shown in Fig. 1.15.

This scheme of control also has been demonstrated experimentally in several instances, for example in the photofragmentation of the Na_2-dimer by Gerber and coworkers[64–66] or the reaction $Xe + I_2 \longrightarrow XeI + I$ by Zewail[67] and coworkers.

1.3.4. From the Tannor-Rice-Kosloff scheme to the few-cycle IR+UV approach

The TRK-approach (*pump-dump*-scheme) is based on the intuitive concept of the pulse structure being resolved in the time-domain. Such a separation underlies also the Infrared(IR) + (Ultraviolet)UV-control scheme. The method bears similarities with the mode-selective approach (see Section 1.3.1), because a given bond of interest is also locally excited as a first step (IR-*pump*). However, the excitation is intended as a preparation for a subsequent electronic excitation (UV-*pump*). Henriksen and Amstrup introduced this *pump-pump*-scheme[68,69] for the photodissociation of HOD and the $^{16}O^{16}O^{18}O$ molecules.

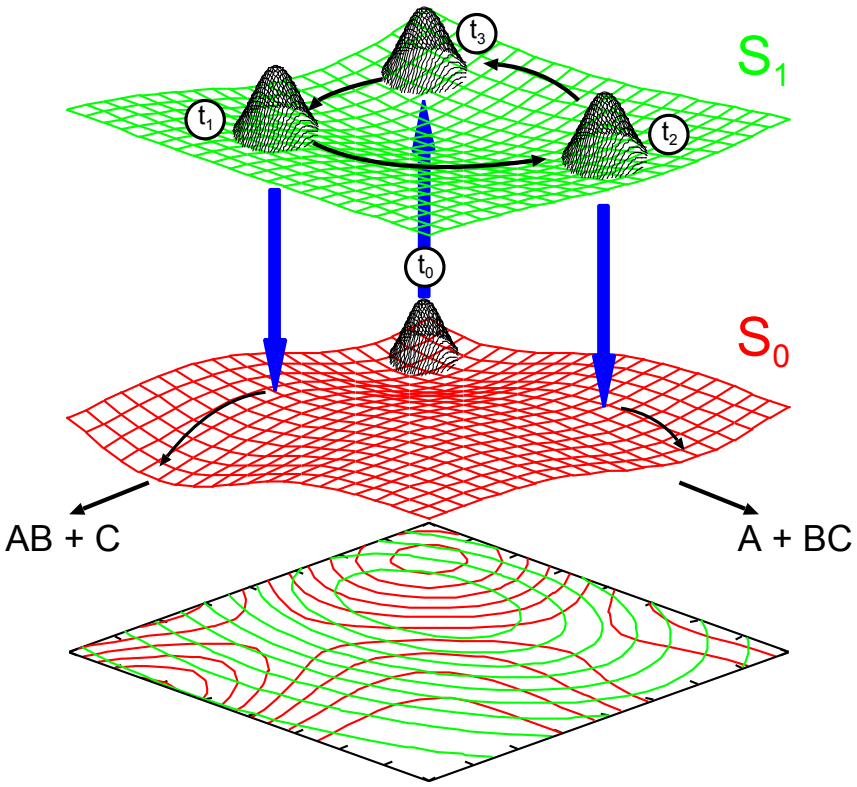

Figure 1.15.: *Pump-dump* Tannor-Rice-Kosloff laser control. The wavepacket in the ground state (S_0) is projected onto the excited state (S_1) with a short *pump*-pulse at t_0 (upward pointing arrow). Subsequently, the wavepacket evolves in time in the S_1 ($t_0 < t_1 < t_2 < t_3$). At t_1, the wavepacket is over the AB + C exit channel, whereas at t_2, it is over the A + BC channel. By timing the *dump*-pulse adequately at t_1 or t_2 (or their periodic recurrences), one can steer the outcome of the photoreaction.

In a reaction of the type

$$\mathrm{H + OD} \xleftarrow{h\nu} \mathrm{HOD} \xrightarrow{h\nu} \mathrm{HO + D}, \tag{1.7}$$

control over the exit channel is achieved through the delay between the two *pumps*. The UV-excitation of the oscillating wavepacket takes place away from the Franck-Condon region. Revisiting Fig. 1.15, the IR-pulse is the *pump*, this time creating the wavepacket in the ground state. The UV-excitation is not a *dump* but a second *pump*, instantly projecting the wavepacket to either one of the exit channels of the excited state.

Of particular interest for the present Thesis is the approach further developed by Manz and coworkers for the same HOD reaction,[70] in which selectivity is not achieved in position space, but rather in momentum space with a few-cycle IR+UV-scheme. The excitation is performed first on the electronic ground state with a few-cycle IR-pulse, tuned to be resonant with the frequency ω_{OH}. Driven by the pulse, the ground state vibra-

tional wavepacket starts to oscillate, gaining a momentum along the OH-mode. If mode-selectivity were intended, the OH-bond would be further excited to higher overtones until its cleavage. Instead, after the IR-excitation, a short ($\sim$ fs) UV-pulse follows at a certain delay, leading to a vertical transition to the excited state. Once the wavepacket is on the excited state potential (whose slope can, in principle, be non-selective), the wavepacket continues to evolve as dictated by direction and sign of the momentum at the instant of the transition. Thus, if the short UV-pulse is timed adequately, the momentum will be driving the wavepacket along the desired exit channel (H + OD in Ref. 70). Figure 1.16 illustrates this principle, where the short UV-*pump* pulses project wavepackets with opposite pointing momenta depending on the delays t_1 and t_2. A number of successful theoretical examples of this type of control have followed.[71–74]

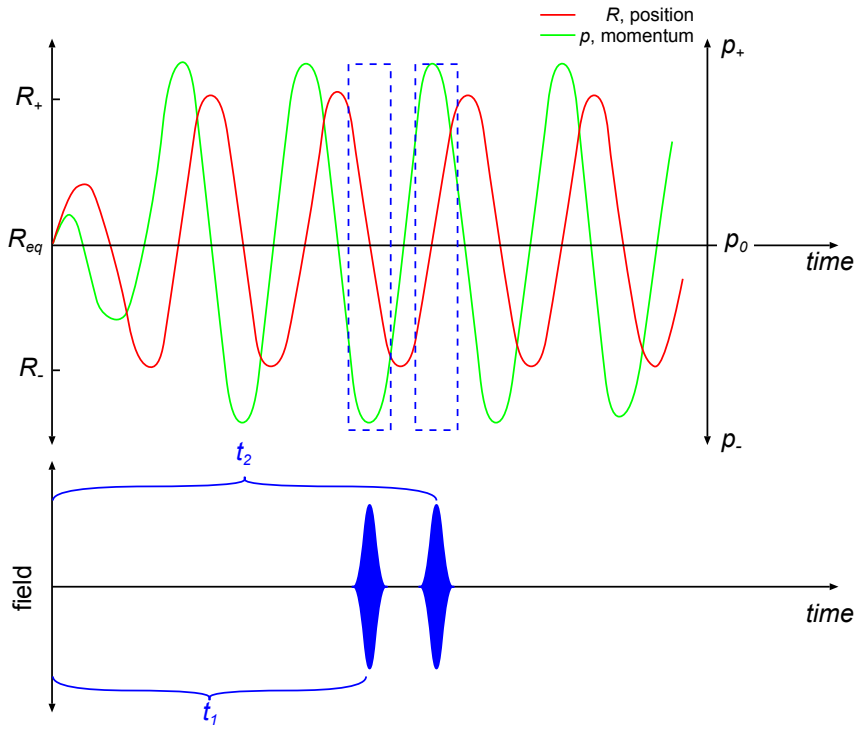

Figure 1.16.: Upper panel: The coordinate of interest R (solid, to be read on the left axis) and the associated momentum p (solid, right axis) evolving in time under the influence of the IR-pre-excitation. R_{eq} is the equilibrium position, R_+ and R_- are the positive and negative turning-points, respectively. p_+ and p_- are the positive and negative directions of the momentum. Dashed: two consecutive Franck-Condon (FC) windows for igniting motion with a short UV-pulse, shown in the lower panel. At the times of ignition (t_1 and t_2), the coordinate, R, is at its equilibrium value (the wavepacket is in the FC-region ($R(t_1) = R(t_2) = R_{eq}$), while the associated momenta are maximal and of opposite directions.

Among these, of particular interest for the present Thesis are the results of Ref. 73, in which the few-cycle IR+UV scheme is used to selectively isomerize a double bond,

triggering unidirectional rotation in a model molecular motor. The mechanism to achieve unidirectionality is analogous to that previously explained for the HOD case. In Ref. 73, the mode being pre-excited with the few-cycle IR-pulse is the torsion of a C=C-double bond. The same approach is used in this THESIS, and is further illustrated in Article 3.5.3 and in Section 3.3.

1.3.5. Optimal control theory: rapidly convergent algorithms

The general idea behind Quantum Optimal Control Theory (OCT), as formulated by Kosloff, Rice, Gaspard, Tersigni, and Tannor[75] and Dahleh, Peirce, Shi, Woody and Rabitz,[76] is to tackle the problem of finding the control field as a maximization problem with boundary conditions. Once the problem is formulated that way, it becomes subject to diverse optimization algorithms that can be imported from other fields, such as engineering.

OCT takes a step away from schemes where distinctions between *pump*- and *dump*-pulses or IR- and UV-pulses exist, and rather uses continuous, *back-and-forth* population transfer between the states involved. Thus, it is less intuitive, and once a pulse has been obtained, its underlying mechanism is less evident, inscrutable in most of the cases.

In this section, the general formulation of the optimal control problem is outlined, and two approaches to its solution are highlighted: a theoretical one and an experimental one. In both of them, a question prior to the OCT problem itself is that of the controllability of the system. That is, the question if a given target can be reached at all with a given controller, in this case, a laser field. Conditions and theorems to proof controllability in quantum systems are given in Refs. 77–79, and for the following, the systems treated in this THESIS are considered controllable.

Once the issue on controllability is settled, the adopted formulation is that of the standard OCT problem, that is, the use of Lagrangian multipliers to arrive at the Lagrange functional J to be maximized:[80]

$$J[\chi, \Psi, \epsilon] = J_1[\Psi] + J_2[\epsilon] + J_3[\chi, \Psi, \epsilon], \tag{1.8}$$

where χ is the Lagrange multiplier, Ψ the wavefunction describing the quantum system, and ϵ the control field. $J[\chi, \Psi, \epsilon]$ bears the conditions for the constrained optimization problem, namely:

- J_1 contains a generic operator $\hat{O}$ to be maximized:

$$J_1[\Psi] = \langle \Psi(T) | \hat{O} | \Psi(T) \rangle \,, \tag{1.9}$$

  where $\Psi(T)$ is the wavefunction at the end ($t = T$) of the control field. The only restriction to $\hat{O}$ is that it must be Hermitian, and all of the operators in quantum

control problems are.

- J_2 is designed to keep the fluency of the field to a minimum:

$$J_2[\epsilon] = \int_0^T \alpha\, \epsilon^2(t)\, \mathrm{d}t, \tag{1.10}$$

where α is a penalty function that can be also time-dependent to constrain the pulse envelope to an experimentally achievable form.

- Lastly, J_3 ensures that the time-evolving wavefunction, $\Psi(t)$, satisfies the time-dependent Schrödinger Equation:

$$J_3[\chi, \Psi, \epsilon] = -2\,\mathrm{Im} \int_0^T \langle \chi(t)| i\frac{\partial}{\partial\, t} - \hat{H}(t)|\Psi(t)\rangle\,. \tag{1.11}$$

The Hamilton operator $\hat{H}(t)$ includes the field interaction through the dipole, in the semiclassical description:

$$\hat{H}(t) = \hat{T} + \hat{V} - \vec{\mu}\cdot\vec{\epsilon}(t), \tag{1.12}$$

where $\hat{T}$ is the kinetic energy operator, $\hat{V}$ the potential energy operator, $\vec{\mu}$ is the dipole moment vector, and $\vec{\epsilon}(t) = \epsilon(t)\cdot\vec{u}_\epsilon$ is the electric field vector, of magnitude $\epsilon(t)$ and polarization direction $\vec{u}_\epsilon$.

Imposing $\delta J = 0$ on the target functional (Eq. (1.8)) delivers a set of equations that can be solved iteratively with numerical algorithms. When the algorithm has converged, the expectation value of $\hat{O}$ has arrived at a maximum value within the constraints, and an optimal control field $\vec{\epsilon}(t)$ has been found. In the cases discussed in this Thesis, $\hat{O}$ is a projection operator $\hat{P}_{|\phi_f\rangle} = |\phi_f\rangle\langle\phi_f|$, where ϕ_f is the desired final wavefunction. Since torsion along a particular coordinate is sought, ϕ_f is a target wavefunction that already possesses momentum pointing along the torsion. One can think of such a target state as the wavefunction corresponding to a certain time-window t_1 or t_2 in Fig. 1.16. Indeed, a comparison of the IR+UV and OCT- approaches is provided in Article 3.5.3. Furthermore, for the particular cases of $\hat{O} = \hat{P}_{|\Phi_f\rangle}$ being a projection operator or a positive definite operator, rapid monotonically convergent algorithms[81,82] exist.

However, even if the system-environment coupling is taken into account by the algorithm,[83] OCT-schemes may have limitations in the laboratory, due to experimental noise or decoherence. OCT still remains the leading theoretical approach for identifying the structure of control fields,[53] and recently, the concept of *Quantum Control Landscapes*[84,85] has emerged to answer the question of why efficient control of diverse quantum systems is possible at all.

1.3.6. Adaptative feedback control

The facts that: (*i*) OCT-solutions depend strongly on realistic model Hamiltonians, and (*ii*) even if those solutions are accurate, the experimental uncertainties affect the robustness of the OCT-pulse, have paved the way to an alternative experimental formulation to quantum optimal control theory, proposed by Rabitz and coworkers in a seminal paper in 1992. The strategy proposed in *Teaching Lasers to Control Molecules*[86] is indeed the control scheme most widely implemented in the laboratory nowadays.[53] The experimental set-up proposed in Ref. 86 biases problems (*i*) and (*ii*) by directly allowing the molecular system *itself* to evaluate the fitness of a trial control field and optimize it *on-site* in the laboratory. The system iteratively improves that field through a fitness parameter in a feedback-loop until convergence is achieved. The elegant analogy[86] is that of the molecular system acting as an analog computer solving its own time-dependent Schrödinger Equation in real-time. A detector coupled to the system performs the readout of a control parameter, against which the fitness of the field is measured. This fitness is then fed back to the pulse-generator and the next pulse is corrected using genetic[87] or evolutionary[88] algorithms. A schematic representation of a generic setup of this type is depicted in Fig. 1.17.

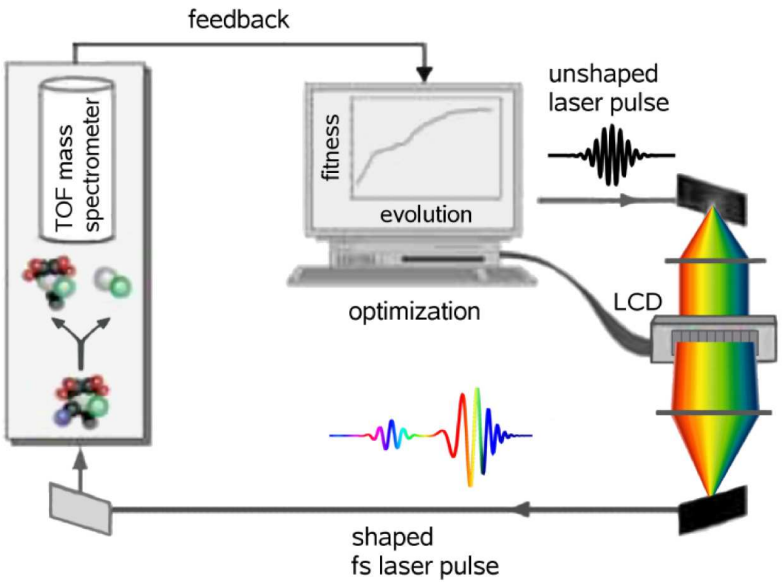

Figure 1.17.: General set-up of a closed-loop experiment. Figure kindly provided by Marquetand, P. (*Ph.D. thesis*, Julius-Maximiliams-Universität Würzburg (2007)).

The first reported experiment including this *adaptative feedback control* (AFC) is the optimization of the electronic population transfer by Wilson and coworkers[89] in 1997,

allowing for control of the fluorescence signal of a laser-dye. Further early optimizations include photodissociation reactions by Gerber and coworkers.[90,91] AFC photofragmentation experiments by Wöste and coworkers[92] were subsequently rationalized theoretically through a combination of femtosecond pump-probe spectroscopy and wavepacket propagations.[93] Very recently, Hill and coworkers[94] deciphered the underlying dynamics of an AFC-triggered Coulomb explosion. Of particular interest for this Thesis are AFC experiments on photoisomerizations, specifically of *cis-trans*-isomerizations. AFC experiments on the retinal molecule in the protein environment[14–16] have already been addressed in Section 1.1.2. Similar *cis-trans*-isomerizations have been controlled via AFC-strategies in cyianines in solution.[95,96] For the *cis-trans*-isomerization in Ref. 96, AFC-studies in Ref. 97 even use the optimally shaped *dump*-pulse itself to gain mechanistic insights about the isomerization process.

1.3.7. Laser control in molecular rotors

So far, control schemes in the context of molecular rotors have been only cited in the IR+UV example[73] in Section 1.3.4. Among other light strategies to control motors (see for instance the surface mounted motors of Michl and coworkers[98] or Engel and coworkers[99]), Fujimura and coworkers have proposed optimally shaped pulses for theoretical control schemes in molecular rotors. The systems used in these cases are chiral molecules where the asymmetry of the potentials along the coordinate of interest -typically the torsion of a double bond- already determines a natural or intuitive direction of rotation. In the weak-field regime, that built-in asymmetry is responsible for unidirectional rotation after a long (30 ps) IR-pulse.[100,101] The pulse is tuned to the average level spacing and is long enough to excite the torsional ground state until it has enough energy to overcome the torsional barriers. This strategy is a rather mode-selective-like approach, where, as stated before, the effects of IVR can hinder the rotation significantly. Indeed, when a system-bath coupling was included in the model,[102] the torsional momentum is hardly maintained even while the pulse is on. This effect was avoided, in a very similar chiral molecule, with a TRK-*pump-dump* scheme,[103] where, again, asymmetries in the potential (now in the excited state potential) determine a preferred direction of rotation when the *dump*-pulse is timed adequately. In this case, rotation had already started after ca. 200 fs. Finally, the authors also apply OCT to the same system[104] and show that both intuitive and counter-intuitive rotation of the motor can be achieved within 500 fs with two optimal pulses, respectively.

2. Theoretical Framework

2.1. The Schrödinger Equation

The time-dependent Schrödinger Equation (TDSE) was briefly introduced in Section 1.3.5 as the condition that the wavefunction has to satisfy in the J_3 functional (Eq. (1.11)) for the OCT constrained optimization. The condition that a wavefunction satisfies the TDSE is indeed imposed by the fifth postulate of quantum mechanics:[105]

> *The wave function or state function of a system evolves in time according to the time-dependent Schrödinger equation*

$$i\hbar\frac{\partial}{\partial t}\Psi(\vec{r},t) = \hat{H}(t)\Psi(\vec{r},t). \tag{2.1}$$

Equation (2.1) governs thus all dynamics of a nonrelativistic quantum system. In cases where the Hamilton operator $\hat{H}(t)$ is not explicitly time-dependent, time t and position $\vec{r}$ are separable, and the TDSE can be further operated to yield the time-independent SE (TISE):

$$\hat{H}\psi_n(\vec{r}) = E_n\psi_n(\vec{r}), \tag{2.2}$$

whose solution contains only time-independent information: the set of spatial wavefunctions $\{\psi_n(\vec{r})\}$ and eigenenergies $\{E_n\}$. Equation (2.2) is a linear eigenvalue problem for the operator $\hat{H}$, and the set of energy eigenvalues E_n constitute its spectrum. The subindex n is the quantum number of each state. The spatial wavefunctions $\psi_n(\vec{r})$ are the stationary states. These are modulated in time through their corresponding E_n-values via the phase factor $e^{-iE_nt/\hbar}$. The stationary states multiplied with the phase yield the total wavefunctions $\Psi_n(\vec{r},t)$:

$$\Psi_n(\vec{r},t) = \psi_n(\vec{r})e^{-iE_nt/\hbar} = \psi_n(\vec{r})e^{-i\omega_nt}, \tag{2.3}$$

where $\omega_n = \frac{E_n}{\hbar}$ has been used.

However, while evolving in time (Eq. (2.1)), the molecular quantum mechanical system is unlikely to be described only by *one* of the solutions given by Eq. (2.3). In fact, the most general solution to Eq. (2.1) is a superposition of different eigenfunctions $\Psi_n(\vec{r},t)$,

each of them weighted by the complex-valued coefficients C_n:

$$\Psi(\vec{r},t) = \sum_n C_n \Psi_n(\vec{r},t). \tag{2.4}$$

Equation (2.4) constitutes a wavepacket, that is, a linear combination of eigenfunctions with different energies and a given phase relation.

2.2. The Born-Oppenheimer Approximation

So far (Eqs. (2.1) to (2.4)), $\vec{r}$ has represented the whole set of molecular coordinates, both nuclear and electronic. These particles have also a coordinate in spin-space, but the spin has no further impact in the following formulation, and will be introduced *ad-hoc* for the electrons in Section 2.3.1.

The Born-Oppenheimer approximation assumes separability of the motion of nuclei and electrons by writing the time-independent molecular eigenfunctions as (cf. Eq. (2.2)):

$$\psi(\vec{r}) = \varphi_e(\vec{r}_e;\{\vec{R}_N\})\psi_N(\vec{R}_N), \tag{2.5}$$

where the subindices e and N denote *electronic* and *nuclear*, respectively. $\{\vec{R}_N\}$ indicates parametric dependence only. The subindex n has been dropped for succinctness; the following applies to any of the n-eigenfunctions.

Inserting Eq. (2.5) in the TISE (cf. Eq. (2.2)) yields two separate TISEs, the electronic TISE and the nuclear TISE, assuming that the terms proportional to the ratio of the masses of electron and nuclei are negligible. The electronic TISE depends on $\vec{r}_e$ explicitely and on the nuclear geometry $\vec{R}_N$ parametrically:

$$\hat{H}_e(\vec{r}_e;\{\vec{R}_N\})\varphi_e^i(\vec{r}_e;\{\vec{R}_N\}) = \varepsilon^i \varphi_e^i(\vec{r}_e;\{\vec{R}_N\}). \tag{2.6}$$

Solution of the electronic TISE yields the set of i electronic wavefunctions, $\varphi_e^i(\vec{r}_e;\{\vec{R}_N\})$, and electronic energies, ε^i, for a fixed molecular geometry $\vec{R}_N$. Typically, Eq. (2.6) is solved for the values of $\vec{R}_N$ that represent molecular geometries that are chemically most significant: equilibrium geometries, transition states, conical intersections, etc. When computationally feasible, Eq. (2.6) is solved for whole ranges of $\vec{R}_N$ along one or more nuclear coordinates of interest. The $\{\vec{R}_N\}$ geometries together with the respective $\{\varepsilon^i\}$ values constitute the potential energy surface (PES) for the chemical context of interest. The PES is a function of $\vec{R}_N$ and the equilibrium and transition state geometries are its critical points ($\nabla_{\vec{R}_N} = 0$), whereas -loosely speaking- the conical intersections are regions of the coordinate space at which the PESs of two or more electronic states are near-degenerated and nonadiabatic population transfer can occur. All these concepts (PES,

minima, transition states and conical intersections) have already been introduced briefly in the introduction, for example in Figs. 1.5 and 1.8.

Analogous to Eq. (2.6), within the Born-Oppenheimer approximation the nuclear TISE is:

$$\hat{H}_N(\vec{R}_N)\psi_N^\nu(\vec{R}_N) = E^\nu\psi_N^\nu(\vec{R}_N). \tag{2.7}$$

For brevity, the vibrational TISE for the nuclei is directly written, omitting the separation of internal and external degrees of freedom (see for instance Ref. 106). Henceforth $\vec{R}_N$ implies only relative displacements of the nuclei with respect to each other, that is, internal vibrations. It follows that in Eq. (2.7) the index ν is the quantum number denoting vibrational states.

The nuclear Hamiltonian is composed by the kinetic energy term $\hat{T}$ and the potential energy term $\hat{V}$:

$$\hat{H}_N(\vec{R}_N) = \hat{T}(\vec{R}_N) + \hat{V}(\vec{R}_N). \tag{2.8}$$

It is through the latter term that the electronic information emerging from Eq. (2.6), the electronic $\varepsilon(\vec{R}_N)$-values of the PES, enter the nuclear TISE, because the effective potential that the nuclei are subject to is defined as:

$$\hat{V}(\vec{R}_N) = \varepsilon(\vec{R}_N) + \hat{V}_{NN}(\vec{R}_N), \tag{2.9}$$

where $\hat{V}_{NN}$ is the repulsive potential between nuclei. Solution of Equation (2.9) demands the PES to be known for a given range of $\vec{R}_N$ for the number of electronic states i of interest. Hence, the PESs are the junction between electronic and nuclear TISEs. In the following paragraphs, the problem of solving the nuclear and electronic SE is addressed.

2.3. Solutions to the Schrödinger Equation

The first postulate of quantum mechanics states that everything that there is to know about a quantum mechanical system is contained in its wavefunction[105] and the fifth postulate states which differential equation that function has to obey. Hence, the full description of a quantum mechanical system is achieved once the corresponding differential equation is solved: the SE (nuclear or electronic, time-dependent or time-independent). The SE cannot, however, be solved exactly in most of the cases without introducing further approximations. Because of that, diverse approaches and techniques arise, each of them adapted to the needs of the quantum problem at hand. In the present Thesis, the problems directly related with solving the SE are:

- obtaining the wavefunctions and energies describing the electronic states of a molecule in order to compute photophysical properties and explain its photochemical behavior.

- describing the torsional dynamics of a molecule, both in the absence and presence of external fields, in order to follow photochemical events and further manipulate them with laser control schemes.

The electronic problem in the first point is addressed by quantum chemistry, which provides a manifold of methodologies to tackle the same problem: solving the electronic TISE. These methods vary in complexity and accuracy. They are implemented in most of the commercial quantum chemistry packages, which have been properly referenced in the Articles 3.5.1 to 3.5.3. A brief overview of the methods used in this Thesis is provided in Section 2.3.1.

The second point falls into the realm of quantum dynamics. The methods at hand are also well-known, and the reader is referred to Refs. 107 and 108 for an overview on available techniques to perform quantum dynamical computations. However, the codes to perform these calculations are less standardized than those for electronic structure calculations, and codes that handle wavepacket propagations with arbitrary Hamilton operators are not widespread. The program WAVEPACKET[109] provides a flexible tool for many simple molecular cases, and in this Thesis many preliminary computations were carried out using this software. However, most of the programs used to solve quantum dynamical problems are written from scratch, implementing selected methodologies from Refs. 107 and 108. These codes are included in the Appendix, each one with a brief description. Section 3.4 provides the mathematical background in the context of the specific quantum dynamical problems treated in this Thesis.

Besides the codes used to solve problems related with the SE, other programs have been developed, most importantly for the pseudo-random conformational search. They have contributed to an effective workflow and data-treatment but they are not included in the publications of Section 3.5. For completeness, these codes have been included in the Appendix with lengthier descriptions for further details..

2.3.1. Quantum chemical methods

The electronic structure methods used in this Thesis can be divided into two different categories: methods which employ wavefunction-based approaches (*ab initio*-methods) and density-based approaches (Density Functional Theory, DFT). The aim of this Section is not to provide the detailed mathematical background to the methods themselves, but rather to outline briefly the chemical concepts and ideas behind the used methods. Further details are provided in Articles 3.5.1 to 3.5.3, and in Section 3.2. The reader is referred to Refs. 110–112 and Refs. therein for completeness.

2.3.1.1. Wavefunction-based methods

Wavefunction-based methods rely on the Hartree-Fock (HF) initial wavefunction:

$$|\varphi_{HF}(\overline{r_{e1}}, \overline{r_{e2}}...\overline{r_{eN_{el}}})\rangle = \frac{1}{\sqrt{N_{el}!}} \begin{vmatrix} \chi_1(\overline{r_{e1}}) & \chi_2(\overline{r_{e1}}) & \dots & \chi_{N_{el}}(\overline{r_{e1}}) \\ \chi_1(\overline{r_{e2}}) & \chi_2(\overline{r_{e2}}) & \dots & \chi_{N_{el}}(\overline{r_{e2}}) \\ \dots & \dots & \dots & \dots \\ \chi_1(\overline{r_{eN_{el}}}) & \chi_2(\overline{r_{eN_{el}}}) & \dots & \chi_{N_{el}}(\overline{r_{eN_{el}}}) \end{vmatrix} = |\varphi_{HF}\rangle\,. \quad (2.10)$$

Equation (2.10) is a Slater-determinant (an antisymmetrized product) of one-particle spin-orbitals, $\chi_j(\overline{r_{ei}})$, which depend only on the coordinates of the i-th electron. The overlined coordinates represent both position and spin-state. These spin-orbitals are in turn product of the spatial orbitals, $\Theta_j(\vec{r}_{ei})$, and the spin-eigenfunctions $\overline{\alpha}$ and $\overline{\beta}$:

$$\chi_j(\overline{r_{ei}}) = \Theta_j(\vec{r}_{ei}) \cdot \begin{cases} \overline{\alpha} \\ \overline{\beta} \end{cases} . \quad (2.11)$$

The HF-approximation is an approximation central to modern chemistry. It provides the simple -yet powerful- picture of electrons occupying molecular orbitals (MOs) that spread all over the molecule. The HF-approximation is equivalent to the MO-approximation, which together with the *ansatz* of linear combination of atomic orbitals (LCAO), defines the playground for most electronic structure calculations, and thus shapes the way in which most quantum chemists think.

The LCAO-*ansatz* expands the spatial part of the spin-orbitals in the basis of N_B atomic orbitals $\theta_k(\vec{r}_{ei})$:

$$\Theta_j(\vec{r}_{ei}) = \sum_k^{N_B} \kappa_{kj} \theta_k(\vec{r}_{ei}). \quad (2.12)$$

Hence, the choice of an appropriate basis set of AOs for Eq. (2.12) lies ahead of the calculation itself. A short discussion on how this choice affects the outcome of the calculation is provided in Section 3.2.

Inserting Eq. (2.12) in Eq. (2.11), results in a Slater-determinant (Eq. (2.10)) function of the expansion coefficients κ_{kj}. The many-particle electronic Hamiltonian $\hat{H}_e(\vec{r}_e)$ is written as a Hartree-Fock-Hamiltonian $\hat{H}^0(\vec{r}_e)$, sum of the N_e one-particle Fock-operators:

$$\hat{H}_e(\vec{r}_e) \approx \hat{H}^0(\vec{r}_e) = \sum_i^{N_e} \hat{f}(\vec{r}_{ei}) = \sum_i^{N_e} \hat{f}_i. \quad (2.13)$$

Substitution of the Slater-determinant (Eq. (2.10)) and the HF-Hamiltonian (Eq. (2.13)) in the electronic TISE (Eq. (2.6)) gives rise to the Roothan-Hall[113,114] equations, which in the HF-method are solved iteratively until the electronic energy has converged to a

minimum value ε^i_{HF}. By virtue of the variational principle,[115] that value represents an upper bond for the exact value of ε^i. The other part of the solution emerging from a HF-calculation is the set of converged expansion coefficients κ^{HF}_{kj} that are used to construct the electronic wavefunction (recall Eq. (2.12)). Ideally, at the end of the iterative HF-procedure, these coefficients do not change from one iteration to the next one, so that the HF-method is included in the group of self consistent field (SCF) methods.

Most molecules are closed-shells in the electronic ground state at the equilibrium geometries, and HF usually provides qualitatively good results for these type of situations. As such, HF is very illustrative for basic electronic structure concepts. However, HF fails to account for open-shell situations (excited states, bond dissociations, or higher spin multiplicities etc). For these cases, modified versions of the HF-method exist, such as unrestricted HF (UHF) or restricted open-shell HF (ROHF). The restriction consists in the optimization of only one spatial orbital for both the $\overline{\alpha}$- and the $\overline{\beta}$-electron of a given spin-orbital (recall Eq. (2.11)). However, none of these HF-methods can describe satisfactory the correlated motion that electrons actually perform. The amount of correlation lacking in a HF-calculation can be expressed as the difference between the exact electronic energy solution to Eq. (2.6) and the HF-energy[1]:

$$E_{corr} = \varepsilon - \varepsilon_{HF}. \tag{2.14}$$

This lack of correlation in the HF-picture has motivated the development of post-HF-methods for accurate energy values. The post-HF-methods provide a more flexible description that aims at recovering the correlation energy lacking in the single-determinant HF-description. An overview of the post-HF methods used in this Thesis follows. Comprehensive monographs on quantum chemical methods in general can be found in Refs. 110 and 112.

Multiconfigurational approaches: from CI to CASSCF Within the variational *ansatz*, the SCF-methodology can be systematically extended by constructing the trial wavefunction with more than one Slater-determinant. To do so, the simplest approach is to use the already available unoccupied MOs emerging from a preceding HF-calculation. The new Slater-determinants can be created by promoting one electron from an occupied MO (a) to a virtual (unoccupied) MO (b), where the indices a and b run over all available occupied and virtual MOs, respectively. Such excitations give rise to the singly excited configuration state functions (CSFs): $\sum_{a,d} |\varphi^d_a\rangle$. Analogously, doubly ($\sum_{\substack{ab\\de}} |\varphi^{de}_{ab}\rangle$) as well triply ($\sum_{\substack{abc\\def}} |\varphi^{def}_{abc}\rangle$) excited CSFs can be created. Extending this treatment to all possible

[1] The index i-denoting electronic state is dropped.

excitations, the full configuration interaction (FCI)-vector can be constructed:

$$|\varphi_{FCI}\rangle = C_{HF}\,|\varphi_{HF}\rangle + \sum_{a,d} C_a^d\,|\varphi_a^d\rangle + \sum_{\substack{a<b\\d<e}} C_{ab}^{de}\,|\varphi_{ab}^{de}\rangle + \sum_{\substack{a<b<c\\d<e<f}} C_{abc}^{def}\,|\varphi_{abc}^{def}\rangle + \ldots \quad . \tag{2.15}$$

The brute force approach is then to initiate a variational SCF-procedure seeking the convergence of the coefficients in Eq. (2.15) to produce an electronic energy value ε_{FCI} even closer to the exact ε. It is brute force because no chemical intuition is used to reduce the huge number of Slater-determinants available *a priori*, and the algorithm is forced to devote equivalent amount of computational effort on each of the possible CSFs of Eq. (2.15). More important, however, is the qualitative jump between a monodeterminantal description of HF and the multideterminantal CI-vector, which can accommodate closed-shell and open-shell CSFs simultaneously. This provides an excellent tool for the computation of excited electronic states. However, the FCI-method is rarely employed except for small molecules and small basis sets.

A chemically conscious reduction of the CSF-space represent the methods in which only single (CIS) or double (CISD) excitations are included in the CI-vector, as is done in the CIS- and CISD-methods, respectively. Beyond the purely intuitive assumption that higher excitations (triple, quadruple, etc) are very unlikely to contribute to the lower-lying electronic states, it can be proven via perturbation theory that most of the corrections to the electronic energy (recall Eq. (2.14)) and one-electron properties are already accomplished with single and double excitations (see Section 13.21 of Ref. 110 and references therein).

The multiconfiguration SCF-method (MCSCF) further implements the spirit of the variational principle. Not only the CI-coefficients of Eq. (2.15) are optimized, but the MOs contained in the CSFs are optimized in the SCF-iteration as well, so that ultimately the initial expansion coefficients κ_{kj}^{HF} are refined from their HF-values. Nevertheless, if guided by the variational principle alone, the MCSCF-procedure also results computationally very expensive, because no discrimination among the available CSFs is done. The complete active space-SCF (CASSCF[116]) offers the possibility to use the chemical knowledge about the system to reduce *a priori* the number of CSFs included in an MCSCF-calculation.

The advantage of the CASSCF-approach lies in the criterion to reduce the number of CSFs. Rather than truncating the CI-expansion at a certain amount of excitation (as do the CIS-, CID-, or CISD-methods), CASSCF allows for the selection of active orbitals which are very likely to play a role in the chemical context of interest. The partition of the available MOs into inactive, active, and virtual is represented in Fig. 2.1.

Once the AS has been chosen (as in Fig. 2.1), an FCI-vector $|\varphi_{CAS}\rangle$ is constructed within the AS (hence, complete AS). Subsequently, a MCSCF-calculation takes place with that CI-vector, so that the MOs in the CSFs and the coefficients of the CI-vector are optimized.

The key aspect in a CASSCF-calculation, besides the basis set, is the choice of the MOs

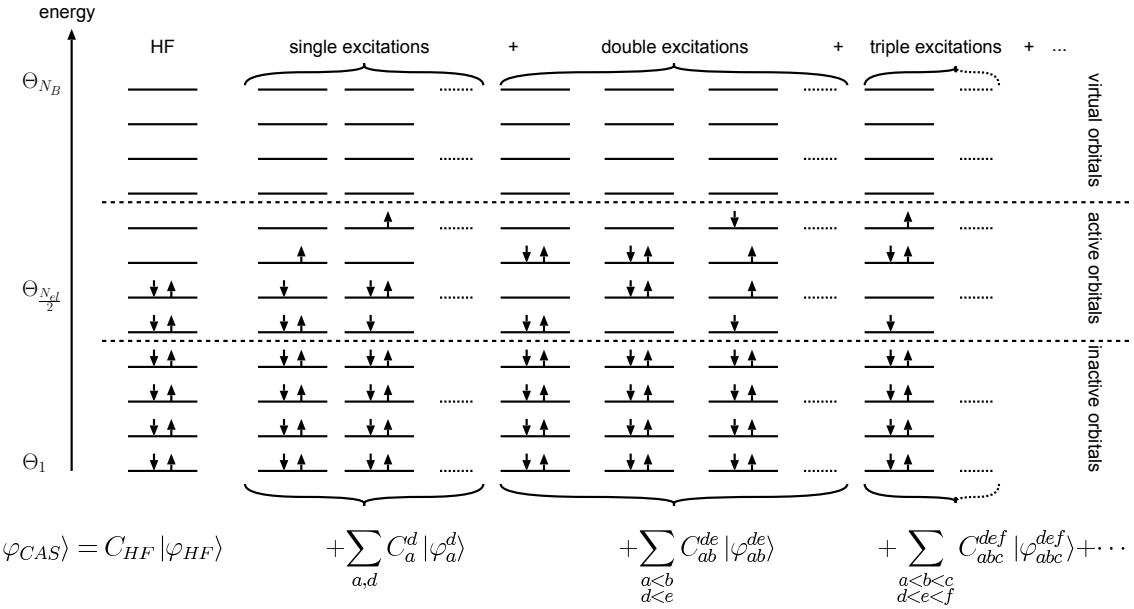

Figure 2.1.: Schematic representation of the MO-partition in the CASSCF-approach. An AS of 4 electrons in 4 orbitals (CAS(4,4)) is shown. Representative single, double, and triple excitations have been chosen. The CASSCF-procedure performs an FCI-calculation within the (4,4)-AS. Thus, the CAS-wavefuntion $|\varphi_{CAS}\rangle$ is expressed in terms of a CI-expansion (cf. Eq. 2.15).

of the AS. The AS has to represent the chemical situation of interest, and the CASSCF-results are very sensitive to this choice. The most prominent example is the computation of excited states of organic compounds. These can be computed accurately at a reduced computational cost, typically by including whole π-systems (the frontier orbitals) in the AS while excluding σ-system. This way, high-level wavefunctions are obtained, which produce high-quality one-electron properties such as polarizabilites or transition dipole moments.

A refinement of the CASSCF-method exists to further reduce the number of CSFs in the CI-vector, and ultimately the computational cost: the restricted CAS-method (RASSCF). In this approach, CFSs are not constructed indiscriminately as FCI in the AS. Instead, the AS is subdivided into RAS1-, RAS2-, and RAS3-subspaces. FCI is performed only in the RAS2-subspace, whereas in the RAS1-subspace only a limited number of *holes* (number of excited electrons) per CSF is allowed. Analogously, only a limited number of electrons are allowed in the RAS3-subspace.

Perturbative approaches: from MP2 to CASPT2 Basing upon the variational solutions to the electronic TISE, a number of perturbative treatments exist. These approaches correct energies and wavefunctions to a given order beyond the variational limit. One of the most widespread formalisms is the second order Møller-Plesset (MP2) perturbation the-

ory.[117,118] The perturbation $\hat{H}'$ is defined as the difference between the HF-Hamiltonian (Eq. (2.13)) and the true electronic Hamiltonian (Eq. (2.6)):

$$\hat{H}' = \hat{H}_e - \hat{H}^0. \tag{2.16}$$

Within MP2, the expression for the second order energy for the electronic ground state is:[110]

$$\varepsilon_0^{(2)} = \sum_{j \neq 0} \frac{|\langle \varphi_j^{(0)} | H' | \varphi_{HF} \rangle|^2}{\varepsilon_0^{(0)} - \varepsilon_j^{(0)}}, \tag{2.17}$$

where $|\varphi_j^{(0)}\rangle$ are all possible unperturbed Slater-determinants except $|\varphi_{HF}\rangle$, and $\varepsilon_j^{(0)}$ is the unperturbed energy of the j-th Slater-determinant. In MP2-calculations, the corrected wavefunctions are first order perturbations of the HF-determinant.

The MP2-procedure is one of the most widely used quantum chemical methods, mainly because of two reasons: the low computational cost with respect to comparable CI-calculations and the facility with which gradients along the PES are computed analytically. Accordingly, MP2-optimizations are typically the procedure of choice when optimizing ground state closed-shell geometries.

The perturbative treatment can be extended not only to wavefunctions of a single determinant. A multiconfigurational wavefunction can also be used as the unperturbed (zeroth-order) reference for a generalized perturbative approach. In the CASTP2-method[119,120] second order perturbation theory is applied to a CASSCF-reference wavefunction. The obtained energy correction provides a high-quality estimate of the FCI-energy. In addition, CASPT2 handles open-shell situations accurately, because it bases upon a multiconfigurational wavefunction. This makes the combined CASPT2/CASSCF-approach a powerful tool in photophysical calculations (or any other open-shell situations) for medium-sized molecules. It delivers (*i*) high-quality wavefunctions, and thus high-quality one-electron properties, and (*ii*) highly accurate ($\pm$ 2 kcal/mol[121]) electronic energies. CASPT2/CASSCF-calculations are not, however, black box calculations, as are MP2- or CI-calculations. One has to bear in mind that CASPT2 only perturbs a reference wavefunction which is optimal within a given AS and a given basis set. Thus, CASSCF/CASPT2 results depend strongly on these choices (AS and basis set) being adequate. A measure for adequacy is a high weight of the original CASSCF-reference wavefunction in the obtained first order perturbed wavefunction.

State-averaged-CASSCF and multi-state-CASPT2 When computing excited states separately, the problem arises that separate state-specific calculations (e.g., one for the ground and one for the first excited state) produce electronic states which are not necessarily orthogonal to each other. This situation is unphysical, since nondegenerate solutions to the

eigenvalue problem posed by the electronic TISE (Eq. (2.6)) must be strictly orthogonal to each other. This artifact is not decisive if the solutions to Eq. (2.6) are energetically far apart from one another, a case typical for ground state geometries. However, in many photochemical situations, most prominently the vicinities of conical intersections, electronic states are close in energy, and single-state variational SCF-procedures fail at resolving *two* different solutions if only *one* of them is actually being optimized. The state emerging from such calculations is usually *contaminated* with the one lying close in energy.

The near-degeneracy problems vanish in state-averaged CASSCF-calculations (SA-CASSCF), where a given number of electronic states is optimized simultaneously in the MCSCF-procedure. Apart from yielding a more physical picture (electronic states are orthogonal), the obtained states are described with the same set of MOs and differ only in the variationally optimized CI-coefficients.

The SA-CASSCF-energies and wavefunctions can be further refined with a CASPT2-calculation for each state in the average (each root). However, for situations in which electronic wavefunctions are mixed with one another at SA-CASSCF level, the multi-state-CASPT2 (MS-CASPT2[122]) is strongly recommended. An effective Hamiltonian is set up, in which the different SA-CASSCF states are coupled at second order. Subsequent diagonalization of this Hamiltonian produces a set of new wavefunctions and energies. The wavefunctions are linear combinations of the original SA-CASSCF states, called perturbatively-modified CASSCF-wavefunctions (PMCAS-CI). The energies are the final MS-CASPT2-corrected energy values. In this manner, the mixing in the original SA-CASSCF-wavefunctions is lifted in the PMCAS-CI wavefunctions.

2.3.1.2. Density functional methods

Two theorems by Hohenberg and Kohn provide the theoretical foundations[123] for DFT calculations. The first, HK-I, states that all molecular electronic properties (including energy and wavefunction) are uniquely determined by the electronic ground state electron density $\rho_0(x, y, z)$. The electronic ground state energy ε^0 becomes a functional of ρ_0:

$$\varepsilon^0 = \varepsilon^0[\rho_0]. \tag{2.18}$$

The second theorem, HK-II, also called the HK-variational theorem, states that the true ground state electronic density $\rho_0(x, y, z)$ minimizes the energy functional, so that the inequality

$$\varepsilon^0[\rho_0] = \varepsilon^0 \leq \varepsilon^0[\rho_{TR}], \tag{2.19}$$

holds for every trial density ρ_{TR}. These two theorems open the door to a non-wavefunction-based approach, in which the magnitude of interest depends only on three coordinates, and not on $3N_e$ coordinates.

The HK-theorems do not provide, however, a form to obtain ε^0 from ρ_{TR}, because the form of the functional is unknown. Kohn and Sham[124] introduced the idea of representing the electron density through an auxiliary set of orbitals, providing an implementation of DFT conceptually and computationally very similar to the HF-procedure. In the KS-formulation, the only unknown left in the functional, $\varepsilon_{DFT}[\rho]$, is the the exchange-correlation part $\varepsilon_{xc}[\rho]$:

$$\varepsilon_{DFT}[\rho] = T[\rho] + \varepsilon_{eN}[\rho] + J[\rho] + \varepsilon_{xc}[\rho], \tag{2.20}$$

where $T[\rho]$ is the kinetic energy part, $\varepsilon_{eN}[\rho]$ the electron-nuclei repulsion, and the $J[\rho]$ Coulomb part.

A number of quality functionals have been developed over the years, differing in their ways of constructing the exchange-correlation part $\varepsilon_{xc}[\rho]$. Hybrid functionals include a part of exact correlation (calculated from the Slater-determinant set up by the KS-orbitals), and the rest fitted to experimental data. Their main advantage is the possibility to include correlation effects in a calculation that costs roughly as much as a HF-calculation. Among these, one of the most widely used is the three-parameter functional B3LYP introduced by Becke,[125] which mixes the exact HF-exchange part with other DFT exchange-correlation parts arising from the Lee-Yang-Parr[126] (LYP) and Vosko-Wilk-Nusair[127] (VWN) functionals.

However, DFT presents some known deficiencies. Apart from the impossibility to systematically improve the accuracy, the vast majority of functionals do not predict properly weak dispersive interactions, such as van der Waal interactions. Furthermore, the partition of the functional in the form Eq. (2.20) is inherently local, so that charge-transfer states are described poorly as well. A detailed monograph on performance and applicability of DFT can be found in Ref. 128.

3. Results

This Section is organized as follows. Sections 3.1 to 3.3 present the most important results of this THESIS in form of *standalone* summaries of their respective Articles, which in turn are presented in Section 3.5 as facsimiles[1]. In Section 3.4 quantum dynamical implementations for Sections 3.1 to 3.3 are presented beyond the details of their respective Articles.

Theoretical investigations have been carried out on the following molecules:

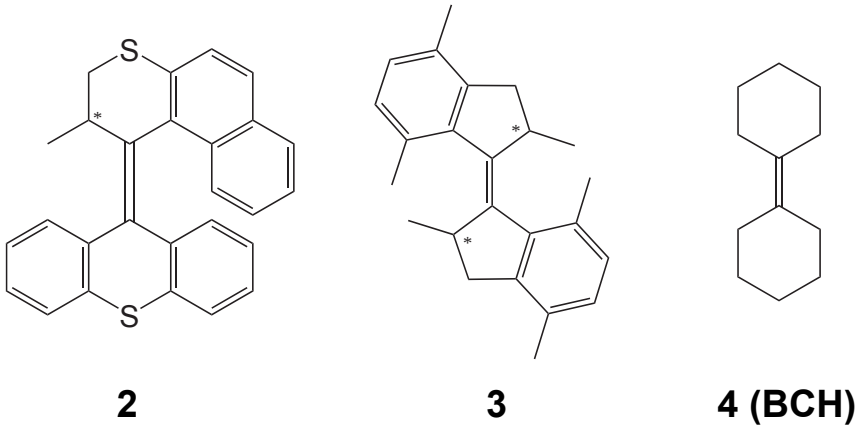

Figure 3.1.: Molecular motors treated in the present THESIS: **2** and **3** are chiral overcrowded alkenes experimentally proven as unidirectional motors. **4** (BCH) is a proposed model system. The asterisks in **2** and **3** mark the chiral centers.

Motor **2** was chosen as a representative of the second-generation molecular motors because it was the first motor of this type to be crafted on surfaces. As mentioned in the introduction (Section 1.2.3), this anchorage is significant for nanotechnological development, such as the manufacture of nano-arrays. But beyond direct nanotechnological application, the anchorage can also be convenient on a molecular scale. First, it provides a possible escape from the Brownian motion surrounding the motor. And secondly, and more relevant for the envisioned laser control processes, the anchorage provides a preorientation of the molecules, making polarized laser interaction more efficient.

Motor **3** belongs to the class of redesigned motors, and it is attractive because it is the motor with the smallest aromatic system showing unidirectionality reported so far. This

[1]The permission of the respective copyright owners has been granted.

fact becomes relevant when considering the electronic structure calculations aimed at characterizing accurately the ground and excited state dynamics, given that the computational cost of these calculations grows exponentially with the size of the systems treated.

Motor **4**, 1,1'-bicyclohexylidene, BCH in short, is a model mimicking the larger systems **2** and **3**. It was chosen to study light-induced dynamics. BCH bears a bistable moiety at its core, analogous to **2** and **3**. Two different isomers exist (*syn*-BCH and *anti*-BCH), and they are interconvertible not only through heat but also through the light-triggered isomerization of the double bond, making BCH a suitable candidate for the investigation of laser-ignited rotatory motion.

The results are presented initially as a comprehensive conformational study of the rotors **2** and **3** (Section 3.1). A number of local minima and transition states are located on a rich ground state potential energy surface. Thus, in Section 3.2 , the simpler model BCH is investigated. An explanation for the controversial UV-spectrum of BCH is provided, and then, strategies for laser control follow in Section 3.3. There, unidirectional rotation of one of the halves of BCH is triggered with diverse laser pules, calculated using both OCT (cf. Section 1.3.5) as well as the more intuitive IR+UV-strategy (cf. Section 1.3.4).

3.1. Ground State Conformations of Overcrowded Alkenes

A conformational study of the motors **2** and **3** is carried out developing a pseudo-random method, as described in Article 3.5.1. The programs written to this end are provided in the Appendix for further detail.

In order to better characterize and understand the thermal steps of the rotatory cycle and its unidirectionality, all possible local minima and transition states (TSs) on the ground state PES are probed. The used method is based on a Monte-Carlo strategy, since it relies on a set of randomly generated initial geometries for subsequent optimization.

The initial geometries are generated by partially perturbing the available X-ray parameters of **2** and **3** within a scalable interval of their equilibrium values. In this context, *partially* means that not all degrees of freedom (DOFs) are subject to the random perturbation, but only those DOFs whose contribution to the rotatory dynamics might be most significant. Chemical intuition has thus to enter the pseudo-random method at this point. The choice of the randomized DOFs must provide the algorithm with enough variability as not to be trapped on a local minimum of the PES. For **2** and **3**, the randomized DOFs are: the length of the central double bond, the dihedral angles governing the boat-chair conformations of the central ring-moieties, and the position of the methyl groups on these rings.

The randomized DOFs, Q, are obtained using the perturbation:

$$Q = Q_0 + \mathcal{R} \cdot \omega \cdot I, \tag{3.1}$$

where Q_0 is the DOF's original value and $\mathcal{R}\cdot\omega\cdot I$ is the perturbation performed upon it. $\mathcal{R}$ is a random number $\epsilon\,[-.5,+.5]$, ω is the *step* or weighting parameter, and I is the interval available to Q_0 (I is different for bond-distances, bond-angles, and dihedral angles). After randomizing the starting geometry, an optimization and a frequency calculation follow at semiempirical level of theory (AM1 as implememented in MOPAC[129]). The procedure is repeated until a number N_G of geometries have converged to local minima of the PES. The converged geometries can be evaluated while the algorithm is continuously running: their heats of formation are collected and analyzed in form of a histogram. The pseudo-random method iterates until the histogram is considered converged.

In order to assess statistical effects and variability, the robustness of the method is investigated with respect to N_G and ω, respectively, before their values for the conformational search are chosen. It is found that, for a fix ω-value, the histogram already adopts a consistent form after 100 converged geometries. This form is conserved as N_G increases, specially in the energy region close to the original geometry. The majority of the local minima that are accessible to the algorithm (for a given ω) are already present in the sample after a relatively small amount of optimizations. Larger N_G-values only result in more individual conformers per local minimum. ω governs the number of unique local minima accessible to the algorithm. The histogram evolves from a single bar ($\omega = .25$), to a spread spectrum of geometries ($\omega = 1.0$). With increasing randomness, the chemical intuition used in the choice of the randomized DOFs is canceled out, because constitutional isomers begin to populate the sample. However, the rotatory cycle is not intended to produce constitutional isomers at any stage. Quick browsing of the individuals of the histograms with the molecular visualization program MOLDEN[130] provides a good estimate of the ratio of stereo-/constitutional-isomers in each sample, a factor that can be considered a signal-to-noise ratio of the histogram.

After testing different values of N_G and ω, the parameters chosen for the pseudo-random searches are $N_G = 1000$ and $\omega = .75$. Elimination of redundancies and constitutional isomers in the samples of **2** and **3** (see Appendix for the corresponding codes) leads to six and seven unique individuals, respectively. Subsequent MP2/6-31G(d) geometry optimization of these individuals produces the refined geometries shown in Fig. 3.2a-f and Fig. 3.3a-d for **2** and **3**, respectively. The obtained MP2/6-31G(d) geometries are in very good agreement with the available X-ray structures in both motors.

In the case of **2**, five additional geometries are recovered besides the starting structure, which is typically called the *stable*-isomer in the rotatory cycles. The Newman projection along its central olefinic bond shows the least distorted olefinc plane. Two more conformers (panels b and c) lie ca. 4-6 kcal/mol higher in energy, with central planes slightly more distorted. From the point of view of the steric hindrance, structures **2a**[2] and **2b** differ

[2]From now on, structures of **2** and **3** are noted according to their respective panels in Figs. 3.2 and 3.3, respectively.

mostly in the orientation of the methyl group. Whereas in the *stable*-form, **2a**, the methyl group is pointing out from the *fjord*-region in axial orientation, its equatorial orientation in the *unstable*-form, (**2b**), results in a destabilization of ca. 4 kcal/mol. In **2c**, the methyl-group is again axial, however a larger destabilization arises from the outer cyclic moieties of stator and rotator being on the same side of the central olefinic plane. Structures **2a**, **2b**, and **2c** have been already assigned to the known stations of the rotatory cycle:[131] the *unstable*-isomer **2b** is the photoproduct of the irradiation of **2a** with UV-light, whereas **2c** is an intermediate (not isolated yet experimentally) in the thermal reversion **2b**→**2a**. Furthermore, a group of three structures destabilized about 11 kcal/mol over the *stable*-isomer are found by the pseudo-random search (panels d-f in Fig. 3.2). The respective Newman projections show very distorted olefinic planes joining stator and rotator, with a twist in the double bond of up to 30° in the case of **2f**. These three structures had not been reported so far in the literature to the best of our knowledge. Their role in the rotatory cycle becomes more clear when the TSs are computed.

For **3**, two pseudo-random searches are performed separately with two available X-ray starting geometries, one for the *cis*- and one for the *trans*-isomer. The searches yield equivalent histograms containing the same isomers. After filtering the samples for redundancies and constitutional isomers, a total of seven unique isomers are found. Among them are three diastereomers, where the the absolute configuration of one chiral center has switched during the geometry randomization. These local minima do not participate in the rotary cycle and as such they are not discussed here. The remaining MP2/6-31G(d)-refined structures are shown in Fig. 3.3a-d. The structures in panels a-d are assigned to the stations of the rotatory cycle of **3**. The assignment of structures **3a** and **3b** is immediate, since they are the X-ray starting structures. They have been isolated experimentally as the *stable*-isomers of the cycle[132] (*cis*- and *trans*-isomer, respectively). In them, the methyl-groups are pointing out of the *fjord*-region in axial configuration. The structures **3c** and **3d** are the *unstable*-isomers of the cycle, products of the UV-irradiation of **3b** and **3a**, respectively. In them, the methyl-groups adopt an equatorial orientation leading to more steric hindrance in the *fjord*-region. The geometries show very good agreement with the available X-ray parameters. All four structures present strained central olefinic planes, with both twisted and folded distortions up to 30°. Furthermore, the central double bond is slightly elongated (ca. 0.1 Å) in the *unstable*-isomers (cf. **3a** *vs* **3c** in Fig. 3.3), as a consequence of the increased steric hindrance in the *fjord*-region.

Once the pool of local minima has been generated for **2** and **3**, possible reaction pathways are investigated through the optimization of TSs between the local minima. TS optimizations are much more sensitive to the starting geometries than the regular minimum optimizations. The algorithms envisioned to generate starting TS geometries typically interpolate iteratively between product and reactants until a suitable guess is found. The

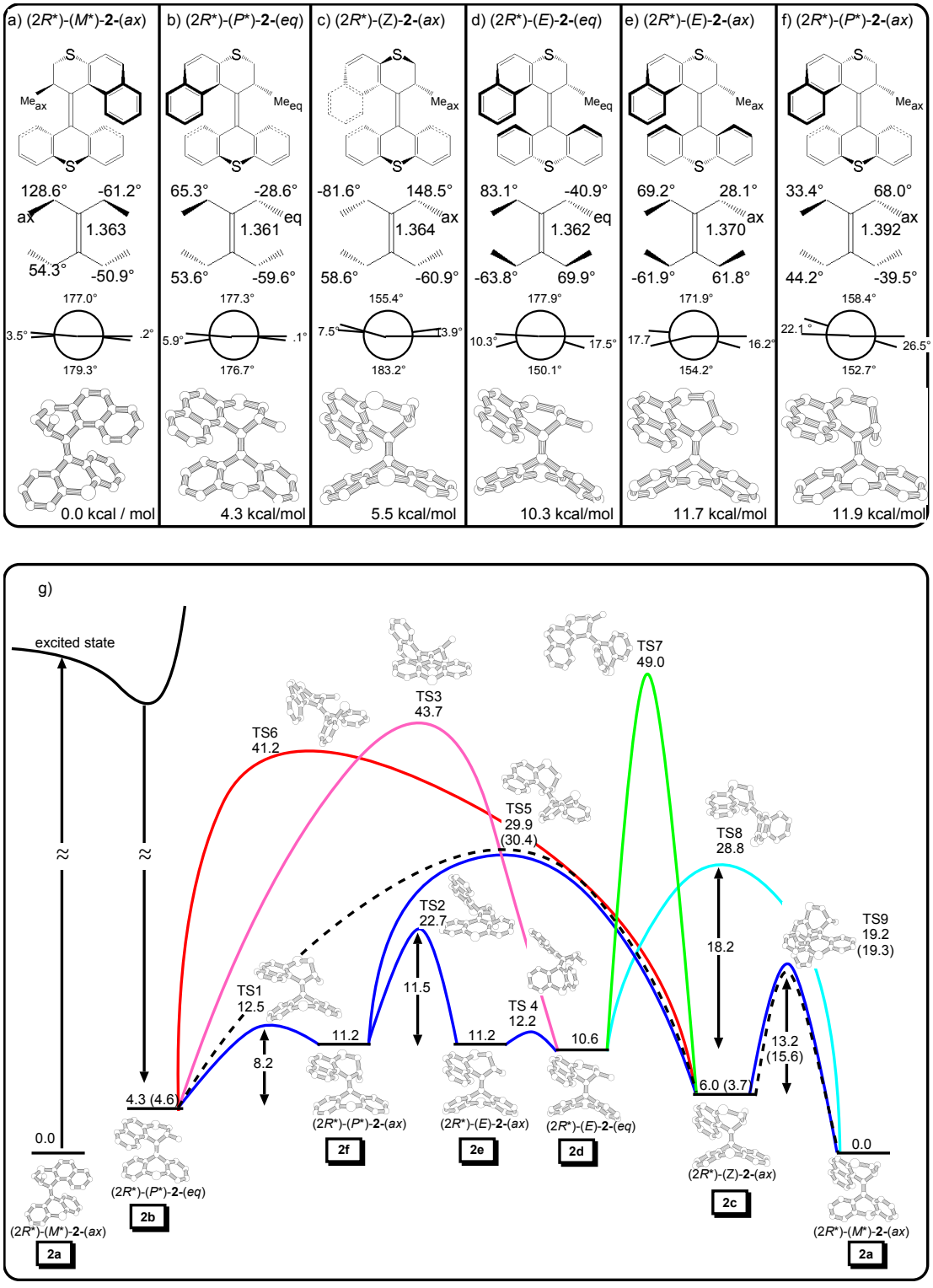

Figure 3.2.: Upper panels (a-f): MP2/6-31G(d)-geometries of **2**. The dihedral angles correspond to the moieties attached to the central double bond. The Newman-projections are along that same bond. Bond-distances are in Å and dihedral angles in degree. Relative MP2/6-31G(d)-stabilities are shown at the bottom of each panel. Lower panel (g): RI-MP2/TZVP energies of the B3LYP/6-31G(d) geometries of the six equilibrium conformers of **2** and the corresponding transition states between them. Energies are given in kcal/mol. Values in parenthesis are taken from Ref. 131. Dashed lines refer to the pathway suggested in Ref. 131. The labels **2a**-**2f** correspond to the upper panels. Adapted from Article 3.5.1.

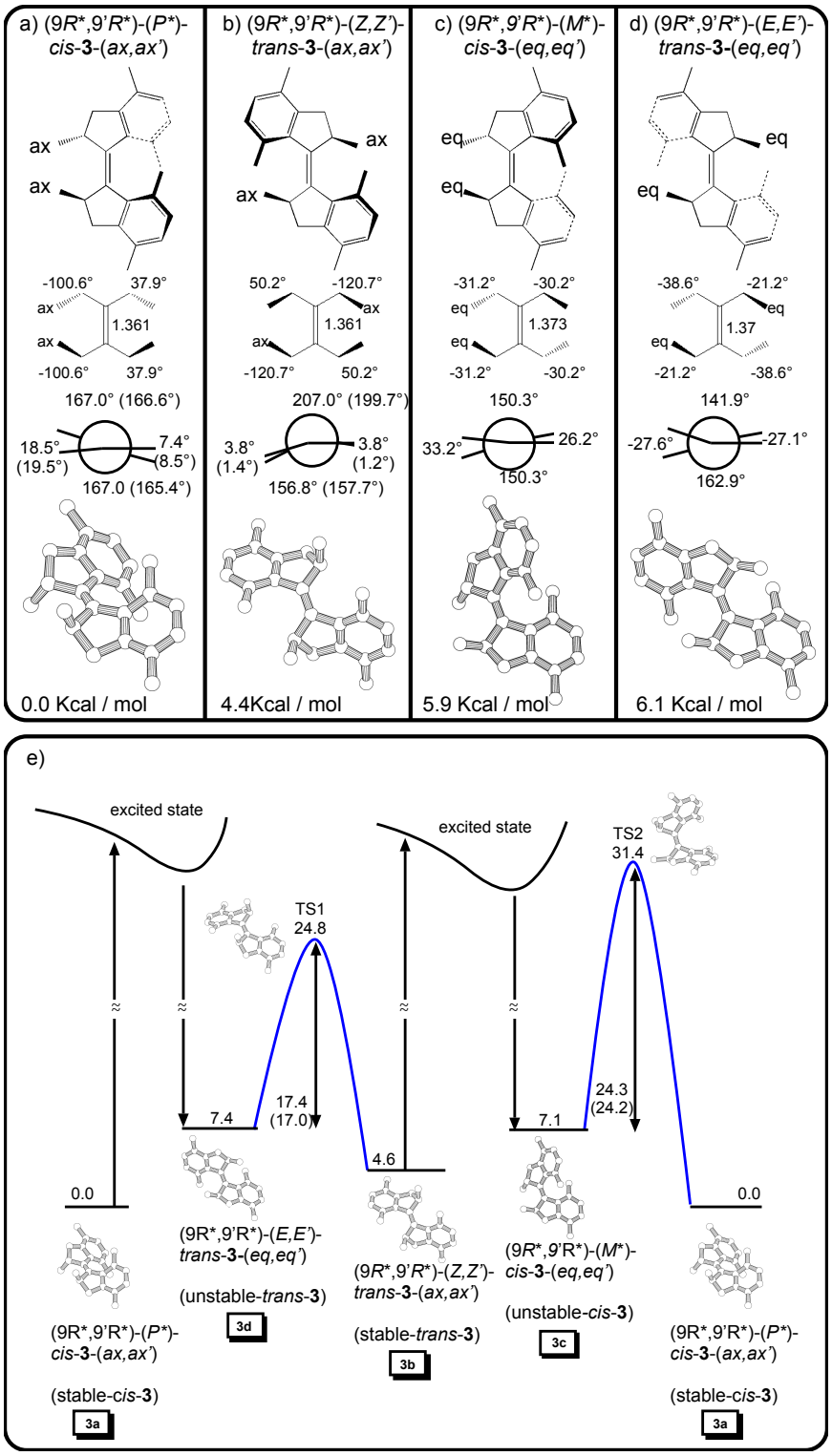

Figure 3.3.: Upper panels (a-d): MP2/6-31G(d)-geometries of **3** that participate in the rotatory cycle. The dihedral angles correspond to the moieties attached to the central double bond. The Newman-projections are along that same bond. Bond-distances are in Å and dihedral angles in degree. Lower panel (e): RI-MP2/TZVP energies of the B3LYP/6-31G(d) geometries of the four equilibrium isomers of **3** and the corresponding transition states between them. Energies are given in kcal/mol. Values in parenthesis correspond to experimental values of Gibbs free energies of activation at 0°C taken from Ref. 132. The labels **3a-3d** correspond to the structures of the upper panels. Adapted from Article 3.5.1.

algorithms available to this end in the software of choice (Gaussian03[133]) did not succeed in that task for **2** and **3**. In order to produce a guess starting geometry as close as possible to the TS for a given reaction, relaxed PES-scans are carried out along the guessed reaction coordinate between reactants and products. Because only the thermal steps are considered, the guessed reaction coordinate typically involved the geometrical parameters shown in Figs. 3.2 and 3.3. A discontinuity in the obtained PES marks the suitable guess of the TS structures, which is then optimized at HF/STO-3G level of theory and refined at the B3LYP/6-31G(d) level of theory. Intrinsic reaction coordinate (IRC) calculations follow at the same level of theory, in order to confirm the computed thermal reaction. Besides the TSs, also the minima are reoptimized at B3LYP/6-31G(d) level of theory, as to compensate for systematic errors and have all critical points of the reaction at the same level of theory. In order to obtain activation energies comparable to the available experimental values, absolute energies are finally recomputed at the more accurate MP2 level of theory, using the resolution of identity (RI)-approximation to reduce computational time, and triple-zeta basis set (RI-MP2/TZVP). The reaction mechanisms of both **2** and **3** will now be addressed separately, because of the difference in complexity in their thermal mechanisms.

The reaction pathways can be rationalized straightforwardly in the case of **3**. In Fig. 3.3e the obtained TSs are shown together with the minima that they connect. Two TSs are found, one for each thermal *unstable*→*stable* step: one for the *cis*-isomer and one for the *trans*-isomer. The main reaction coordinate is the evolution of the methyl-groups from the unstable position (both in equatorial orientation) to the stabler configuration, where both are oriented axially. The *trans*-TS (TS1 in Fig. 3.3e) bears an activation energy E_a of 17.4 kcal/mol, whereas the *cis*-TS (TS2 in Fig. 3.3e) has a higher value of 24.3 kcal/mol. These two values are in very good agreement with the available[132] Gibbs free energies of activation at 0° of 17.0 and 24.2 kcal/mol, respectively. Furthermore, the geometries of both TSs do not belong to the point-group symmetry C_2 (as do the minima), but have no symmetry at all. For the reaction *unstable*-cis-**3**→TS2→*stable*-cis-**3**, at the TS one methyl group has already accessed a pseudo-axial configuration, whereas the other needs to correct slightly its equatorial orientation to let the former cross the *fjord*-region. That is, the reaction occurs not synchronically in both halves of the motor.

The PES landscape is more complex in the case of **2**, where a variety of reaction pathways are possible *a priori* for the thermal step of the rotary cycle. In Fig. 3.2g, minima and TSs have been arranged as to accommodate all located pathways from left to right. At the beginning of the thermal step (immediately after the photoreaction) the motor is in the minimum **2b** (second from the left), whereas the end of the thermal step, the motor is in the minimum **2a** (rightmost isomer). If direct reaction from **2b**→**2c** is attempted, a high E_a of ca. 41 kcal/mol is needed (TS6). In previous calculations,[131] the direct step **2b**→**2c**

via TS5 was computed as having E_a of ca. 25 kcal/mol, in very good agreement with the experimental value of ca. 25 kcal/mol.[35] However, the IRC calculations of Article 3.5.1 connect the TS5 structure with the new intermediate **2f**, which is a shallow minimum lying between **2b** and **2c**. This branch of the thermal reaction is thus **2b**→TS1→**2f**→TS5→**2c**. The other two higher-energy structures **2e** and **2d** are nearly degenerated, and their interconversion only bears an activation energy of 1 kcal/mol (TS4). These minima might be populated when warming **2f**, since the E_a to access **2e** and **2d** via TS2 is one half of the E_a of TS5. However, to continue the reaction towards **2a** via TS8, the E_a needed to undergo **2d**→**2a** is higher than that of the back reaction **2d**→**2e**→**2f**. Thus, the most probable reaction for the thermal step is **2b**→TS1→**2f**→TS5→**2c**→TS9→**2a**. The less probable pathway, **2b**→TS1→**2f**→TS2→**2e**→TS4→**2d**→TS8→**2a**, has, however, a rate-determining step, TS8, that also lies ca. 25 kcal/mol above the reactant **2b**, also in good agreement with the measured Gibbs free energies of activation.

The motors **2** and **3** thus present different complexity in their reaction pathways, and whereas in the case of **3** the pathway appears to occur without intermediates and only in one possible way, the motor **2** evolves in a rich PES with alternative pathways and local minima.

3.2. Photochemistry of the Model Olefin BCH

In Article 3.5.2, the electronic TISE (Eq. (2.6)) is solved for the model system BCH (see **4** in Fig. 3.1) using the MS-CASPT2/SA-CASSCF-procedure (recall Section 2.3.1), in oder to explain the UV-spectrum of the molecule.

BCH's UV-spectrum presents two bands in solid-, liquid-, and gas-phase. The main problem in their interpretation so far is the apparent contradiction between π-electron theory, which predicts only *one* intense HOMO→LUMO transition upon excitation, and the *two* bands present in BCH's spectrum. An intense (π,π^*)-transition was readily assigned to one of the two bands. As for the other band, different proposals have been put forward over the years for the nature of the underlying electronic transition, basing both on experiments and theory. Initially, other valence transitions were invoked,[134–139] e.g., (σ, σ^*), (π, σ^*), and $(\pi(CH_2), \pi^*)$-charge-transfer (CT) transitions[3]. More recently, the Rydberg states entered the discussion[140,141] as possible explanation, and configuration mixing between Rydberg and valence states was put forward as an explanation to BCH's photophysical behavior. This explanation was based partly on photoelectron spectroscopy experiments[140] and configuration interaction singles (CIS) calculations.[141]

Early computations[136–139] purposely excluded Rydberg excitations by choosing compact basis sets. These basis sets are hardly able to represent the typically very diffuse

[3] See Table 1 in Article 3.5.2 and references therein for details.

electronic wavefunctions that account for Rydberg states. As such, the mentioned studies always obtained valence-like excitations for the second band, about 2 electronVolts (eV) higher in energy than the experimental values (around 6-7 eV). The opposite effect arose when the basis sets were chosen purposely diffuse, as not to exclude *a-priori* other possible, typically less-bright, lower-lying Rydberg states. In a theoretical study where the basis set is systematically incremented with diffuse functions,[141] the obtained wavefunctions progressively loose the compact, valence-like character and become more diffuse, Rydberg-like, as the basis set is incremented. Accordingly, the associated transitions start to loose intensity (as given by the oscillator strength f) and appear at lower excitation energies. More importantly, the compact nature of the involved π^*-MO is also lost, and its antibonding character can be found spread over more than one MO. The assignment of the (π, π^*)-transition to one of the available diffuse -and yet bright- electronic states becomes less than trivial.

In order to obtain results which are more robust with respect to the lack of diffusivity (or excess thereof) in the chosen basis set, a Rydberg basis set is optimized in Article 3.5.2. This is done with the GENANO utility of the MOLCAS[142,143] suite of programs for electronic structure calculations. The goal is to optimize the coefficients of the atomic natural orbitals (ANOs) in the generally contracted basis[144] used to represent the AOs of Eq. (2.12). The point of such an optimization is avoiding the undiscriminated inclusion of diffusivity in the basis set, as not to force the subsequent SCF-procedure to deal with artificial mixing of the wavefunctions.

GENANO averages over an input-set of electronic wavefunctions. These wavefunctions are the electronic states to be described optimally. Their wavefunctions are computed initially with the basis set of choice carrying an additional group of diffuse, uncontracted basis functions placed upon a *ghost*-center, a center which does not have further influence in the calculation. GENANO then averages the resulting density matrices and diagonalizes that average. The obtained eigenvectors are used as contraction coefficients to contract the initial functions of the *ghost*-atom.

Two wavefunctions were averaged for *anti*-BCH: the ground state singlet (π^2) of *anti*-BCH and the ground state of *anti*-BCH's cation, which should resemble BCH's Rydberg-states. The calculations made use of the C_{2h} point-group symmetry of *anti*-BCH, reducing significantly the computational costs. *anti*-BCH was chosen because it is the crystalline form of BCH. The optimized basis set is denoted as ANO-L-R.

Once the ANO-L-R basis set is available, an active space (AS) suitable for representing valence and Rydberg states needs to be chosen (recall Section 2.3.1 and Fig. 2.1). To avoid biasing *a priori* the calculation, the AS must include the Rydberg orbitals, which are typically denoted with the atomic labels $3s$, $3p$, $3d$ and so on. In the C_{2h}-framework, the MOs are assigned to the four irreducible representations of the C_{2h}-point-symmetry

group: a_g, a_u, b_g, and b_u. For the Rydberg orbitals, the assignment is:

- $a_g : 3s,\ 3d_{xy},\ 3d_{z^2},\ 3d_{x^2-y^2}$
- $b_g : 3d_{xz},\ 3d_{yz}$
- $a_u : 3p_z$
- $b_u : 3p_x, 3p_y$

The valence orbitals π and π^* are b_u and a_g, respectively. The total AS includes thus 11 MOs: 5 (a_g), 2 (b_g), 1 (a_u), and 3 (b_u). The number of active electrons is 2, hosted in the π orbital. Hence, the CAS(2,11) is chosen as active space for BCH.

With an adequately trimmed basis set and an AS flexible enough to describe the states of interest, a state-averaged CASSCF(2,11)/ANO-L-R calculation is carried out, followed by MS-CASPT2 treatment to correct excitation energies and produce PMCAS-CI wavefunctions. The obtained energies and wavefunctions are shown in Table 3.1.

The most significant feature of Table 3.1 is that the PMCAS-CI wavefunctions correct the contributions of the $3s_R$(Rydberg)- and the π^*-MO from the SA-CASSCF wavefunctions. In the corrected electronic states, the $3s_R$- and the π^*-MO ($16a_g$ and $15a_g$, respectively) are redistributed into two distinct wavefunctions, to 70% and 85%, respectively. The oscillator strengths reflect the change in the nature of the wavefunctions, clearly distinguishing between the bright (π, π^*)-band ($f = .44$ for the 2^1B_u state) and the less

Table 3.1.: CASPT2/CASSCF(2,11)/ANO-L-R and MS-CASPT2/PMCAS-CI(2,11)/ANO-L-R results for the first five ^1B_u states of *anti*-BCH using C_{2h} symmetry.

	CASPT2/ CASSCF				MS-CASPT2/ PMCASCI			
State	Excitation	%Weight	f	$\Delta E/eV$	Excitation	%Weight	f	$\Delta E/eV$
1^1A_g	$(14b_u)^2$	96	-	0	$(14b_u)^2$	96	-	0
1^1B_u	$14b_u \rightarrow 16a_g$ $14b_u \rightarrow 17a_g$	76 18	0.049	5.99	$14b_u \rightarrow 16a_g$ $14b_u \rightarrow 17a_g$	70 17	0.096	5.95
2^1B_u	$14b_u \rightarrow 15a_g$ $14b_u \rightarrow 18a_g$	54 35	0.227	7.18	$14b_u \rightarrow 15a_g$ $14b_u \rightarrow 16a_g$	85 7	0.438	6.82
3^1B_u	$14b_u \rightarrow 17a_g$ $14b_u \rightarrow 19a_g$	49 28	0.048	7.90	$14b_u \rightarrow 18a_g$ $14b_u \rightarrow 17a_g$	60 30	0.062	7.82
4^1B_u	$14b_u \rightarrow 15a_g$ $14b_u \rightarrow 16a_g$ $14b_u \rightarrow 19a_g$	15 15 58	0.159	8.16	$14b_u \rightarrow 19a_g$ $14b_u \rightarrow 18a_g$	83 9	0.054	8.16
5^1B_u	$14b_u \rightarrow 18a_g$ $14b_u \rightarrow 15a_g$	47 28	0.502	8.04	$14b_u \rightarrow 17a_g$ $14b_u \rightarrow 18a_g$	46 30	0.095	8.51

intense transition $(\pi, 3s_R)$, with $f = 0.10$ for the first excited state 1^1B_u.

Not only the spurious valence-Rydberg mixing is resolved with the MS-CASPT2-calculation. The associated vertical excitation energies of 5.95 and 6.82 eV (rightmost values in Table 3.1) are are in excellent agreement with the experimental values 5.95 and 6.82 eV. However, even if the band centers are predicted correctly and the artificial mixing is removed, the question remains why the Rydberg band at 5.95 eV is so intense. Analogous calculations performed in Article 3.5.2 for *syn*-BCH yield values of 6.41 and 6.68 eV, excluding strong contributions from *syn*-BCH-bands to the lower-lying Rydberg intensity of *anti*-BCH in the Franck-Condon (FC) region.

Hence, to explain the unusual intensity, the origin of the (π, π^*)-band of *anti*- and *syn*-BCH is computed. A band certainly peaks at the value for the vertical transition (FC principle), but it can extend its vibrational profile over a range of energies. Its origin is marked by the 0–0 vibronic transition between the electronic states. Graphically, this transition corresponds to the diagonal arrow in Fig. 3.4a, where the electronic states of interest are displayed.

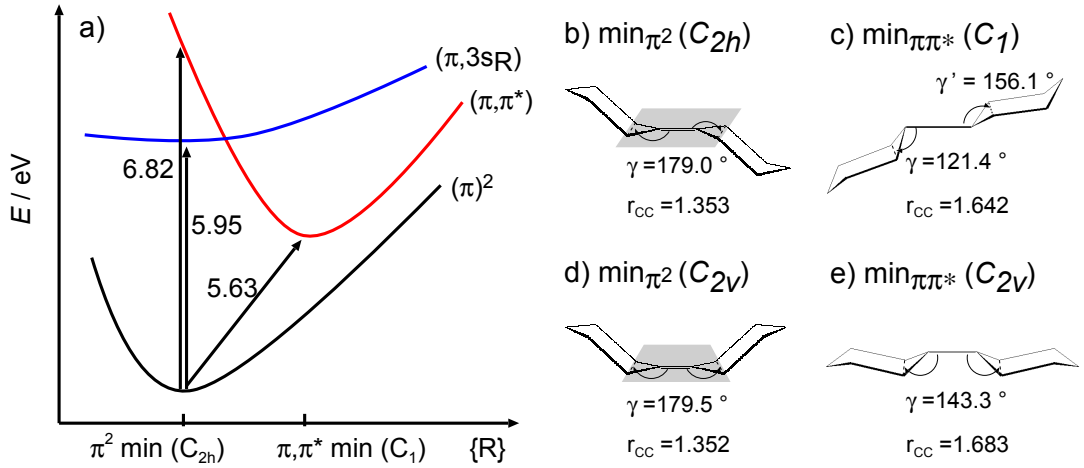

Figure 3.4.: a) Schematic representation of the ground and first two excited electronic states in *anti*-BCH. The vertical excitation energies (in eV) correspond to the values in Table 3.1. The diagonal transition represents the origin of the (π, π^*)-band, computed also at the MS-CASPT2-level of theory, but without symmetry considerations. b-c: (π^2)- and (π, π^*)-minima of *anti*-BCH. d-e: (π^2)- and (π, π^*)-minima of *syn*-BCH. Values in degrees and Å. Adapted from Article 3.5.2.

In order to find this non-vertical energy difference, the molecular geometry of the minimum of the (π, π^*)-state is computed. Hence, SA2-CAS(2,2)/6-31G(d) optimizations are carried out, following the gradient along the PES of the (π, π^*)-state. The chosen level of theory for this optimization is mandatory, because: (i) the compact, double-zeta basis set excludes the intrusion of Rydberg states and (ii) the SA-CASSCF-method can resolve two electronic states as they come close in energy (cf. the (π^2)- and (π, π^*)-curves at

the (π,π^*)-minimum in Fig. 3.4). Both the *syn*- and *anti*- ground state (π^2)-minima are also reoptimized at the same level of theory, to compensate for systematic errors. Finally, electronic energies are recomputed at the MS-CASPT2/PMCAS-CI level of theory. Figure 3.4b-e shows the SA2-CASSCF(2,2)-geometries of the minima for *anti*-BCH and *syn*-BCH. As could be expected, both structures have elongated their double bonds, as corresponds to the antibonding nature of the (π,π^*)-state. Both sp^2 carbon atoms are pyramidalized, resulting in distortions of up to 60° in the olefinic plane. The (π,π^*)-origin for *syn*-BCH is computed at 6.0 eV, so that an overlap with the Rydberg band in that region of the UV-spectrum is hardly possible (cf. Table 3.1). Thus, *syn*-BCH very unlikely contributes to the intensity around that region. In contrast, the origin of the *anti*-(π,π^*)-band is found at ca. 5.6 eV. Starting at that value, the vibrational progression of the *anti*-(π,π^*)-band has to increase in intensity until its peak at 6.8 eV, allowing for a significant contribution to the Rydberg intensity around 6.0 eV.

This interpretation is further supported by vibrational analysis of the *anti*-(π,π^*)-minimum. Harmonic frequencies and normal modes are computed at the same SA2-CASSCF(2,2) level of theory. It is found that the C=C-stretching and the C=C$-$C$_2$-scissoring of the central bond are the normal modes along which the *anti*-(π^2)-minimim can evolve to the *anti*-(π,π^*)-minimum. It is concluded that vibrational progressions of 3-4 and 9-10 quanta in the scissoring and stretching modes, respectively, create a broad, intense, underlying continuum of the valence *anti*-(π,π^*)-band. The Rydberg transition lies on top of that band and borrows intensity from it. Within the emerging photophysical picture, valence-Rydberg mixing can be discarded as the true origin of the unexpected intensities.

3.3. Light-Triggered Unidirectional Rotation of BCH

In Article 3.5.3, light-triggered unidirectional rotation is investigated in the model system BCH. Shaped laser pulses are used to drive a one-dimensional (1D) wavepacket from the ground torsional state to unidirectional rotation in the excited state. The motion is described with the torsional coordinate β, which accounts for the rotary motion in BCH via isomerization of the double bond. The PES along β is computed at the same level of theory of Section 3.2 (i.e., Article 3.5.2): MS-CASPT2/SA-CASSSCF/ANO-L-Rydberg. The obtained curves are shown in Fig. 3.5a. The curves represent the adiabatic potentials for the ground (V_1) and first excited (V_2) electronic singlet states. The ground state is a (π^2) state. Due to the lack of symmetry, the nature of the excited state forcedly mixes the $(3s_R)$-character of the pure *anti*-BCH calculated with symmetry (see Section 3.2) with the (π,π^*)-character of the second excited state. However, both excited states present a similar topology of double well, and since the V_1 is also a bright state, the dynamics are

performed on it.

The system BCH is highly symmetric along β. The symmetry axes lie at $\beta = 0$ and $\beta = \pi$, where both the *syn*- and the *anti*-isomer have their respective minima in the V_1. The dipole moment surfaces (DMSs) also show this symmetry. Figure 3.5b and c shows the DMSs, which are either symmetric or antisymmetric with respect to 0 or π.

The first step towards the dynamics is the computation of BCH's torsional eigenstates, that is, the solution of the nuclear TISE for the adiabatic potentials in Fig. 3.5a and the field field-free Hamilton operator. This procedure is implemented in the program `mydiag.f90` (see Appendix) through the diagonalization of the system's Hamiltonian matrix using a spectral representation. Further details are provided in Section 3.4.2. Only the results are presented here.

In the ground state, the lower-lying torsional eigenstates are centered at $\beta = 0$ (*anti*-BCH) or $\beta = \pi$ (*syn*-BCH). The potentials are near-harmonic in the vicinity of the minima, with torsional frequencies $\omega^{\text{syn}} = 51.95\ \text{cm}^{-1}$ and $\omega^{\text{anti}} = 66.20\ \text{cm}^{-1}$, in very good agreement with those resulting from a harmonic frequency calculation.

In the excited state, V_2, the lower-lying torsional eigenstates are centered at $\beta = \frac{\pi}{2}$ and $\beta = \frac{3\pi}{2}$ (degenerated minima), giving rise to a doublet structure. The two degenerated eigenstates contained in every level can, by virtue of sharing the same energy eigenvalue, be linearly combined to create equivalent sets of torsional eigenstates. Of these possible sets, two are useful when visualizing the eigenfunctions, namely the delocalized basis set

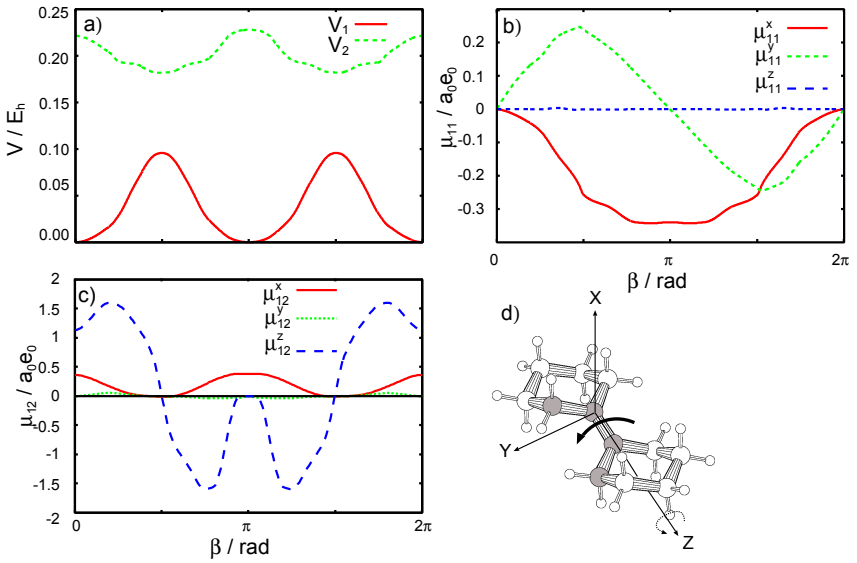

Figure 3.5.: a) Potential energy curves, b) permanent dipole momentsj, and c) transition dipole moments computed at the MS-CASPT2/SA-CASSCF/ANO-L-Rydberg level of theory for BCH, shown in d). The curved arrow indicates the torsional angle β, defined by the carbon atoms colored in gray. Adapted from Article 3.5.3.

and localized basis set. Both sets are totally equivalent for further use in the following propagations.

The propagations are aimed at achieving unidirectional rotation of one half of BCH with respect to the other with an external laser field. The molecule is considered to be oriented along the z-axis and one of its halves is fixed (see Fig. 3.5d), thus acting as the stator of the overcrowded alkenes anchored to surfaces (recall Section 1.2.3). Several OCT- optimizations of the field, with different constraints are carried out, yielding different rates of success. In addition, the intuitive IR+UV-strategy is also tested, as an emerging strategy from the OCT-simulations. Details regarding the implementation of the propagation and the OCT-algorithm with the programs written to this end are given in Sections 3.4.3 and 3.4.4. The programs `mypropS0.f90`, `propagS0.f90`, and `getlaser.f90` are included (with a short description) in the Appendix.

The goal of the OCT-simulations is to obtain a laser pulse that maximizes the overlap between the initial wavefunction (lowest torsional eigenstate of *syn*-BCH in the V_1) and the target wavefunction (a Gaussian wavefunction imprinted with torsional momentum in the V_2). At first, only electronic transitions are allowed by forcing the pulse to interact only with the transition dipole moments (Fig. 3.5c). Little unidirectional momentum is transferred to the excited state after 500 fs. After convergence of the OCT-algorithm, the overlap achieves a maximum value of ca. 65%. The associated field is linearly polarized along the x-direction, and its central frequency is in the UV-domain, in resonance with the vertical transition $V_1 \rightarrow V_2$ at the geometry of the *syn*- and *anti*-minima.

Torsional transitions in the ground state are included when the permanent dipole moments (Fig. 3.5b) are also taken into account in a second OCT-simulation. The pulse is allowed to last 2 ps. In this case, the obtained pulse achieves an overlap of ca. 75% at convergence of the algorithm. The associated transition is now polarized along the x- and y-directions. The Fourier transform (FT) of the OCT-field shows that it now carries frequencies in the UV-domain (only x-component) and IR-domain (x- and y-components). In order to resolve these two frequency domains in time, a spectrogram of the pulse is computed. The spectrogram shows that the IR-frequencies peak at early times lasting over almost 800 fs, while the UV-peak is much shorter and *sits* on top of smaller intensities distributed over the whole duration of the pulse.

This separation of IR- and UV-frequencies in time bears certain similarities with the IR+UV-scheme, where the pulse is intuitively constructed as a torsional pre-excitation in the ground electronic state (few-cycle IR-pulse), followed by a vertical electronic transition between the V_1 and the V_2 (UV-pulse). The idea behind such a construct is to (*i*) create a torsional wavepacket in the ground state whose momentum is maximum while it crosses the equilibrium position and (*ii*) project that momentum to the excited state, where it continues to evolve in the direction of the transferred momentum (recall Section 1.3.4).

Such a pulse and the unidirectional motion that it triggers on the motor BCH is shown in Fig. 3.6. Panel a) shows the applied pulse, with IR- and UV-components (along the y- and the x-axis, respectively) clearly separated in time. This delay between the pulses is the control parameter of the IR+UV-scheme, since it governs the directionality of the motion after the UV-excitation. The remaining parameters (frequencies, intensities, and lengths of the pulses) are chosen as to excite optimally the torsional ladder in the vicinity of the *syn*-region of the potential. A detailed the discussion on choice of these parameters can be found in Article 3.5.3.

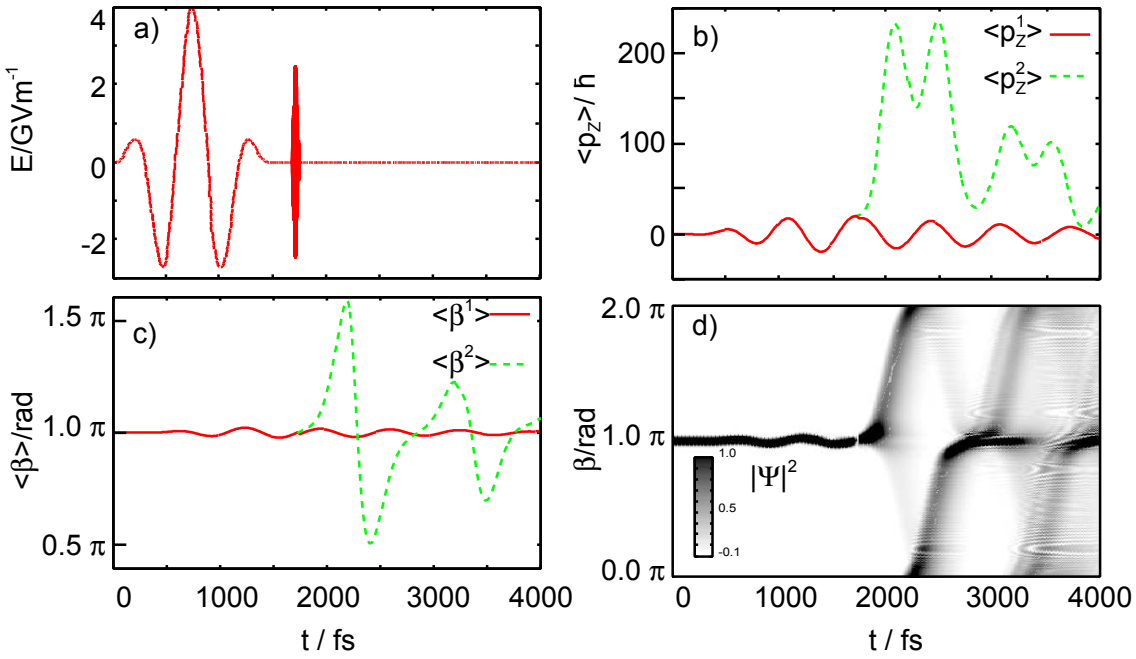

Figure 3.6.: IR+UV-strategy. a) The laser pulse applied. b) The expectation values of the torsional momentum in the ground and excited state. c) The expectation values of the torsional angle in the ground and excited state. d) The probability density of $\Psi(t,\beta)$. After the UV-pulse, over 95% of $\Psi|(t,\beta)|^2$ is in the excited state. Several cycles of the unidirectional rotation are shown, as $\Psi|(t,\beta)|^2$ exits and re-enters the periodic boundaries in the direction $\pi \rightarrow 2\pi = 0 \rightarrow \pi$ at times $t \approx 2$ ps and $t \approx 3.1$ ps. Adapted from Article 3.5.3.

In Fig. 3.6b) and c), the position and the torsional momentum are shown as they oscillate driven by the IR+UV-field. At the time of the UV-irradiation (1675 fs), the torsional momentum is at its maximum positive value (ca. 20 units of $\hbar$), and once the wavepacket is projected to the excited state, the gradient further accelerates the wavepacket, making the momentum peak at values of ca. 220 $\hbar$ (see panel c). This amount of momentum is enough to surmount the potential energy barriers that the wavepacket encounters as it moves along the positive β direction. Figure 3.6d) shows that unidirectional motion. The probability density evolves unidirectionally, exiting and re-entering the periodic boundaries

of the $[0, 2\pi]$ coordinate space for several times. Also, the spreading of the wavepacket can be appreciated, as well as a small portion of population that is reflected back every time the wavepacket crosses a potential energy barrier.

After the intuitive IR+UV-scheme has been proven successful, an OCT-optimization without any kind of polarization constraint is carried out. Unidirectional motion is also achieved in a much shorter timescales (100 fs) with an elliptically laser polarized (see Section 3.2. in Article 3.5.3). The mechanism of this pulse is not intuitive enough as to be rationalized.

3.4. Computational Implementations

3.4.1. Nuclear SE: torsional quantum dynamics

In the following Sections, different aspects of the quantum dynamical calculations carried out in this THESIS are addressed. These quantum dynamics are performed in the context of the sought light-triggered torsional motion of the model system BCH. The results emerging from these calculations are presented in Article 3.5.3. The FORTRAN90 programs written to perform these calculations can be found in the Appendix, and further reference to the codes will be done in the following.

In Section 3.4.2, a spectral representation via an orthogonal basis set of functions is chosen to solve the nuclear TISE. In Section 3.4.3 a pseudospectral representation of spatially localized functions is chosen to solve the nuclear TDSE on a grid. Reference 107 and chapter 11 of Ref. 108 (and references therein) provide helpful overviews on these and other methods to represent (and subsequently solve) the SE in Hilbert space, both in time-independent and time-dependent situations. In this Section, these two representations of quantum dynamics are illustrated because they provide complementary approaches to represent the Hilbert subspace in which a quantum chemical system exists.

3.4.2. TISE solved using a spectral representation

The numerical computation of the vibrational eigenstates of BCH (**4** in Fig. 3.1), is done with the program `mydiag.f90` (see Appendix). As pointed out in Section 2.2, the problem at hand is to solve the vibrational nuclear TISE (Eq. (2.7)). The vibration of interest the torsion associated with BCH's two halves rotating in opposite directions about the central double bond. Henceforth the problem is addressed as torsional problem, torsional wavefunctions, and so on. This type of diagonalization is applied in Article 3.5.3.

The torsion is described with the dihedral angle $\beta \in [0, 2\pi]$, (Fig. 3.5d). β is the only dimension of the vector $\vec{R}_N$ (cf. Eq. (2.7)), along which the needed PES for the ground

and first excited electronic states have been calculated (recall Eq. (2.9)):

$$\hat{V}(\vec{R}_N) = \hat{V}(\beta). \tag{3.2}$$

The PESs in Eq. (3.2) are shown Fig. 3.5a.

Equation (2.7) is re-expressed in matrix notation[4]:

$$\mathbf{H}\psi_\nu = E_\nu \psi_\nu, \quad \nu = 0, +1, +2, ... \tag{3.3}$$

where ν is the torsional quantum number. The problem ahead is to solve the linear eigenvalue problem of Eq. (3.3) by diagonalizing the matrix $\mathbf{H}$, as to find its eigenvectors $\{\psi_\nu\}$ and corresponding eigenenergies $\{E_\nu\}$.

From the programming point of view, two tasks arise: (*i*) setting up the $\mathbf{H}$ matrix and (*ii*) choosing a suitable algorithm that takes $\mathbf{H}$ as input and produces the unitary matrix $\mathbf{U}$ as output, so that:

$$\mathbf{\Omega} = \mathbf{U}^\dagger \mathbf{H} \mathbf{U}, \tag{3.4}$$

where $\mathbf{\Omega}$ is the diagonalized Hamiltonian matrix with the torsional eigenvalues $\{E_\nu\}$ on its diagonal.

Task (*ii*) has less impact on the efficiency of the program, because once $\mathbf{H}$ is constructed, very efficient numerical routines for diagonalization of matrices are available. They are included in linear algebra libraries such as the `LAPACK`-package[145] or described in the *Numerical Recipes* series.[146] These routines are coded to optimally tackle specific types of matrices, depending for example on whether the matrices to diagonalize are real- or complex-valued, Hermitian or only symmetric. Task (*i*), however, has more influence on the efficiency of the program. Depending on what representation is chosen, the accuracy and the computational effort to set up $\mathbf{H}$ by evaluating its matrix elements can vary. In this section, the solution of Eq. (3.3) in terms of a spectral representation is illustrated.

If one introduces a truncated orthonormal basis set (a spectral representation) of k elements, the column vector ψ_ν has k elements, and $\mathbf{H}$ is a $k \times k$ matrix. Let the spectral basis be $\{\phi_l\}$, then the matrix elements H_{lm} of the Hamiltonian are (recall Eq. (2.8)):

$$H_{lm} = \langle \phi_l | \hat{H} | \phi_m \rangle = \langle \phi_l | \hat{T} + \hat{V} | \phi_m \rangle = \langle \phi_l | \hat{T} | \phi_m \rangle + \langle \phi_l | \hat{V} | \phi_m \rangle \,. \tag{3.5}$$

The PES has been evaluated in β space along a series of points, and then interpolated to a discrete grid of N_g equally spaced β_g points. The change from a continuous β to a discrete β_g can be interpreted as a set of δ-functions $\{\beta_g\}$ centered about the $\beta(g)$

[4] The subindex N for *nuclear* is dropped for succinctness, since all quantities are nuclear. Bold, upright symbols are matrices, such as $\mathbf{H}$.

positions:

$$\beta(g) = g\Delta\beta, \quad g = 1, 2, ...N_g, \quad \Delta\beta = \frac{2\pi}{N_g}. \tag{3.6}$$

Computationally, Eq. (3.6) implies that all functional dependencies on β (continuous) become dependencies on g (integer). Thus, the evaluation of the potential energy matrix elements in β-space[5]:

$$V_{lm} = \langle\phi_l(\beta)|\hat{V}(\beta)|\phi_m(\beta)\rangle = \int_0^{2\pi} \phi_l^*(\beta)\hat{V}(\beta)\phi_m(\beta)\ \mathrm{d}\beta, \tag{3.7}$$

becomes a discrete sum over the index g:

$$V_{lm} = \sum_{g=1}^{N_g} \phi_l^*(g)V(g)\phi_m(g)\ \Delta\beta. \tag{3.8}$$

Note that, for Eq. (3.8), the relation $\hat{V}(\beta)=V(\beta)=V(g)$ has been used, and thus evaluation of V_{lm} is straightforward regardless of the functional form of the basis $\{\phi_l\}$, because all quantities $\phi_l^*(g)$, $V(g)$, and $\phi_m(g)$ are known exactly for all g=1, 2...N_g values. Integration is performed using Simpson's rule.[147] Recalling then task (i), the evaluation of V_{lm} is not decisive in choosing an appropriate spectral basis set $\{\phi_l\}$. That is not the case for the kinetic energy matrix elements T_{lm}. $\hat{T}(\beta)$ has the following form in β-space:

$$\hat{T}(\beta) = -\frac{1}{2I_z}\frac{d^2}{d\beta^2}, \tag{3.9}$$

where atomic units have been introduced ($\hbar$=1). I_z is the moment of inertia for one of the six-membered rings of BCH rotating while the other remains fixed, as to mimic the situations where the molecular motors have the stator anchored to a solid surface (recall Section 1.2.3). Equation (3.9) includes two consecutive differentiations of the basis $\{\phi_l\}$ in β-space. In order to avoid the costly -and less accurate- numerical differentiation on a grid, the natural option for $\{\phi_l\}$ is to choose the own eigenfunctions of $\hat{T}(\beta)$, in which evaluation of T_{lm} results immediate and exact. The problem in which $\hat{H}(\beta)=\hat{T}(\beta)$ is the free particle. In a cyclic space with cyclic boundary conditions (as is the β-space), the spectral basis of eigenfunctions for a free particle (plane waves) are called particle-in-a-ring[148] functions, and have the form:

$$\phi_l(\beta) = \left(\frac{1}{2\pi}\right)^{1/2} e^{il\beta}, \tag{3.10}$$

where $l=0, \pm1, \pm2, \pm3...$ is the definite torsional momentum of each pair of functions and

[5] The spatially localized β_g functions represent actually the introduction of a pseudospectral basis set for the evaluation of the potential. However, since once the V_{lm} elements are known, the resulting **H** is diagonalized in terms of the spectral basis $\{\phi_l\}$, the name *spectral* is kept.

i is the imaginary unit. Thus,

$$\hat{T}(\beta)\phi_l(\beta) = -\frac{1}{2I_z}\frac{d^2}{d\beta^2}\left(\frac{1}{2\pi}\right)^{1/2} e^{il\beta} = \frac{l^2}{2I_z}\phi_l(\beta), \tag{3.11}$$

and it follows immediately that the resulting kinetic energy matrix, $\mathbf{T}$, is diagonal with the elements:

$$T_{lm} = \frac{l^2}{2I_z}\delta_{lm}. \tag{3.12}$$

$\mathbf{H}$ is constructed via the evaluation of the H_{lm} matrix elements with Eqs. (3.8) and (3.12) for its upper (or lower) half only, since $\mathbf{H}$ is Hermitian and thus $H_{lm}=H^*_{ml}$. In $\mathbf{H}$ the β-dependence has been integrated out. $\mathbf{H}$ is subsequently parsed to the diagonalization routine (see `mydiag.f90` in the Appendix), and the routine returns the unitary matrix $\mathbf{U}$ and the eigenvalues E_ν. Tasks (i) and (ii) can be considered accomplished, and solving Eq. (3.3) can be viewed as change of basis set, where the initial basis set (particle-in-a-ring functions) is rotated to the final basis set (torsional eigenfunctions of $\mathbf{H}$) using the obtained unitary matrix $\mathbf{U}$ (Eq. (3.4)):

$$\psi_\nu = \sum_{l=1}^{k} U_{l\nu}\phi_l. \tag{3.13}$$

Finally, for visualization purposes one needs to transform Eq. (3.13) to the β-space, where the ν-torsional eigenstate is re-expressed in β-space functions

$$\psi_\nu = \sum_{g=1}^{N_g} \psi_{g\nu}\beta_g. \tag{3.14}$$

Each coefficient ψ_{g_ν} represents the amplitude of the eigenfunction at the point g of the grid. These amplitudes are computed by summing over all the elements of the basis functions ϕ_l multiplied with their respective contribution $U_{l\nu}$ for that given point g:

$$\psi_{g\nu} = \sum_{l=1}^{k} U_{l\nu}\phi_l(g). \tag{3.15}$$

When the sum in equation Eq. (3.15) has been computed for a given ν-th torsional eigenstate ψ_ν for all g points, the representation along the β coordinate of that ν-th state is available.

3.4.3. TDSE: solved on a grid (time-propagation)

The time-propagation of the torsional wavefunction using the Split-Operator-(SO) technique[149] is illustrated in the present section. Part of the one-dimensional (1D) propagations in Article 3.5.3 were carried out with this technique. The programs written to this end are `mypropa.f90`, `propagSO.f90`, and `getlaser.f90`. These three codes are provided with further explanations in the Appendix. As in the preceding section, the time-propagation can be split into two tasks: (*i*) setting up a Hamilton operator and (*ii*) subsequently solving the TDSE.

Setting up the Hamilton operator After invoking the Born-Oppenheimer approximation, and having separated the translational and rotational degrees of freedom, the TDSE in matrix notation adopts the form:

$$i\hbar\frac{\partial}{\partial t}\begin{pmatrix}\psi_1(\beta,t)\\ \psi_2(\beta,t)\end{pmatrix} = \mathbf{H}(\beta,t)\begin{pmatrix}\psi_1(\beta,t)\\ \psi_2(\beta,t)\end{pmatrix}, \tag{3.16}$$

where β is the torsional coordinate of the preceding Section 3.4.3.

The goal is to describe photochemical events triggered by external laser fields which couple the two electronic states S_0 and S_1 of BCH, i.e., ground and first electronically excited state, respectively. Hence the two-dimensions (2D) of the wavefunctions and the Hamiltonian matrix in Eq. (3.16), in order to include populations both in the ground ($\psi_1(\beta,t)$) and excited state ($\psi_2(\beta,t)$).

The Hamiltonian matrix $\mathbf{H}(\beta,t)$ is now time-dependent because it includes the light-matter interaction of the molecule with the external field. Within the dipole approximation, this interaction is accounted for with a field-dipole coupling operator

$$\hat{W}(\beta,t) = -\hat{\mu}(\beta)\cdot\vec{\epsilon}(t), \tag{3.17}$$

where $\hat{\mu}(\beta)$ is the dipole moment operator and $\vec{\epsilon}(t)$ is the oscillating laser field. The operator $\hat{W}(\beta,t)$ is added to the field-free Hamiltonian (cf. Eq. (2.8)). In matrix notation:

$$\mathbf{H}(\beta,t) = \mathbf{T}(\beta) + \mathbf{V}(\beta) + \mathbf{W}(\beta,t). \tag{3.18}$$

Recall that in Eq. (3.18) the matrices have elements ij, and these subindices do not denote elements of a spectral basis (as did the subindices lm in Eq. (3.5)), but rather refer to the electronic states 1 and 2. That is, the Hamiltonian is:

$$\mathbf{H}(\beta,t) = \begin{pmatrix}-\frac{1}{2I_z}\frac{d^2}{d\beta^2} & 0\\ 0 & -\frac{1}{2I_z}\frac{d^2}{d\beta^2}\end{pmatrix} + \begin{pmatrix}V_{11}(\beta) & 0\\ 0 & V_{22}(\beta)\end{pmatrix} - \begin{pmatrix}\vec{\mu}_{11}(\beta) & \vec{\mu}_{12}(\beta)\\ \vec{\mu}_{21}(\beta) & \vec{\mu}_{22}(\beta)\end{pmatrix}\cdot\vec{\epsilon}(t), \tag{3.19}$$

where $V_{11}(\beta)$ and $V_{22}(\beta)$ are the PESs for the ground and first excited electronic states, respectively. The fact that Eq. (3.19) has no off-diagonal kinetic or potential terms is a direct consequence of the Born-Oppenheimer approximation. In the emerging adiabatic representation, the only off-diagonal terms come from the dipole matrix $\boldsymbol{\mu}(\beta)$. The matrix $\boldsymbol{\mu}(\beta)$ has three-dimensional (3D) vectors as matrix elements $\vec{\mu}_{ij}(\beta)$, which are defined in the same 3D xyz-space in which the field $\vec{\epsilon}(t)$ is propagating. Thus, the elements of $\mathbf{W}(\beta,t)$ (last term in Eq. (3.19)) are:

$$W_{ij}(\beta,t) = -\vec{\mu}_{ij}(\beta)\cdot\vec{\epsilon}(t) = -\mu_x^{ij}(\beta)\epsilon_x(t) - \mu_y^{ij}(\beta)\epsilon_y(t) - \mu_z^{ij}(\beta)\epsilon_z(t). \tag{3.20}$$

The dipole vector components are computed together with the PESs for the same range of β, giving rise to dipole moment surfaces (DMSs), as shown in Fig. 3.5b and c. The diagonal elements of $\boldsymbol{\mu}(\beta)$ correspond to the permanent dipole moment of the ground ($i=j=1$) and first excited ($i=j=2$) electronic states. The off-diagonal elements ($i\neq j$) correspond to the transition dipole moment between the two electronic states. In the adiabatic representation, only these off-diagonal elements enable population transfer between the two electronic states when the field is on.

In Eq. (3.20) all three field components are shown, although only two of them can physically interact with the molecule through the dipole. The third is the direction along which $\vec{\epsilon}(t)$ propagates in the 3D-space. However, it is Eq. (3.20) that has been implemented in `mypropa.f90` to make the program general. That way, fields propagating along the x-, y-, and z-directions can be used without further changes in the code. The third dipole is set automatically as equal to zero through the input specifications of the program.

The dipole couplings are incorporated as a part of the time-dependent potential term:

$$\mathbf{V}(\beta,t) = \mathbf{V}(\beta) + \mathbf{W}(\beta,t). \tag{3.21}$$

This is of practical use when implementing the Split-Operator Method, as will be shown next.

Discretizing time Up to this point, only the question on how to set up the $\mathbf{H}(\beta,t)$ operator in β-space has been addressed, but not how to solve the associated TDSE (Eq. (3.16)). To do so, the solution of the TDSE for the time-independent Hamiltonian, $\mathbf{H}(\beta)$, is used as approximate solution for the time-dependent Hamiltonian, $\mathbf{H}(\beta,t)$. In that case, integrating Eq. (3.16) in β-space yields:

$$\begin{pmatrix}\psi_1(\beta,t)\\ \psi_2(\beta,t)\end{pmatrix} = e^{-i\mathbf{H}(\beta,t-t_0)/\hbar}\begin{pmatrix}\psi_1(\beta,t)\\ \psi_2(\beta,t)\end{pmatrix}. \tag{3.22}$$

The approximation of Eq. (3.22) requires this equation to be evaluated between two instants in time (t_1 and t_2) close enough so that $\mathbf{H}(\beta, t_1) \sim \mathbf{H}(\beta, t_2)$. That is, t becomes discretized in N_t timesteps for a total time T. The timesteps t_τ are separated by the stepsize Δt:

$$t_\tau(\tau) = t_0 + \tau\Delta t, \quad \Delta t = \frac{T}{N_t}, \quad \tau = 0, 1, 2...N_t. \tag{3.23}$$

Thus, the t-dependency becomes computationally a τ-dependence and the time-evolution operator $e^{-i\mathbf{H}(\beta,t_\tau)/\hbar}$ becomes $e^{-i\mathbf{H}_\tau(\beta)\Delta t/\hbar}$.

After discretization of time, Eq. (3.22) is rewritten as:

$$\begin{pmatrix} \psi_1(\beta, \tau+1) \\ \psi_2(\beta, \tau+1) \end{pmatrix} = e^{-i\mathbf{H}_\tau(\beta)\Delta t} \begin{pmatrix} \psi_1(\beta, \tau) \\ \psi_2(\beta, \tau) \end{pmatrix}, \tag{3.24}$$

where atomic units ($\hbar = 1$) have been introduced. The time-evolution operator propagates the two-dimensional vector on the RHS[6] of Eq. (3.24) from the τ-th instant to the τ+1-th instant of the LHS, i.e., $\Psi(\beta, \tau) \rightarrow \Psi(\beta, \tau+1)$, by operating the exponential of the τ-th Hamiltonian on the wavefunction. The choice of the parameter Δt becomes a trade-off between the computational effort of having to evaluate Eq. (3.24) a large number of instants for a given propagation time(large N_t, see Eq. (3.23)) and the inaccuracy of approximating $\mathbf{H}_\tau(\beta) \sim \mathbf{H}_{\tau+1}(\beta)$ (large Δt, see Eq. (3.23)).

Discretizing position and momentum space: the Split-Operator implementation Once Δt has been chosen, the evaluation of Eq. (3.24) is accomplished with the second order Split-Operator method.[149] The split is performed upon the time-evolution operator symmetrically, so that:

$$e^{-i\mathbf{H}_\tau(\beta)\Delta t} = e^{-i\mathbf{T}(\beta)\Delta t/2} \cdot e^{-i\mathbf{V}_\tau(\beta)\Delta t} \cdot e^{-i\mathbf{T}(\beta)\Delta t/2} + O(\Delta t^3), \tag{3.25}$$

with an error of third-order in Δt, due to the noncommutability of kinetic and potential energy operators. Note that in Eq. (3.25) only the potential term bears the time-dependence through the index τ. The split of $\mathbf{H}_\tau(\beta)$ in $\mathbf{T}(\beta)$ and $\mathbf{V}_\tau(\beta)$ results effective when working on a grid because once the Hamiltonian is split, evaluation of kinetic and potential energy occurs separately on the reciprocal grids, in which both operators are multiplicative. The discretization of the position space or β-space is described with Eqs. (3.6) and (3.14). Analogously, the reciprocal torsional momentum-space or p-space is discretized as:

$$p(g) = g\Delta p, \quad g = \pm 0, 1, ... \frac{N_g}{2}, \quad \Delta p = \frac{2\pi}{N_g \Delta\beta} = \frac{2\pi}{2\pi} = 1, \tag{3.26}$$

[6] Right hand side. LHS is left hand side

from where it follows p=g, further implying that p is integer-valued in momentum space. The wavefunction in momentum space for the instant τ is denoted $\Psi_p(\tau)$. Its two components $\psi_1^p(\tau)$ and $\psi_2^p(\tau)$ are the sums:

$$\psi_i^p(\tau) = \sum_{g=\frac{-N_g}{2}}^{\frac{+N_g}{2}} \psi_{ig}^p(\tau) p_g, \quad i = 1, 2. \tag{3.27}$$

where p_g are δ-functions centered about the g-th value of the momentum, which is numerically identical to the value g-itself. Analogously, for the two components of the wavefunction $\Psi_\beta(\tau)$ in β-space:

$$\psi_i^\beta(\tau) = \sum_{g=1}^{N_g} \psi_{ig}^\beta(\tau) \beta_g, \quad i = 1, 2. \tag{3.28}$$

Equations (3.27) and (3.28) summarize the key of the pseudospectral grid representation in localized δ-functions, where the weights of the expansion coefficients of the wavefunction are the values of the wavefunction itself in space. The switch between the p- and β-spaces of Eqs. (3.27) and (3.28) is accomplished with the Fourier transform (FT), which the code `propagSO.f90` is implemented in its Fast Fourier transform (FFT) version. In these two reciprocal spaces, kinetic and potential energy will be evaluated multiplicatively as $\mathbf{T}(p)$ and $\mathbf{V}(\beta)$, respectively.

Furthermore, the evaluation of the RHS of Eq. (3.24) involves the exponentiation of matrices in order to obtain the time-evolved wavefunction. If a given matrix to exponentiate $\mathbf{D}$ is already diagonal, with the elements λ_{kk}, its exponential is directly written as matrix of exponentials:

$$e^{\mathbf{D}} = \exp\left[\begin{pmatrix} \lambda_{11} & \cdots & 0 \\ \vdots & \ddots & \vdots \\ 0 & \cdots & \lambda_{kk} \end{pmatrix}\right] = \begin{pmatrix} e^{\lambda_{11}} & \cdots & 0 \\ \vdots & \ddots & \vdots \\ 0 & \cdots & e^{\lambda_{kk}} \end{pmatrix}. \tag{3.29}$$

However, if the matrix to exponentiate $\mathbf{A}$ is not diagonal, but its unitary transformation $\mathbf{U}$ to diagonal $\mathbf{D}$ is known:

$$\mathbf{D} = \mathbf{U}^\dagger \mathbf{A} \mathbf{U}, \tag{3.30}$$

$\mathbf{A}$ is exponentiated by:

$$e^{\mathbf{A}} = \mathbf{U} e^{\mathbf{D}} \mathbf{U}^{-1} = \mathbf{U} \begin{pmatrix} e^{\lambda_{11}} & \cdots & 0 \\ \vdots & \ddots & \vdots \\ 0 & \cdots & e^{\lambda_{kk}} \end{pmatrix} \mathbf{U}^{-1}. \tag{3.31}$$

Thus, unitary matrices and eigenvalues are necessary to evaluate the non-diagonal (cf. Eq. (3.21)) potential term $\mathbf{V}_\tau(\beta)$ in Eq. (3.25). In addition, matrix diagonalizations are needed for every timestep of the propagation, because $\mathbf{V}_\tau(\beta)$ changes for every instant, τ, as long as the field is on. The series of FFTs and diagonalizations needed for every timestep will be now illustrated for one step of the propagation, $\tau \rightarrow \tau+1$. These operations are performed by the program `propagSO.f90`

According to Eq. (3.25), the first term to be evaluated is $e^{-i\mathbf{T}(\beta)\Delta t/2}$ acting on the wavefunction at the τ-instant. The first step of the propagation is thus to use the FFT to change to momentum space (FFT^{+1}).

$$\mathrm{FFT}^{+1}\left[\sum_{i=1}^{2}\sum_{g=1}^{N_g}\psi_{ig}^{\beta}(\tau)\beta_g\right] = \sum_{i=1}^{2}\sum_{g=-\frac{N_g}{2}}^{+\frac{N_g}{2}}\psi_{ig}^{p}(\tau)p_g, \tag{3.32}$$

which for compactness is written as:

$$\mathrm{FFT}^{+1}\Psi_\beta(\tau) = \Psi_p(\tau) \tag{3.33}$$

The kinetic energy operator is diagonal in p-space, and when evaluated in each g-point of the discrete p-space, the eigenvalues are computed as:

$$\mathbf{T}(p) = \sum_{p=-\frac{N_g}{2}}^{+\frac{N_g}{2}}\mathbf{T}_g, \quad \mathbf{T}_g = \begin{pmatrix} \frac{\hat{p}_g^2}{2I_z} & 0 \\ 0 & \frac{\hat{p}_g^2}{2I_z} \end{pmatrix} = \begin{pmatrix} \frac{p_g^2}{2I_z} & 0 \\ 0 & \frac{p_g^2}{2I_z} \end{pmatrix} = \begin{pmatrix} \frac{g^2}{2I_z} & 0 \\ 0 & \frac{g^2}{2I_z} \end{pmatrix}, \tag{3.34}$$

where the relation $g{=}p$ has been used. The evaluation of the kinetic energy exponential is straightforward for every g-point:

$$\begin{aligned} e^{-i\mathbf{T}_g\Delta t/2} = \exp\left[\begin{pmatrix} -i\frac{g^2}{2I_z}\frac{\Delta t}{2} & 0 \\ 0 & -i\frac{g^2}{2I_z}\frac{\Delta t}{2} \end{pmatrix}\right]\begin{pmatrix}\psi_{1g}^p(\tau)\\ \psi_{2g}^p(\tau)\end{pmatrix} = \\ \begin{pmatrix} e^{-i\frac{p^2}{2I_z}\frac{\Delta t}{2}} & 0 \\ 0 & e^{-i\frac{p^2}{2I_z}\frac{\Delta t}{2}} \end{pmatrix}\begin{pmatrix}\psi_{1g}^p(\tau)\\ \psi_{2g}^p(\tau)\end{pmatrix} = \begin{pmatrix}\psi_{1g}^p(\tau_{1/3})\\ \psi_{2g}^p(\tau_{1/3})\end{pmatrix}, \end{aligned} \tag{3.35}$$

and then, for all g-points:

$$\Psi_p(\tau_{1/3}) = \sum_{g=-\frac{N_g}{2}}^{+\frac{N_g}{2}}\begin{pmatrix}\psi_{1g}^p(\tau_{1/3})\\ \psi_{2g}^p(\tau_{1/3})\end{pmatrix}. \tag{3.36}$$

The index 1/3 denotes that one third of the $\mathbf{H}_\tau$ operator has been already applied. The

back Fourier-transformation (FFT^{-1})

$$\mathrm{FFT}^{-1}\Psi_p(\tau_{1/3}) = \Psi_\beta(\tau_{1/3}), \tag{3.37}$$

switches back to β-space, where the evaluation of the potential energy term $e^{-i\mathbf{V}_\tau(\beta)\Delta t}$ on $\Psi_\beta(\tau_{1/3})$ (cf. Eq. (3.25)) takes place. For this operation the matrix $\mathbf{V}_\tau(\beta)$ at the instant τ needs to be diagonalized for every g-point. Although analytic diagonalization is possible and convenient for a 2-level system (as is the present model of two electronic potentials), the program `propagSO.f90` implements a numerical diagonalization as to keep the program usable for more potentials without complication (see Appendix for more details). This diagonalization takes place directly on basis of the g-points of the $\beta(g)$-grid (cf. Eq. (3.6)):

$$\mathbf{V}_\tau(\beta) = \sum_{g=1}^{N_g} \mathbf{V}_{g\tau}. \tag{3.38}$$

That is, for each g-point of the β-space, the following 2×2 matrix,

$$\mathbf{V}_{g\tau} = \begin{pmatrix} V_{11}^{g\tau} & V_{12}^{g\tau} \\ V_{21}^{g\tau} & V_{22}^{g\tau} \end{pmatrix}, \tag{3.39}$$

is parsed for the instant τ to the diagonalization routine, and the matrices $\mathbf{U}_{g\tau}$ and $\mathbf{D}_{g\tau}$ (cf. Eq. (3.31) are produced as output. Then, for every point g-point of β-space, the operation computed is:

$$\begin{aligned} e^{-i\mathbf{V}_{g\tau}\Delta t} = \exp\left[\begin{pmatrix} -iV_{11}^{g\tau}\Delta t & -iV_{12}^{g\tau}\Delta t \\ -iV_{21}^{g\tau}\Delta t & -iV_{22}^{g\tau}\Delta t \end{pmatrix}\begin{pmatrix} \psi_{1g}^{\beta}(\tau_{1/3}) \\ \psi_{2g}^{\beta}(\tau_{1/3}) \end{pmatrix}\right] = \\ \mathbf{U}\begin{pmatrix} -iD_{11}^{g\tau}\Delta t & 0 \\ 0 & -iD_{22}^{g\tau}\Delta t \end{pmatrix}\mathbf{U}^{-1}\begin{pmatrix} \psi_{1g}^{\beta}(\tau_{1/3}) \\ \psi_{2g}^{\beta}(\tau_{1/3}) \end{pmatrix} = \begin{pmatrix} \psi_{1g}^{\beta}(\tau_{2/3}) \\ \psi_{2g}^{\beta}(\tau_{2/3}) \end{pmatrix}, \end{aligned} \tag{3.40}$$

and

$$\sum_{g=1}^{N_g}\begin{pmatrix} \psi_{1g}^{\beta}(\tau_{2/3}) \\ \psi_{2g}^{\beta}(\tau_{2/3}) \end{pmatrix} = \Psi_\beta(\tau_{2/3}), \tag{3.41}$$

where the index 2/3 indicates that two thirds of $\mathbf{H}_\tau$ have been evaluated. After Fourier-transforming $\Psi_\beta(\tau_{2/3})$ again to momentum space,

$$\mathrm{FFT}^{+1}\Psi_\beta(\tau_{2/3}) = \Psi_p(\tau_{2/3}), \tag{3.42}$$

the final evaluation of the second half of the kinetic energy is carried out by repeating the

local evaluation of the kinetic energy of Eq. (3.35):

$$\exp\left[\begin{pmatrix} -i\frac{g^2}{2I_z}\frac{\Delta t}{2} & 0 \\ 0 & -i\frac{g^2}{2I_z}\frac{\Delta t}{2} \end{pmatrix}\right]\begin{pmatrix}\psi^p_{1g}(\tau_{2/3})\\ \psi^p_{2g}(\tau_{2/3})\end{pmatrix} = \begin{pmatrix} e^{-i\frac{p^2}{2I_z}\frac{\Delta t}{2}} & 0 \\ 0 & e^{-i\frac{p^2}{2I_z}\frac{\Delta t}{2}} \end{pmatrix}\begin{pmatrix}\psi^p_{1g}(\tau_{2/3})\\ \psi^p_{2g}(\tau_{2/3})\end{pmatrix} = \begin{pmatrix}\psi^p_{1g}(\tau_{3/3})\\ \psi^p_{2g}(\tau_{3/3})\end{pmatrix}, \tag{3.43}$$

and

$$\sum_{g=-\frac{N_g}{2}}^{+\frac{N_g}{2}}\begin{pmatrix}\psi^p_{1g}(\tau_{3/3})\\ \psi^p_{2g}(\tau_{3/3})\end{pmatrix} = \Psi_p(\tau_{3/3}). \tag{3.44}$$

The so-obtained $\Psi_p(\tau_{3/3}) = \Psi_p(\tau+1)$ is the final, propagated wavefunction at the instant τ+1. The wavefunction can be Fourier-transformed back to β-space, if a visual representation of the torsional motion is desired:

$$\mathrm{FFT}^{-1}\Psi_p(\tau{+}1) = \Psi_\beta(\tau{+}1), \tag{3.45}$$

However, for efficient propagation one can keep the momentum representation and start immediately the next propagation step by inserting $\Psi_p(\tau{+}1)$ in Eq. (3.35) and repeating the three steps with the updated Hamilton operator containing the new term $\mathbf{V}_{\tau+1}(\beta)$.

The grid propagations carried out using the technique described above are shown in Fig. 3.6. The figure displays the time-evolution of the expectation values of momentum (panel b) and torsion (panel c) of the wavepacket (panel d) as it evolves in time, driven by the IR+UV-pulse (panel a).

In addition, the SO-technique is also implemented in the OCT-algorithm used in Article 3.5.3, in order to obtain other non-intuitive control fields different from that shown in Fig. 3.6a. How this algorithm is implemented is the subject of the following section.

3.4.4. Implementation of the OCT-algorithm

The rapidly convergent algorithm proposed by Rabitz and coworkers in Ref. 81, is used in Article 3.5.3, where light-triggered unidirectional rotation in the model system BCH is sought. The code written to implement the algorithm can be found in the Appendix under the name `oct.f90`.

The propagations needed to optimize the laser pulse are carried out with the Split-Operator technique, as exposed in the preceding section. In this section, emphasis is done in the iterative scheme for improving the laser field, and the propagation scheme is not decisive. As a matter of fact, both the Split-Operator and a Spectral-method were implemented to obtain the various laser pulses presented in Article 3.5.3. Both approaches

imply discretization of the time variable. However, to remain succinct in the notation in this section, the continuous variable t is not exchanged for the discrete t_τ in the following paragraphs.

Choice of the target and initial states The algorithm presented in Ref. 81 optimizes the overlap between an initial $\Psi_i(\beta)$ and final $\Psi_f(\beta)$ states at the end of a pulse $\epsilon_{OCT}(t)$ of total length T. As initial state, the lowest torsional eigenstate, ψ_0, is chosen, which corresponds to the *syn*-BCH-isomer. In order to obtain an unidirectionally accelerated wavefunction after the pulse, positive torsional momentum is imprinted upon the target state, by displacing a normal Gaussian function in momentum space to a positive value of p_d:

$$\Psi_f(\beta) = \left(\frac{2}{\pi a^2}\right)^{\frac{1}{4}} \exp\left[i\beta p_d - \left(\frac{\beta-\beta_0}{a}\right)^2\right], \tag{3.46}$$

where $\beta_0 = \pi$ and a is the width-parameter,adjusted to fit the width of ψ_0.

Iteration procedure The scheme of Rabitz and coworkers[81] incorporates the information from one iteration into the next iteration in an entangled fashion. Each iteration includes two propagations: one forward (FW) propagation of the initial wavefunction ($\Psi_{FW}(t_0)$=ψ_0) and one backward (BW) propagation of the final wavefunction ($\Psi_{BW}(T)$=Ψ_f). Two symmetric algorithms exist, depending if one chooses to start each iteration with the BW or FW propagation. In the present implementation, which follows that presented in Ref. 80, the algorithm starts with the BW propagation. The first backwardly propagated wavefunction Ψ_{BW} evolves under the initial guess of the laser pulse $\vec{\epsilon}_g(t)$. The guess may have an arbitrary form, even $\vec{\epsilon}_g = 0$, as long as the overlap $\langle\Psi_{BW}|\Psi_{FW}\rangle$ is different from the exact zero after the pulse.

The first iteration is started as:

$$\Psi^0_{BW}(t_0) \xleftarrow{\vec{\epsilon}_g(t)} \Psi^0_{BW}(T). \tag{3.47}$$

where the arrow pointing from right to left indicates the backward direction of time. Next, Ψ^1_{FW} is propagated forwardly

$$\Psi^1_{FW}(t_0) \xrightarrow{\vec{\epsilon}_0(t)} \Psi^1_{FW}(T). \tag{3.48}$$

using the field $\vec{\epsilon}_0(t)$, which already incorporates information from the target state through the product:

$$\vec{\epsilon}_0(t) = -\frac{1}{\alpha_0}\mathrm{Im}[\langle\Psi^1_{FW}(t)|\Psi^0_{BW}(t)\rangle\,\langle\Psi^0_{BW}(t)|\vec{\mu}|\Psi^1_{FW}(t)\rangle] \tag{3.49}$$

The first iteration is then completed. The second iteration starts again with the back-

ward propagation, analogous to Eq. (3.47), only this time using a field which contains information from the first iteration. That is:

$$\Psi^1_{BW}(t_0) \xleftarrow{\vec{\epsilon}_1(t)} \Psi^1_{BW}(T), \tag{3.50}$$

with the field

$$\vec{\epsilon}_1(t) = -\frac{1}{\alpha_0}\mathrm{Im}[\langle\Psi^1_{FW}(t)|\Psi^1_{BW}(t)\rangle\,\langle\Psi^1_{BW}(t)|\vec{\mu}|\Psi^1_{FW}(t)\rangle]. \tag{3.51}$$

The forward propagation of iteration 2 follows:

$$\Psi^2_{FW}(t_0) \xrightarrow{\vec{\epsilon}_2(t)} \Psi^2_{FW}(T), \tag{3.52}$$

with the field:

$$\vec{\epsilon}_2(t) = -\frac{1}{\alpha_0}\mathrm{Im}[\langle\Psi^2_{FW}(t)|\Psi^1_{BW}(t)\rangle\,\langle\Psi^1_{BW}(t)|\vec{\mu}|\Psi^2_{FW}(t)\rangle]. \tag{3.53}$$

The iterative scheme has thus the equations

$$\vec{\epsilon}_k(t) = -\frac{1}{\alpha_0}\mathrm{Im}[\langle\Psi^k_{FW}(t)|\Psi^k_{BW}(t)\rangle\,\langle\Psi^k_{BW}(t)|\vec{\mu}|\Psi^k_{FW}(t)\rangle], \tag{3.54}$$

and

$$\vec{\epsilon}_{k+1}(t) = -\frac{1}{\alpha_0}\mathrm{Im}[\langle\Psi^{k+1}_{FW}(t)|\Psi^k_{BW}(t)\rangle\,\langle\Psi^k_{BW}(t)|\vec{\mu}|\Psi^{k+1}_{FW}(t)\rangle], \tag{3.55}$$

for the fields of the backward and forward propagations in the k-th iteration, respectively. The algorithm continues to iterate until a convergence criterion is fulfilled, which in `oct.f90` is chosen as the overlap between initial and target wavefunction.

From a programming point of view, it is noteworthy that, for any given iteration, Eqs. (3.54) and (3.55) require knowledge of $\Psi_{FW}(t)$ or $\Psi_{BW}(t)$ of the immediately preceding propagation (FW or BW) over the whole range of times $t\,\epsilon\,[t_0, T]$ *and* over the whole range of $\beta\,\epsilon\,[0, 2\pi]$. Thus, wavefunctions need to be stored in memory from one iteration to the next one. However, in order to keep the program's memory requirements low, and because beyond a given size of the wavefunction, its readout can last longer than its recomputation, three propagations (instead of two) are implemented for each k-th iteration. The third propagation produces the needed wavefunction (Ψ_{FW} or Ψ_{BW}) by repeating its original propagation (FW or BW) in reverse, avoiding the necessity for storage and readout.[80]

3.5. Articles

3.5.1. Mechanistic insight into light-driven molecular rotors: a conformational search in chiral overcrowded alkenes by a pseudo-random approach

Guillermo Pérez-Hernández and Leticia González

*In the following article, the ground state conformational dynamics of motors **2** and **3** (see Fig. 3.1) are investigated in the ground state using a pseudo-random approach. A high number of semi-empirical (AM1) geometry optimizations are carried out using starting geometries that have been generated randomly. The initial randomness converges to a reduced number of just a few local minima of the ground state PES. These are subsequently optimized at the MP2/6-31G(d) level of theory. Further analysis of the obtained geometries leads to an assignment in the respective rotatory cycles of **2** and **3**. Transition state geometries (TSs) are computed at the B3LYP/6-31G(d) level of theory, and internal reaction coordinate (IRC) calculations follow, in order to obtain the mechanisms behind the thermal steps of the rotatory cycle. Energies of the DFT structures (minima and TSs) are recomputed at the RI-MP2/6-31G(d) level of theory. The resulting activation energies along the reaction paths are in very good agreement with the experimental data. However, the two motors present different ground state PES topologies, with six minima in the case of **2** and four in **3**. For **2**, new intermediates are found and alternative pathways are proposed. For **3**, the PES is less complicated, since the algorithm has found no further local minima different from the known geometries of the rotary cycle.*

Original can be found at http://dx.doi.org/10.1039/c0cp00324g.

PAPER www.rsc.org/pccp | Physical Chemistry Chemical Physics

Mechanistic insight into light-driven molecular rotors: a conformational search in chiral overcrowded alkenes by a pseudo-random approach†

Guillermo Pérez-Hernández and Leticia González*

Received 23rd April 2010, Accepted 15th July 2010
DOI: 10.1039/c0cp00324g

Chiral overcrowded alkenes are capable of unidirectional rotation *via* a series of *cis-trans* photochemical and helix-inversion thermal steps. Using a pseudo-random conformational search we have located different ground state minima belonging to the potential energy surface of two different overcrowded alkenes that function as molecular rotors. The transition states connecting the minima allow identifying different reaction pathways which are possible in the thermal helix-inversion steps. The mechanisms found for the two studied molecular rotors are different and provide a valuable insight into the conformational dynamics of the rotary cycle. While in one case the thermal step occurs *via* a single transition state, in the other, several intermediates are accessible. The associated energy barriers are in agreement with the experimental values, supporting the proposed mechanisms.

1. Introduction

The design and control of molecular machines is a fascinating quest in science and nanotechnology.[1–4] Among the different possible nanodevices intended to accomplish motion, linear and rotatory molecular motors have received a lot of attention since many synthetic examples have been reported during the last years.[5–13] Although functionality can be triggered in different ways, an interesting source of energy is the use of light. Light-driven molecular motors are attractive because they can be very fast, efficient, and cleaner than those driven by other external sources of energy (for a recent review, see ref. 14). For instance, the use of lasers offers ultrashort time domains as well as nanometre resolution. With this in mind, some efforts have been devoted to achieve unidirectional rotation with femtosecond laser pulses.[15–21] The fundamental aspects of controlling molecular rotors with femtosecond lasers have been recently revised by Fujimura and coworkers.[22]

In 1999 the group of Feringa reported[5] a class of artificial rotatory molecular motors based on chiral overcrowded alkenes, with a naphthalene moiety as a chromophore linked *via* a C=C double bond to an identical chromophore. An example of such "first generation" of molecular rotors with symmetric biphenanthrylidenes is **1** in Scheme 1. Faster rotations are achieved in the so-called "second generation" of molecular motors (see *e.g.* **2** in Scheme 1), where distinct upper and lower halves as well as heteroatoms are introduced.[23] Molecular motors of the type **2** have been mounted on a surface of gold,[12] gold nanoparticles,[24] and quartz surfaces[25] *via* a thioether linker on the lower half—the stator, while the upper half can act as a propeller. Recently,[26] this first and second generation of motors have been redesigned by exchanging the naphthalene moiety by a dimethyl-substituted phenyl group, see **3**. While preserving the molecular function, this new molecular motor is up to now the smallest of its type and it is anticipated that will facilitate the synthesis of other functionalized motors with tunable velocities.

In all these systems unidirectionality is achieved in four steps through a light-triggered *cis–trans* isomerization around the C=C double bond followed by an irreversible thermally activated helix-inversion. The direction of rotation (clockwise or counter-clockwise) is governed by the stereogenic centers present in the molecules, the interplay of steric hindrance in the so-called *fjord*-region (see Scheme 1), and the intrinsic helicity of the isomers. Scheme 2 illustrates the mechanism to achieve unidirectionality, taking as an example the rotor **3**. Step 1 is a *cis–trans* photoisomerization around the central double bond connecting the stable-*cis*-**3** structure with the unstable-*trans*-**3** one. Due to the steric effects between the upper and lower *p*-xylene moieties, the photoisomerization takes place only in one direction, namely in that which has the least steric hindrance. In step 2, a helicity inversion is triggered thermally, going from the unstable-*trans*-**3** to the stable-*trans*-**3** conformer. Key to the non-reversibility of this step is the relative stability of the isomers. Analogous to step 1, step 3 is a photoisomerization in which the stable-*trans*-**3** isomer

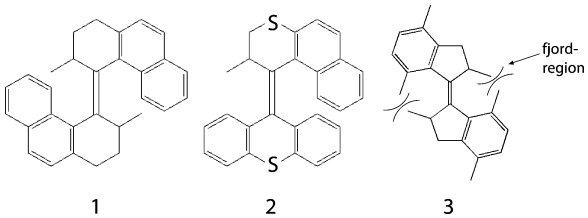

Scheme 1 First (**1**), second (**2**), and redesigned (**3**) generation of light-driven molecular rotors. The so-called *fjord*-region, where the steric hindrance determining the unidirectionality of the rotation occurs, is indicated in **3**.

Institut für Physikalische Chemie, Friedrich-Schiller-Universität Jena, Helmholtzweg 4, 07743 Germany.
E-mail: leticia.gonzalez@uni-jena.de

† Electronic supplementary information (ESI) available: Cartesian coordinates of all the structures of Fig. 5 and 8. See DOI: 10.1039/c0cp00324g

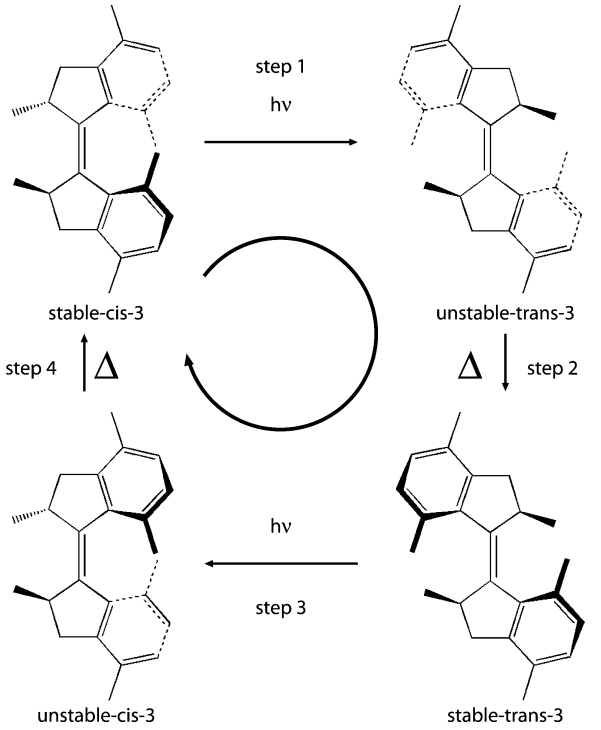

Scheme 2 Four-step mechanism to achieve unidirectionality in **3**, adapted from ref. 26.

evolves only in the direction in which the *p*-xylene moieties encounter less steric hindrance giving the unstable-*cis*-**3** structure. Finally, and similar to the step 2, a non reversible, thermally activated helicity inversion takes place in the step 4, converting the unstable-*cis*-**3** conformer into the stable-*trans*-**3**.

To characterize the structure and function of molecular motors diverse techniques can be employed. When the stages of the rotary cycle can be obtained as a solid, X-ray crystallography is the natural method of choice. In solution, structures can be probed with ^{1}H-NMR spectroscopy through the chemical shifts and coupling constants of the protons bonded to sp^{3} carbon atoms.[23] Also possible are kinetic studies by following these signals in time. UV-spectroscopy can be used to measure shifts in the absorption spectra after *cis–trans* photoisomerization. Furthermore, the inspection of helix-inversion and, ultimately, the unidirectionality of the cycle are carried out with circular dichroism techniques.

In addition to these experimental techniques, theory can be a useful tool to elucidate key aspects of the structures, energetics, and the mechanism underlying unidirectional molecular rotors. For instance, semiempirical calculations have been used to obtain ground state energies of the stable *cis* and *trans* conformers of **1**[27] and of some second generation rotors[23] different from **2**. Density functional theory (DFT) calculations have been employed to determine the expected geometry of unstable forms and the energy barriers involved in the thermal isomerization process of similar overcrowded alkenes[28] and also of **2** in particular.[29] Car–Parrinello molecular dynamic simulations using restricted open-shell Kohn–Sham theory[30] have shed some light on the photoinduced *cis–trans* mechanism of **1**. Recently, Torras and coworkers[31] have used DFT and MP2 theory to obtain the ground state potential energy profile along the torsion coordinate of **1** and of a similar motor where the six-membered ring is substituted by a five-membered one. The latter calculations were done in gas and in chloroform solution, both implicitly and explicitly, using polarized continuum models and quantum mechanics/molecular mechanics (QM/MM), respectively.[31]

In this paper, we use a pseudo-random method inspired in Monte-Carlo strategies[32,33] to search for all the ground state conformers which could be involved in the rotary cycle of these complex systems. Our conformational search is applied to the overcrowded alkenes **2** and **3**, for which structural information on intermediates is lacking. As in previous theoretical studies,[30,31] the present study also uses the known X-ray crystallography geometries of the stable conformers as starting geometries for the conformational space search. They serve as templates for creating pseudo-random variations in the conformational space. The generated structures will be subsequently optimized at the semiempirical level of theory. So-defined, the search departs from the original geometries and samples other possible orientations of the fragments. Because of its random nature, geometries are generated neglecting any thermal effects. Thus, the outcome of the method are relative energy differences and corresponding geometries. Rather than devising possible pathways between the known structures or to provide a precise structural description, the first step of the pseudo-random search aims at converging statistically to a distribution of all possible local minima of the ground state potential energy surface (PES), regardless of how they can be accessed. Then, the obtained geometries serve as starting points for subsequent optimizations at a higher level of theory. Certainly, not only stereoisomers of the template structure can appear; also constitutional isomers with other connectivities which do not play any role in the rotary cycle isomers can be the outcome of the pseudo-random search. With this method, all different conformers involved in the PES of the unidirectional rotary cycle of the overcrowded alkenes **2** and **3** have been located.

The rest of the paper is organized as follows. In the next section we describe the features which are relevant to the pseudo-random conformational search and we introduce the adopted notation. The conformational search method is explained in section 3. Section 4 is devoted to the results, first focusing on the general characteristics of the method and then on the conformers found thereby. Calculating the transition states connecting the minima of **2** and **3** allow us to complete the mechanism of rotation for each rotor. Finally, section 5 summarizes.

2. Molecular models and nomenclature

The stable starting geometries to be fed into the conformational search are depicted in Scheme 3. In the case of **2**, the symmetric lower dithioxantylene moiety, designed to be further functionalized[23] for ultimate connection to a solid surface,[12,25] is called stator and the upper half, the methyl-substituted napthothiopyran, is the propeller or rotor. In the case of **3**, both lower (stator) and upper (rotor) halves are identical.

In general, we label the conformations according to five descriptors, (i) absolute configuration of the chiral center (*R* or *S*), (ii) isomerism around the double bond (*cis* or *trans*), (iii) helicity (*M* or *P*), (iv) relative orientation of methyl groups and the *p*-xylene (**2**) or the naphthalene (**3**) moieties, (*Z* or *E*), and (v) orientation of the methyl group at the chiral carbon atom (axial or equatorial). These descriptors will be used when they are required to distinguish between two conformations and they will be dropped if unnecessary; *e.g.* in some molecules with *cis*-*trans* isomerism and in others without overall helicity we adopt *Z*/*E* nomenclature instead.

While in molecular motor **3** *R* and *S* configurations are possible at carbons 9 and 9′, in **2** only one chiral center is present at carbon 2. Accordingly, we shall label the motor **2** as (2*R*), and the motor **3** as (9*R*,9′*R*), see Scheme 3. In the particular case of **2**, due to its symmetrical stator, there are no *cis* or *trans* isomers, and therefore this label is only required in **3**. The relative orientation of the two halves can give the overall helicity of the molecule, *P* or *M*. The initial stable structure of motor **2** presents negative helicity and it is called *M*. From the two stable structures of **3**, one is *P* and the other does not have helicity, but can be distinguished with the *Z*/*E* label, in this particular case *Z*,*Z*′ for the lower and upper halves, respectively. In principle, the methyl group at the chiral center can be at axial or equatorial positions. However, due to steric hindrances this stereogenic methyl group is forced to a pseudo-axial or pseudo-equatorial positions. Both the starting geometries of **2** and **3** have the stereogenic methyl group in pseudo-axial position.

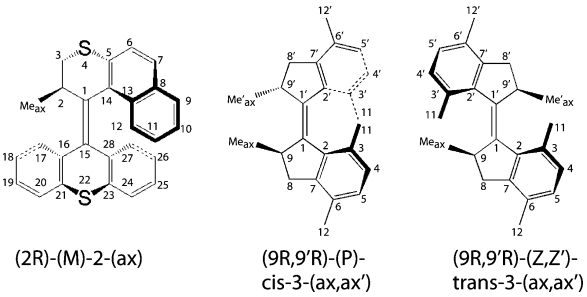

Scheme 3 Initial starting geometries used in the pseudo-random method with their labeling.

Accordingly, we shall globally name the initial geometry of the molecular motor **2** as (2*R*)-(*M*)-**2**-(*ax*). Similarly, in the case of **3** the geometries are (9*R*,9′*R*)-(*P*)-*cis*-**3**-(*ax*,*ax*′) and (9*R*,9′*R*)-(*Z*,*Z*′)-*trans*-**3**-(*ax*,*ax*′), see Scheme 3.

3. The pseudo-random conformational search approach

Globally, the method consists of three main steps: (i) the generation of a random ensemble of all chemically sensible molecular structures which belong to the full dimensional PES, (ii) a pre-selection of the most stable minima *via* an inexpensive optimization, and (iii) the refinement of the lowest-energy chemical species at a reliable higher level of theory.

Fig. 1 is a flux diagram with the different steps of the conformational search algorithm. The first step is the so-called randomizer, where molecular geometries are generated according to chemical criteria as explained below. The random generation is made in internal coordinates which allows to work with Z-matrices. We call the search *pseudo*-random because not all of the internal coordinates are randomly changed at the beginning of each optimization but chemical intuition is used to reduce meaningfully the conformational space. Random values are generated and combined only for those internal degrees of freedom which affect the conformations of the systems appropriately. In the case we are interested, *i.e.* the rotational profile of molecular motors of the type shown in Scheme 1, we allow random generation only for

(i) the length and twist of the central double bond, which results in *cis* or *trans* conformers,

(ii) the dihedral angles which determine the boat-chair conformation of the rings attached to the double bond (and inherently, the *Z* and *E* conformations),

(iii) the position of the methyl groups bound to the chiral atoms, which can be equatorial, axial, pseudo-equatorial or pseudo-axial, and gives rise to *R* or *S* enantiomers, and finally

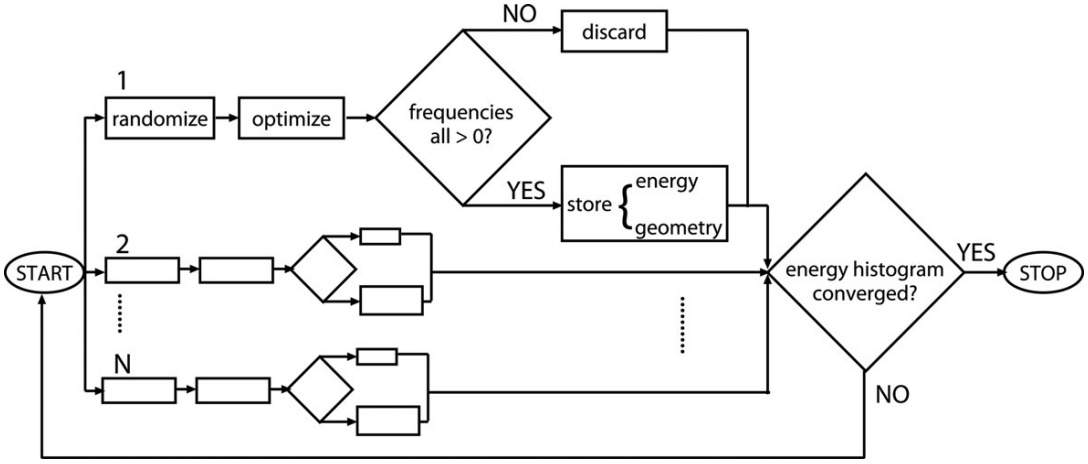

Fig. 1 Flux diagram of the pseudo-random conformational search. The procedure can be parallelized up to *N* processors.

Table 1 Internal degrees of freedom allowed to adopt random values in **2** (center column) and **3** (right column). In the case of **3** only one set of coordinates (without prime) is shown, but their symmetric counterparts (with prime) were also randomized. Numbers correspond to atom labels shown in Scheme 3. Except for the last row, all parameters are dihedral angles.

	Rotor	
Parameter	**2**	**3**
Boat-chair	14-1-2-3 1-2-3-4 15-28-23-22 28-23-22-21	1-1′-9-8
Helicity	4-5-14-13 1-15-28-24	8-7-2-3
Twist	2-1-15-28	9-1-1′-9
Methyl	15-1-2-Me	2-1-9-Me
Bond	1-15	1-1′

(iv) the dihedral angles which affect the helicity of the ring-moieties (*P* or *M*).

The randomizer does not change the form of the external ring moieties which are assumed to remain the same in all isomers of interest. As a result, the basic structure of rotor and stator is conserved in the initial randomly generated geometries. In this way, the conformational space is considerably reduced, avoiding chemical species irrelevant to the problem at hand. The detailed internal coordinates which have been randomized in compounds **2** and **3** are summarized in Table 1.

A random number is generated for every internal degree of freedom Q to be randomized such that $r \in [-0.5, +0.5]$. In order to determine how far away from its original value the random coordinate departs, we introduce a weighting factor $\omega \in [0,1]$. Then, the new value of the degree of freedom Q is obtained as

$$Q = Q_0 + r \cdot \omega \cdot I, \qquad (1)$$

where Q_0 is the initial value. The initial values Q_0 for **2** and **3** are taken from X-ray data, from ref. 12 and 26, respectively. For **2**, only one stable structure is available, while for **3** two conformers have been isolated, see Scheme 3. The interval range allowed for each type of coordinate is given by I; this range is different for bond distances, bond angles or dihedral angles, so that $I = Q_0$ for bond-lengths, $I = 180^\circ$ for bond angles and $I = 360^\circ$ for dihedral angles.

After generating a large ensemble of molecular geometries, these are optimized with an inexpensive method (see Fig. 1). In this work, we employ the semiempirical AM1 method, as implemented in MOPAC 2009,[34] but certainly any quantum chemical method can be used. All the optimizations are done without any symmetry restrictions. The next step is to perform a frequency calculation for each converged optimization to assure that only true minima are obtained. We note that all these steps can be trivially parallelized in as much each structure is optimized in one processor. Each AM1 converged geometry provides a heat of formation, which is collected and plotted in a histogram. Each peak corresponds to a narrow distribution of energy values associated to local minima within a chosen energy range. Here we use a range of 0.1 kcal/mol for a quick browsing of geometries in different energy ranges. When the energy histogram is converged, the geometries of each peak are analyzed and redundancies are eliminated until single isomers are isolated and assigned to particular energy values. Finally, once the group of distinct isomers has been isolated, each isomer is reoptimized at a more accurate level of theory. In this work the geometries have been optimized at the MP2/6-31G* level of theory with the Gaussian03 suite of programs.[35] An additional calculation of the Hessian at the same level of theory is done to guarantee that the obtained geometry is still a minimum of the MP2/6-31G*-hypersurface.

4. Results and discussion

4.1 Performance of the pseudo-random conformational search

In order to examine the robustness of the conformational search, here we analyze the performance of the method paying attention to several parameters. Exemplarily, we illustrate the procedure taking (2*R*)-(*M*)-**2**-(*ax*) as an initial structure. Once the set of internal coordinates have been chosen, three variables need to be set up to achieve a certain reproducibility: the seeding value with which the FORTRAN90 code harvests a table of random numbers, the number of iterations N_G (geometries which are converged to a minimum), and the weighting parameter ω (see eqn (1)). The seeding value does not have a physical meaning since it is automatically generated based on the actual time on the processor. Different seeding

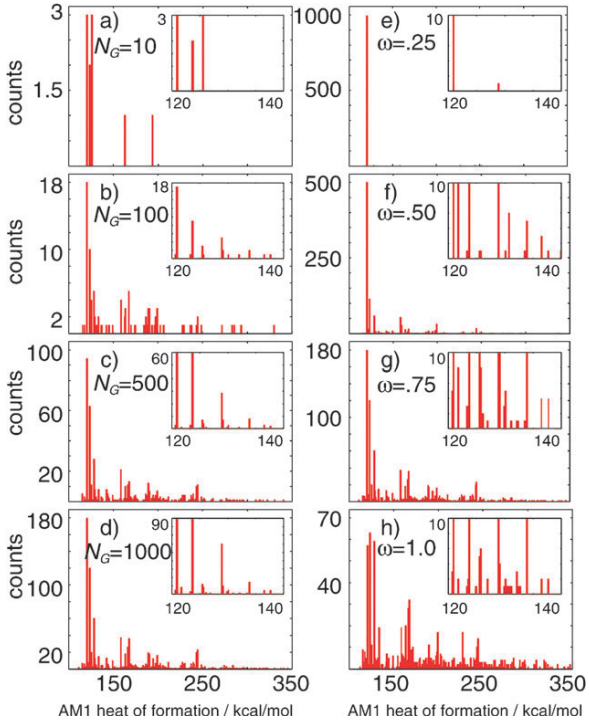

Fig. 2 Performance of the pseudo-random search method with respect to the number of converged iterations (panels a–d, $\omega = 0.75$) and to the weighting parameter ω (panels e–h). The number of converged geometries N_G is 10(a), 100(b), 500(c), and 1000(d). The insets display the low-energy range, close to the energy of the starting geometry of (2*R*)-(*M*)-**2**-(*ax*). In panels e-h the shown distributions are for $N_G = 1000$ converged geometries.

values will generate the same histogram of energies. The convergence of the method with the number of iterations is shown in Fig. 2 (panels a–d) for a fixed $\omega = 0.75$ value. The histograms, *i.e.* the number of counts per energy interval, are depicted for $N_G = 10$, 100, 500, and 1000 iterations. The insets zoom up the low energy range. As it can be seen, after 100 iterations there is little change in the energy distributions, meaning that no additional geometries are found but only the number of counts for a particular energy increases. The right column of Fig. 2 (panels e–h) displays the behavior of the energy distributions with respect to ω, using $N_G = 1000$ converged geometries. If the weighting factor is very tight, $\omega = 0.25$, *i.e.* the internal degrees of freedom are randomized only up to 25%, practically 100% of the generated geometries converge to the same structure—to the initial geometry of the template. A larger $\omega = 0.50$ enriches the energy distribution, making other geometries appear. The same trend is observed when ω increases to 0.75, and finally to the loosest value of 1.0. Although larger distributions are achieved with higher values of ω, increasing ω makes the histogram more widespread. The number of counts per given energy or the peak-heights in the histogram become smaller from panel (e) to (h); note the different scales. This is a pure statistical behavior because the more geometries become available to the randomizer through a larger ω, the less sensible geometry is generated and thus the less optimizations converge. That is, even if a large number of iterations are desirable to cover as much conformational space as possible, once the pair of values for ω and for the *seed* is chosen, the energy distributions take shape after a relatively small amount of iterations. For the following conformational searches a total of 1000 geometries ($N_G = 1000$) were computed with the ω parameter set to 0.75.

4.2 Potential energy surface of molecular rotor 2

4.2.1 Equilibrium conformers of 2. In this section we discuss the conformers generated out of (2*R*)-(*M*)-**2**-(*ax*), recall Scheme 3. Note that in the rotary cycle of this complex, depicted in Scheme 4, one photochemical step followed by a thermal step reverts the molecule to a geometry indistinguishable from the starting one. Only if **2** is fixed to a surface, as in ref. 12 and 25, these indistinguishable geometries have different orientations relative to the solid. However, in solution, or in gas phase, as we are treating here, the two thermal products are totally equivalent. By means of our algorithm we intend to search for the unstable photochemical

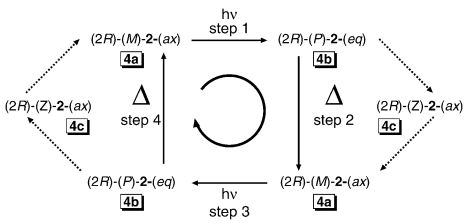

Scheme 4 Schematic representation of the rotary cycle of **2**. Solid arrows represent the photochemical and thermal steps (1–4) of the cycle. Dotted arrows indicate the intermediate species in the thermal steps according to ref. 29. The labels 4a–c correspond to the structures of Fig. 4.

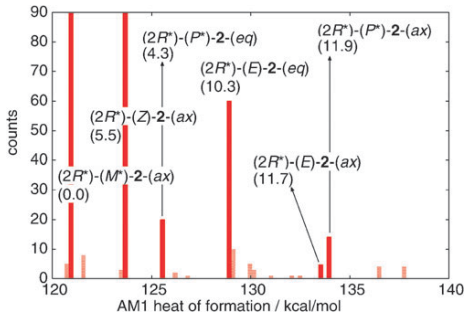

Fig. 3 Low energy range of the histogram for (2*R*)-(*P*)-**2**-(*ax*). The relevant geometries are labeled; the * indicates that both enantiomers (*R* and *S*, or *M* and *P*) are included. The MP2/6-31G* relative energy in kcal/mol is given in parenthesis.

geometries or other minima which could be involved in the cycle.

In Fig. 3 the histogram obtained after 1000 iterations is presented. The picture is already restricted to the useful energy range and shows MP2/6-31G* relative energies in parenthesis. Among all the peaks, only six correspond to structures sharing the same connectivity as the molecular motor **2** and only those have been labeled. These isomers have been drawn in Fig. 4, indicating the relevant parameters of the central olefinic plane and the moieties around it. We note that the relative order of the optimized conformers at AM1 level of theory is different than at MP2. The most stable structure is, as expected, the initial (2*R*)-(*M*)-**2**-(*ax*) conformer and its enantiomeric counterpart (2*S*)-(*P*)-**2**-(*ax*); for simplicity we denote the pair by racemic notation (2*R**)-(*M**)-**2**-(*ax*). Analogously, each peak of the histogram contains the two members of the enantiomeric pair and they will be denoted correspondingly. The next conformer higher in energy is the (2*R**)-(*P**)-**2**-(*eq*), which we identify as the photochemical product of the rotary cycle, on the basis of its helicity (P) and the position of the methyl group (equatorial), see Fig. 4b. The energy difference between the two most stable conformers is 4.3 kcal/mol at MP2/6-31G* level of theory. Recent results obtained by the group of Feringa *et al.*[29] predict a value of 4.6 kcal/mol at DFT/6-31G** level of theory for this structure.

Besides the most stable conformer of **2** and its photochemical product (2*R**)-(*P**)-**2**-(*eq*), another four additional minima have been found. They differ in the helicity, the position of the methyl group and the relative orientation of the methyl group with respect to the naphtalene moiety. In the conformer closest in energy (only 1.2 kcal/mol above the photoproduct), both rotor and stator moieties are on the same side of the central olefinic plane. The overall helicity is thereby lost and because the methyl group and the naphthalene moiety (both on the rotor) point towards the same side of the olefinic plane of the central double bond (*cf.* Fig. 4c), the *Z* descriptor is used; hence, this structure is designated as (2*R**)-(*Z*)-**2**-(*ax*).

The three additional isomers have relative stabilities *ca.* 11 kcal/mol above the most stable one, (2*R**)-(*M**)-**2**-(*ax*). The next conformer higher in energy (10.3 kcal/mol) is (2*R**)-(*E*)-**2**-(*eq*), which also possesses no helicity but the methyl group, now on equatorial position, is on opposite side of the naphthothiopyran moiety, corresponding to an *E* arrangement (see Fig. 4d). The

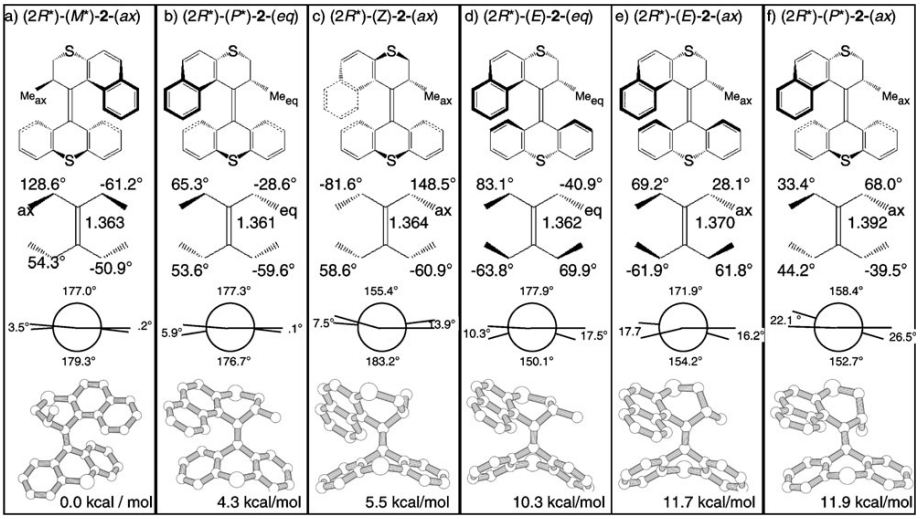

Fig. 4 Conformers of **2**. For each panel, from top to bottom: chemical structures, dihedral angles of the groups attached to the central double bond, Newman projections as observed through the central double bond, and PLUTO drawings. Relative energies in kcal/mol at the MP2/6-31G* level of theory. Angles in degrees and bond lengths in Å.

conformer (2*R**)-(*E*)-**2**-(*ax*) is only 1.5 kcal/mol higher in energy and, as seen in Fig. 4e, it is the result of changing the methyl group from equatorial to pseudo-axial position. Finally, the most unstable structure—almost degenerated with the previous one—differs in the orientation of the stator moiety, now flipped to the opposite side as the rotor moiety, while keeping the methyl in axial position, see Fig. 4f. This conformer possesses again overall helicity and is thus labeled (2*R**)-(*P**)-**2**-(*ax*).

The relative stabilities are a consequence of steric factors and they are best explained with the help of Newman projections along the double bond connecting rotor and stator (Fig. 4). In the case of the two most stable isomers, the projections clearly show the least distorted olefinic planes, with fold angles of *ca.* 177° and deviations from planarity in the sp^2 carbons of maximum 6° (see Fig. 4a and b). Furthermore, in these two structures, the stator and rotor are accommodated on opposite sides of the olefinic plane, so that steric hindrances are minimized. In (2*R**)-(*Z*)-**2**-(*ax*) (Fig. 4c) both stator and rotor are flipped to the same side of the olefinic plane. This strain upon the double bond is reflected by higher fold angles (*ca.* 155°). However, this structure is stabilized by having the methyl group in an axial position, pointing outwards of the highly populated *fjord*-region. That is not the case of (2*R**)-(*E*)-**2**-(*eq*) (Fig. 4d), about 5 kcal/mol higher in energy than the previous structure. The other two remaining higher-energy structures (Fig. 4e and f) are twisted in the olefinic plane with angles between 16° and 28° and pyramidalized at the sp^2 carbons around *ca.* 25°. Interestingly, in all the conformers the C=C bond distances differ little, ranging from 1.361 to 1.364 Å, except in (2*R**)-(*P**)-**2**-(*ax*), where this bond is stretched to 1.392 Å as a consequence of the large strain between the stator and rotor.

In the following we are concerned with the role of the different conformers in the "four-step" rotary cycle of compound **2** (see Scheme 4). Whereas the thermal (Fig. 4a), (2*R**)-(*M**)-**2**-(*ax*), and photochemical (Fig. 4b), (2*R**)-(*P**)-**2**-(*eq*), products involved in step 1 have been experimentally detected, the others have not been isolated so far. The conformer (2*R**)-(*Z*)-**2**-(*ax*), (Fig. 4c), has been recently calculated[29] to be an intermediate at 3.7 kcal/mol in the thermal helicity inversion (step 2 in Scheme 4), even if it has not been detected experimentally. Such an intermediate is not surprising taking into account that helicity inversion also occurs through *meso* forms in similar systems, such as other first[36] and second[29] generation molecular rotors as well as byphenanthrylidenes.[27] Moreover, stepwise helicity inversion has also been theoretically predicted in other bistricyclic aromatic overcrowded alkenes.[37]

The three remaining conformers found by the algorithm (Fig. 4d–f) have not been reported so far as part of the rotary cycle. Therefore, in order to provide insight into the role of all the optimized conformers and undercover the overall mechanism of the rotary cycle, transition states (TS) connecting the minima have been calculated. These shall be presented and discussed in the following section.

4.2.2 Transition state geometries of 2. The search of TS requires suitable starting geometries. To this aim, relaxed potential energy scans were performed at the AM1 semi-empirical level of theory. The scans were carried out by simultaneously changing one, two, or three internal coordinates, typically those characterizing the dihedral angles shown in Fig. 4, while allowing the rest of the coordinates to relax. Such scans deliver energy curves with a discontinuity that marks the change from the reactant side to the product side of the potential. For each curve, the structure prior to the discontinuity was then optimized at HF/STO-3G level of theory using standard TS search algorithms as implemented in Gaussian03.[35] After a TS is optimized, the geometries and energies were refined using B3LYP/6-31G*. The level of theory MP2/6-31G* could not be used since the search of TS

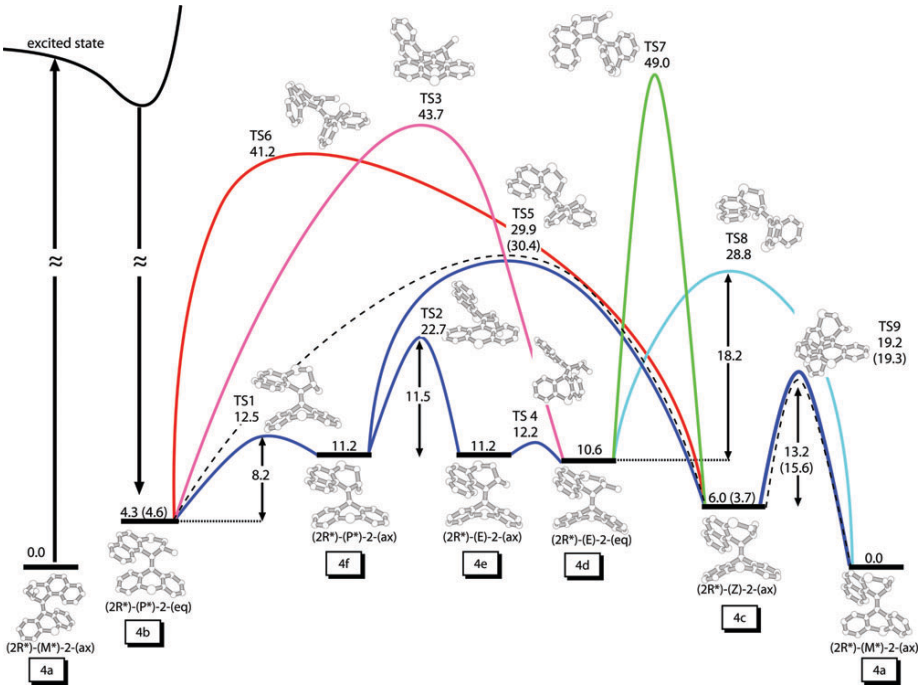

Fig. 5 RI-MP2/TZVP energies at the B3LYP/6-31G* geometries of the six equilibrium conformers of **2** and the corresponding transition states between them. Energies are given in kcal/mol. Values in parenthesis are taken from ref. 29. Dashed lines refer to the pathway suggested in ref. 29. The labels 4a–4f correspond to the isomers of Fig. 4.

requires the computation of force constants which are unfeasible at this level of the theory in our present computers. For consistency in the reaction paths, all the minima have been reoptimized at the same DFT level of theory as the TS. In order obtain more accurate energy values on these geometries, single-point energy calculations were then carried out with a polarized triple-zeta basis set (TZVP[38]) at the second-order Møller–Plesset perturbation theory level using the resolution of identity approximation (RI-MP2[39,40]) as implemented in the TURBOMOLE quantum chemical software.[41,42] Finally, intrinsic reaction coordinate (IRC, as implemented in Gaussian03[35]) calculations were carried out at DFT level to determine the reactants and products linked to a given transition state. A total of nine TS were located. They are labeled TS1 through TS9 and are depicted together with the minima they link in Fig. 5. For simplicity in the following discussion, the minima will be addressed with the labels 4a–4f from Fig. 4.

The relative stabilities of the TS and corresponding minima with respect to the most stable thermal 4a minimum are also given in Fig. 5. The obtained values agree well with those available in the literature. After irradiation, the photochemical product 4b is obtained and then several mechanisms can be conceived. Until now it has been suggested[29] that the intermediate 4c, conformer (2*R**)-(*Z*)-**2**-(*ax*), is reached *via* the TS5 (dashed line in Fig. 5). Therefore, TS5 can be ascribed as the rate-limiting step of the stepwise helix inversion from 4b to 4a, (*i.e.* the reaction (2*R**)-(*P**)-**2**-(*eq*) → (2*R**)-(*M**)-**2**-(*ax*)). The activation barrier E_a = 25.6 kcal/mol from 4b to TS5, both in this study and in ref. 29, is in agreement with the experimental value of the activation energy of 24.92 ± 0.92 kcal/mol[23] for that helix inversion. Furthermore, this value is also in agreement with the semiempirical value of 24.3 kcal/mol obtained by Biedermann *et al.*[37] for the helix inversion of dithioxantylene, a related overcrowded alkene with a thioxanthylene group both as stator and rotor. As calculated by Klok *et al.*[29] and confirmed in this work, from the intermediate 4c the final thermally stable product 4a is reached *via* the TS9. The obtained activation barrier E_a is about 13 kcal/mol, about 2 kcal/mol lower than in ref. 29.

Our IRC calculations, however, do not connect the TS5 directly with the photochemical product 4b, but with the intermediate 4f, (2*R**)-(*P**)-**2**-(*ax*), which belongs to the group of three isomers lying around 11 kcal/mol above the minimum. If we start from the photoproduct 4b we find a small activation energy (TS1 with E_a = 8.2 kcal/mol), which is required to change the methyl group from equatorial to axial position. This change can revert almost barrierless since the corresponding local minimum 4f is very shallow, lying only 1.3 kcal/mol under TS1. According to our calculations, the unstable intermediate 4f is further linked with the conformer 4e *via* the TS2. This TS corresponds to the flip of the stator unit. It lies *ca.* 23 kcal/mol above the thermal stable minimum and leads to an activation energy of 11.5 kcal/mol, for both the forward and backward reactions from 4f and 4e. The conformer 4e, as was 4f, is a very shallow minimum. Not only the reaction axial ↔ equatorial (4e ↔ 4d) occurs almost barrierless *via* the TS4 (E_a = 1 kcal/mol), but 4e and 4f are nearly degenerated. A direct path to 4d from 4b can be achieved *via* TS3 at a much more energetic expense, E_a ~ 39 kcal/mol.

From the conformer 4d (which at room temperature should be indistinguishable from 4e) several pathways with different

activation energies are available. The lowest energy path is a stepwise reversion to the photoproduct 4b *via* the series of TS4, TS2, and TS1, as described before. In this path TS2 is the rate-limiting step with E_a = 12.1 kcal/mol. A direct reversion pathway is also possible through TS3 but with a much higher E_a of 33.1 kcal/mol. The forward reaction towards the stable form 4a goes either directly through TS8 with an activation energy E_a = 18.2 kcal/mol or stepwise through TS7 → 4c → TS9 → 4a. The latter pathway *via* the intermediate 4c is unlikely, since TS7 bears a very large activation energy (E_a = 35.9 kcal/mol) and other lower-energy pathways are accessible.

Note that in view of the calculated paths, the intermediate 4c is only accessible in the stepwise manner 4b → TS1 → 4f → TS5 → 4c, and not as 4b → TS5 → 4c (dashed line[29]). A single step is yet possible, but the corresponding TS, which is TS6, lies at *ca.* 41 kcal/mol and it is not likely to be populated. The intermediate 4c has not been found experimentally, as kinetic data[23] on the thermal decay of 4b indicated a first order reaction in the thermal helix-inversion. The explanation is that because the energy barrier of TS9 is so small the reaction occurs too fast to detect 4c on an NMR timescale.

In conclusion, Fig. 5 indicates that several paths are possible in going from the photoproduct 4b, (2*R**)-(*P**)-**2**-(*eq*), to the thermally stable 4a, (2*R**)-(*M**)-**2**-(*ax*). The reaction is multi-step and it can undergo either *via* the rate limiting steps TS5 or TS8. In both cases the activation energies lie around 24 to 25 kcal/mol, in excellent agreement with the experimental value 24.92 ± 0.92 kcal/mol.[23] Besides 4c, the least stable isomers 4f, 4e, and 4d above 10 kcal/mol are all energetically accessible.

However, these local minima appear to be very shallow, making the reaction easily reversible *via* the TS1, TS2, and TS4, respectively. Thus, it is very probable that TS8 is never populated. Instead, the rotary cycle should undergo as 4a → 4b → TS1 → 4f → TS5 → 4c → TS9 → 4a.

4.3 Potential energy surface of molecular rotor 3

4.3.1 Equilibrium conformers of 3. The low-energy range of the histogram obtained for **3** is presented in Fig. 6 for ω = .75 and N_G = 1000. The two available *cis* and *trans* X-ray structures (see Scheme 3) produced similar histograms. In contrast to the histogram of **2** where single peaks are observed, here six broad distributions are obtained. Within each of them, the geometries correspond to changes of the hydrogen atoms of the methyl groups of the *p*-xylene moieties from eclipsed to staggered. Among the different structures, only the lowest energy ones were then optimized at MP2/6-31G* level of theory. Fig. 7 collects the found structures, showing the Newman projections along the central double bond (C1–C1′), the dihedral angles of the moieties attached to the olefinic plane, and PLUTO drawings. As in **2**, the notation (*R**,*R**)-*P** and (*R**,*R**)-*M** contains both enantiomers, (*R*,*R*)-*P*/(*S*,*S*)-*M* and (*R*,*R*)-*M*/(*S*,*S*)-*P*, respectively. Similarly, (*R**,*S**)-*M** contains four identical stereoisomers (*R*,*S*)-*M*, (*R*,*S*)-*P*, (*S*,*R*)-*M* and (*S*,*R*)-*P*, which are related to each other through a reflection or through the exchange of the rotor and stator halves.

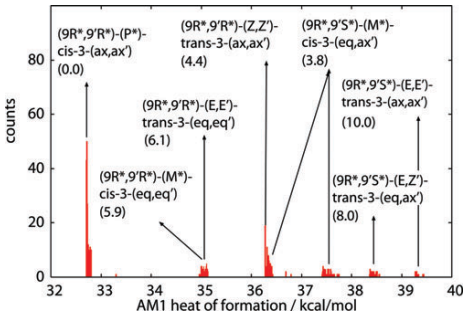

Fig. 6 Low energy range of the histogram for (9*R*,9′*R*)-(*P*)-*cis*-**3**-(*ax*,*ax*′) or (9*R*,9′*R*)-(*Z*,*Z*′)-*trans*-**3**-(*ax*,*ax*′). The relevant geometries are labeled; the * indicates that both enantiomers (*R* and *S*, or *M* and *P*) are included. The MP2/6-31G* relative energy in kcal/mol is given in parenthesis.

Among the six energy distributions we have found seven different conformers, see Fig. 7a–g. The lowest in energy is labeled (9*R*,9′*R*)-(*P*)-*cis*-**3**-(*ax*,*ax*′) and corresponds to the initial stable-*cis*-**3** structure of the rotary cycle, see Scheme 2. The stable-*trans*-**3** structure of the rotary cycle corresponds to (9*R*,9′*R*)-(*Z*,*Z*′)-*trans*-**3**-(*ax*,*ax*′) and lies 4.4 kcal/mol higher in energy. The algorithm has found another two structures at 6.1 and 5.9 kcal/mol, respectively, which show the same absolute configurations on carbons 9 and 9′ and both methyl groups on equatorial or pseudo-equatorial position (Fig. 7c and d). They are ascribed to the two photochemical products, unstable-*trans*-**3** and unstable-*cis*-**3**, resulting after step 1 and step 3 of the rotary cycle.[26] In our notation these two conformers are named (9*R*,9′*R*)-(*E*,*E*′)-*trans*-**3**-(*eq*,*eq*′) and (9*R*,9′*R*)-(*M*)-*cis*-**3**-(*eq*,*eq*′). All four conformers discussed above possess C_2 symmetry. As in the case of **2**, the most stable isomers are the ones where the stereogenic methyl groups are on axial position (Fig. 7a and b). Additionally, the conformer search arrived at three additional diastereomers in which the absolute configuration of the chiral carbon atoms (C9 and C9′) differs from one half to the other (Fig. 7e–g). Since during the unidirectional rotation the absolute configurations of the chiral carbons must be conserved, we conclude that these structures are not involved in the rotary cycle and thus will not be further discussed.

The X-ray structures of the thermal products of **3** show a twisted central olefin moiety.[26] This distortion can be seen in the fold angles of the double bond (167° and 207°) in Fig. 7a and c, respectively. Note that the optimized theoretical values are in very good agreement with the experimental available ones (in parenthesis). The same distortion is appreciated in the photochemical products (Fig. 7b and d). This distortion is due to the steric hindrance arising from accommodating the sp^3 carbon atoms of the chiral center 9′ and of the *p*-xylene moieties in the *fjord*-region. In fact, as compared to **2**, the *fjord*-region has to accommodate one additional methyl-group. This increase of the steric hindrance can be responsible for the absence of other minima equivalent to those of **2**.

4.3.2 Transition state geometries of 3. The TS that connect the conformers participating in the rotary cycle of **3** were computed at the B3LYP/6-31G* level of theory in the same fashion as for **2**. For consistency, the minima were also

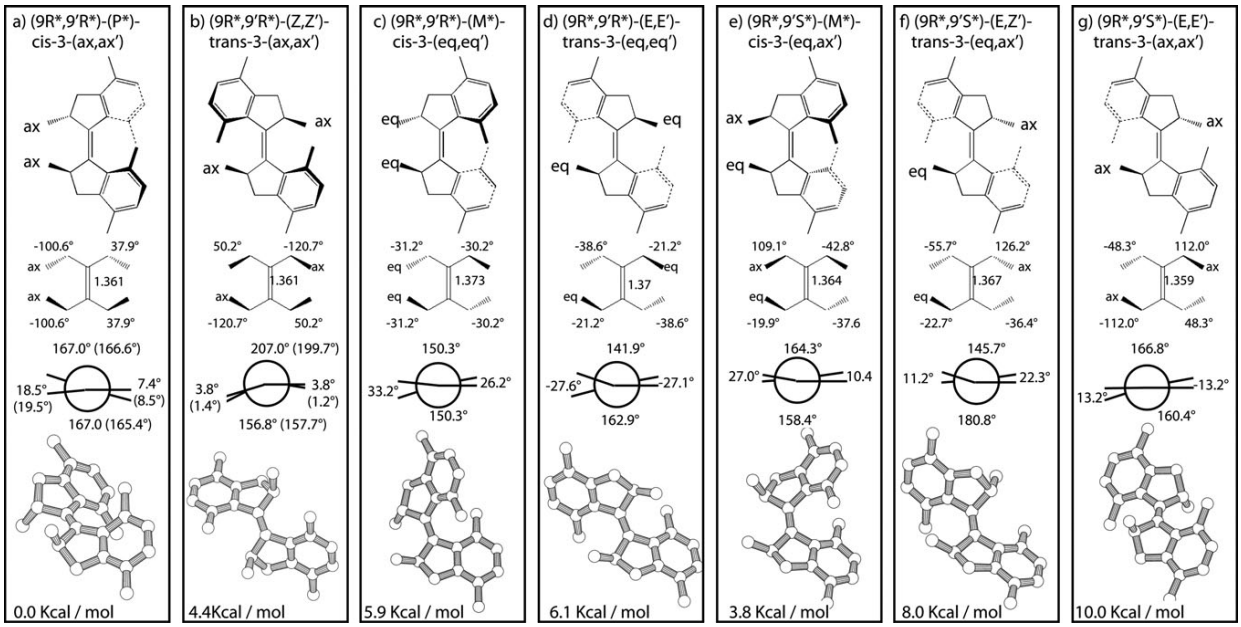

Fig. 7 Conformers of **3**. For each panel, from top to bottom: chemical structures, dihedral angles of the groups attached to the central double bond, Newman projections as observed through the central double bond, and PLUTO drawings for the conformers of **3**. Relative energies at the MP2/6-31G* level of theory are also displayed. Angles in degrees and bond lengths in Å. When available, experimental values from ref. 26 are given in parenthesis.

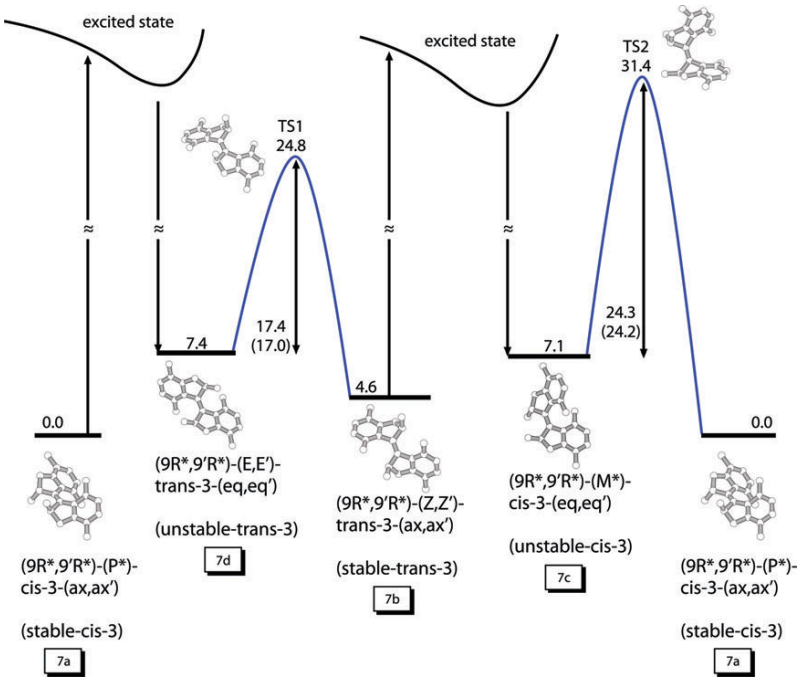

Fig. 8 RI-MP2/TZVP energies at the B3LYP/6-31G* geometries of the four equilibrium conformers of **3** and the corresponding transition states between them. Energies are given in kcal/mol. Values in parenthesis correspond to experimental values of Gibbs free energies of activation at 0 °C taken from ref. 26. The labels 7a–7d correspond to the structures of Fig. 7.

reoptimized at B3LYP/6-31G* level of theory. Single-point energy calculations at the RI-MP2/TZVP level of theory were then performed on all the obtained geometries. The resulting energy profile for this rotor, with geometries and relative internal energies to the global minimum is summarized in Fig. 8.

Contrary to what it was found for rotor **2**, there is no intermediate in the thermal helicity inversion of **3**. The steps 2

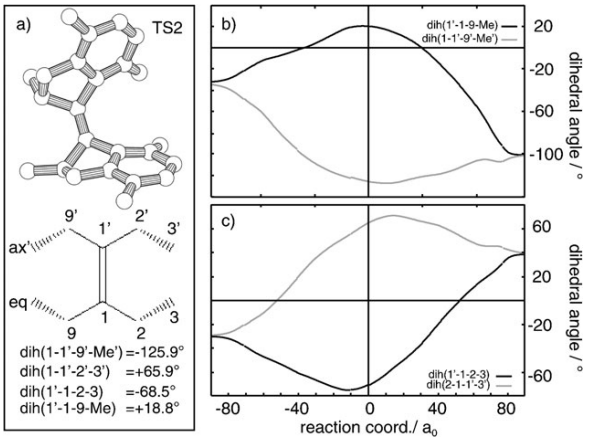

Fig. 9 Transition state TS2 for the thermal step unstable-*cis*-**3** → stable-*cis*-**3** at B3YLYP/6-31G* level of theory. (a) PLUTO drawing and values of the dihedral angles of moieties attached to the central double bond. (b) and (c) Dihedral angles along the reaction coordinate as computed by an IRC calculation at B3YLYP/6-31G* level of theory. Reaction coordinate 0 marks the transition state TS2.

and 4 of the rotary cycle (Scheme 2) occur in a single step *via* the TS1 and TS2, respectively. The obtained E_a values of 17.4 kcal/mol and 24.3 kcal/mol are in good agreement with the experimental Gibbs free energies[26] of 17.0 and 24.2 kcal/mol, respectively.[43] Interestingly, whereas all the minima of the rotary cycle present C_2 point-group symmetry, none of the found TS does. The IRC calculations show that the motion of the two equivalent molecular halves is not synchronous. Exemplarily, Fig. 9 shows this asymmetric behavior for the step 4 of the rotary cycle *via* TS2. From both TS, this is the most prominent example of asymmetry because TS2 has one methyl group clearly on axial position and the other in equatorial one. Fig. 9a shows a PLUTO drawing of TS2 with the dihedral angles around its central olefinic plane indicated. Fig. 9b and c show the evolution of these dihedral angles against the reaction coordinate; panel b shows the motion the stereogenic methyl substituents (with and without prime) and panel c the motion the *p*-xylene moieties. The TS occurs at the reaction coordinate 0. From Fig. 9b we see that both methyl groups (at C2 and C2′) start at the same value of $-30°$ (equatorial position). When the geometry has arrived at TS2, the dihedral angle of the methyl group at C2 has been displaced *ca.* 50°, whereas the one at C2′ has changed by almost twice as much ($\sim$95°). From TS2 onwards the behavior is inverted: the methyl at C2 must change *ca.* 120° to go from equatorial to axial, whereas the one at C2′ only needs to adjust by $\sim$25°. A similar behavior is observed in Fig. 9c. The asynchronous mechanism implies that an equivalent pathway for step 4 is possible, where the methyl at C2′ is the one that moves first, and then the one at C2 follows.

5. Conclusions

This paper provides insight into the thermal mechanism of two chiral overcrowded alkenes which act as light-triggered unidirectional molecular rotors, **2** (so-called second-generation rotor) and **3** (*redesigned* rotor). A *pseudo*-random approach has been implemented to locate ground state minima belonging to the potential energy surface of **2** and **3**. In the case of **2**, a total of six local minima have been found. Three of them, lying at about 11 kcal/mol above the absolute minimum, had not been reported so far and their possible role in the thermal steps of rotary cycle is discussed. Transition states connecting the six available conformers are located allowing to estimate activation energy values for different isomerization pathways. Our calculations indicate that the thermal helicity inversion step of the rotary cycle of **2** is multistep involving several intermediates and corresponding transition states. The limiting energy barrier is estimated to be *ca.* 26 kcal/mol, which agrees well with the experimental value of *ca.* 25 kcal/mol.[23] In the case of the rotor **3**, seven isomers were found, from which only four belong to the rotary cycle, while the other three conformers are diastereoisomers of the rotor. The two calculated TS for the thermal helix inversion of **3** deliver energies of activation of $\sim$17 and $\sim$24 kcal/mol, also in excellent agreement with the experimental ones.[26]

On the quest to find efficient control strategies of light-triggered molecular rotors, as *e.g.* involving shaped laser pulses, the understanding of the mechanism underlying this class of light-triggered molecular rotors is essential. Here we have characterized the potential energy landscapes of the thermal steps. An analysis of the photochemical pathways is currently in progress.

Acknowledgements

The authors thank the Deutsche Forchungsgemeinschaft (GO 1059/2-1) and the Jenaer Graduierten-Akademie for financial support. N. Pérez-Hernández and J. González-Vázquez are also acknowledged for useful comments. The computing facilities (ZEDAT) of the Freie Universität Berlin and Friedrich-Schiller-Universität Jena are also acknowledged for computer time.

References

1 *Molecular Switches*, ed. B. L. Feringa, Wiley-VCH, Weinheim, 2001.
2 *Molecular Machines and Motors*, ed. J. P. Sauvage, Springer, Berlin, 2001.
3 *Molecular Motors*, ed. M. Schliwa, Wiley-VCH, Weinheim, 2003.
4 *Molecular Devices and Machines-Concepts and Perspectives for the Nanoworld*, ed. V. Balazani, A. Credi and M. Venturi, Wiley-VCH, Weinheim, 2008.
5 N. Koumura, R. W. J. Ziljstra, R. A. van Delden, B. L. Feringa and N. Harada, *Nature*, 1999, **401**, 152–155.
6 T. R. Kelly, H. D. Silva and R. A. Silva, *Nature*, 1999, **401**, 150–152.
7 X. Zheng, M. E. Mulcahy, D. Horinek, F. Galeotti, T. F. Magnera and J. Michl, *J. Am. Chem. Soc.*, 2004, **126**, 4540–4542.
8 G. S. Kottas, L. I. Clarke, D. Horinek and J. Michl, *Chem. Rev.*, 2005, **105**, 1281–1376.
9 J. Vacek and J. Michl, *Adv. Funct. Mater.*, 2007, **17**, 730–739.
10 E. R. Kay, D. A. Leigh and F. Zerbetto, *Angew. Chem., Int. Ed.*, 2007, **46**, 72–191.
11 J. Michl and E. C. H. Sykes, *ACS Nano*, 2009, **3**, 1042–1048.
12 R. A. van Delden, M. K. J. ter Wiel, M. M. Pollard, J. Vicario, N. Koumura and B. L. Feringa, *Nature*, 2005, **437**, 1337–1340.
13 J. F. Stoddart, *Acc. Chem. Res.*, 2001, **34**, 410–411.
14 V. Balzani, A. Credi and M. Venturi, *Chem. Soc. Rev.*, 2009, **38**, 1542–1550.

15 K. Hoki, M. Yamaki, S. Koseki and Y. Fujimura, *J. Chem. Phys.*, 2003, **119**, 12393–12398.
16 K. Hoki, M. Yamaki, S. Koseki and Y. Fujimura, *J. Chem. Phys.*, 2003, **118**, 497–504.
17 K. Hoki, M. Yamaki and Y. Fujimura, *Angew. Chem., Int. Ed.*, 2003, **42**, 2976–2978.
18 Y. Fujimura, L. González, D. Kröner, J. Manz, I. Mehdaoui and B. Schmidt, *Chem. Phys. Lett.*, 2004, **386**, 248–253.
19 K. Hoki, M. Sato, M. Yamaki, R. Sahnoun, L. González, S. Koseki and Y. Fujimura, *J. Phys. Chem. B*, 2004, **108**, 4916–4921.
20 P. Marquetand, S. Gräfe, D. Scheidel and V. Engel, *J. Chem. Phys.*, 2006, **124**, 054325.
21 G. Pérez-Hernández, A. Pelzer, L. González and T. Seideman, *New J. Phys.*, 2010, **12**, 075007.
22 M. Yamaki, S. Nakayama, K. Hoki, H. Kono and Y. Fujimura, *Phys. Chem. Chem. Phys.*, 2009, **11**, 1662–1678.
23 N. Koumura, E. M. Geertsema, M. B. van Gelder, A. Meetsma and B. L. Feringa, *J. Am. Chem. Soc.*, 2002, **124**, 5037–5051.
24 M. M. Pollard, M. K. J. ter Wiel, R. van Delden, J. Vicario, N. Koumura, C. R. van den Brom, A. Meetsma and B. L. Feringa, *Chem.–Eur. J.*, 2008, **14**, 11610–11622.
25 M. M. Pollard, M. Lubomska, P. Rudolf and B. L. Feringa, *Angew. Chem., Int. Ed.*, 2007, **46**, 1278–1280.
26 M. M. Pollard, A. Meetsma and B. L. Feringa, *Org. Biomol. Chem.*, 2008, **6**, 507–512.
27 R. W. J. Zijlstra, W. F. Jager, B. de Lange, P. T. van Duijnen, B. L. Feringa, H. Goto, A. Saito, N. Koumura and N. Harada, *J. Org. Chem.*, 1999, **64**, 1667–1674.
28 J. Vicario, M. Walko, A. Meetsma and B. L. Feringa, *J. Am. Chem. Soc.*, 2006, **128**, 5127–5135.
29 M. Klok, M. Walko, E. M. Geertsema, N. Ruangsupapichat, J. C. M. Kistemakea, A. Meetsma and B. L. Feringa, *Chem.–Eur. J.*, 2008, **14**, 11183–11193.
30 S. Grimm, C. Bräuchle and I. Frank, *ChemPhysChem*, 2005, **6**, 1943–1947.
31 J. Torras, F. Rodríguez-Ropero, O. Bertran and C. Alemán, *J. Phys. Chem. C*, 2009, **113**, 3574–3580.
32 G. Chang, W. C. Guida and W. C. Still, *J. Am. Chem. Soc.*, 1989, **111**, 4379–4386.
33 D. M. Ferguson and D. J. Raber, *J. Am. Chem. Soc.*, 1989, **111**, 4371–4378.
34 J. J. P. Stewart, *MOPAC2009*, Stewart Computational Chemistry Colorado Springs, CO, USA, 2009, http://OpenMOPAC.net.
35 M. J. Frisch, G. W. Trucks, H. B. Schlegel, G. E. Scuseria, M. A. Robb, J. R. Cheeseman, J. A. Montgomery, Jr., T. Vreven, K. N. Kudin, J. C. Burant, J. M. Millam, S. S. Iyengar, J. Tomasi, V. Barone, B. Mennucci, M. Cossi, G. Scalmani, N. Rega, G. A. Petersson, H. Nakatsuji, M. Hada, M. Ehara, K. Toyota, R. Fukuda, J. Hasegawa, M. Ishida, T. Nakajima, Y. Honda, O. Kitao, H. Nakai, M. Klene, X. Li, J. E. Knox, H. P. Hratchian, J. B. Cross, V. Bakken, C. Adamo, J. Jaramillo, R. Gomperts, R. E. Stratmann, O. Yazyev, A. J. Austin, R. Cammi, C. Pomelli, J. W. Ochterski, P. Y. Ayala, K. Morokuma, G. A. Voth, P. Salvador, J. J. Dannenberg, V. G. Zakrzewski, S. Dapprich, A. D. Daniels, M. C. Strain, O. Farkas, D. K. Malick, A. D. Rabuck, K. Raghavachari, J. B. Foresman, J. V. Ortiz, Q. Cui, A. G. Baboul, S. Clifford, J. Cioslowski, B. B. Stefanov, G. Liu, A. Liashenko, P. Piskorz, I. Komaromi, R. L. Martin, D. J. Fox, T. Keith, M. A. Al-Laham, C. Y. Peng, A. Nanayakkara, M. Challacombe, P. M. W. Gill, B. Johnson, W. Chen, M. W. Wong, C. Gonzalez and J. A. Pople, *GAUSSIAN 03 (Revision D.01)*, Gaussian, Inc., Wallingford, CT, 2004.
36 M. K. J. ter Wiel, R. A. van Delden, A. Meetsma and B. L. Feringa, *J. Am. Chem. Soc.*, 2005, **127**, 14208–14222.
37 P. U. Biedermann, J. Stezowski and I. Agranat, *Eur. J. Org. Chem.*, 2001, 15–34.
38 A. Schäfer, C. Huber and R. Ahlrichs, *J. Chem. Phys.*, 1994, **100**, 5829–5835.
39 F. Weigend and M. Häser, *Theor. Chem. Acc.*, 1997, **97**, 331–340.
40 F. Weigend, M. Häser, H. Patzelt and R. Ahlrichs, *Chem. Phys. Lett.*, 1998, **294**, 143–152.
41 R. Ahlrichs, M. Bär, M. Häser, H. Horn and C. Kölmel, *Chem. Phys. Lett.*, 1989, **162**, 165–169.
42 R. Ahlrichs, *et al.*, *TURBOMOLE V5.10*, Universität Karlsruhe, 2008, http://www.turbomole-gmbh.com.
43 Ref. 26 does not report E_a values. In similar rotors where comprehensive kinetic studies have been carried out, E_a values are in average about $\sim$1 kcal/mol lower than $\Delta^{\ddagger}G^{\theta}$ at rt, *e.g.* ref. 23.

3.5.2. Rydberg or valence? The long-standing question in the UV absorption spectrum of 1,1'-bicyclohexylidene

Guillermo Pérez-Hernández, Leticia González, and Luis Serrano-Andrés.

In order to implement light-triggered control of rotation in the model system BCH (4 in Fig. 3.1), the following article, BCH is investigated from a photophysical point of view. High-level ab-initio *methods (MS-CASPT2(2,11)) are used to unravel the apparent contradiction between the UV-spectrum of BCH (two intense bands in gas-, solid-, and liquid-phase) and the predictions of π-electron-theory (only one). It is found that a $(\pi, 3s)$-Rydberg-transition is responsible for the other band at low energies in the gas phase. As confirmed through the calculation of the origin of the (π, π^*)-band, the Rydberg-band's apparent intensity is rationalized with the vibronic progression of the intense (π, π^*)-band lying underneath the $(\pi, 3s_R)$-band.*

Original can be found at http://dx.doi.org/10.1002/cphc.200800454.

 A summary of the results can be found in Section 3.2.

 A summary of the results can be found in Section 3.2.

3.5.3. Biologically-inspired molecular machines driven by light. optimal control of a unidirectional rotor

Guillermo Pérez-Hernández, Adam Pelzer, Leticia González, and Tamar Seideman.

*Once the model system BCH (**4** in Fig. 3.1) has been studied from the photochemical point of view (see Article 3.5.2), the possibility of unidirectional, light-triggered rotation is investigated. Unidirectionality has to be achieved not through a built-in asymmetry (see Article 3.5.1), but coherently through the dipole-field interaction. High-level* ab-initio *(MS-CASPT2(2,11)) PESs are computed for the ground and first excited states along the torsional coordinate, and one-dimensional (1D) quantum dynamical simulations are carried out using diverse control fields. Optimal control theory and intuitive IR+UV-pulses are used to initiate the unidirectional rotation, lasting several picoseconds. Propagations are carried out using both the grid representation as well as the state representation.*

Original can be found at http://dx.doi.org/10.1088/1367-2630/12/7/075007.

New Journal of Physics
The open-access journal for physics

Biologically inspired molecular machines driven by light. Optimal control of a unidirectional rotor

Guillermo Pérez-Hernández[1], Adam Pelzer[2], Leticia González[1] and Tamar Seideman[2,3]

[1] Friedrich-Schiller-Universität Jena, Institut für Physikalische Chemie, Helmholtzweg 4, D-07743 Jena, Germany
[2] Department of Chemistry, Northwestern University, 2145 Sheridan Road, Evanston, IL 60208-3113 USA
E-mail: t-seideman@northwestern.edu

New Journal of Physics **12** (2010) 075007 (24pp)
Received 17 December 2009
Published 8 July 2010
Online at http://www.njp.org/
doi:10.1088/1367-2630/12/7/075007

Abstract. We investigate the extent to which unidirectional intramolecular torsional motion can be created in an oriented bicyclic model system driven solely by laser light. We apply the machinery of quantum control via specifically tailored laser pulses to induce such motion, eliminating the need for the thermally constrained steps conventionally used in molecular motor systems. Our approach does not rely on specific details of the potential surfaces to create a preferred direction. Rather, we use matter–field interaction and the tools of coherent optimal control to create a wave packet with nonzero angular momentum among unbound torsional states on an excited electronic surface. Analysis of the results of the control algorithm provides general insight into when and how optimal control theory can find solutions that could not be generated through simple intuitive schemes. We find that, under constrained polarization, the control algorithm reduces to a simple intuitive coherent control strategy wherein a first IR pulse creates a non-stationary wave packet on the ground surface and a subsequent UV pulse transfers it to the excited state. Allowing for polarization shaping, however, we find new control routes that go beyond the intuitive scheme.

[3] Author to whom any correspondence should be addressed.

Contents

1. Introduction

The development of molecular machines has grown, during the past two decades, into an active and diverse subdiscipline of nanoscience. The understanding of natural molecular mechanical motions has inspired researchers in chemistry, physics and materials science to create synthetic systems with similar capabilities with the goal of assembling complex machines from molecular components. Artificial nanoscale devices have taken the form of molecular switches [1], propellers [2], muscles [3], gears [4], shuttles [5] and rotors [6], to name but a few of many imaginative examples (for a comprehensive monograph, see [7]).

Conventional molecular machines are driven incoherently, as an ensemble, for instance by changes in temperature [8], pH-value [9], redox potential [10] or light [11]–[13]. The more recent literature on current-driven dynamics in molecular-scale electronics [14]–[18], has illustrated the possibility of driving molecular machines individually, on a single device level, in the dry state. Here coherence is maintained (in the complete electronic + vibrational space) but the opportunities for control are limited, as the driving force is electronic. Together, the early research on incoherently driven, light-triggered molecular rotors [11]–[13] and the recent work on individually addressed, current-driven molecular machines in junctions [14]–[18] suggest the application of control theory to drive molecular motors with coherent light.

The latter field, the control of molecular systems with coherent light sources, has been extensively reviewed [19]–[28] and is well understood. Concepts and techniques of coherent control have been applied to problems as diverse as atomic physics and gas-phase molecular dynamics, solid-state physics and semiconductor device technology, solution chemistry and biology. Underlying the success of coherent control is the understanding that the coherence properties of laser light can be imprinted on the quantum state of the system through the light–matter interaction, along with the development of light sources that allow precise control over the spectral composition and phase properties of the electromagnetic field.

Among coherent control approaches, optimal control theory (OCT), wherein a systematic procedure is employed to determine the field properties that optimize a desired system observable, has been gaining increasing popularity. The success of this class of techniques owes to their rigorous theoretical understanding [24, 29, 30], the increasing power of computational

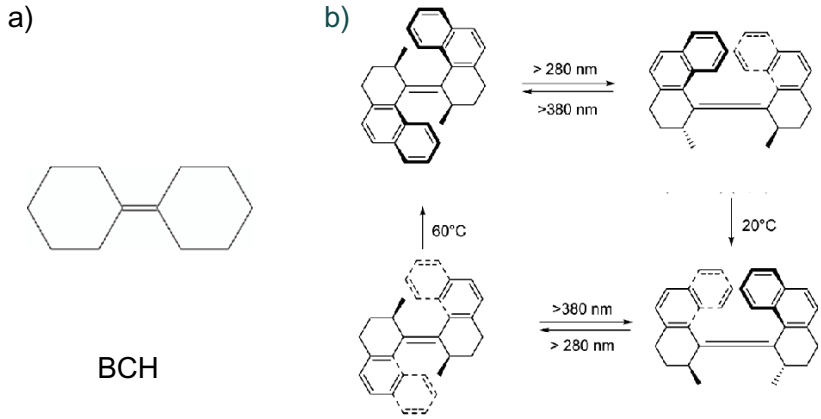

Figure 1. (a) Bicyclohexylidene (BCH). (b) So-called *first generation* molecular rotors, adapted from [6].

systems, and the advance of modern pulse shaping technologies [31]–[41]. The extent to which OCT can unravel control routes that could not be designed by simple intuitive schemes, however, has been a matter of controversy.

Here we apply OCT to develop a new form of molecular machines, one that marries the attractive features of conventional light-driven machines [42, 43] and individually triggered, current-driven machines [14]–[16], [18]. Specifically, we consider the problem of creating unidirectional intra-molecular rotation in a simple (but general) oriented model system, representing a class of biological molecules. A number of previous calculations have illustrated unidirectional torsion with short linear or circularly polarized pulses. Hoki *et al* [44, 45] show that linearly polarized pulses can be used to create unidirectional torsion in a chiral, randomly oriented system with an asymmetric ground state potential surface, via state ladder climbing, while circularly polarized pulses must be used to achieve the same effect in an oriented chiral molecule [44]. In these cases, the asymmetry of the potentials creates a preferred direction of motion. Yamaki *et al* [46] apply OCT to the same system to show that a single linearly polarized shaped pulse can make use of the asymmetries of both the ground and the excited state surfaces to drive unidirectional motion in either direction, and that the mechanism can be rationalized as a simple pump–dump process. An intuitive procedure based on a sequence of an IR and a UV unshaped pulses, with which wave packet localization on the ground surface is followed by projection onto the excited surface, was also shown to successfully achieve unidirectionality [47].

Our goal in the present work is three-fold. Firstly, we explore the possibility of using coherent control tools and concepts to drive sustained, unidirectional torsion in a symmetric system. Secondly, we ask to what extent OCT can devise control routes that go beyond intuitive schemes, rather than reduce to a simple pulse sequence that could have been guessed ahead of the optimization. Thirdly, and most interestingly, we illustrate the potential of polarization shaping as an efficient way of breaking symmetry and producing unidirectional motions.

As a simple but general model system we choose 1, 1′-bicyclohexylidene (BCH). This simple olefin, shown in figure 1(a), is used as a 1D model of a class of much more complicated molecular rotors [6, 48, 49] (see figure 1(b)), that nonetheless shares their essential structural motives. Research in the field of conventional molecular machines has achieved intramolecular rotation in these systems through a series of steps consisting of a thermally induced inversion

of helicity followed by a photochemically induced *cis–trans*-isomerization of the central C=C double bond. Our goal in the present contribution is to induce continuous unidirectional torsion in BCH coherently, solely through the interaction with a laser pulse. We are specifically interested in the case where the potential energy surfaces (PESs) and dipole moments along the torsional coordinate are totally symmetric. As in the experiments of [49, 50], our system is oriented and fixed onto a surface. Hence unidirectional motion induced in the molecular frame is not averaged out in the laboratory frame. We recognize the complexity of realistic molecules and hence begin our study with an *ab initio* calculation of the underlying PESs and dipole functions at a high level of the theory. Our calculations omit inter-nuclear vibrational motions and focus only on the torsional states of the ground and first excited state Hamiltonians.

In the following section, we first provide details of the electronic structure and spectroscopy of BCH and next outline our methods of time propagating the wavefunction and our control approaches. Section 3.1 examines the results of calculations performed with linear polarization alone. Finally, in section 3.2 we illustrate the potential of polarization optimization in this context. Our conclusions are summarized in the final section.

2. Model and methods

2.1. Model system. Spectroscopy and quantum chemistry

The nature of the electronically excited states of BCH has been the subject of discussion for several years, both experimentally [51]–[54] and theoretically [55]–[60]. Spectroscopically, one observes bands centered about 5.95 and 6.82 eV in the vapor phase [51], 5.95 and 6.32 eV in the crystalline phase [51] and 6.01 and 6.94 eV in *n*-pentane solution [52]. Whereas one strong absorption band may have been expected in the BCH UV-spectrum (corresponding to the $\pi \rightarrow \pi^*$-transition) [61], the appearance of two strong bands in the gas phase as well as in condensed phases is surprising. The $\pi \rightarrow \pi^*$-bands of the *anti*- and *syn*-isomers were numerically found identical [57]. Furthermore, the observation of two bands in the UV-spectrum of BCH crystal, where only the *anti*-isomer is present [51], rules out the possibility that the two $\pi \rightarrow \pi^*$-bands result from two different isomers that absorb at different energies. Whereas other possible valence excitation types have been proposed experimentally ($\sigma \rightarrow \sigma^*$ [51] and $\pi \rightarrow (CH)_2\pi^*$ [52]) and numerically ($\pi \rightarrow \sigma^*$ [58]), the Rydberg nature of this band was illustrated only recently, first experimentally [54] and later numerically [59]. Its anomalous intensity was attributed to valence mixing [59] of the $\pi \rightarrow \pi^*$-state and the π, Rydberg manifold of states. A subsequent study provided a somewhat different explanation [60], based on calculation of both the $\pi \rightarrow \pi^*$-state and the first Rydberg ($\pi \rightarrow 3s_R$) state within multiconfigurational complete active space self-consistent-field second-order perturbation theory in its multi-state version (MS-CASPT2). The main conclusion of [60] is that no valence mixing between the $\pi \rightarrow \pi^*$-state and the $\pi \rightarrow 3s_R$-state occurs in the excited state wavefunctions. The $\pi \rightarrow \pi^*$-band origin is located beyond the vertical excitation energy of the Rydberg band. Thus, much of the apparent Rydberg intensity can be ascribed to the underlying, strongly absorbing valence-$\pi \rightarrow \pi^*$-band. Details can be found in [60].

In the present work we compute adiabatic PESs and transition and permanent dipole moments surfaces for the ground electronic state and the first excited electronic singlet state along the BCH torsional coordinate β, starting in the *anti*-BCH MP2/6-31G* equilibrium geometry (figures 2, 3), whereas the other coordinates are kept fixed at their equilibrium configurations. Our results are summarized in figure 4. The ground state potential (V_1) shows

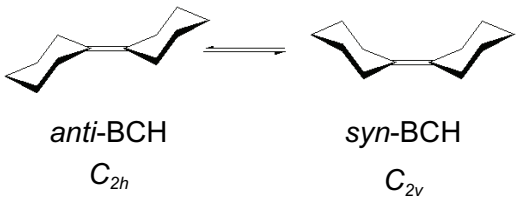

Figure 2. *Anti-* and *syn*-BCH.

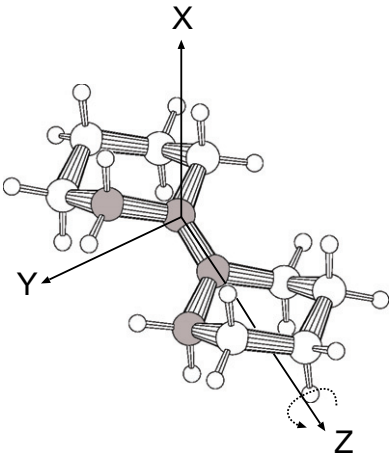

Figure 3. Ball-and-stick diagram of oriented *anti*-BCH. The curved arrow indicates the torsional angle β. Carbon atoms defining the dihedral angle are shown as dark gray balls.

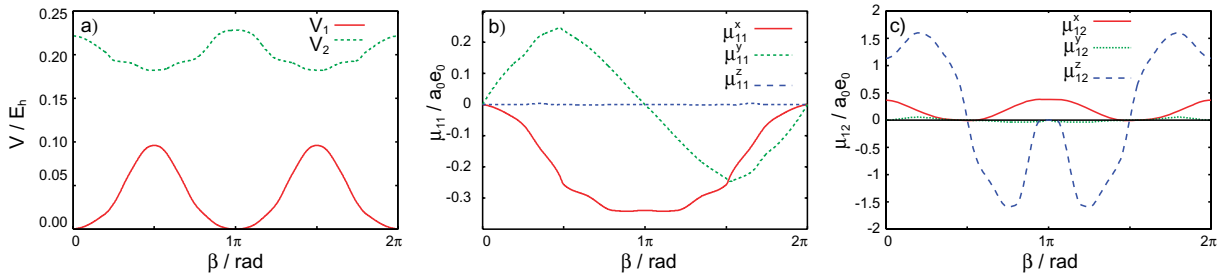

Figure 4. Potential energy curves (a), permanent dipole functions (b) and transition dipole functions (c) computed at the MS-CASPT2/SA(12)-CASSCF/ANO-L-Rydberg level of theory [60].

minima at $\beta = 0$ (*anti*-conformation) and π (*syn*-) with transition states at $\beta = \pi/2$ and $3\pi/4$. The first excited state (V_2) shows the opposite topology, with a barrier of about 25 kcal mol^{-1} at $\beta = \pi$, while minima are observed for $\beta = \pi/2$ and $3\pi/4$. As determined in [60], at the *anti*-conformation using C_{2h} symmetry conditions, V_2 has $\pi \rightarrow 3s_R$ character, while the $\pi \rightarrow \pi^*$-state is higher in energy (V_3). In calculations without symmetry considerations, both states mix and therefore the PESs for the $\pi \rightarrow 3s_R$ and $\pi \rightarrow \pi^*$ states show the same topological profile; accordingly, both states are bright. For simplicity, in this paper we have chosen the lowest-lying adiabatic state (V_2), assuming that the dynamical results would vary at most little if the V_3 state was chosen.

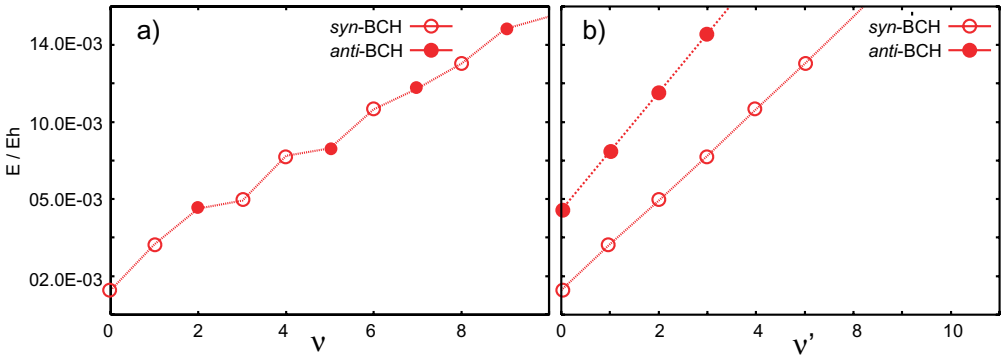

Figure 5. (a) Lowest ten eigenvalues of the ground state Hamiltonian. (b) The eigenvalues of panel (a) sorted into *syn* and *anti* manifolds. In panel (b), the ordinate shows the number of nodes in the state corresponding to the shown eigenvalue.

2.2. *Eigenfunctions and eigenenergies*

The torsional eigenfunctions and eigenenergies of BCH, $\{\Phi_\nu, E_\nu\}$, were computed by diagonalization of the field free torsional Hamiltonian

$$\hat{H}(\beta) = \hat{T}(\beta) + \hat{V}(\beta) = \begin{pmatrix} -\frac{1}{2I_z}\frac{\mathrm{d}^2}{\mathrm{d}\beta^2} & 0 \\ 0 & -\frac{1}{2I_z}\frac{\mathrm{d}^2}{\mathrm{d}\beta^2} \end{pmatrix} + \begin{pmatrix} V_1(\beta) & 0 \\ 0 & V_2(\beta) \end{pmatrix}, \tag{1}$$

where β is the torsion angle, V_1 and V_2 are the S_0 and S_1 potential surfaces, respectively, I_z is the moment of inertia associated with the torsional motion,

$$I_z = \sum_\alpha r_\alpha^2 m_\alpha, \tag{2}$$

$$r_\alpha = \sqrt{x_\alpha^2 + y_\alpha^2}, \tag{3}$$

and α runs over the atoms (I_z=1218 789.7374 a.u.). The eigenenergies and eigenfunctions were computed up to $\{E_i, \Phi_i\}$, $i = 700$ for the ground and excited states on a grid of 4096 points.

Several considerations regarding the symmetry of the system will prove useful. The torsion is symmetric with respect to $\beta \to -\beta$ and $\beta \to \pi - \beta$, but not with respect to $\beta \to \pi/2 - \beta$. As a consequence, the minima in V_1 at $\beta = 0$ (*anti*-BCH) and $\beta = \pi$ (*syn*-BCH) are not identical, the *syn*-conformation being about 87 cm^{-1} lower in energy than the *anti*-BCH. Due to their slightly different energies and curvatures, the ground state eigenfunctions $\{\Phi_\nu^1\}$ are preferentially localized in one of the two minima. The excited state potential, V_2, by contrast, has a symmetric double-well structure and consequently the excited state eigenvalue spectrum is doubly degenerate.

Figures 5(a) and (b) show the energy eigenvalues $\{E_\nu^1\}$ of the ground state Hamiltonian. Note that because the *syn*- and *anti*-BCH have different absolute energies, two of the eigenvalues of the *syn*-conformation are lower than the lowest *anti* eigenvalue (see figure 5(a). In figure 5(b) the eigenvalues are sorted into *syn* and *anti* eigenvalues. Within each manifold, the linearity

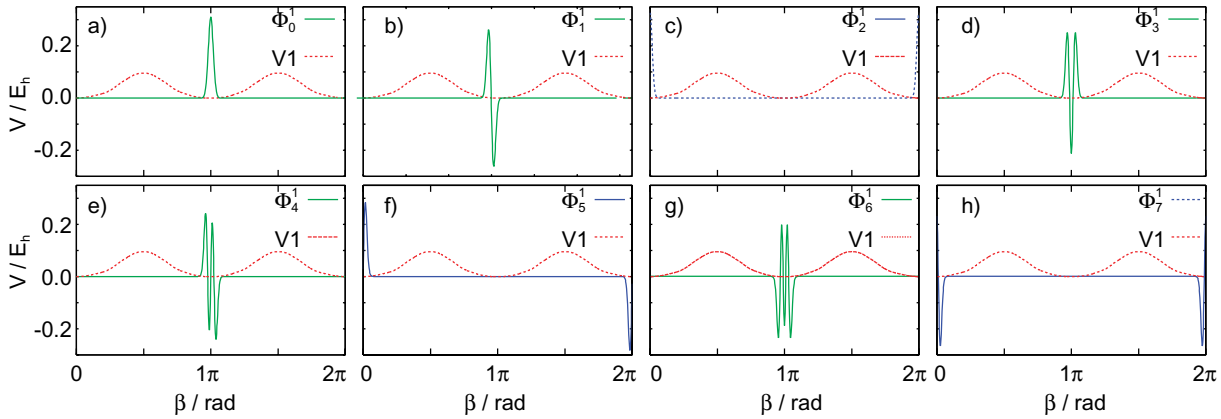

Figure 6. The lowest eight eigenfunctions of the ground state Hamiltonian superimposed on the corresponding potential. Panels (a), (b), (d), (e) and (g) show the *syn*-states, and panels (c), (f) and (h) show the *anti*-states.

in the vibrational index ν' indicates that the ground state eigenfunctions $\{\Phi^1_\nu\}$ are essentially harmonic at low excitation.

Figure 6 displays the corresponding eigenfunctions $\{\Phi^1_\nu\}$. As seen in figure 5(b), both wells are essentially harmonic in the vicinity of the minima, with harmonic frequencies of $\omega^{\text{syn}} = 51.95\,\text{cm}^{-1}$ and $\omega^{\text{anti}} = 66.20\,\text{cm}^{-1}$, calculated as the average respective level spacing of the first ten eigenvalues. These frequencies are extremely low, as would be expected for a torsion of this type, where a very stable carbon–carbon double bond is being forced out of planarity, and a large mass ($\sim 1.2 \times 10^6 a_0^2 m_e$) is moved. Consequently, the density of vibrational states is large, about $261\,\text{eV}^{-1}$. As has been found previously [57], the *syn*-isomer is the more stable of the two isomers, even on the unrelaxed PES. *Syn*-BCH (C_{2v}) and *anti*-BCH (C_{2h}) were optimized at the MP2/6-31G* level using the Gaussian03 [62] quantum chemical software. At 0 K, the ZPE-corrected values give the relative stability of *syn*-BCH as 7.56 meV. Energies of the PES for the *syn*- and *anti*-minima, corrected with $\frac{1}{2}\omega^{\text{syn}}$ and $\frac{1}{2}\omega^{\text{anti}}$, respectively, yield a value of 11.2 meV. For comparison, the value computed in [57] (MP2/6-311G ** on a HF/6-31G geometry) is 2.21 meV. Harmonic frequencies were also calculated at the MP2/6-31G * level of theory, yielding $\omega_0^{\text{syn}} = 73.48\,\text{cm}^{-1}$ and $\omega_0^{\text{anti}} = 71.22\,\text{cm}^{-1}$. The discrepancy between the harmonic frequencies (ω_0) and the frequencies arising from diagonalizing the PES (ω) is larger for the syn conformation ($\sim 20\,\text{cm}^{-1}$) than for the anti ($\sim 5\,\text{cm}^{-1}$) because the geometry of the PES is not relaxed for the *syn* isomer.

Approximately 350 eigenvalues lie on each side of the barrier. Given the near harmonicity of the well, transitions between these levels obey the $\Delta\nu = \pm 1$ selection rule to a good approximation. Assuming an average energy spacing of about $50\,\text{cm}^{-1}$ for all the states under the barrier, one can calculate the period T_P of the associated radiation as

$$T_\text{P} = \frac{1}{\lambda} = \frac{1}{\omega c} = 667.281\,\text{fs}. \tag{4}$$

Thus, relatively long times would be needed to climb up the torsional ladder and hence transition from one isomer to the other through a ladder climbing mechanism is unlikely, requiring of order 350 transitions. Equation (4) illustrates also the small likelihood of thermal isomerization by twist of a carbon–carbon double bond.

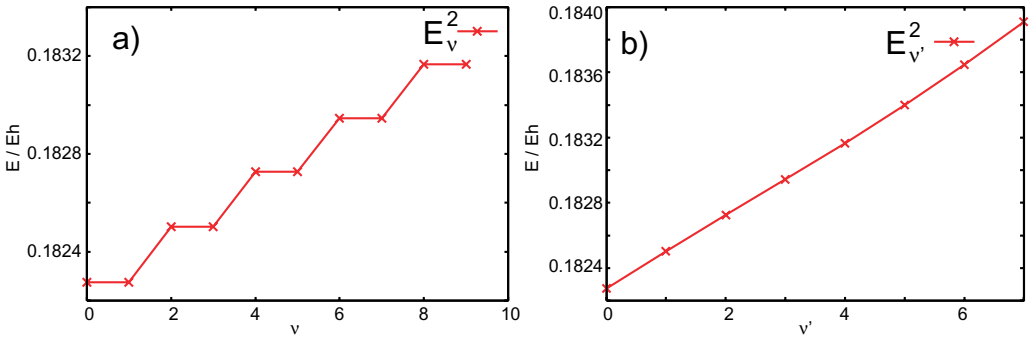

Figure 7. (a) The lowest ten eigenvalues of the excited state Hamiltonian. (b) One eigenvalue per each of the doublets shown in panel (a), illustrating the nearly harmonic behavior of the spectrum for low excitation.

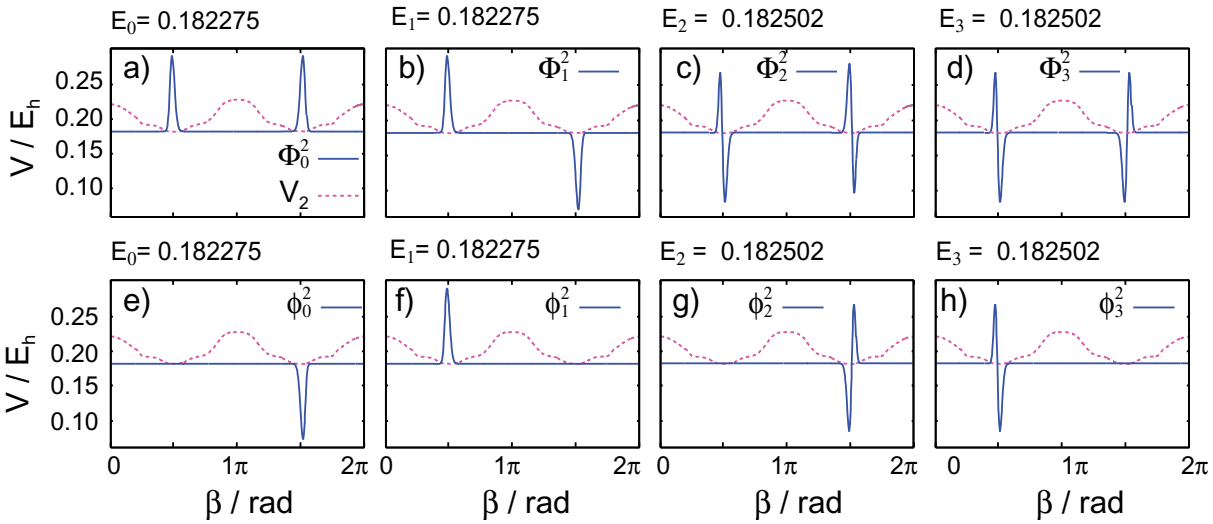

Figure 8. (a)–(d) First four eigenfunctions Φ of the excited state Hamiltonian, superimposed on the potential V_2, with the corresponding eigenenergies. (e)–(h) First four superpositions $\phi_\pm$ defined in equation (5).

The lowest ten eigenvalues $\{E_\nu^2\}$ of the excited state Hamiltonian are plotted in figure 7, where the doublet structure is readily observed. As discussed above, the frequency is small in comparison with the barrier height, hence tunneling does not take place at the level of excitation of figure 7, the tunneling splitting is negligible and the degeneracy is nearly rigorous. Because the two corresponding eigenvectors, Φ_1^ν and Φ_2^ν, span a subspace of the Hamiltonian with essentially equal energies, any linear superposition of these functions is likewise an eigenfunction of H with the same eigenvalue $E_\nu^1 \approx E_\nu^2$. Several examples are shown in figure 8. Of particular interest are the superpositions ϕ_+ and ϕ_- (figures 8(e)–(h)),

$$\phi_\pm = \frac{1}{\sqrt{2}}(\Phi_1^2 \mp \Phi_2^2), \tag{5}$$

because they are localized at the geometry of the ground state transition state connecting the *syn*- and *anti*-isomers. Similar to the ground state counterparts, the energies behave *quasi*-harmonically in the vicinity of the minima, with a level spacing of $\sim 50\,\mathrm{cm}^{-1}$.

In section 3.1 we use a grid representation of the operators. In this method, the position space ($\beta \in [0, 2\pi]$) and the momentum space ($p \in [-p_{\max}, +p_{\max}]$) are discretized into N_p grid points on reciprocal grids, with $\Delta x = 2\pi/N_p$ and $p_{\max} = \pi/N_p \Delta x$. A fast Fourier transform (FFT) is used to switch between the two spaces. The Hamilton matrix (equation (1)) is then diagonalized, yielding the eigenenergies $\{E_\nu\}$ and eigenfunctions $\{\Phi_\nu(\beta)\}$ directly expressed in the position grid.

A complementary representation of the system, which will be useful below, is in terms of the eigenstates of the Hamiltonian operator (equation (1)). To construct these states, we begin by defining a primitive basis as the eigenstates of the kinetic portion of equation (1), the particle-on-a-ring states $(1/\sqrt{2\pi})e^{in\theta}$, $n = 0, \pm1, \pm2, \ldots \pm n_{\max}$ with eigenenergies $E_n = \hbar^2 n^2/2I$ and periodicity 2π. With this primitive basis, the kinetic energy operator is diagonal, and the potential matrix elements are readily evaluated analytically by expanding the potentials as Fourier series

$$V(\beta) = \sum_{b=1}^{b^{\max}} a_b \sin\frac{b\beta}{2} \tag{6}$$

and using the relation

$$\frac{a_b}{2\pi}\int_0^{2\pi} e^{in\beta}\sin(b\beta/2)e^{im\beta}d\beta = \frac{a_b * 4b}{2\pi(-4m^2 - 8nm - 4n^2 + b^2)}, \quad b = \text{odd}, \tag{7}$$

$$= 0, \quad b = \text{even}. \tag{8}$$

Diagonalizing the total Hamiltonian in the particle-on-a-ring basis, we obtain the stationary states of the system as

$$\Phi_\nu(\beta) = \sum_{n=-n_{\max}}^{n_{\max}} c_n^\nu e^{in\beta}. \tag{9}$$

The time evolving wave packet is expanded in terms of the stationary eigenstates as

$$\Phi_{\text{total}}(\beta, t) = \sum_{\nu=0}^{\nu_{\max}} d_\nu(t)\Phi_\nu(\beta), \tag{10}$$

where $\nu_{\max}$ is the total number of stationary states in the superposition. In the calculations of section 3.2, $\nu_{\max} = 81$, of which eight are in the ground electronic state and the remaining 73 in the excited state. This basis size was chosen by including only the states with enough amplitude around π to have a significant overlap ($\geqslant 10^{-4}$) with the initial state, as these are the only states that will participate in the system dynamics. Clearly, this method yields the same observables and energy eigenvalues as the grid representation outlined above, but each representation lends itself to a different description of the OCT targets, as discussed in section 3.2.

2.3. Time-dependent nuclear dynamics

The time-dependent nuclear dynamics evolve the following time-dependent Schrödinger equation:

$$i\frac{\partial}{\partial t}\begin{pmatrix}\Psi^1(\beta, t)\\ \Psi^2(\beta, t)\end{pmatrix} = \hat{H}(\beta, t)\begin{pmatrix}\Psi^1(\beta, t)\\ \Psi^2(\beta, t)\end{pmatrix}, \tag{11}$$

where $|\Psi^1(\beta,t)|^2$ and $|\Psi^2(\beta,t)|^2$ represent the adiabatic populations on the ground and excited state surfaces, respectively. Assuming that the two states are not non-radiatively coupled, the complete Hamiltonian is

$$\hat{H}(\beta,t) = \begin{pmatrix} -\frac{1}{2I_z}\frac{\mathrm{d}^2}{\mathrm{d}\beta^2} & 0 \\ 0 & -\frac{1}{2I_z}\frac{\mathrm{d}^2}{\mathrm{d}\beta^2} \end{pmatrix} + \begin{pmatrix} V_1(\beta) & 0 \\ 0 & V_2(\beta) \end{pmatrix} - \begin{pmatrix} \vec{\mu}_{11}(\beta)\cdot\vec{\epsilon}(t) & \vec{\mu}_{12}(\beta)\cdot\vec{\epsilon}(t) \\ \vec{\mu}_{12}(\beta)\cdot\vec{\epsilon}(t) & \vec{\mu}_{22}(\beta)\cdot\vec{\epsilon}(t) \end{pmatrix}, \quad (12)$$

where $\vec{\epsilon}(t)$ is the electromagnetic field.

In section 3.1, equation (11) is integrated in time using the split operator method [63, 64], within which the time evolution operator is approximated as

$$\mathrm{e}^{-\mathrm{i}\hat{H}\Delta t} \approx \mathrm{e}^{-\mathrm{i}(\hat{T}/2)\Delta t}\cdot\mathrm{e}^{-\mathrm{i}\hat{V}\Delta t}\cdot\mathrm{e}^{-\mathrm{i}(\hat{T}/2)\Delta t}, \quad (13)$$

$\hat{V}$ being the complete potential operator (including the field–matter interaction). Attractive features of the method are its simplicity and the scaling of the error as the third order in the time step Δt.[4] As above, the kinetic terms of the time evolution operator are evaluated by using the FFT to switch between position and momentum spaces.

In section 3.2, the state space-based wave packet of equation (10) is propagated via the fourth-order complex Runge–Kutta algorithm. The method has a local truncation error which is fourth order in Δt, and lends itself well to optimal control calculations with a target operator in state space. This can be important for calculations like those of section 3.2, as the level of convergence of the algorithm is much more strongly dependant on the precision of the integration than a simple time propagation.

2.4. *Optimization of the laser pulse*

Having developed potential energy and dipole moment curves in section 2.1 and explored the spectroscopic and dynamical properties in sections 2.2 and 2.3, respectively, we proceed in this subsection to introduce a unidirectional rotor based on BCH. To that end we apply OCT [65] to determine the pulse shape that will set BCH into sustained unidirectional torsion. Within this approach [65], the functional to be maximized is

$$J_{\mathrm{fi}} = |\langle\Psi_{\mathrm{i}}(T)|\phi_{\mathrm{f}}(T)\rangle|^2 - \alpha_0(t)\int_0^T [\epsilon(t)]^2\,\mathrm{d}t - 2\,\mathrm{Re}[\langle\Psi_{\mathrm{i}}(T)|\phi_{\mathrm{f}}(T)\rangle \times \int_0^T \langle\Psi_{\mathrm{i}}(t)|\frac{\partial}{\partial t} + \mathrm{i}\hat{H}(t)|\Psi_{\mathrm{i}}(t)\rangle\,\mathrm{d}t], \quad (14)$$

where $\Psi_{\mathrm{i}}(t)$ is the time-evolving wavefunction, $\Psi_{\mathrm{i}}(0) = \psi_{\mathrm{i}}(0)$ is the initial wavefunction, $\phi_{\mathrm{f}}(T)$ is the target state at final time T and $\alpha_0(t)$ is a parameter weighting the intensity. Requiring that $\delta J_{\mathrm{fi}} = 0$ and exploiting the time invariance relation,

$$\langle\Psi_{\mathrm{i}}(T)|\phi_{\mathrm{f}}(T)\rangle = \langle\Psi_{\mathrm{i}}(t)|\Psi_{\mathrm{f}}(t)\rangle, \quad (15)$$

[4] Equivalently, $\hat{H}$ in the exponent can be split in the order $\hat{V}/2$, $\hat{T}$ and $\hat{V}/2$.

one obtains a pair of differential equations for the time evolution of $\Psi_i(t)$ and $\Psi_f(t)$, which we solve iteratively, using the algorithm of [65]. We omit details of the method, as these are extensively discussed elsewhere in this issue, and note the specific parameters used in section 3.

3. Results

In this section we examine the possibility of inducing unidirectional torsion in the class of biological molecules represented here by their common BCH moiety using OCT. We ask also when and to what extent the results of OCT can be intuitively anticipated, that is, reduce to a simple, readily understood scheme. We begin, in section 3.1, by restricting the control algorithm to linear polarization. In section 3.2 we show that a more flexible approach, where the polarization is shaped, provides substantially more extensive control. The initial state for all propagations is the lowest torsional state of the ground Hamiltonian,

$$\Psi(t=0) = \begin{pmatrix} \Phi_1^1 \\ 0 \end{pmatrix}. \tag{16}$$

3.1. Linear polarization

In order to achieve unidirectional rotation on the excited state surface, the excited state wave packet needs to have torsional momentum of only one sign, positive or negative. Thus, a simple formulation of a target wavefunction for the OCT algorithm is obtained by fitting a Gaussian function to Φ_1^1, and displacing it in momentum space to be centered about a momentum $p_d \neq 0$,

$$\Phi_f(T) = \left(\frac{2}{\pi a^2}\right)^{1/4} \exp\left[i\beta p_d - \left(\frac{\beta - \beta_0}{a}\right)^2\right] \tag{17}$$

with

$$\Psi_f(T) = \begin{pmatrix} 0 \\ \Phi_f(T) \end{pmatrix}. \tag{18}$$

Here we take the target wave packet center to be $\beta_0 = \pi$ and its width to be 0.09 rad.

As discussed in [65], if the initial and target states are orthogonal to each other, there is a trivial, solution for the optimal field, namely $\vec{\epsilon}(t) = 0$. From equation (18) it is evident that $\langle \Psi_i(t) | \Psi_f(t) \rangle = 0$ at all times for the first iteration. Thus, for $\vec{\epsilon}(t) = 0$ subsequent iterations will not generate nonzero overlap. To circumvent this problem, we use a very weak nonzero initial field. The initial frequency does not necessarily have to be resonant with $\Delta V_{2-1}(\pi) = V_2(\pi) - V_1(\pi) = 0.228 E_h$, since it only needs to transfer *some* population from the ground to the excited state, producing a nonzero overlap that will generate a nonzero $\vec{\epsilon}(t)$ solution in the course of the OCT iteration. The seeding pulse is taken to be of the form

$$|\vec{\epsilon}(t)| = \epsilon_0 \sin(\omega_0 t), \tag{19}$$

where $\omega_0 = 0.250 E_h$, and $\epsilon_0 = 10^{-6}$ a.u., resulting in a population transfer of less than 10^{-6}. Two different scenarios were simulated, a pure electronic transition and a vibronic transition.

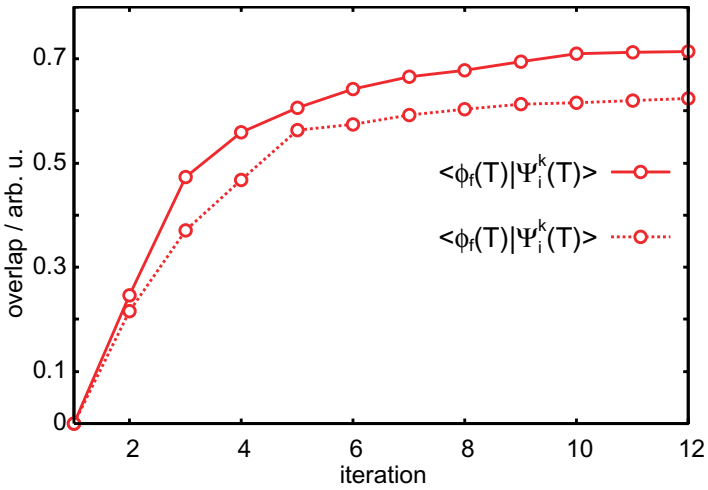

Figure 9. Convergence behavior of the OCT-algorithm, observed through the overlap of the target state $\phi_f(T)$ and the wave packet at the kth iteration, $\Psi_i^k(t)$. The dotted curve corresponds to a constrained optimization, where only electronic transitions are included. The solid curve corresponds to an optimization where both electronic and vibrational transitions are involved.

3.1.1. Pure electronic transition. The length of the sought optimal pulse was set to 500 fs and the field was taken to be polarized along the X-axis. The target momentum was taken to be $p_d = 30.0\,\hbar$, centered about $\beta = \pi$. No penalty function α_0 or envelope was added to the field. The dotted curve in figure 9 shows the overlap of the target state $\Phi_f(T)$ (17) and the function $\Psi_i^k(t)$ at iteration k versus the iteration number, and tests the convergence behavior of the algorithm. The algorithm converges to an overlap of ∼65% within ten iterations. The dotted curves in figures 10(a) and (b) show, respectively, the obtained field in the time domain, and the field-driven population transfer from the ground to the excited state. At the end of the pulse, almost the entire wave packet (>99%) is in the excited state. The Fourier transform of the pulse (not shown) illustrates how the pulse evolves from its initial value of $0.25E_h$. As could have been expected, the frequency has shifted towards a central value resonant with the UV transition at $\beta = \pi$, with $\Delta V_{2-1} \sim 0.228E_h$. The spectrogram of the pulse shows no significant frequency chirp. The ∼65% overlap of Ψ_i and ϕ_f at the final time T does not suffice for Ψ_i to have the desired expectation value of the torsional momentum; only negligible torsional momentum is created in the excited state at the end of the 500 fs long pulse. This observation can be ascribed to the fact that the only nonzero transition dipole moment, $\vec{\mu}_{12}^x$ is symmetric about $\beta = \pi$. We show below that much better control is obtained when the permanent dipole moments are taken into account, and the pulse length is increased, to allow for more flexible dynamics.

3.1.2. Vibrational and electronic transition. We proceed by setting the pulse length to two picoseconds and including the nonzero components of the permanent dipole vector, $\vec{\mu}_{11}$ in equation (12). As in the previous simulation, a seed pulse with $\omega_0 = 0.250E_h$ and $\epsilon_0 = 10^{-6}$ a.u. is used as a trial pulse amplitude to couple the two electronic states. The target wavefunction is the same as above (see equation (17)). The solid curve in figure 9 illustrates the overlap element $\phi_f(t)|\Psi_i^k$ versus k, and serves to study the convergence properties of the algorithm. Convergence is reached after about 12 iterations, at which point the overlap element reaches ∼71.4%. The X- and Y-components of the optimized field are displayed in figure 10 (the field components

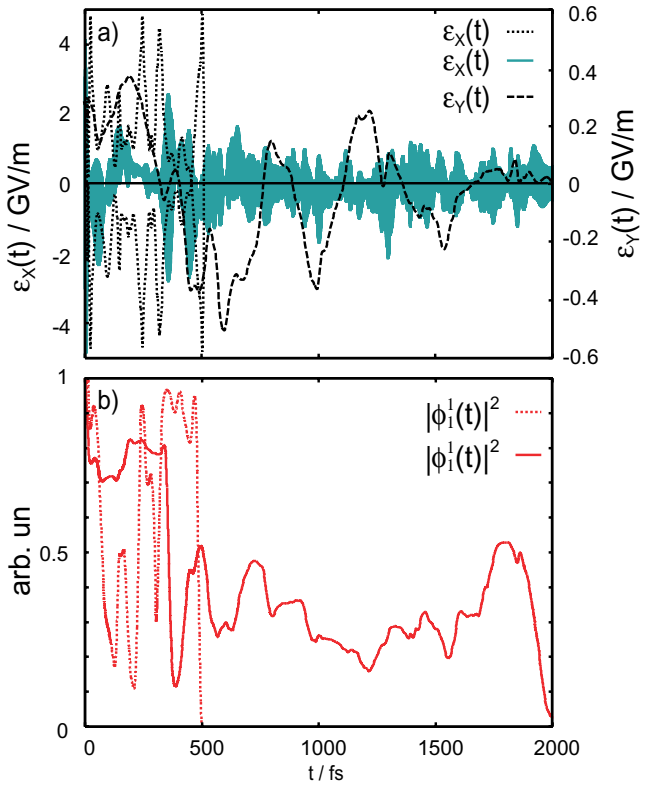

Figure 10. (a) Optimal electric field. The dotted curve corresponds to a constrained optimization, where only electronic transitions are included (only the pulse envelope is shown). The solid and dashed curves give the X- and Y-components of the field resulting from an optimization where both electronic and vibrational transitions are involved. (b) Population transfer from the ground to the excited electronic state. The dotted and solid curves distinguish the two types of optimization as in part (a).

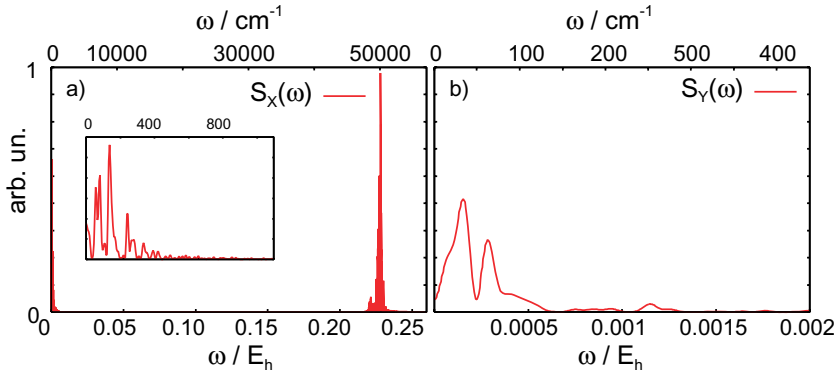

Figure 11. Fourier transform (FT) of the pulse shown in figure 10(a). (a) FT of the X-component, with the inset displaying the intensities of the very low frequencies. (b) FT of the Y-component.

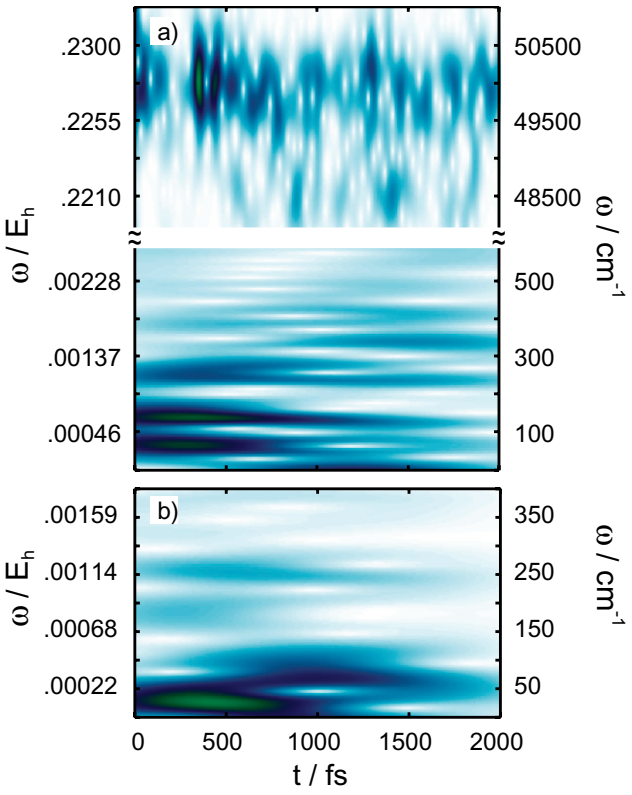

Figure 12. Spectrograms of (a) $\epsilon_X(t)$ and (b) $\epsilon_Y(t)$ of figure 10. The former spectrogram has been divided into two different frequency regimes, so as to distinguish the low- and high-frequency components (cf figure 10(a)). For the low-frequency regime, a gating function of 1 ps FWHM was used to resolve the two low IR-frequencies. For the high-frequency regime, a shorter gating function (FWHM = 50 fs) was set, providing good resolution in the frequency and time domains. The left ordinate shows the frequency in E_h and the right ordinate in cm^{-1}.

differ since they interact with differently structured dipole moment components (recall figure 4)). The Fourier transform again reveals one group of frequencies centered about $\Delta V_{2-1} = 0.228 E_h$. Interestingly, however, the OCT-algorithm has made use also of IR-transitions, as can be seen by the intensity peaks at very low frequencies in figure 11. With the pulse of figures 10(a) and (b), the expectation value of $\langle \Psi_i(T)|\hat{p}_z|\Psi_i(T)\rangle$ is $5.80\,\hbar$ after the 2 ps pulse, showing significant torsional momentum transfer to the excited state. The spectrograms of the X- and Y-components of the field are displayed in figure 12. The time/energy resolution of the spectrogram depends on the duration of the gating function. Since a Gaussian function has been used, this period is defined by its full-width at half-maximum (FWHM). Short gating functions resolve the pulse in time while smearing out the frequency information and vice versa.

Although figure 12 involves a tradeoff, it illustrates clearly that the low-frequency (IR) components peak strongly at early times, whereas the high-frequency (UV) components are nearly equally distributed over the pulse duration. Thus, the control algorithm reveals that (within the constraint of linear polarization) the best combination of fields to achieve unidirectional torsion consists of a short IR followed by a narrow band UV subpulse. The IR pulse populates a ground torsional wave packet, which the UV subpulse projects onto the

excited surface at an opportune instant, when the torsional wave packet has reached the turning point and the ground–excited overlap is optimized.

Furthermore, it is seen that the IR pulse duration is under ∼800 fs. Considering that the IR frequencies are in the range of 40–200 cm^{-1}, application of equation (4) shows that the pulse includes very few optical cycles, just one in the case of the lowest frequency (for 40 cm^{-1} $T_p \sim 834$ fs) and four in the highest. The optimal control algorithm thus confirms the usefulness of the IR + UV strategy, applied in the previous research to similar problems [47], [66]–[69]. In the next subsection, we ask to what extent and how could the pulse parameters be set intuitively, bypassing the optimization, to yield the same level of control. In section 3.2 we investigate the extent to which unconstrained (polarization shaping) OCT can generate new solutions, that significantly surpass those of intuitive schemes.

3.1.3. IR + UV strategy. The goal of the IR + UV strategy is to create torsional momentum in the ground state and then transfer it with an ultrashort (short with respect to torsional motions) pulse to the excited state. We use the same parameters as in the OCT calculations discussed in the previous subsection but with the target state on the electronic ground state,

$$\Psi_{\mathrm{f}}(T) = \begin{pmatrix} \Phi_{\mathrm{f}}(T) \\ 0 \end{pmatrix}, \tag{20}$$

where $\Phi_{\mathrm{f}}(T)$ is a Gaussian wavefunction (equation (17)) having 30.0 $\hbar$ of initial torsional momentum, centered about $\beta = \pi$. The field is linearly polarized and hence only the $\vec{\mu}^{y}_{11}$ component of the dipole contributes to the field–matter interaction. In this case, the overlap $\Psi_{\mathrm{i}}(t)|\Psi_{\mathrm{f}}(t)$ is not necessarily zero, because both functions belong to the same Hamiltonian, thus no seeding pulse is needed to start the algorithm. A period of 2 ps is simulated and no envelope function or weighting function is used. Inspecting the convergence behavior of the overlap, analogous to the discussion of the previous subsection, we find that the algorithm is able to increase the overlap up to ∼87%, with the final wavefunction having a momentum expectation value of 18.00$\hbar$. The optimized field is a sinusoidal function, with a central feature of about 52.0 cm^{-1}, as determined through Fourier transform of the final field. This result has been expected: the underlying mechanism is torsional ladder climbing, and in order to excite the *syn*-isomer, the pulse needs to be resonant with the level spacing around $\beta = \pi$. These results confirm the conclusion of the previous subsection that, under the conditions of the constraint optimization considered, the best method to achieve sustained unidirectional torsion in BCH is the IR + UV strategy.

It remains to discover, however, how sensitive the results are to the parameters of an analytically constructed pulse. We thus proceed to examine the results of a pulse of the form

$$\vec{\epsilon}(t) = E_{\mathrm{IR}}(t) \cdot \vec{\varepsilon}_Y + E_{\mathrm{UV}}(t) \cdot \vec{\varepsilon}_X, \tag{21}$$

where

$$E_j(t) = E_j^0 \cdot \sin(\omega_j t) \cdot s_j(t), \quad j = \mathrm{IR}, \mathrm{UV}, \tag{22}$$

and $s_j(t)$ is an envelope function of duration t_p. The parameters of the two pulses are chosen to satisfy the following conditions:

1. The IR frequency is resonant with the transitions in the *syn* configuration of the ground state, so that ladder climbing is facile (cf figure 5(b)), slope of the solid curve).
2. The IR-pulse duration allows only a few half-cycles.

3. $E^0_{\rm IR}$ allows sufficient torsional momentum to be gained in the electronic ground state. In order to maintain comparable fluence while decreasing the pulse duration with respect to that of the OCT algorithm, we are required to increase the field amplitude.
4. The UV frequency is resonant with ΔV_{2-1} in the vicinity of $\beta = 0$.
5. The UV-pulse duration is chosen such that the expectation value of the torsional momentum $p^1_z(t)$ during the electronic transition remains close to its maximum $p^1_{z\,\max} \sim 19.5\hbar$.
6. $E^0_{\rm UV}$ is chosen so that population transfer is >95%.

We find that these conditions are satisfied with the IR-laser parameters set to: $\omega_{\rm IR} = 51.0\,{\rm cm}^{-1} = 0.232 \times 10^{-3} E_h$, $E^0_{\rm IR} = 4.0\,{\rm GV\,m}^{-1}$, $t^{\rm IR}_{\rm p} = 1485\,{\rm fs}$,

$$s_{\rm IR}(t) = \begin{cases} \sin\left(\dfrac{\pi t}{t^{\rm IR}_{\rm p}}\right), & 0 \leqslant t \leqslant t^{\rm IR}_{\rm p}, \\ 0, & t > t^{\rm IR}_{\rm p} \end{cases} \tag{23}$$

and the UV-laser parameters to: $\omega_{\rm UV} = 50\,000\,{\rm cm}^{-1} = 0.228 E_h$, $E^0_{\rm UV} = 2.5\,{\rm GV\,m}^{-1}$, $t^{\rm UV}_{\rm p} = 80\,{\rm fs}$

$$s_{\rm UV}(t) = \begin{cases} \sin\left(\dfrac{\pi t}{t^{\rm UV}_{\rm p}}\right), & 1675.0 \leqslant t \leqslant 1675.0 + t^{\rm UV}_{\rm p}, \\ 0, & t > 1675.0 + t^{\rm UV}_{\rm p}. \end{cases} \tag{24}$$

Although we show below that the IR + UV pulse sequence induces the desired motion, the sensitivity to the precise detail of the pulse suggests the advantage of OCT.

Figure 13 summarizes the results obtained with the analytical pulse sequence of equation (21) (section 3.1.3). The laser pulse is depicted in panel (a). Panel (b) shows the oscillations in the expectation values of the torsional momenta $p_z(t)$ for the electronic ground and excited states. While for the former $p^1_z(t)$ oscillates around zero (solid curve), in the latter, once the UV-laser has triggered the electronic transition, $p^2_z(t)$ maintains a positive value (dashed curve), undergoing acceleration and deceleration depending on the slope of V_2 at the center of the wave packet. Panel (c) shows the evolution of the expectation value of the torsion angle, $\beta(t)$, in the ground (solid) and excited (dashed) states. A full rotation cannot be depicted in this representation, because β spans the $0 \to 2\pi$ range. A complementary view of the same dynamics in thus provided in panel (d), which shows the probability density $|\Psi(t, \beta)|^2$ versus time and position.

An alternative way of describing the same driven torsional dynamics is in terms of the torsional eigenstates, as calculated in the previous section,

$$C^1_\nu(t) = \langle \Psi^1(t, \beta) | \Phi^1_\nu(\beta) \rangle \tag{25}$$

for the ground and

$$C^2_\nu(t) = \langle \Psi^2(t, \beta) | \Phi^2_\nu(\beta) \rangle \tag{26}$$

for the excited state, where the β-dependence has been integrated out. The square absolute value of these coefficients after turn off of the pulse is shown in figure 14 . Whereas the ground state is dominated by the lowest few torsional components, the excited state torsional wave packet is centered about $\nu = 485$ and is broad, involving $\sim$20 significantly populated states. Clear dominance of the odd components reflects our breaking of the symmetry of the two torsion senses. The need to determine the pulse parameters to high accuracy, however, limits the applicability of the method.

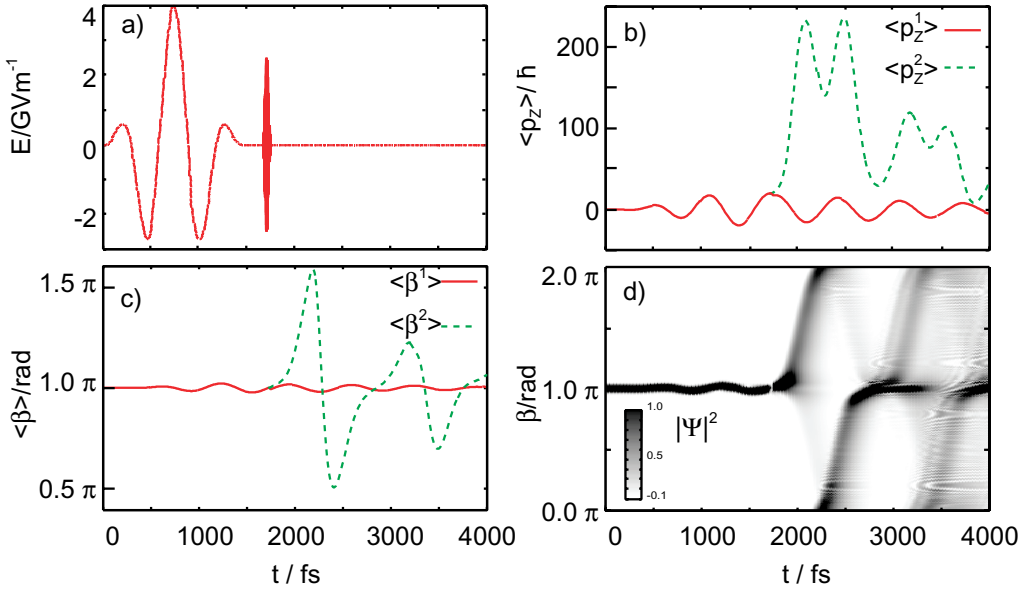

Figure 13. IR + UV strategy. (a) The laser pulse applied. (b) The expectation values of the torsional momentum in the ground and excited states. (c) The expectation values of the torsional angle in the ground and excited states. (d) The squared absolute value of $\Psi(t, \beta)$. After the UV pulse $>95\%$ of $|\Psi(t, \beta)|^2$ is in the excited state. Several cycles of the unidirectional rotation are shown, as the probability density exits and re-enters the periodic boundaries in the direction $2\pi \rightarrow 0$ at times $t \sim 2$ ps and $t \sim 3.1$ ps.

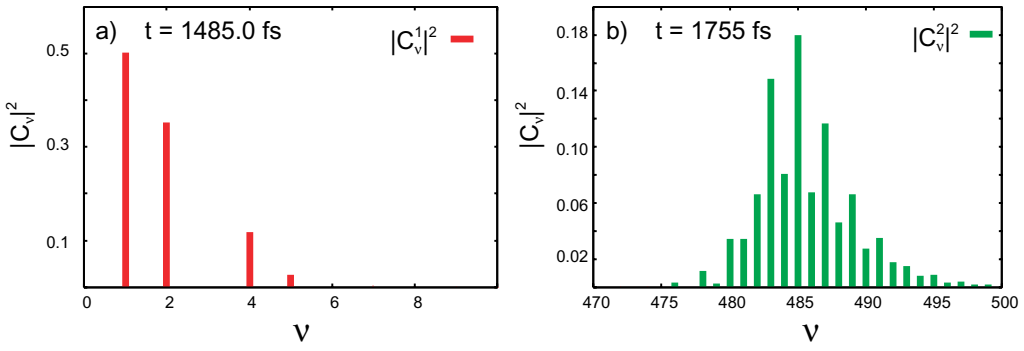

Figure 14. Squared modulus of the projection of $\Psi(t, \beta)$ onto its torsional components in the ground (a) and excited (b) states.

3.2. Polarization shaping

In this section we relax the constraint of linear polarization imposed in section 3.1 and allow the control algorithm to vary with time the polarization of the field to explore the potential advantage of polarization shaping. We remark that polarization shaping has been demonstrated in several experiments [41], [70]–[75].

To gain complementary insight into the controlled torsional dynamics, we perform the calculations in basis set space, rather than in grid space (see section 2.3). A target operator that

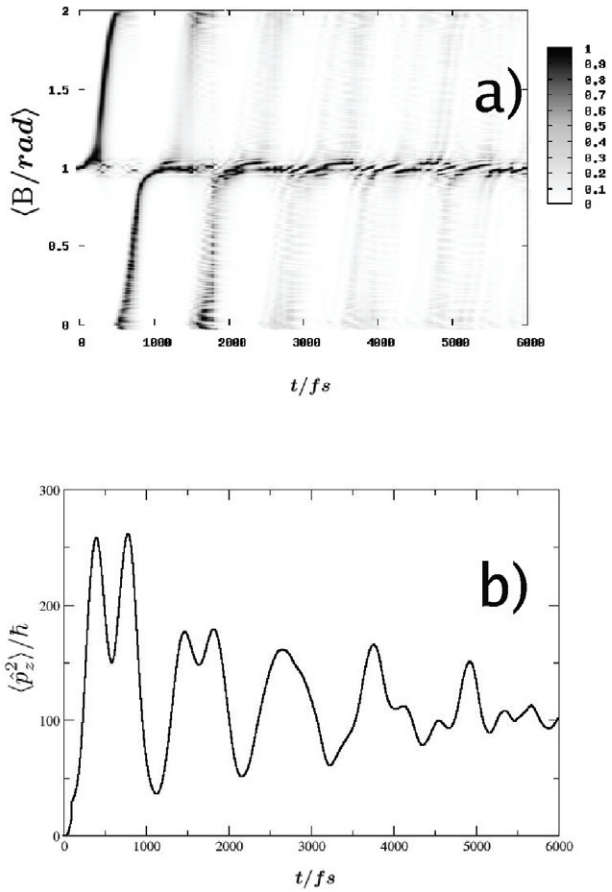

Figure 15. Polarization shaping. (a) The squared modulus of $\Phi(\beta, t)$. (b) The expectation value of the angular momentum. The polarization-shaped pulse is 100 fs long.

embodies the dynamics that we seek to control is a projector onto states with positive angular momentum,

$$\hat{O}_{\text{target}} = \sum_{n>0}^{n_{\max}} |e^{in\theta}\rangle\langle e^{in\theta}|. \tag{27}$$

In these calculations, we have used a penalty function amplitude of $\alpha_o = 50$ and a penalty function shape of the form described in [76]. This restricts the field strength and ensures that the field grows from zero at a finite rate and approaches zero smoothly toward the target time. Using this method, we are able to restrict ourselves to very short timescales (10–100 fs) while significantly improving our control over the torsional dynamics as compared to the linear polarization approach.

Figure 15 displays the results. Panel (a) may be compared with figure 13(d) for the IR + UV scheme of section 3.1.3. The probability density exhibits unidirectional motion beginning immediately after the short pulse and persisting for several cycles before (coherent) dephasing begins to spread the wave packet. Noteworthy is the difference in the extent of reflection from interaction with the barriers in figures 15 and 13(d). At the point where the wave packet first

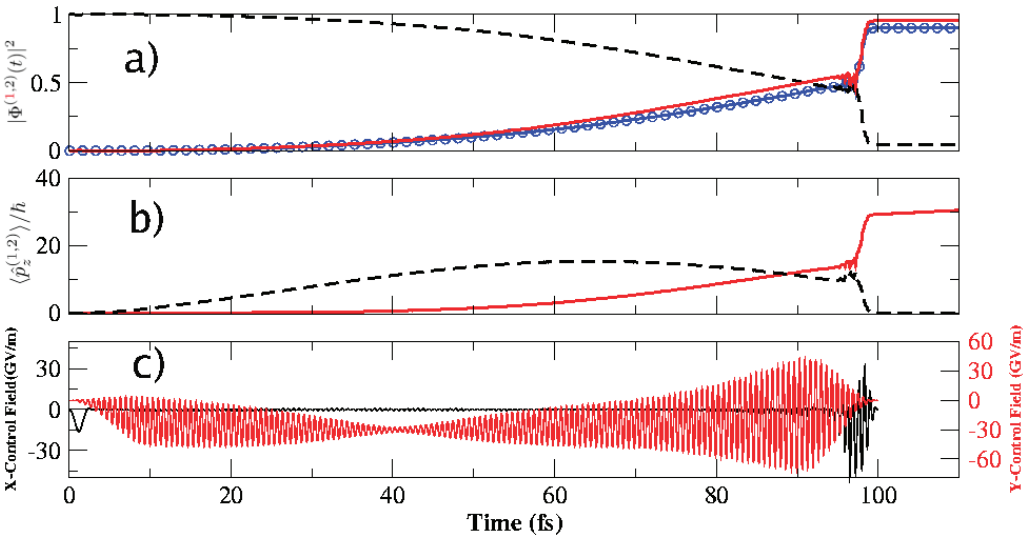

Figure 16. Results of polarization shaping with all dipole/field interactions included. (a) Ground (- - -) and excited (solid) state population along with the portion of the excited state population above the central barrier at 0.22809 Hartrees (solid curve with superimposed circles). (b) Ground (- - -) and excited (solid) state angular momentum during and immediately after the pulse. (c) X- (left ordinate) and Y- (right ordinate) field components. Note the scale difference indicating that the Y-component of the field is much more intense.

encounters the excited state torsional barrier at the $0/2\pi$ juncture (see figure 4(a)), a faint line can be seen moving in the direction counter to the bulk of the wave packet, which continues rotating onward to emerge from the $\beta = 0$ side of the coordinate system. This represents portions of the total wave packet that are reflected from the barrier. This happens most noticeably for wave packets that have a great deal of population at energies not too far above the peak value of the torsional barrier. In figure 15(a), however, such reflection is not observed, since in the polarization-shaped case the center of the wave packet lies energetically above the highest bound state, as seen in figure 17 and discussed below.

Within the IR + UV scheme, the ground state angular momentum must be built up before it can be transferred to the excited state. Within the optimized polarization scheme, the creation of the phase relations necessary for unidirectional rotation and the population of the excited state are done simultaneously. Panel (b) displays the excited state angular momentum after the pulse, where it is seen that unidirectional rotation begins immediately after the pulse turnoff. The magnitude of this angular momentum once the wave packet accelerates down the slope of the potential approaches $250\hbar$, and maintains a large positive value, persisting picoseconds.

Although population transfer occurs steadily through the interaction time with the pulse, it is not until the last 10 fs that the excited state angular momentum begins to change appreciably (figure 16(b)). Thus, the phase information necessary for unidirectionality builds up gradually in the course of population transitions, but is only triggered in the final sharp sub-pulse near 100 fs. The differences between the dynamics induced by the IR + UV scheme and those induced by the polarization-shaped pulse are twofold. Firstly, the polarization-shaped pulse is able to increase the Y-component of the field at the expense of the X-component, thus offsetting the large

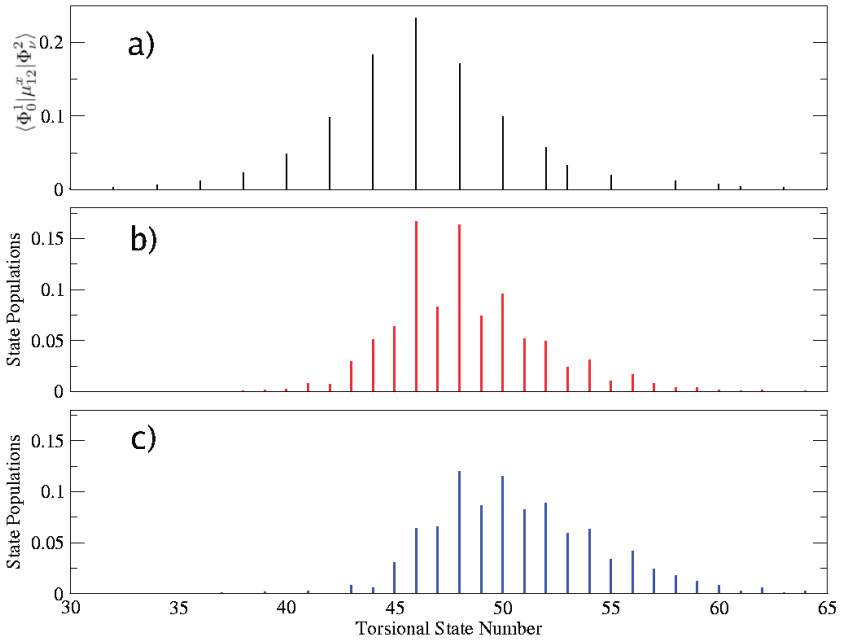

Figure 17. The correspondence between the transition strengths $\langle\Phi_1^1|\mu_{12}^x|\Phi_\nu^2\rangle$ (a) and the populations of torsional states in the excited electronic state after the pulse (b), (c). Panel (b) corresponds to the IR + UV scheme and panel (c) to the polarization shaping approach. The shift of the center of the wave packet towards higher energy states is clearly seen. The state numbers here refer to the most highly populated subset of the 73 total excited states. In this representation, state number 46 marks the highest bound state.

difference between the X- and Y-components of the dipole function (see figure 4) that hinders unidirectional rotation. Secondly, the optimal pulse produces a higher energy torsional wave packet, dominated by states whose energy is above the central torsional barrier (figures 16(a) and 17). This wave packet decohers more slowly than the one due to the IR + UV scheme as it suffers less from collisions.

Within the IR + UV scheme, there is an anticipated close correspondence between the populations in the excited state levels after the pulse sequence and the strengths of their transitions from the ground torsional state. Inevitably, the strength of transitions into bound states is well above that for transitions into states above the barrier, and hence the excited state wave packet contains ∼26% of bound states. The short shaped pulse, by contrast, is able to concentrate the pulse fluence in a short time and thus offset the trend determined by the transition strengths and place ∼90% of the excited state population in torsional states above the $0.22809 E_h$ barrier.

Examination of the control fields involved in the polarization shaping approach shows that in some respects similar mechanisms apply in this case as in the IR + UV scheme. Figure 18 shows the Fourier transforms of the X- and Y-components of the field, illustrating that the frequency spectrum of the Y-component (red) is reminiscent of that shown in figure 11 for the linearly polarized field. While both the X- and Y-field components contain frequencies corresponding to ground-to-ground, excited-to-excited and ground-to-excited transitions, the

IOP Institute of Physics DEUTSCHE PHYSIKALISCHE GESELLSCHAFT

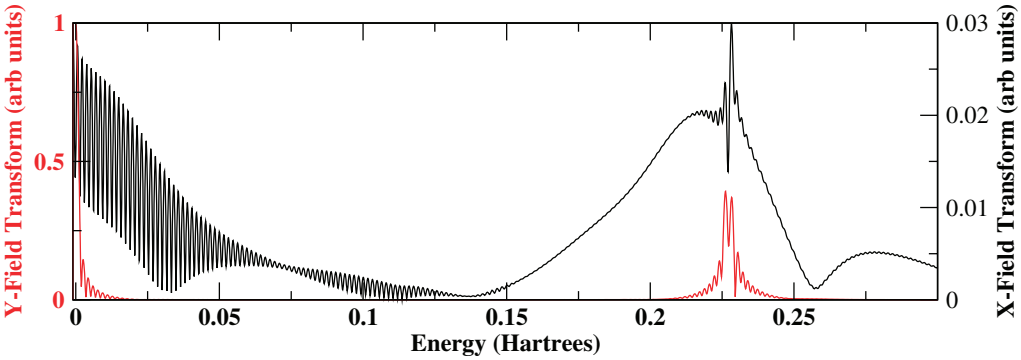

Figure 18. Frequency domain representation of the X- (black) and Y- (red) components of the field, where the X-component is referred to the right ordinate and the Y-component to the left ordinate. The X-component is considerably weaker and much broader in frequency space.

Y-component of the polarization-shaped pulse is not nearly as broad in frequency space as the X-component. Both the high- and the low-frequency components of the Y field component are active throughout the pulse, leading to greater resolution in the frequency domain relative to the X field component, which is much more concentrated in time and hence broader in frequency domain. Further, one observes a large difference between the peak intensity of the most represented frequency in the Y field component (normalized to 1 for ease of comparison) and that of the X-component (only 0.03). As noted above, this is due to the large difference in strengths of the X- and Y-components of the transition dipole in figure 4(c). The relevant parameter is the interaction strength $\epsilon_X(t)\langle\Phi_a^1|\mu|\Phi_v^2\rangle$, which requires a much lower field strength to be comparable to $\epsilon_Y(t)\langle\Phi_a^1|\mu|\Phi_v^2\rangle$.

Complementary insights are provided by the temporal evolution of the fields, provided in figure 16(c). Here we find that the Y-component of the field is shaped in both the low-frequency (overall envelop) and high-frequency (fine structure) regimes and that its amplitude is high throughout. The X-component, by contrast, has a very small (although nonzero) amplitude at all but the very early and very late portions of the interaction time, leading to a broadening in the frequency domain representation. As will be seen below, this does not reduce to a simple two pulse control field, as the small oscillations in the X-component of the field lead to definite polarization when taken in concert with the Y-component of the field. Population transfer from the ground to the excited electronic state continues steadily during the pulse, but with low amplitude oscillations that indicate the creation of coherences. This interpretation is further supported by the results of calculations with only one of the field components. When only $\epsilon_X(t)$ is applied and $\epsilon_Y(t)$ is set to zero, only $\sim$30% of the population is transferred to the excited state. When only $\epsilon_Y(t)$ is applied, $\sim$60% of the population is in the excited state, the results of section 3.1.1 are reproduced, but with no unidirectionality to the excited state wave packet. The wave packet splits into two counter-propagating wave packets, leaving the net angular momentum zero.

Lastly, it is instructive to examine the evolution of the total electric field over time. Here we clearly see the use of multiple elliptical polarizations spanning tens of femtoseconds along with more exotic forms where the polarization changes rapidly with time. By plotting the changes

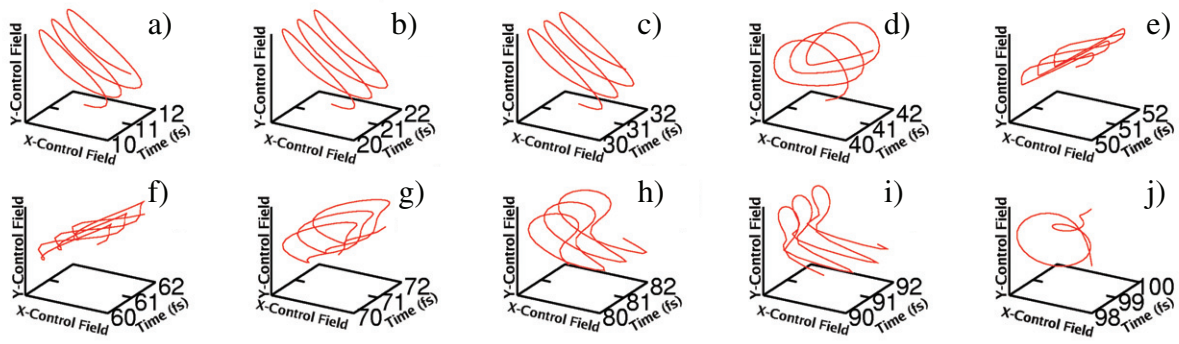

Figure 19. Time evolution of the polarization properties of the optimal field. (a) 10–12 fs, (b) 20–22 fs, (c) 30–32 fs, (d) 40–42 fs, (e) 50–52 fs, (f) 60–62 fs, (g) 70–72 fs, (h) 80–82 fs, (i) 90–92 fs, and (j) 98–100 fs.

in the X and Y control fields simultaneously, we can follow the establishment and change of particular pulse polarizations (figure 19). At early times, $t \sim 0$–40 fs, the pulse is elliptically polarized (panels (a)–(d)) with a slight change of the orientation around 40 fs (panel (d)). An entirely different behavior, however, is found in the later portions of the pulse, $t \sim 50$–90 fs (panels (e)–(i)), where the polarization direction varies rapidly. Finally, the pulse ends with a slowly varying elliptical polarization that decreases in amplitude as the pulse smoothly decays to zero (panel (j)). Figure 19 thus clarifies the manner in which the polarization-shaped pulse breaks the rotational symmetry of the system and optimally induces unidirectional torsion.

4. Conclusion

In the preceding sections we explored the extent to which coherent light–matter interactions alone could drive unidirectional rotation in a symmetric system. We addressed also the more general question if and when can optimal control strategies provide solutions that could not be attained by intuitive approaches. Time-dependent approaches based on momentum space and state space formulations were used in the application of complimentary coherent control techniques, and useful information about wave packet shaping in multiple regimes was unraveled. As an experimentally relevant model system we used the BCH molecule, a simple olefin that serves as a prototype of a class of more complicated molecular rotors that share its essential structural motives. Our conclusions, however, are largely general.

Under constrained polarization conditions, we find that the optimal control algorithm reduces to a simple two-pulse sequence, where a first IR pulse excites a wave packet of torsional states and a subsequent UV pulse, timed to an instance where the system is localized at the ground state turning point, projects it onto an excited PES. The structure of the excited surface gives rise to unidirectional motion along the torsional coordinate. We found, however, that with the restriction to linear polarization removed, significantly better solutions are unraveled. In particular, an interesting polarization shaping approach is introduced, where elliptically polarized light breaks the symmetry between the two senses of torsion.

Acknowledgments

TS is grateful to the National Science Foundation (Award Number CHE-0616927) for support. LG thanks the Deutsche Forschungsgemeinschaft (Project Number GO-1059/2-1) for financial support. Additionally, B Schmidt is gratefully acknowledged for providing the authors with the QMBOUND software.

References

[1] Feringa B L (ed) 2001 *Molecular Switches* (Weinheim: Wiley-VCH)
[2] Iwamura H and Mislow K 1988 *Acc. Chem. Res.* **21** 175
[3] Jiménez M C, Dietrich-Buchecker C and Sauvage J-P 2000 *Angew. Chem., Int. Ed. Engl.* **39** 3284
[4] Koga N, Kawada Y and Iwamura H 1983 *J. Am. Chem. Soc.* **105** 5498
[5] Badjić J D, Balzani V, Credi A, Silvi S and Stoddart J F 2004 *Science* **303** 1845
[6] Koumura N, Zijlstra R W J, van Delden R A, Harada N and Feringa B L 1999 *Nature* **401** 152
[7] Balazani V, Credi A and Venturi M 2008 *Molecular Devices and Machines—Concepts and Perspectives for the Nanoworld* (Weinheim: Wiley-VCH)
[8] Bottari G, Dehez F, Leigh D A, Nash P J, Pérez E M, Wong J K Y and Zerbetto F 2003 *Angew. Chem., Int. Ed. Engl.* **42** 5886
[9] Garaudée S, Silvi S, Venturi M, Credi A, Flood A H and Stoddart J F 2005 *ChemPhysChem* **6** 2145
[10] Tseng H, Vignon S A and Stoddart J F 2003 *Angew. Chem., Int. Ed. Engl.* **42** 1491
[11] Kottas G S, Clarke L I, Horinek D and Michl J 2005 *Chem. Rev.* **105** 1281
[12] Kay E R, Leigh D A and Zerbetto F 2007 *Angew. Chem., Int. Ed. Engl.* **46** 72
[13] Kolomeisky A B and Fisher M E 2007 *Ann. Rev. Phys. Chem.* **58** 675
[14] Seideman T 2003 *J. Mod. Opt* **50** 2393
[15] Král P and Seideman T 2005 *J. Chem. Phys.* **123** 184702
[16] Kaun C-C and Seideman T 2005 *Phys. Rev. Lett.* **94** 226801
[17] Jorn R and Seideman T 2006 *J. Chem. Phys.* **124** 084703
[18] Jorn R, Livshits E, Baer R and Seideman T 2007 *Isr. J. Chem.* **47** 99
[19] Rabitz H A, Hsieh M M and Rosenthal C M 2004 *Science* **303** 1998
[20] Shapiro M and Brumer P 2003 *Principals of Quantum Control of Molecular Processes* (New York: Wiley)
[21] Brixner T and Gerber G 2003 *ChemPhysChem* **4** 418
[22] Vitanov N V, Halfmann T, Shore B W and Bergmann K 2001 *Ann. Rev. Phys. Chem.* **52** 763
[23] Vitanov N V, Fleischhauer M, Shore B W and Bergmann K 2001 *Adv. At. Mol. Opt. Phys.* **46** 55
[24] Rice S and Zhao M 2000 *Optical Control of Molecular Dynamics* (New York: Wiley)
[25] Rabitz H, de Vivie-Riedle R, Motzkus M and Kompa K 2000 *Science* **288** 82
[26] Gordon R J and Rice S A 1997 *Ann. Rev. Phys. Chem.* **48** 601
[27] Brumer P and Shapiro M 1992 *Ann. Rev. Phys. Chem.* **43** 257
[28] de Vivie-Riedle R, Rabitz H and Kompa K L (ed) 2001 *Chem. Phys., Special Issue on Laser Control of Quantum Dynamics* vol 267 (Amsterdam: Elsevier)
[29] Huang G M, Tarn T J and Clark J W 1983 *J. Math. Phys.* **24** 2608
[30] Rabitz H, Peirce A P and Dahleh M A 1988 *Phys. Rev.* A **37** 4950
[31] Assion A, Baumert T, Bergt M, Brixner T, Kiefer B, Seyfried V, Strehle M and Gerber G 1998 *Science* **282** 919
[32] Glaß A, Rozgonyi T, Feurer T, Sauerbrey R and Szabó G 2000 *Appl. Phys.* B **71** 267
[33] Bartels R, Backus S, Zeek E, Misoguti L, Vdovin G, Christov I P, Murnane M M and Kapteyn H C 2000 *Nature* **406** 164
[34] Brixner T, Damrauer N H and Gerber G 2001 *Adv. Mol. Opt. Phys.* **46** 1
[35] Levis R J, Menkir G M and Rabitz H 2001 *Science* **292** 709

[36] Herek J L, Wohlleben W, Cogdell R J, Zeidler D and Motzkus M 2002 *Nature* **417** 533
[37] Hornung T, Motzkus M and de Vivie-Riedle R 2002 *Phys. Rev.* A **65** 021403
[38] Daniel C, Full J, González L, Lupulescu C, Manz J, Merli A, Vajda Š and Wöste L 2003 *Science* **299** 536
[39] Kurtz L, Rabitz H and de Vivie-Riedle R 2002 *Phys. Rev.* A **65** 032514
[40] Cardoza D, Baertschy M and Weinacht T C 2005 *J. Chem. Phys.* **123** 074315
[41] Wollenhaupt M, Krug M, Köhler J, Bayer T, Sarpe-Tudoran C and Baumert T 2009 *Appl. Phys.* B **95** 245
[42] Balzani V, Credi A and Venturi M 2009 *Chem. Soc. Rev.* **38** 1542
[43] Browne W R and Feringa B L 2009 *Ann. Rev. Phys. Chem.* **60** 407
[44] Hoki K, Yamaki M, Koseki S and Fujimura Y 2003 *J. Chem. Phys.* **118** 497
[45] Hoki K, Yamaki M, Koseki S and Fujimura Y 2003 *J. Chem. Phys.* **119** 12393
[46] Yamaki M, Hoki K, Kono H and Fujimura Y 2008 *Chem. Phys.* **347** 272
[47] Fujimura Y, González L, Kröner D, Manz J, Mehdaoui I and Schmidt B 2004 *Chem. Phys. Lett.* **386** 248
[48] Koumura N, Geertsema E M, van Gelder M B, Meetsma A and Feringa B L 2002 *J. Am. Chem. Soc.* **124** 5037
[49] van Delden R A, ter Wiel M K J, Pollard M M, Vicario J, Koumura N and Feringa B L 2005 *Nature* **437** 1337
[50] Pollard M M, Lubomska M, Rudolf P and Feringa B L 2007 *Angew. Chem., Int. Ed. Engl.* **46** 1278
[51] Snyder P A and Clark L B 1970 *J. Phys. Chem.* **52** 998
[52] Allan M, Snyder P A and Robin M B 1985 *J. Phys. Chem.* **89** 4900
[53] Snyder P A, Hansen R W C and Rowe E M 1996 *J. Phys. Chem.* **100** 17756
[54] Rijkenberg R A, Buma W J, van Walree C A and Jenneskens L W 2002 *J. Phys. Chem.* A **106** 5249
[55] Hoogesteger F J, van Lenthe J H and Jenneskens L W 1996 *Chem. Phys. Lett.* **259** 178
[56] Havenith R W A, van Lenthe J H, Jenneskens L W and Hoogesteger F J 1997 *Chem. Phys.* **225** 139
[57] Havenith R W A, Jenneskens L W and van Lenthe J H 1998 *Chem. Phys. Lett.* **282** 39
[58] Havenith R W A, van Dam H J J and van Lenthe J H 1999 *Chem. Phys.* **246** 49
[59] Rijkenberg R A, Buma W J, van Lenthe J H, Jenneskens L W and Schmal L P 2003 *ChemPhysChem* **4** 97
[60] Pérez-Hernández G, González L and Serrano-Andrés L 2008 *ChemPhysChem* **9** 2544
[61] Robin M B 1985 *Higher Excited States of Polyatomic Molecules* vol III (New York: Academic)
[62] Frisch M J *et al* 2004 *Gaussian 03, Revision C.02* (Wallingford, CT: Gaussian, Inc.)
[63] Feit M D, Fleck J Jr and Steiger A 1982 *J. Comput. Phys.* **47** 412
[64] Feit M D and Fleck J Jr 1983 *J. Chem. Phys.* **78** 301
[65] Zhu W, Botina J and Rabitz H 1997 *J. Chem. Phys.* **108** 1953
[66] Elghobashi N, Krause P, Manz J and Oppel M 2003 *Phys. Chem. Chem. Phys.* **5** 4806
[67] Elghobashi N, González L and Manz J 2004 *J. Chem. Phys.* **120** 8002
[68] Elghobashi N and González L 2004 *Phys. Chem. Chem. Phys.* **6** 4071
[69] Rozgonyi T and González L 2008 *Chem. Phys. Lett.* **459** 39
[70] Brixner T 2003 *Appl. Phys.* B **76** 531
[71] Brixner T, Krampert G, Niklaus P and Gerber G 2002 *Appl. Phys.* B **74** S133
[72] Brixner T, Damrauer N H, Krampert G, Niklaus P and Gerber G 2003 *J. Opt. Soc. Am.* B **20** 878
[73] Brixner T and Gerber G 2001 *Opt. Lett.* **26** 557
[74] Golan B, Fradkin Z, Kopnov G, Oron D and Naaman R 2009 *J. Chem. Phys.* **130** 064705
[75] Weber S M, Plewicki M, Weise F and Lindigner A 2008 *J. Chem. Phys.* **128** 174306
[76] Atabek O, Dion C and Haj-Yedder A 2003 *J. Phys. B: At. Mol. Opt. Phys.* **36** 4667

4. Conclusions and Outlook

The present THESIS is a theoretical work on light-triggered molecular motors. Three molecules have been studied (see Fig. 3.1), posing a number of different problems: pure electronic structure calculations, reaction dynamics (time-dependent and time-independent), conformational search, and laser control. Ground state and excited state properties have been subject of investigation, yielding mechanistic insights into the motors' thermochemistry and photochemistry. Commercial codes as well as codes written for this THESIS have been used.

The motors **2** and **3** belong to the class of light-triggered unidirectional molecular motors based on chiral overcrowded alkenes, a group of molecular motors over which extensive experimental control exists. The unidirectional rotation that this class of motors performs is based partly upon a thermal process (a molecular helicity inversion), and partly upon a light-triggered, ultrafast *cis-trans*-isomerization. Under certain experimental conditions, these two processes occur irreversibly towards one preferred rotatory direction, leading to an overall unidirectionality of the molecular motion. This preference of rotation is based entirely upon semi-rigid substituents built into the molecule through clever synthesis. In this THESIS, the thermal helicity inversion in **2** and **3** has been investigated. First, a conformational search has been carried out using a Monte-Carlo-based search algorithm, in order to find all possible local minima of **2** and **3** in the electronic ground state. Subsequently, pathways connecting the found minima have been obtained through the calculation of TSs and associated IRCs. All of the calculated geometries of the minima and the corresponding E_a-values (available through the TSs and the IRCs) are in excellent agreement with the available values from the literature, both for **2** and **3**.

However, even if both motors function similarly, their respective PESs differ substantially in complexity. For **2**, the search-algorithm has found six minima, three of which had not been reported so far. This manifold of isomers and the calculated TSs give rise to alternative pathways in the thermal, irreversible step of the overall unidirectional rotation. Two of the three newly found isomers have E_a-values that allow the backward thermal *escape* from these minima at the experimental temperatures. Moreover, one of the newly-found minima, **2f**, is proposed as an additional intermediate in the thermal helix inversion of **2**. In accordance with the experimental observations, the computed difference in stability (> 5 kcal/mol) of the minima (regardless of E_a-values) guarantees that the desired *stable* minimum, **2a**, is populated almost exclusively under thermal conditions,

ensuring the irreversibility of the reaction under the experimental conditions.

These stability relations hold also for the motor **3**, but in a less complicated PES. In this case, the search-algorithm has found four isomers that correspond to the minima reported in the literature. Again, the obtained relative stabilities (> 5 kcal/mol) between reactants and products of the thermal reaction account for the process' irreversibility under experimental conditions. Computation of the TSs yields E_a-values in excellent agreement with those provided in the literature, sustaining the mechanism proposed.

Given the fact that overcrowded alkenes present differently shaped thermal pathways, and that accurate *ab-initio* methods are mandatory for a realistic description of the light-matter interaction, a simpler alkene (**4**, BCH) has been investigated as a model for unidirectional rotation. This olefin, which can be considered as a building block of larger overcrowded alkenes, exhibits a *syn-anti*-bistability which can be triggered with UV-light. Additionally, BCH serves as a model in which unidirectional rotation has to be achieved alone through the field-dipole interaction, due to BCH's lack of built-in asymmetric factors. In order to describe properly that interaction, BCH's electronic structure has been investigated thoroughly with high-level *ab-initio* quantum chemical methods at first.

Despite its apparent simplicity, the photochemistry of BCH has been matter of controversy in the literature over the last decades. The discussion has focused on the presence of two intense bands in the low-energy range of the UV-spectrum, in the gas phase as well as in condensed phases. One of the bands was readily assigned to a HOMO→LUMO (π, π^*)-transition, according to π-electron theory predictions. Different, contradicting assignments of the nature of the other band have followed. Early investigations offered other low-lying valence-like transitions as an explanation, even if such assignments were unexpected within π-electron theory. A possible Rydberg-character of the second transition was initially excluded (both in theoretical and experimental works) due to the band's persistence in condensed phases. Most recent experimental and theoretical studies have interpreted both bands as a mixture of the (π, π^*)-electronic state with a low-lying, diffuse $3d_R$-Rydberg state.

In order to carry out electronic structure calculations that do not exclude a given electronic nature *a priori*, a one-particle basis set of atomic orbitals has been newly developed from the ANO-L basis set. It has been specifically optimized to accommodate both the diffuse and the compact electronic wavefunctions that need to be simultaneously described. The performed CASSCF calculations included all possible Rydberg excitations in the chosen active space. Subsequent multi-state perturbation-theory computations (MS-CASPT2) resolved the first two excited electronic states into two differentiated states: one Rydberg-like $(\pi, 3s)$-state and one valence-like (π, π^*)-state. The associated vertical excitation energies (5.95 and 6.83 eV, respectively) and oscillator strengths are in excellent agreement with the reported band peaks. The resulting MS-CASPT2-assignment reverses

the order of the states assumed so far, because the calculations predict the Rydberg state lying at lower energies than the valence state. The apparent intensity of the Rydberg-band in condensed phases needs further rationalization. To do so, the origin of the vibrational progression of the (π,π^*)-band has been computed. Optimizing the (π,π^*)-minimum yields an energy value of 5.63 eV for the associated non-vertical electronic transition in the *anti*-BCH (the one present in the solid). This value allows the (π,π^*)-band to extend beyond the peak of the Rydberg intensity (ca. 5.95 eV), via progressions along the C=C-stretching and C=C−CH_2-scissoring modes. The (π,π^*)-vibronic spectrum serves thus as an underlying continuum, on top of which the Rydberg band appears more intense, even in condensed phases.

Finally, quantum dynamical simulations have been carried out to probe light-induced, unidirectional molecular rotation. The adiabatic potentials have been constructed along the torsion about BCH's double bond. The model includes the ground and first excited states, and the associated permanent and transition dipoles, computed at the MS-CASPT2-level of theory with the optimized Rydberg basis set. As opposed to **2** and **3**, BCH is highly symmetric, with quasi-degenerated (ground) and degenerated (excited state) double-well, cyclic PESs. Prior to the investigation of the light-induced dynamics, the system's torsional eigenstates have been computed, and torsional frequencies for the *syn*- and *anti*-isomers have been obtained, in good agreement with the corresponding harmonic frequencies of the associated torsional normal mode.

Diverse control strategies have been used to drive the sought unidirectional rotation in BCH. These include OCT under different assumptions for the induced transitions, OCT polarization shaping, and the more intuitive few-cycle IR+UV-strategy. Contrary to **2** and **3**, BCH does not rely upon thermal steps for full rotation. Thus, alone the interaction of the dipole with the shaped light introduces the asymmetry into the pre-oriented system. The amount of unidirectional momentum transferred to the excited state increases if the OCT-optimization includes ground state torsional transitions. The obtained pulse shows a certain time-separation of the carried IR- and UV-frequencies. This principle of time-separation of frequencies is subsequently exploited in the few-cycle IR+UV-simulation, which triggers unidirectional rotation in the excited state lasting for over two picoseconds.

Conical intersections can play a major role in the ultrafast *cis-trans*-isomerizations of double bonds.[150] This fact, mentioned in the introduction for the case of retinal, is very likely to be behind the ultrafast isomerization ($>$ 300 ps) measured for chiral overcrowded alkenes. Whereas in the case of BCH no conical intersection was found, several conical intersections have been located for the motors **2** and **3** between the ground state, (π^2), and the first excited state (π,π^*). It is thus mandatory that quantum dynamical simulations of **2** or **3** include conical intersections if efficient laser control strategies in the excited state are to be devised. Beyond the torsion, such simulations must include pyramidalization

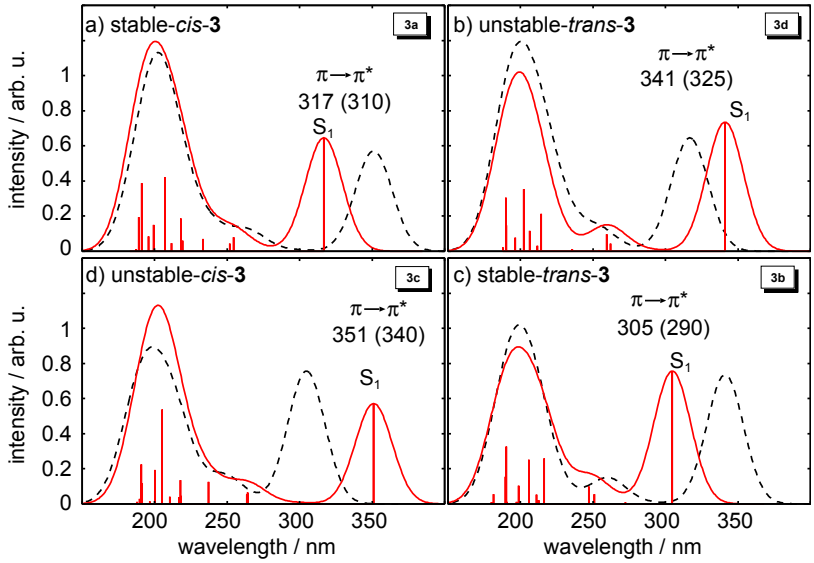

Figure 4.1.: B3LYP/6-31G(d) UV-spectra of the four isomers of **3**. The panels are ordered clockwise a)→b)→c)→d)→a) following the rotary cycle of Fig. 3.3e. The upper-right squared label in each panel a-d) contains the label of the corresponding isomer in Fig. 3.3a-d), where the isomers were ordered by energy. To represent best the shifts in the band peaks throughout the rotary cycle, the preceding isomer's spectrum is presented in dashed black lines. Band peaks are shown in nm, with the experimental values in parenthesis.

(re-hybridization) of the sp^2 carbon atoms of the central double bond, since the obtained conical intersections present a twisted-pyramidalized[150] geometry.

The photochemical results including conical intersections as well as a time-dependent DFT (TDDFT) study of the excited states of **2** and **3** are currently being prepared for publication. The obtained TDDFT spectra are shown exemplarily for the four isomers of **3** in Fig. 4.1. The electronic character of the lowest excitation around 300 nm is of (π, π^*)-nature in the central double bond (the axle) of all motors. The associated batho- and hypsochromic shifts in the band peaks are consistent with the different degrees of distortion of the central olefinic plain. Additional MS-CASPT2 computations have been carried out to obtain more accurate vertical excitation energies for **3**, the motor for which such high level of theory is affordable. Together with the computation of minimum energy paths (MEPs, currently being computed), a complete PES landscape emerges.

5. Zusammenfassung

Die vorliegende Doktorarbeit beschäftigt sich mit quantenchemischen und quantendynamischen Berechnungen von molekularen Rotoren. Außerdem werden Laserkontrollstrategien zur unidirektionellen Rotation vorgeschlagen.

Vier Ideen bilden die Grundlage dieser Forschungsarbeit: (*i*) Wichtige biologische Prozesse basieren auf einer maschinenartigen Funktionsweise von großen Biomolekülen. (*ii*) Heutzutage bietet Nanotechnologie eine Vielfalt an molekularen Maschinen, welche zum Teil auch von biologischen Systemen inspiriert sind. Eine Klasse solcher Maschinen sind die molekulare Rotoren, in denen eine Drehbewegung auf molekularer Ebene stattfindet. (*iii*) Sowohl in den biologischen als auch in den nanotechnologischen molekularen Maschinen spielt die quantenmechanische Natur der Materie eine entscheidende Rolle und (*iv*) quantenmechanische Phänomene lassen sich anhand externer Laserfelder steuern. Punkt (*i*) wird an den Beispielen der ATP-Synthase und des Chromophors Retinal erläutert, in denen mechanische Eigenschaften auf molekularer Ebene weitere Folgen auf zellulärer Ebene haben: Energieverwaltung im Fall der ATP-Synthase und der erste Schritt des Sehprozesses im Fall des Retinals. In Zusammenhang mit Punkt (*ii*) wird die Klasse der chiralen, sog. überladenen (*overcrowded*) Alkene eingeführt, die als unidirektionelle, lichtinduzierte molekulare Rotoren erfolgreich experimentell eingesetzt worden sind. Ihre Funktionsweise basiert auf der Kombination mehrerer Faktoren: Einer vorhandenen Asymmetrie in den Potentialenergieflächen (von mindestens einem chiralen Zentrum verursacht), einer konformationellen Flexibilität und der *cis-trans*-Bistabilität. Die Wichtigkeit rein quantenmechanischer Prozesse (Punkt (*iii*)) wird weiter am Beispiel der ultraschnellen (ca. 200 fs) Isomerisierung des Retinalmoleküls betrachtet. Diese Isomerisierung wird durch nichtadiabatische Kopplungen der beteiligten elektronischen Zustände ermöglicht. Grundlegende Aspekte der Lasersteuerung chemischer Prozesse (Punkt (*iv*)) werden auch diskutiert, mit dem Schwerpunkt auf *Optimal Control Theory* (OCT) und der intuitiven Infrarot + Ultraviolett (IR+UV)-Strategie, durch welche eine gerichtete Rotation in molekularen Rotoren ausgelöst wird.

In dieser Arbeit werden die Moleküle aus Abb. 5.1 als Modellsysteme verwendet. Die Moleküle **2** und **3** gehören der Klasse der chiralen überladene Alkene an. **4** (BCH) hingegen ist ein einfaches Alken, das als Kernbaustein vieler Rotoren zu finden ist. BCH alleine verfügt auch über *syn-anti* Bistabilität, die sich mittels UV-Licht steuern lässt, und wird daher als Modell für Laserkontrollstrategien benutzt. **2** und **3** werden aus unterschiedlichen Gründen

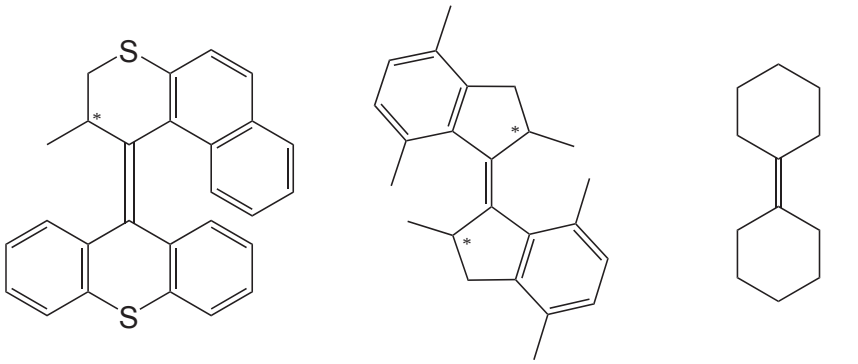

Abbildung 5.1.: Molekulare Motoren, die in der vorliegenden Arbeit behandelt wurden.

ausgewählt. **2** ist eines der überladenen Alkene, das als Rotor auf einer festen Oberfläche verankert wurde, was im Üblichen die Voraussetzung für weitere nanotechnologische Anwendungen ist. Im Gegensatz dazu konnte **3** bisher nur in der Gasphase erfolgreich als Rotor eingesetzt werden. Dieser stellt jedoch einen der einfachsten solcher Rotoren dar, was vom Standpunkt des rechnerischen Aufwandes her besonders wünschenswert ist. In Rotoren wie **2** und **3** führt das Zusammenspiel des Überladens und einer gewissen Rigidität der Substituenten an der zentralen Doppelbindung zu einer axialen Chiralität: *P*- oder *M*-Helizität. Die thermisch irreversible Inversion dieser Helizität trägt zur Funktionsweise von **2** und **3** bei, denn die Rotation wird im Experiment zum Teil thermisch gesteuert. Darum spielt die Topologie der Potentialenergiefläche des elektronischen Grundzustandes eine Rolle und deswegen wird die konformationelle Dynamik der Rotoren **2** und **3** im Artikel 3.5.1 untersucht. Anhand einer selbst-programmierten Monte-Carlo-Konformer-Suche werden alle möglichen Konformere von **2** und **3** mit semiempirischen Rechenmethoden generiert, um letztendlich mit der quantenchemischen MP2/6-31(d)-Methode optimiert zu werden. Zusätzlich werden auch Übergangsstrukturen zwischen den erhaltenen Konformeren mit der B3LYP/6-31(d)-DFT-Methode optimiert. Wenn Edukte, Produkte und Übergangszustände einer gewissen Reaktion vorhanden sind, werden Aktivierungsbarrieren (E_a) mit der genaueren RI-MP2/TZVP-Methode berechnet.

Sowohl für **2** als auch für **3** stimmen die berechneten Geometrien und Energiedifferenzen sehr gut mit den verfügbaren experimentellen Werten überein. Allerdings erfolgt die Auswertung unterschiedlich für beide Rotoren. **3** weist eine relativ einfache Konformer-Landschaft auf, wo die aufgefundenen vier Isomere sich den entsprechenden vier Etappen der Rotation klar zuordnen lassen: Zwei stabile *cis*-Konformere und zwei instabile *trans*-Konformere, mit jeweils einer Übergangsstruktur, wobei die berechneten Aktivierungsbarrieren sehr gut mit den experimentellen Werten übereinstimmen (± 0.4 kcal/mol). Im Fall des Rotors **2** ist die Potentialenergiefläche des Grundzustandes reicher an lokalen Mi-

nima (sechs), und neben den drei Isomeren, von denen in der Literatur schon berichtet wurde, findet der Algorithmus weitere drei instabilere Isomere. Mit Hilfe der berechneten Übergangsstrukturen lässt sich die mögliche Rolle dieser Minima in der Rotation weiter untersuchen. Die zweite Hälfte der thermisch induzierten Helizitätsinversion ist schon in der Literatur als schrittweise Reaktion beschrieben worden. Ein neuer Zwischenschritt in der ersten Hälfte dieser Helizitätsinversion wird zum ersten Mal postuliert. Eine alternative, weniger wahrscheinliche Reaktionsroute wird zusätzlich für den zweiten Teil der Inversion vorgeschlagen.

Wie aus Artikel 3.5.1 hervorgeht, können chirale überladene Alkene unterschiedlich komplizierte Dynamiken im Grundzustand aufweisen. Hinzu kommt noch die Tatsache, dass angeregte Zustände genau berechnet werden müssen, um realistisch die Licht-Materie-Wechselwirkung beschreiben zu können und um letztendlich Laserkontrollstrategien zu entwerfen. Quantenchemische und quantendynamische Berechnungen sind einfacher am Modellsystem **4** (BCH) durchzuführen. Als erstes erfolgt im Artikel 3.5.2 eine gründliche Untersuchung der angeregten Zustände von BCH, die schon seit langem in der Literatur kontrovers diskutiert werden. Im Prinzip scheint das mehrfach aufgenommene UV-Spektrum von BCH (in der Gasphase, im Festkörper und in Lösung) im Gegensatz zur π-Elektron-Theorie zu stehen. Denn als einfaches Alken sollte nur der (π,π^*)-Übergang (HOMO→LUMO) als einziger starker Übergang im Spektrum auftauchen. Jedoch weist das UV-Spektrum von BCH (das im Festkörper nur als *anti*-BCH vorkommt) zwei starke Banden auf. Der elektronische Charakter der zweiten Bandes ist umstritten, und sowohl Valenz- (z. B. (σ,σ^*)) als auch Rydberg-Übergange wurden seitens Theorie und Experiment in Betracht gezogen.

Im Artikel 3.5.2 wird problemspezifisch ein Basissatz entwickelt, der den diffusen Charakter von Rydberg-Wellenfunktionen beschreiben kann, aber trotzdem den Valenz-Wellenfunktionen nicht uneingeschränkt Diffusität hinzufügt. Die *ab-initio* SA-CASSCF-Methode, zusammen mit diesem Rydberg-Basissatz, wird eingesetzt, um im Anschluss mittels Störungstheorie (MS-CASPT2) gleichzeitig Valenz-Zustände (Grundzustand (π^2) und angeregter Zustand (π,π^*)) und Rydberg-Zustände zu berechnen. Der *active space* wird so gewählt, dass im Prinzip alle möglichen, symmetrie-erlaubten Übergänge berechnet werden können. Die elektronischen Energiewerte und Wellenfunktionen der MS-CASPT2-Rechnung bestimmen den $(\pi,3s_R)$-Übergang (Rydberg) als ersten angeregten Singulett-Zustand und den (π,π^*)-Übergang (Valenz) als zweiten. Die jeweiligen Anregungsenergien 5.95 eV und 6.82 eV stimmen sehr gut mit verfügbaren experimentellen Werten überein, ebenso die jeweiligen Oszillatorstärken. Es bleibt jedoch zu klären, warum ein Rydberg-Übergang sogar in der kondensierten Phase zu einer so starken Bande führt. Zu diesem Zweck werden die (π,π^*)-Minima von *anti*- und *syn*-BCH berechnet. Dadurch wird wiederum eine Energiedifferenz berechenbar, die dem Ursprung der Schwingungsprogression der (π,π^*)-Bande im

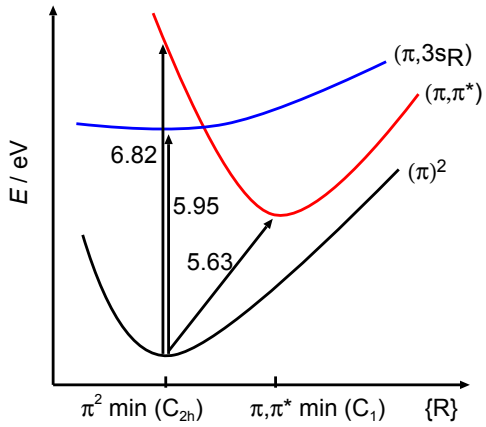

Abbildung 5.2: Schematische Darstellung des elektronischen Grundzustandes und der ersten beiden angeregten Zuständen in *anti*-BCH. Anregungsenergien für vertikale und nicht-vertikale Übergänge sind aufgetragen (in eV). Aus Artikel 3.5.2.

UV-Spektrum entspricht. Das bedeutet, der nicht-vertikale Übergang zwischen (π^2)- und (π, π^*)-Minimum wird berechnet. Eine graphische Darstellung davon ist in Abb. 5.2 aufgetragen. Für *anti*-BCH wird ein Wert von 5.63 eV als Ursprung der (π, π^*)-Bande gefunden, d.h. diese starke Bande kann sich bis weit unterhalb der ($\pi, 3s_R$)-Bande (5.93 eV) erstrecken. Die zugehörige Schwingungsprogression wird untersucht, indem die harmonischen Schwingungsmoden und -frequenzen beider Minima berechnet werden. Progressionen entlang der Scheren- und Streck-Schwingungen tragen zum Profil des *anti*-(π, π^*)-Übergangs bei.

In Artikel 3.5.3 werden unterschiedliche Laserkontrollstrategien für BCH vorgeschlagen. Voraussetzung dafür ist der photochemische Einblick aus Artikel 3.5.2. Dieselbe quantenchemische Methode (MS-CASPT2 mit Rydberg-Basissatz) wird eingesetzt. Eine eindimensionale Potentialenergiekurve entlang der periodischen Torsionskoordinate β (der Diederwinkel der Doppelbindung in BCH, Abb. 5.1) wird für den elektronischen Grundzustand und den ersten angeregten Zustand berechnet. Entsprechend werden auch permanente und Übergangsdipolmomente berechnet.

Der Grundzustand weist das Profil eines quasi-entarteten Doppelminimums auf, mit jeweils einem Minimum für die *anti*-BCH- ($\beta = 0 = 2\pi$) und die *syn*-BCH Geometrie ($\beta = \pi$), die nicht identisch stabil sind. Diese zwei Positionen entsprechen auch den Symmetrieachsen im β-Raum $\epsilon\, [0, 2\pi]$: Alle vorhandene Elemente, die f(β) sind, sind entweder *gerade* oder *ungerade* bei β=0=2π oder β=π. Der angeregte Zustand weist hingegen ein entartetes Doppelminimumpotential auf, in dem die Minima bei $\beta = \frac{\pi}{2}$ und $\beta = \frac{3\pi}{2}$ zu finden sind. Beide Potentiale werden auf ihre Eigenfunktionen und Eigenwerte untersucht, indem die entsprechende Kern-Schrödingergleichung durch eine Matrixdiagonalisierung gelöst wird. Für den Grundzustand sind die berechneten Eigenfunktionen entweder um das *syn*- oder das *anti*-Minimum zentriert, wobei jeweils ca. 350 Torsionseigenzustände unter der Barriere im Grundzustand liegen. Die durch die Diagonalisierung erhaltene Schwingungsfrequenzen für die Torsion von *syn*- und *anti*-BCH entsprechen in guter Übereinstimmung den Werten aus einer harmonischen Frequenzrechnung. Die Diagonalisierung für den Fall

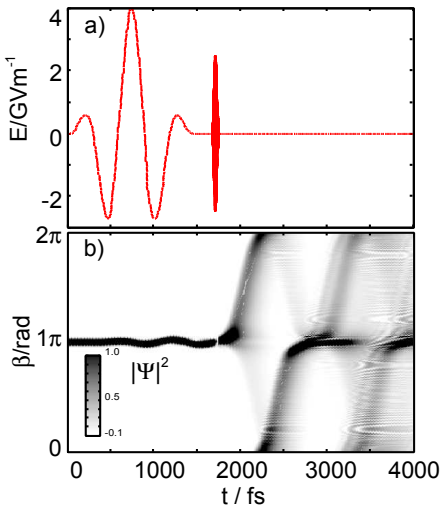

Abbildung 5.3: *Few-cycle* IR+UV-Laserkontrollstrategie. Abb. a) zeigt den verwendeten Laserpuls, in dem IR- und UV-Komponenten zeitlich getrennt und gezielt verzögert sind. Abb. b) zeigt die durch den Laser-Puls induzierte Wellenpaketdynamik. Bis zum Zeitpunkt des UV-Subpulses erfolgt die Dynamik im Grundzustand. Nach der Anregung befindet sich >99% der Wahrscheinlichkeitsdichte $|\Psi(t,\beta)|^2$ im angeregten Zustand. Die Rotation wird unidirektionell ausgelöst, und zwei vollständige Zyklen ($\pi \rightarrow 2\pi = 0 \rightarrow \pi$) werden angezeigt. Aus Artikel 3.5.3.

des angeregten Zustandes ergibt einen Satz von zweifach entarteteten Eigenfunktionen, die bei $\beta = \frac{\pi}{2}$ und $\beta = \frac{3\pi}{2}$ zentriert sind.

Die Torsionspotentiale und Eigenfunktionen werden weiter in einer Untersuchung von Laserkontrollstrategien mittels OCT und few-cycle IR+UV-Theorie eingesetzt. Ziel der Untersuchung ist die Rotation allein durch Laser-Pulse auszulösen. Die Formulierung des Kontrollproblems im Rahmen der OCT erfolgt anhand Anfangszustand und Zielzustand. Als Anfangszustand wird die niedrigste Torsionseigenfunktion gewählt, die dem *syn*-isomer ($\beta = \pi$) entspricht. Als Zielzustand wird eine normierte Gaußfunktion im angeregten Zustand verwendet. Diese ist auch um $\beta = \pi$ zentriert und ist erheblich in der positiven Drehrichtung beschleunigt. Bei der Betrachtung des erhaltenen OCT-Pulses mittels eines Spektrogrammes taucht eine gewisse zeitliche Differenzierung der IR- und UV-Frequenzen auf. Diese Art von Unterteilung des Kontrollpulses erfolgt ganz intuitiv, wenn das Kontrollproblem im Rahmen der *few-cycle* IR+UV-Strategie formuliert wird. Es wird ein *few-cycle*-Anfangspuls benutzt, der in Resonanz mit den ersten Schwingungsübergängen des *anti*-BCH im Grundzustand ist. Es folgt ein kurzer UV-Puls der resonant beide elektronischen Zustände koppelt. Die gezielte Verzögerung des UV-Pulses bestimmt die Rotationsrichtung des Wellenpaketes im angeregten Zustand. In Abb. 5.3 wird der Laserpuls und die dadurch induzierte Dynamik gezeigt. Nach der UV-Strahlung vollendet das angeregte Wellenpacket zwei vollständige Rotationszyklen. Das eindimensionale BCH-Model erweist sich dadurch als geeigneter lichtinduzierter Motor.

Derzeit durchgeführte Berechnungen beschäftigen sich mit den angeregten Zuständen der Motoren **2** und **3**, mit besonderer Berücksichtigung der konischen Durchschneidungen und ihren Folgen in der lichtinduzierten Dynamik.

Bibliography

[1] Boyer, P. D. Energy, life, and ATP (Nobel lecture). *Angew. Chem. Int. Ed.*, **37**, 2296–2307 (1998). 2
Walker, J. E. ATP synthesis by rotary catalysis (Nobel lecture). *Angew. Chem. Int. Ed.*, **37**, 2308–2319 (1998).

[2] Boyer, P. D. The binding change mechanism for ATP synthase – some probabilities and possibilities. *Biochim. Biophys. Acta*, **1140**, 215–250 (1993). 3

[3] Stock, D., Leslie, A. G. W., and Walker, J. E. Molecular architecture of the rotary motor in ATP synthase. *Science*, **286**, 1700–1705 (1999).

[4] Elston, T., Wang, H., and Oster, G. Energy transduction in ATP synthase. *Nature*, **391**, 510–513 (1998).
Oster, G. and Wang, H. Reverse engineering a protein: the mechanochemistry of ATP synthase. *Biochim. Biophys. Acta*, **1458**, 482–510 (2000).
Oster, G., Wang, H., and Grabe, M. How F_0-ATPase generates rotary torque. *Philos. T. Roy. Soc. B*, **355**, 523–528 (2000).

[5] Allison, W. S. F1-ATPase: a molecular motor that hydrolyzes ATP with sequential opening and closing of catalytic sites coupled to rotation of its γ subunit. *Acc. Chem. Res.*, **31**, 819–826 (1998). 3

[6] Block, S. M. Real engines of creation. *Nature*, **386**, 217–219 (1997). 3

[7] Crick, F. *What Mad Pursuit: A Personal View of Scientific Discovery.* Basic Books (1988). 3

[8] Casiday, R. and Frey, G. Adapted from the website Vision and Light-Induced Molecular Changes with kind permission from the authors. www.chemistry.wustl.edu/~edudev/LabTutorials/Vision/Vision.html. ix, 5

[9] Dugave, C. and Demange, L. *cis-trans* isomerization of organic molecules and biomolecules: Implications and applications. *Chem. Rev.*, **103**, 2475–2532 (2003). 4

[10] Schoenlein, R. W., Peteanu, L. A., Mathies, R. A., and Shank, C. V. The first step in vision: femtosecond isomerization of rhodopsin. *Science*, **254**, 412–415 (1991). 5, 6

[11] Miller, R. J. D., Ernstorfer, R., Harb, M., Gao, M., Hebeisen, C. T., Jean-Ruel, H., Lu, C., Moriena, G., and Sciaini, G. Making the molecular movie: first frames. *Acta Crystallogr. Sect. A*, **66**, 137–156 (2010). 5

[12] Garavelli, M., Bernardi, F., Olivucci, M., Vreven, T., Klein, S., Celani, P., and Robb, M. A. Potential-energy surfaces for ultrafast photochemistry static and dynamic aspects. *Faraday Discuss.*, **110**, 51–70 (1998). 6

[13] González-Luque, R., Garavelli, M., Bernardi, F., Merchán, M., Robb, M. A., and Olivucci, M. Computational evidence in favor of a two-state, two-mode model of the retinal chromophore photoisomerization. *Proc. Natl. Acad. Sci. USA*, **97**, 9379 –9384 (2000). 6

[14] Vogt, G., Nuernberger, P., Brixner, T., and Gerber, G. Femtosecond pump–shaped-dump quantum control of retinal isomerization in bacteriorhodopsin. *Chem. Phys. Lett.*, **433**, 211–215 (2006). 6, 25

[15] Prokhorenko, V. I., Nagy, A. M., Waschuk, S. A., Brown, L. S., Birge, R. R., and Miller, R. J. D. Coherent control of retinal isomerization in bacteriorhodopsin. *Science*, **313**, 1257–1261 (2006).

[16] Florean, A. C., Cardoza, D., White, J. L., Lanyi, J. K., Sension, R. J., and Bucksbaum, P. H. Control of retinal isomerization in bacteriorhodopsin in the high-intensity regime. *Proc. Natl. Acad. Sci. USA*, **106**, 10896 –10900 (2009). 6, 25

[17] Ohtsuki, Y., Ohara, K., Abe, M., Nakagami, K., and Fujimura, Y. New quantum control pathway for a coupled-potential system. *Chem. Phys. Lett.*, **369**, 525–533 (2003). 6

[18] Flores, S. C. and Batista, V. S. Model study of coherent-control of the femtosecond primary event of vision. *J. Phys. Chem. B*, **108**, 6745–6749 (2004).

[19] Abe, M., Ohtsuki, Y., Fujimura, Y., and Domcke, W. Optimal control of ultrafast *cis-trans* photoisomerization of retinal in rhodopsin via a conical intersection. *J. Chem. Phys.*, **123**, 144508 (2005).

[20] Marquetand, P., Nuernberger, P., Vogt, G., Brixner, T., and Engel, V. Properties of wave packets deduced from quantum control fitness landscapes. *Europhys. Lett.*, **80**, 53001 (2007). 6

[21] Polli, D., Altoe, P., Weingart, O., Spillane, K. M., Manzoni, C., Brida, D., Tomasello, G., Orlandi, G., Kukura, P., Mathies, R. A., Garavelli,

M., and Cerullo, G. Conical intersection dynamics of the primary photoisomerization event in vision. *Nature*, **467**, 440–443 (2010). ix, 6

[22] Wang, Q., Schoenlein, R. W., Peteanu, L. A., Mathies, R. A., and Shank, C. Vibrationally coherent photochemistry in the femtosecond primary event of vision. *Science*, **266**, 422–424 (1994). 6

[23] Sauvage, J. P., editor. *Molecular Machines and Motors*. Springer, Berlin (2001). 7

[24] Schliwa, M., editor. *Molecular Motors*. Wiley-VCH, Weinheim (2003).

[25] Feringa, B. L., editor. *Molecular Switches*. Wiley-VCH, Weinheim (2001). 9

[26] V. Balzani, A. Credi, M. V., editor. *Molecular Devices and Machines-A Journey into the Nanoworld*. Wiley-VCH, Weinheim (2003). 7

[27] Kelly, T. R., editor. *Molecular Machines*. Springer, Berlin (2006). 7

[28] E. R. Kay, D. A. Leigh, F. Z. Synthetic molecular motors and mechanical machines. *Angew. Chem. Int. Ed.*, **46**, 72–191 (2007). 7

[29] Soong, R. K., Bachand, G. D., Neves, H. P., G.Olkhovets, A., Craighead, H. G., and Montemagno, C. D. Powering an inorganic nanodevice with a biomolecular motor. *Science*, **290**, 1555–1558 (2000). 8

[30] Soong, R. and Montemagno, C. Engineering hybrid nano-devices powered by the F1-ATPase biomolecular motor. *Int. J. Nanotechnol.*, **2**, 371 – 396 (2005). 8

[31] Eelkema, R., Pollard, M. M., Vicario, J., Katsonis, N., Ramon, B. S., Bastiaansen, C. W. M., Broer, D. J., and Feringa, B. L. Molecular machines: Nanomotor rotates microscale objects. *Nature*, **440**, 163 (2006). 8

[32] Feringa, B. L., van Delden, R. A., and ter Wiel, M. K. J. In control of switching, motion, and organization. *Pure Appl. Chem.*, **75**, 563–575 (2003). 9

[33] Feringa, B. L. The art of building small: From molecular switches to molecular motors. *J. Org. Chem.*, **72**, 6635–6652 (2007). 9

[34] Koumura, N., Ziljstra, R. W. J., van Delden, R. A., Harada, N., and Feringa, B. L. Light-driven monodirectional molecular rotor. *Nature*, **401**, 152–155 (1999). ix, 9, 10, 12

[35] Koumura, N., Geertsema, E. M., van Gelder, M. B., Meetsma, A., and Feringa, B. L. Second generation light-driven molecular motors. Unidirectional

rotation controlled by a single stereogenic center with near-perfect photoequilibria and acceleration of the speed of rotation by structural modification. *J. Am. Chem. Soc.*, **124**, 5037–5051 (2002). x, 11, 14, 46

[36] Vicario, J., Walko, M., Meetsma, A., and Feringa, B. L. Fine tuning of the rotary motion by structural modification in light-driven unidirectional molecular motors. *J. Am. Chem. Soc.*, **128**, 5127–5135 (2006).

[37] Pollard, M. M., Klok, M., Pijper, D., and Feringa, B. L. Rate acceleration of light-driven rotary molecular motors. *Adv. Func. Mater.*, **17**, 718–729 (2007). 11, 13, 15

[38] G. S. Kottas, L. I. Clarke, D. H. J. M. Artificial molecular rotors. *Chem. Rev.*, **105**, 1281–1376 (2005). 13

[39] Schuddeboom, W., Jonker, S. A., Warman, J. M., de Haas, M. P., Vermeulen, M. J. W., Jager, W. F., de Lange, B., Feringa, B. L., and Fessenden, R. W. Sudden polarization in the twisted, phantom state of tetraphenylethylene detected by time-resolved microwave conductivity. *J. Am. Chem. Soc.*, **115**, 3286–3290 (1993). 13
Zijlstra, R. W. J., van Duijnen, P. T., Feringa, B. L., Steffen, T., Duppen, K., and Wiersma, D. A. Excited-State dynamics of tetraphenylethylene: Ultrafast stokes shift, isomerization, and charge separation. *J. Phys. Chem. A*, **101**, 9828–9836 (1997).

[40] Atkins, P. and de Paula, J. *Physical Chemistry*. Oxford University Press, Oxford (2006). 13

[41] Koumura, N., Geertsema, E. M., Meetsma, A., and Feringa, B. L. Light-driven molecular rotor: Unidirectional rotation controlled by a single stereogenic center. *J. Am. Chem. Soc.*, **122**, 12005–12006 (2000). 14

[42] Pollard, M. M., ter Wiel, M. K. J., van Delden, R. A., Vicario, J., Koumura, N., van den Brom, C. R., Meetsma, A., and Feringa, B. L. Light-driven rotary molecular motors on gold nanoparticles. *Chemistry - A European Journal*, **14**, 11610–11622 (2008). 14

[43] van Delden, R. A., ter Wiel, M. K. J., Pollard, M. M., Vicario, J., Koumura, N., and Feringa, B. L. Unidirectional molecular motor on a gold surface. *Nature*, **437**, 1337–1340 (2005). 14

[44] Pollard, M. M., Lubomska, M., Rudolf, P., and Feringa, B. L. Controlled rotary motion in a monolayer of molecular motors. *Angew. Chem. Int. Ed.*, **46**, 1278–1280 (2007). 14

[45] ter Wiel, M. K. J., van Delden, R. A., Meetsma, A., and Feringa, B. L. Increased speed of rotation for the smallest light-driven molecular motor. *J. Am. Chem. Soc.*, **125**, 15076–15086 (2003). 14

[46] Klok, M., Boyle, N., Pryce, M. T., Meetsma, A., Browne, W. R., and Feringa, B. L. MHz unidirectional rotation of molecular rotary motors. *J. Am. Chem. Soc.*, **130**, 10484–10485 (2008). 15

[47] Kulago, A. A., Mes, E. M., Klok, M., Meetsma, A., Brouwer, A. M., and Feringa, B. L. Ultrafast light-driven nanomotors based on an acridane stator. *J. Org. Chem.*, **75**, 666–679 (2010). 15

[48] Rabitz, H. CHEMISTRY: shaped laser pulses as reagents. *Science*, **299**, 525–527 (2003). 15

[49] Dantus, M. and Lozovoy, V. V. Experimental coherent laser control of physicochemical processes. *Chem. Rev.*, **104**, 1813–1860 (2004). 15

[50] Brixner, T. and Gerber, G. Quantum control of gas-phase and liquid-phase femtochemistry. *ChemPhysChem*, **4**, 418–438 (2003). 15
Nuernberger, P., Vogt, G., Brixner, T., and Gerber, G. Femtosecond quantum control of molecular dynamics in the condensed phase. *Phys. Chem. Chem. Phys.*, **9**, 2470 (2007).

[51] Brumer, P. W. and Shapiro, M. *Principles of the Quantum Control of Molecular Processes*. Wiley-Interscience, Hoboken, NJ, USA (2003). 15, 16, 17

[52] Rice, S. A. and Zhao, M. *Optical Control of Molecular Dynamics*. Wiley-Interscience, New York, USA (2000). 15, 19

[53] Brif, C., Chakrabarti, R., and Rabitz, H. Control of quantum phenomena: past, present and future. *New. J. Phys.*, **12**, 075008 (2010). 15, 23, 24

[54] Crim, F. F. State- and bond-selected unimolecular reactions. *Science*, **249**, 1387–1392 (1990). 15

[55] Rabitz, H., de Vivie-Riedle, R., Motzkus, M., and Kompa, K. Whither the future of controlling quantum phenomena? *Science*, **288**, 824–828 (2000). 15

[56] Brumer, P. and Shapiro, M. Control of unimolecular reactions using coherent light. *Chem. Phys. Lett.*, **126**, 541–546 (1986). x, 17, 18

[57] Shapiro, M., Hepburn, J. W., and Brumer, P. Simplified laser control of unimolecular reactions: Simultaneous (ω_1, ω_3) excitation. *Chem. Phys. Lett.*, **149**, 451–454 (1988). 18

[58] Zhu, L., Kleiman, V., Li, X., Lu, S. P., Trentelman, K., and Gordon, R. J. Coherent laser control of the product distribution obtained in the photoexcitation of HI. *Science*, **270**, 77–80 (1995). 19

[59] Zhu, L., Suto, K., Fiss, J. A., Wada, R., Seideman, T., and Gordon, R. J. Effect of resonances on the coherent control of the photoionization and photodissociation of HI and DI. *Phys. Rev. Lett.*, **79**, 4108 (1997).

[60] Fiss, J. A., Zhu, L., Suto, K., He, G., and Gordon, R. J. Mechanism of the coherent control of the photoionization and photodissociation of HI and DI. *Chem. Phys.*, **233**, 335–341 (1998). 19

[61] Tannor, D. J. and Rice, S. A. Control of selectivity of chemical reaction via control of wave packet evolution. *J. Chem. Phys.*, **83**, 5013–5018 (1985). 19

[62] Tannor, D. J., Kosloff, R., and Rice, S. A. Coherent pulse sequence induced control of selectivity of reactions: Exact quantum mechanical calculations. *J. Chem. Phys.*, **85**, 5805–5820 (1986).

[63] Tannor, D. J. and Rice, S. A. Coherent pulse sequence control of product formation in chemical reactions. In *Adv. Chem. Phys.*, volume 70, pages 441–523. John Wiley & Sons, Inc., Hoboken, NJ, USA (1988). 19

[64] Baumert, T., Bühler, B., Thalweiser, R., and Gerber, G. Femtosecond spectroscopy of molecular autoionization and fragmentation. *Phys. Rev. Lett.*, **64**, 733–736 (1990). 19

[65] Baumert, T., Grosser, M., Thalweiser, R., and Gerber, G. Femtosecond time-resolved molecular multiphoton ionization: The Na_2 system. *Phys. Rev. Lett.*, **67**, 3753–3756 (1991).

[66] Baumert, T., Helbing, J., and Gerber, G. Coherent control with femtosecond laser pulses. In *Adv. Chem. Phys.*, volume 101, pages 47–82. John Wiley & Sons, Inc., Hoboken, NJ, USA (1997). 19

[67] Potter, E. D., Herek, J. L., Pedersen, S., Liu, Q., and Zewail, A. H. Femtosecond laser control of a chemical reaction. *Nature*, **355**, 66–68 (1992). 19

[68] Amstrup, B. and Henriksen, N. E. Control of HOD photodissociation dynamics via bond-selective infrared multiphoton excitation and a femtosecond ultraviolet laser pulse. *J. Chem. Phys.*, **97**, 8285–8295 (1992). 19

[69] Amstrup, B. and Henriksen, N. E. Two-pulse laser control of bond-selective fragmentation. *J. Chem. Phys.*, **105**, 9115–9120 (1996). 19

[70] Elghobashi, N., Krause, P., Manz, J., and Oppel, M. IR+UV laser pulse control of momenta directed to specific products: Quantum model simulations for $HOD^* \rightarrow H+OD$ versus HO+D. *Phys. Chem. Chem. Phys.*, **5**, 4806–4813 (2003). 20, 21

[71] Elghobashi, N. and Gonzalez, L. Breaking the strong and weak bonds of OHF^- using few-cycle IR + UV laser pulses. *Phys. Chem. Chem. Phys.*, **6**, 4071–4073 (2004). 21

[72] Elghobashi, N., Gonzalez, L., and Manz, J. Quantum model simulations of symmetry breaking and control of bond selective dissociation of FHF^- using IR+UV laser pulses. *J. Chem. Phys.*, **120**, 8002–8014 (2004).

[73] Fujimura, Y., González, L., Kröner, D., Manz, J., Mehdaoui, I., and Schmidt, B. Quantum ignition of intramolecular rotation by means of IR + UV laser pulses. *Chem. Phys. Lett.*, **386**, 248–253 (2004). 21, 22, 25

[74] Rozgonyi, T. and González, L. Control of the photodissociation of CH_2BrCl using a few-cycle IR driving laser pulse and a UV control pulse. *Chem. Phys. Lett.*, **459**, 39–43 (2008). 21

[75] Kosloff, R., Rice, S. A., Gaspard, P., Tersigni, S., and Tannor, D. J. Wavepacket dancing: Achieving chemical selectivity by shaping light pulses. *Chem. Phys.*, **139**, 201–220 (1989). 22

[76] Shi, S., Woody, A., and Rabitz, H. Optimal control of selective vibrational excitation in harmonic linear chain molecules. *J. Chem. Phys.*, **88**, 6870–6883 (1988). 22

Dahleh, M., Peirce, A. P., and Rabitz, H. Optimal control of uncertain quantum systems. *Phys. Rev. A*, **42**, 1065–1079 (1990).

Shi, S. and Rabitz, H. Optimal control of bond selectivity in unimolecular reactions. *Comp. Phys. Comm.*, **63**, 71–83 (1991).

[77] Huang, G. M. On the controllability of quantum-mechanical systems. *J. Math. Phys.*, **24**, 2608 (1983). 22

[78] Schirmer, S. G., Fu, H., and Solomon, A. I. Complete controllability of quantum systems. *Phys. Rev. A*, **63**, 063410 (2001).

[79] Ramakrishna, V., Salapaka, M. V., Dahleh, M., Rabitz, H., and Peirce, A. Controllability of molecular systems. *Phys. Rev. A*, **51**, 960 (1995). 22

[80] Werschnik, J. and Gross, E. K. U. Quantum optimal control theory. *J. Phys. B*, **40**, R175–R211 (2007). 22, 65, 66

[81] Zhu, W., Botina, J., and Rabitz, H. Rapidly convergent iteration methods for quantum optimal control of population. *J. Chem. Phys.*, **108**, 1953–1963 (1998). 23, 64, 65, 176

[82] Zhu, W. and Rabitz, H. A rapid monotonically convergent iteration algorithm for quantum optimal control over the expectation value of a positive definite operator. *J. Chem. Phys.*, **109**, 385–391 (1998). 23

[83] Ohtsuki, Y., Zhu, W., and Rabitz, H. Monotonically convergent algorithm for quantum optimal control with dissipation. *J. Chem. Phys.*, **110**, 9825–9832 (1999). 23

[84] Rabitz, H. A., Hsieh, M. M., and Rosenthal, C. M. Quantum optimally controlled transition landscapes. *Science*, **303**, 1998–2001 (2004). 23

[85] Moore, K., Hsieh, M., and Rabitz, H. On the relationship between quantum control landscape structure and optimization complexity. *J. Chem. Phys.*, **128**, 154117 (2008). 23

[86] Judson, R. S. and Rabitz, H. Teaching lasers to control molecules. *Phys. Rev. Lett.*, **68**, 1500–1503 (1992). 24

[87] Goldberg, D. E. *Genetic Algorithms in Search, Optimization, and Machine Learning*. Addison-Wesley Professional, Reading, Mass., USA (1989). 24

[88] Schwefel, H. P. *Evolution and Optimum Seeking*. Wiley VCH, New York, USA (1995). 24

[89] Bardeen, C. J., Yakovlev, V. V., Wilson, K. R., Carpenter, S. D., Weber, P. M., and Warren, W. S. Feedback quantum control of molecular electronic population transfer. *Chemical Physics Letters*, **280**, 151–158 (1997). 24

[90] Assion, A., Baumert, T., Bergt, M., Brixner, T., Kiefer, B., Seyfried, V., Strehle, M., and Gerber, G. Control of chemical reactions by feedback-optimized phase-shaped femtosecond laser pulses. *Science*, **282**, 919–922 (1998). 25

[91] Brixner, T., Damrauer, N. H., Niklaus, P., and Gerber, G. Photoselective adaptive femtosecond quantum control in the liquid phase. *Nature*, **414**, 57–60 (2001). 25

[92] Daniel, C., Full, J., González, L., Kaposta, C., Krenz, M., Lupulescu, C., Manz, J., Minemoto, S., Oppel, M., Rosendo-Francisco, P., Vajda, S., and Wöste, L. Analysis and control of laser induced fragmentation processes in $CpMn(CO)_3$. *Chem. Phys.*, **267**, 247–260 (2001). 25

[93] Daniel, C., Full, J., González, L., Lupulescu, C., Manz, J., Merli, A., Štefan Vajda, and Wöste, L. Deciphering the reaction dynamics underlying optimal control laser fields. *Science*, **299**, 536–539 (2003). 25

[94] Chen, G.-Y., Wang, Z. W., and Hill, W. T. Adaptive control of the CO_2 bending vibration: Deciphering field-system dynamics. *Phys. Rev. A*, **79**, 0114014 (2009). 25

[95] Vogt, G., Krampert, G., Niklaus, P., Nuernberger, P., and Gerber, G. Optimal control of photoisomerization. *Phys. Rev. Lett.*, **94**, 068305 (2005). 25

[96] Dietzek, B., Brüggemann, B., Pascher, T., and Yartsev, A. Mechanisms of molecular response in the optimal control of photoisomerization. *Phys. Rev. Lett.*, **97**, 258301 (2006). 25

[97] Dietzek, B., Brüggemann, B., Pascher, T., and Yartsev, A. Pump-shaped dump optimal control reveals the nuclear reaction pathway of isomerization of a photoexcited cyanine dye. *J. Am. Chem. Soc.*, **129**, 13014–13021 (2007). 25

[98] Vacek, J. and Michl, J. Artificial surface-mounted molecular rotors: Molecular dynamics simulations. *Adv. Func. Mater.*, **17**, 730–739 (2007). 25

[99] Marquetand, P., Gräfe, S., Scheidel, D., and Engel, V. Local control of the quantum dynamics in multiple potential wells. *J. Chem. Phys.*, **124**, 054325 (2006). 25

[100] Hoki, K., Yamaki, M., and Fujimura, Y. Chiral molecular motors driven by a nonhelical laser pulse. *Angew. Chem. Int. Ed.*, **42**, 2976–2978 (2003). 25

[101] Hoki, K., Yamaki, M., Koseki, S., and Fujimura, Y. Molecular motors driven by laser pulses: Role of molecular chirality and photon helicity. *J. Chem. Phys.*, **118**, 497–504 (2003). 25

[102] Hoki, K., Yamaki, M., Koseki, S., and Fujimura, Y. Mechanism of unidirectional motions of chiral molecular motors driven by linearly polarized pulses. *J. Chem. Phys.*, **119**, 12393–12398 (2003). 25

[103] Hoki, K., Sato, M., Yamaki, M., Sahnoun, R., González, L., Koseki, S., and Fujimura, Y. Chiral molecular motors ignited by femtosecond Pump-Dump laser pulses. *J. Phys. Chem. B*, **108**, 4916–4921 (2004). 25

[104] Yamaki, M., Hoki, K., Kono, H., and Fujimura, Y. Quantum control of a chiral molecular motor driven by femtosecond laser pulses: Mechanisms of regular and reverse rotations. *Chem. Phys.*, **347**, 272–278 (2008). 25

[105] McQuarrie, D. A. *Quantum Chemistry*. University Science Books, Sausalito, CA, USA (2007). 27, 29

[106] Herzberg, G. *Molecular Spectra and Molecular Structure I*. Van Nostrand Reinhold Company, New York (1950). 29

[107] Balakrishnan, N., Kalyanaraman, C., and Sathyamurthy, N. Time-dependent quantum mechanical approach to reactive scattering and related processes. *Physics Reports*, **280**, 79–144 (1997). 30, 54

[108] Tannor, D. J. *Introduction to Quantum Mechanics: A Time-Dependent Perspective*. University Science Books, Sausalito, CA., USA (2006). 30, 54

[109] Schmidt, B. WAVEPACKET: F90-version of QMBOUND and QMPROPA (1993-1997). Freie Universität Berlin. 30

[110] Levine, I. N. *Quantum Chemistry*. Prentice Hall (1999). 30, 32, 33, 35

[111] Hehre, W. J., Radom, L., v. R. Schleyer, P., and Pople, J. A. *Ab initio molecular orbital theory*. Wiley, New York, USA (1986).

[112] Jensen, F. *Introduction to Computational Chemistry*. Wiley, Hoboken, NJ, USA (2006). 30, 32

[113] Roothan, C. C. J. New developments in molecular orbital theory. *Rev. Mod. Phys.*, **23**, 69 (1951). 31

[114] Hall, G. G. The molecular orbital theory of chemical valency. VIII. A method of calculating ionization potentials. *Proc. R. Soc. London, Ser. A*, **205**, 541 (1951). 31

[115] Szabo, A. and Ostlund, N. S. *Modern Quantum Chemistry: Introduction to Advanced Electronic Structure Theory*. Dover, New York (1996). 32

[116] Roos, B. O., Taylor, P. R., and Siegbahn, P. E. M. A complete active space SCF method (CASSCF) using a density matrix formulated super-CI approach. *Chem. Phys.*, **48**, 157–173 (1980). 33

[117] Møller, C. and Plesset, M. S. Note on an approximation treatment for many-electron systems. *Phys. Rev.*, **46**, 618–621 (1934). 35

[118] Bartlett, R. J. Many-Body perturbation theory and coupled cluster theory for electron correlation in molecules. *Ann. Rev. Phys. Chem.*, **32**, 359–401 (1981). 35

[119] Andersson, K., Malmqvist, P.-Å., Roos, B. O., Sadlej, A. J., and Wolinski, K. Second-order perturbation theory with a CASSCF reference function. *J. Phys. Chem.*, **94**, 5483–5488 (1990). 35

[120] Andersson, K., Malmqvist, P.-Å., and Roos, B. O. Second-order perturbation theory with a complete active space self-consistent field reference function. *J. Chem. Phys.*, **96**, 1218–1226 (1992). 35

[121] Lund University. *MOLCAS version 7.4 User's Manual* (2004). 35

[122] Finley, J., Malmqvist, P.-Å., Roos, B. O., and Serrano-Andrés, L. The multi-state CASPT2 method. *Chem. Phys. Lett.*, **288**, 299–306 (1998). 36

[123] Hohenberg, P. and Kohn, W. Inhomogeneous electron gas. *Phys. Rev.*, **136**, B864–B874 (1964). 36

[124] Kohn, W. and Sham, L. J. Self-consistent equations including exchange and correlation effects. *Phys. Rev.*, **140**, A1133–A1138 (1965). 37

[125] Becke, A. D. Density-functional thermochemistry. III. The role of exact exchange. *J. Chem. Phys.*, **98**, 5648–5652 (1993). 37

[126] Lee, C., Yang, W., and Parr, R. G. Development of the Colle-Salvetti correlation-energy formula into a functional of the electron density. *Phys. Rev. B*, **37**, 785–789 (1988). 37

[127] Vosko, S., Wilk, L., and Nusair, M. Accurate spin-dependent electron liquid correlation energies for local spin density calculations: a critical analysis. *Can. J. Phys.*, **58**, 1200–1211 (1980). 37

[128] Koch, W. and Holthausen, M. C. *A Chemist's Guide to Density Functional Theory, 2nd Edition*. Wiley-VCH, Weinheim (2001). 37

[129] Stewart, J. J. P. *MOPAC2009*. Stewart Computational Chemistry, Colorado Springs, CO, USA, `http://OpenMOPAC.net` (2009). 41, 183

[130] Schaftenaar, G. and Noordik, J. H. MOLDEN: a pre- and post-processing program for molecular and electronic structures. *J. Comput.-Aided Mol. Design*, **14**, 123–134 (2000). 41, 194

[131] Klok, M., Walko, M., Geertsema, E. M., Ruangsupapichat, N., Kistemaker, J. C. M., Meetsma, A., and Feringa, B. L. New mechanistic insight in the thermal helix inversion of second-generation molecular motors. *Chem. Eur. J.*, **14**, 11183–11193 (2008). xi, 42, 43, 45

[132] Pollard, M. M., Meetsma, A., and Feringa, B. L. A redesign of light-driven rotary molecular motors. *Org. Biomol. Chem.*, **6**, 507–512 (2008). xi, 42, 44, 45

[133] Frisch, M. J., Trucks, G. W., Schlegel, H. B., Scuseria, G. E., Robb, M. A., Cheeseman, J. R., Montgomery, Jr., J. A., Vreven, T., Kudin, K. N., Burant, J. C., Millam, J. M., Iyengar, S. S., Tomasi, J., Barone, V., Mennucci, B., Cossi, M., Scalmani, G., Rega, N., Petersson, G. A., Nakatsuji, H., Hada, M., Ehara, M., Toyota, K., Fukuda, R., Hasegawa, J., Ishida, M., Nakajima, T., Honda, Y., Kitao, O., Nakai, H., Klene, M., Li, X., Knox, J. E., Hratchian, H. P., Cross, J. B., Bakken, V., Adamo, C., Jaramillo, J., Gomperts, R., Stratmann, R. E., Yazyev, O., Austin, A. J., Cammi, R., Pomelli, C., Ochterski, J. W., Ayala, P. Y., Morokuma, K., Voth, G. A., Salvador, P., Dannenberg, J. J., Zakrzewski, V. G., Dapprich, S., Daniels, A. D., Strain, M. C., Farkas, O., Malick, D. K., Rabuck, A. D., Raghavachari, K., Foresman, J. B., Ortiz, J. V., Cui, Q., Baboul, A. G., Clifford, S., Cioslowski, J., Stefanov, B. B., Liu, G., Liashenko, A., Piskorz, P., Komaromi, I., Martin, R. L., Fox, D. J., Keith, T., Al-Laham, M. A., Peng, C. Y., Nanayakkara, A., Challacombe, M., Gill, P. M. W., Johnson, B., Chen, W., Wong, M. W., Gonzalez, C., and Pople, J. A. Gaussian 03, Revision D.01. Gaussian, Inc., Wallingford, CT, 2004. 45

[134] Snyder, P. A. and Clark, L. B. Polarization assignments in the electronic spectra of mono-olefins. *J. Chem. Phys.*, **52**, 998–999 (1970). 46

[135] Allan, M., Snyder, P. A., and Robin, M. B. Electronic excitations in bicyclohexylidene. *J. Phys. Chem.*, **89**, 4900–4903 (1985).

[136] Hoogesteger, F. J., van Lenthe, J. H., and Jenneskens, L. W. Assignment of the two lowest valence transitions of 1,1'-bicyclohexylidene: An ab initio MRD-CI investigation. *Chem. Phys. Lett.*, **259**, 178–184 (1996). 46

[137] Havenith, R. W. A., van Lenthe, J. H., Jenneskens, L. W., and Hoogesteger, F. J. The lowest valence transitions of 1,1'-bicyclohexylidene and 1,1';4',1'-tercyclohexylidene. An ab initio MRDCI study. *Chem. Phys.*, **225**, 139–152 (1997).

[138] Havenith, R. W. A., Jenneskens, L. W., and van Lenthe, J. H. The effect of *syn-anti* isomerism on the lowest valence transitions of 1,1'-bicyclohexylidene. an ab initio MRDCI investigation. *Chem. Phys. Lett.*, **282**, 39–48 (1998).

[139] Havenith, R. W. A., van Dam, H. J. J., van Lenthe, J. H., and Jenneskens, L. W. The excitation energies of 1,1'-bicyclohexylidene and 1,1':4',1"-tercyclohexylidene: A comparison of multi-reference configuration interaction and perturbation theory approaches. *Chem. Phys.*, **246**, 49–56 (1999). 46

[140] Rijkenberg, R. A., Buma, W. J., van Walree, C. A., and Jenneskens, L. W. Isolated building blocks of photonic materials: High-resolution excited-state photoelectron spectroscopy of jet-cooled tetramethylethylene and 1,1'-bicyclohexylidene. *J. Phys. Chem. A*, **106**, 5249–5262 (2002). 46

[141] Rijkenberg, R. A., Buma, W. J., van Lenthe, J. H., Jenneskens, L. W., and Schmal, L. P. Rydberg-valence interactions in monoolefins: Dispersing electronic properties in 1,1'-bicyclohexylidene. *ChemPhysChem*, **4**, 97–101 (2003). 46, 47

[142] Karlström, G., Lindh, R., Malmqvist, P.-Å., Roos, B. O., Ryde, U., Veryazov, V., Widmark, P.-O., Cossi, M., Schimmelpfennig, B., Neogrady, P., and Seijo, L. MOLCAS: a program package for computational chemistry. *Comp. Mater. Sci.*, **28**, 222–239 (2003). 47

[143] Veryazov, V., Widmark, P.-O., Serrano-Andrés, L., Lindh, R., and Roos, B. O. 2MOLCAS as a development platform for quantum chemistry software. *Int. J. Quant. Chem.*, **100**, 626–635 (2004). 47

[144] Almlöf, J. and Taylor, P. R. General contraction of gaussian basis sets. I. Atomic natural orbitals for first- and second-row atoms. *J. Chem. Phys.*, **86**, 4070–4077 (1987). 47

[145] Anderson, E., Bai, Z., Bischof, C., Blackford, S., Demmel, J., Dongarra, J., Du Croz, J., Greenbaum, A., Hammarling, S., McKenney, A., and Sorensen, D. *LAPACK Users' Guide*. Society for Industrial and Applied Mathematics, Philadelphia, PA, USA (1999). 55, 153

[146] Press, W. H., Teukolsky, S. A., Vetterling, W. T., and Flannery, B. P. *Numerical Recipes in Fortran 90, Vol. 2*. Cambridge University Press (1996). 55, 153

[147] I. N. Bronshtein and K. A. Semendyayev. *Handbook of mathematics*. Springer, Heidelberg (1998). 56

[148] Atkins, P. and Friedman, R. *Molecular Quantum Mechanics*. Oxford University Press, USA (2005). 56

[149] Feit, M., Jr., J. F., and Steiger, A. Solution of the Schrödinger equation by a spectral method. *J. Comput. Phys.*, **47**, 412–433 (1982). 58, 60
Feit, M. D. and Fleck, J. A. Solution of the Schrödinger equation by a spectral method II: vibrational energy levels of triatomic molecules. *J. Chem. Phys.*, **78**, 301–308 (1983).

[150] Levine, B. G. and Martínez, T. J. Isomerization through conical intersections. *Ann. Rev. Phys. Chem.*, **58**, 613–634 (2007). 117, 118

name	Guillermo Pérez Hernández
birth	7.7.1982 in Santa Cruz de Tenerife, Tenerife, Spain
work address	Friedrich-Schiller-Universität Jena
	Institut für Physikalische Chemie
	Helmholtzweg 4, 07743 Jena
email	guille.perez@uni-jena.de
web	www.theochem.uni-jena.de/guille.perez

degrees

2005	Chemistry, Span. *Licenciado en Ciencias Químicas* (Ger. *Diplom*)
	Universidad de la Laguna, Tenerife, Spain
2006	Certificate of Teacher's Competence, Universidad Complutense, Madrid
2000	*Selectividad* (Spanish university entrance degree)
	Abitur (German university entrance degree)

education

2004 - 2005	Freie Universität Berlin and Technische Universität Berlin
2000 - 2004	Universidad de La Laguna
1987 - 2000	School and high school at the *Deutsche Schule* (German school), Tenerife

scientific experience

2007 - 2010	Doctoral research in the group of Prof. Dr. L. González, FSU
2005 - 2007	Pre-doctoral and doctoral research in the group of PD. Dr. L. González, FUB

scholarships and contracts

2010	Short-term scholarship of the Graduate Academy of the FSU
2007 - 2009	Scientific coworker (Ger. *Wiss. Mit.*) of the FSU, funded by the DFG
2006 - 2007	Scientific coworker (Ger. *Wiss. Mit.*) of the FUB, funded by the DFG
2006	Fellowship of the Research Training School GK#788 at FUB
2005	Short-term scholarship of the GK#788 at FUB
2005	Doctoral-grant (Span. *FPU*), funded by the Spanish Department for Science and Education (declined)
2004 - 2005	*Erasmus* scholarship, funded by the EU
	Mobility Aid scholarship, funded by the Canary Islands Government

stages in external groups

2009	Prof. T. Seideman, Northwestern University, USA (2 months)
2008	Prof. T. Seideman, Northwestern University, USA (2 months)
2007	Prof. L. Serrano-Andrés, Universidad de Valencia, Spain (10 days)
2006	Prof. T. Seideman, Northwestern University, USA (1 month)

teaching experience

FSU	Supervision of three diploma-thesis (C. von Eiff, 2010, Dipl. Chem. M. Aßmann, 2009, and Dipl. Chem. S. Kupfer, 2009)
	Supervision of two research practica (ger. *Forschungspraktikum*)
	Exercises of Physical Chemistry (8^{th} semester), Quantum Chemistry (8^{th} semester), and Fortran90 (7^{th} semester)
FUB	Exercises of Physical Chemistry (6^{th} semester)

language skills

Spanish	Mother tongue
German	C1 European Language Level (ELL). *Abitur* equivalent
English	C1 (self-assesed). Advanced degree (B2) certified
Italian	Fluent

IT skills

scientific	FORTRAN90 (programing skills), quantum chemistry suites (Gaussian03, MOLCAS, TUROBOMOLE, MOLPRO, MOPAC), molecular and scientific visualization software, LaTeX
general	Office suites, Windows and UNIX/Linux based OSs

attended conferences

2009	*Concepts and Methods in Quantum Control*, Santa Barbara, USA
	One-day Symposium Molecular Dynamics and Control, London, UK
	Summer School *Coherent Control of Molecules*, London, UK
2008	*American Conference on Theoretical Chemistry*, Evanston, USA
	Gordon Research Conference *Atomic & Molecular Interactions*, New London, USA
2007	XVII International Conference *Horizons in Hydrogen Bond* & Graduate Student Research School on Hydrogen Bonding, St. Petersburg, Russia
	XXIII *International Conference on Photochemistry* ICP2007, Köln, Germany
2006	Triple Symposium GK#894/1-GK#788-GK#782, Freyburg (Unstrut), Germany
	Summer School *Modern Developments in Spectroscopy*, Noordwijk, The Netherlands
2005	1st. Student Congress of Chemistry, La Laguna, Spain

8. Assmann, M., Sanz-Sanz, C., Pérez-Hernández, G., Worth, G. A., and González, L. Excited state dynamics of a model asymmetric molecular rotor: a five-dimensional study on 2-cyclopentylidene-tetrahydrofuran. *Chem. Phys.*, (2010). DOI 10.1016/j.chemphys.2010.08.019.

7. Pérez-Hernández, G., Pelzer, A., González, L., and Seideman, T. Biologically inspired molecular machines driven by light. optimal control of a unidirectional rotor. *New. J. Phys.*, **12**, 075007 (2010). DOI 10.1088/1367-2630/12/7/075007.

6. Pérez-Hernández, G. and González, L. Mechanistic insight into light-driven molecular rotors: a conformational search in chiral overcrowded alkenes by a pseudo-random approach. *Phys. Chem. Chem. Phys.*, **12**, 12279–12289 (2010). DOI 10.1039/c0cp00324g.

5. Assmann, M., Pérez-Hernández, G., and González, L. On the Light-Driven isomerization of a model asymmetric molecular rotor: Conformations and conical intersections of 2-Cyclopentylidene-tetrahydrofuran. *J. Phys. Chem. A*, **114**, 9342–9348 (2010). DOI 10.1021/jp104898t.

4. Matute, R. A., Contreras, R., Pérez-Hernández, G., and González, L. The chromophore structure of the cyanobacterial phytochrome Cph1 as predicted by Time-Dependent density functional theory. *J. Phys. Chem. B*, **112**, 16253–16256 (2008). DOI 10.1021/jp807471e.

3. Barth, I., Manz, J., Pérez-Hernández, G., and Sebald, P. Towards toroidal hydrogen bonds. *Z. Phys. Chem.*, **222**, 1311–1331 (2008). DOI 10.1524/zpch.2008.5390.

2. Pérez-Hernández, G., González, L., and Serrano-Andrés, L. Rydberg or valence? the long-standing question in the UV absorption spectrum of 1,1prime-Bicyclohexylidene. *ChemPhysChem*, **9**, 2544–2549 (2008). DOI 10.1002/cphc.200800454.

1. González, L., Rozgonyi, T., Ambrosek, D., and Pérez-Hernández, G. Laser control of wavepacket photodissociation and photoisomerization dynamics in isolated molecules. *AIP Conf. Proc.*, **963**, 576–585 (2007). DOI 10.1063/1.2827044.

Acknowledgments

Jena, September 2010

There is a human aspect to every scientific work. Science has had its share in the previous pages. I want to devote the following paragraphs to thank the people who played a role in this Thesis. Without their support, scientific, personal, or whatsoever, this work simply would not exist.

I want to start by giving credit to my family, because this Thesis is theirs as it is mine. I am most grateful to both of my parents, **María Rosa** and **Julio**. By now, they also know better than anyone else what it really means to do a doctoral thesis. I hereby pronounce them *Doctora et Doctor honoris causa* on account of their endurance during these years. I cannot start to imagine what it would have been like without them: their patience and support, whether from Tenerife or during their visits, made me stay focused. The hard last lap would just not have happened without them. Thanks for the roots and thanks for the wings.[1]

Where do I start to thank my sister, **Natalia** (**Dr. Pérez-Hernández**), with whom I have always shared good *and* bad times? To be fair, she has gotten to hear more about the bad ones, these last times. Her support, scientific, personal, and of all kinds, together with her understanding, was crucial whenever important decisions had to be made. I accept my role as a young brother gladly, because having an older sister like mine is a privilege. It is with her that toasts are made every the same battles are won, but most importantly, when they are lost. *Brindo por las veces que perdimos las mismas batallas.*[2]

Anna, what can I say? My life is better with you by my side. Your comfort and presence simply makes everything easier. Part of what I am I owe to you, because *I got you under my skin.*[3]

Now to my scientific family. How can I thank **Prof. Dr. Leticia González**? It has been a long way since I knocked on her door in Berlin, as a last-year Erasmus-student keen on quantum chemistry, and greeted the fellow Spaniard, soon-to-be *Privatdozentin* Leti. I thank her for trusting me from the very beginning, when she very soon provided me with the means and the *know-how* to enter the world of scientific research. We have spent many hours together, and it is through her eyes that I approached *ab-initio* quantum chemistry: first as my teacher at FUB, then as my scientific advisor. She was generous and patient whenever the occasion called for it, a situation not uncommon when doing one's PhD.

[1] *Two things shall children receive from their parents: roots and wings.* J. W. von Goethe
[2] Jorge Drexler
[3] Cole Porter by Frank Sinatra

Surely, there's been a lot of changes along the way, but to some extent we are still that student and that teacher.

Once in Jena, the **AG González** created a unique working atmosphere, with an excellent group of people from whom it was a pleasure to learn. Among them, I want to single out first of all **Dr. Jesús González-Vázquez** as a fundamental influence on me. Having my desk next to his for two years is one of the luckiest things that happened when moving from Berlin to Jena. If one is able to keep up with his fast-paced train of thought, 30 minutes of vivid discussion are worthier than whole semesters of lectures. Very useful, physicochemical images in my mind originate from conversations with him. Also, my programing skills are, to some extent, shaped by **Jesus**' love and fascination for computers and by one's ability to get them to do what we want (in most cases).

I had the chance to sit with **PD Dr. Burkhard Schmidt** (FU Berlin) for long hours in the early days in Berlin, and his program WAVEPACKET has been a useful reference throughout the years whenever my own codes stubbornly refused to work. In these matters, I am also grateful to **Dr. Holger Naundorf** (*system admin* in Berlin) and **Dr. Dirk Bender** (Jena) for readily assisting me when the IT-difficulties were beyond my reach.

Special credit deserves also **Dr. Inés Corral**, from whom I also learned quantum chemistry in the early days in Berlin. Because of that, I always consider **Inés** as a reference if a challenging electronic structure question arises. Fellow PhD-student **Daniel Escudero** has shared the office with me for the last three years, among others. Apart from being a friend, from him I have learned how important it is to remain practical and not spend so much time in the scientific conundrums that usually take me hours to figure out. Very often I catch myself thinking: *What would* **Dani** *do?* Fellow office-mates and PhD-students **Daniel Kinzel** and **Hartmut Preuß** have also been supportive all these years, and I always enjoyed having scientific, political, and linguistic discussions with them. Once I leave, who will keep asking these guys the article preceding a given German word? A similar thing applies to **Dr. Julien Guthmuller** and my broken use of the French language. **Dr. Marta Łabuda** is deeply thanked for something as important as her sense of humor and warmth. I am glad she was there to make the working atmosphere a nicer one. Fellow student and hopefully soon-to-be Dr. **Verónica Leyva** also contributes significantly to a nice AG González. First in Berlin, now in Jena, the coffee-break is worth it because she comes along (not because of the coffee itself, that everyone agrees upon). I have had the opportunity to tutor the diploma-theses of **Mariana Aßman**, **Stephan Kupfer** (both now in the AG), and currently of **Caroline von Eiff**, who is surely relieved, now that I again have time for her questions. I do not know if they notice, but I also learn a lot by spending time with them, and for that they are thanked. As visiting students in our office, **Cristian Buendía**, **André Santos**, **Dr. Diniz Sena** and **Dr. Ricardo Matute** provided their share of good vibrations to the working atmosphere, and that I thank them so much.

Special mention deserves also **Dr. Philipp Marquetand**, who has managed to cheer me up in more occasions than anyone else in the few months since his arrival. He has given me great advice, both on scientific and personal matters, but most importantly when both of these two matters are actually the same thing. On top of that, **Philipp** has been kind enough to proof-read this manuscript, even at late night, so *merci, mon ami* so much.

Melanie Grigsby is also acknowledged for linguistic corrections in parts of the manuscript.

This project has given me possibility to spend several months with our collaboration partners from Northwestern University in Chicago: **Prof. Tamar Seideman**, **Dr. Ramakrishna Sesha Shankar**, and **Dr. Adam Pelzer**. Working with them in Evanston was excellent, both scientific and personally.

Also, **Prof. Luis Serrano-Andrés**, from the Instituto de Ciencia Molecular in Valencia, is gratefully acknowledged. What started as a shy email inquiry on the MOLCAS program ended up as a publication I am very proud of. In person, *via* email or through the pages of the MOLCAS manual, his remarks on electronic structure are always enlightening. [*Prof. Luis Serrano-Andrés passed away unexpectedly on September, 15. The previous words are left as written prior to his death. He will always be present to those who knew him.*]

I am lucky to be close friends with **Dr. Peter Tolstoy** and **Dr. Ingo Barth**, both physicists and outstanding scientists. I got to know **Peter** in the very early Berlin times. He has always shown a genuine interest in whatever science crossed his way, and I have exploited that fact to learn much about physics in general. His approach is unique, often provocative and humorous, and our discussions are happily settled after a couple of beers (or vodkas). As for **Ingo**, with whom I got to share the office in Berlin, I asked questions about Hamilton operators, kinetic couplings and laser pulses, and not only did **Ingo** offer answers, but friendship and family as well.

Before I close the Berlin chapter, I also want to acknowledge **Prof. Dr. Jörn Manz** and **Prof. Dr. Hans-Heinrich Limbach** for their support in the early, uncertain stages of the PhD, specially through the *Graduiertenkolleg* #788.

Back in Jena, I want to thank my friends of the now legendary **Spanisch Stammtisch**. People come and go, but the backbone of that *Stammtisch* (**Catha**, **Jutta**, **Dani**, **Valentina**, **Raúl**, **Bea**, **Emilio**, **Eliseo**, **Katrin**, **Sergio**, **Alejandro**, **Fernando**, **Ana**...) was always a fun, solid community that I was lucky to be a part of. Thank you so much guys.

I close with the city that started it all. **Berlin**, and the **friends** that I made in my **Eramus** (**Javi**, **Dani**, **Ale**, **Marga**, **Laura**, **Patri**...). That city and that people enriched my life, and have a great deal to do with my decision of staying in Germany. Thank you.

Agradecimientos

Cualquier trabajo científico se genera en unas circunstancias humanas concretas. Sobre la ciencia ya se ha hablado en las páginas anteriores. Quiero dedicarle los párrafos siguientes a todas las personas sin cuyo apoyo (científico, personal o de cualquier otro tipo), esta tesis sencillamente no existiría.

Empiezo dándole las gracias mi familia: esta tesis es tan suya como mía. Le doy las gracias a mis padres **María Rosa** y **Julio**, que, llegados a este punto, ya saben de memoria el tipo de esfuerzo que requiere una tesis doctoral. Por la presente les otorgo el título de *Doctora et Doctor honoris causa* por la resistancia admirable que han demostrado tener durante estos años. No quiero ni pensar en cómo hubiera sido todo esto sin su apoyo y su paciencia. Me alentaron y consiguieron mantenerme centrado, especialmente en una complicada recta final. Gracias por las alas y gracias por las raíces.[4]

No sabría por dónde empezar a darle las gracias a mi hermana **Natalia** (**Dra. Pérez-Hernández**), con quien siempre comparto buenos y malos tiempos. Para ser justos, he compartido más los malos, sobretodo en ésta última etapa. Su apoyo tanto personal como científco, y su complicidad han sido imprescindibles cuando ha habido que tomar decisiones importantes. Para mí es un placer poder ejercer de atolondrado hermano menor, porque tener una hermana mayor como la mía es un privilegio. *Brindo por las veces que perdimos las mismas batallas.*[5]

¿**Anna**, qué puedo decir? Mi vida mejora si tú estás a mi lado. Todo se vuelve más fácil con tu presencia y tu aliento. Parte de lo que soy te lo debo a tí, porque *I got you under my skin.*[6]

Ahora, mi familia científica. ¿Cómo agradecerle a la profesora **Dª Leticia González**? Cuando toqué en la puerta de su despacho de Berlín, como estudiante Erasmus acabando la carrera, y saludé a Leti -una compatriota acabando su habilitación- no pensé que fuera para recorrer tanto camino. Desde el primer momento, me dio su confianza y me acogió en su grupo, poniendo a mi disposición sus medios y su experiencia para introducirme en la investigación científica. Hemos pasado muchas horas juntos, y empecé a ver la química quántica *ab-initio* a través de sus ojos: primero como mi profesora en la FU, después como mi directora de tesis. Ha sabido ser paciente y generosa cuando la ocasión lo requería, y en cualquier doctorado, la ocasión lo requiere de vez en cuando. Incluso con todo este camino recorrido, creo que todavía somos un poco aquel estudiante y aquella profesora.

[4] *Dos cosas deberán recibir los hijos de sus padres: raíces y alas.* J. W. von Goethe
[5] Jorge Drexler
[6] Cole Porter por Frank Sinatra

Una vez en Jena, la **AG González** se convirtió en un grupo espléndido de trabajo, con gente excelente de la que aprender. De todo ellos, el **Dr. Jesús González-Vázquez** merece un lugar especial en estos agradecimientos. Su influencia en mí ha sido fundamental. Que mi mesa y la suya estuvieran al lado durante dos años es lo mejor que pudo pasar al mudarme desdeberlinajena. Si uno es capaz se seguirle el ritmo, en media hora con **Suso** se puede aprender más que en un semestre de clases. Parte de mi cabeza científica está amueblada con muebles de **Jesús**. Sucede lo mismo a la hora de ponerme a programar, donde **Jesús** me transmitió su amor por los programas, que hacen *lo que nosotros les decimos que hagan*, aunque a veces no se lo consigamos decir con la claridad suficiente.

En materia de programación, también quiero nombrar al **PD Dr. Burkhard Schmidt** (FU Berlin) ya que siempre tuvo tiempo para mí en Berlín, y porque sus códigos del programa WAVEPACKET me mostraban el camino cuando mis propios códigos flaqueaban. Para las visicitudes informáticas de mayor envergadura, los Drs. **Holger Naundorf** (responsable de sistemas en Berlín) y **Dirk Bender** (Jena) siempre supieron lo que había que hacer en cada momento.

A la **Dra. Inés Corral** también le tocó enseñarme mucha química cuántica al principio, en Berlín. Por ello es mi persona de referencia para cuestiones avanzadas de estructura electrónica. Con mi compañero **Daniel Escudero** he compartido oficina los últimos tres años. Aparte de ser un amigo, de él he aprendido a ser práctico y no irme por las ramas en los *puzzles* científicos en los que a veces me entretengo. Muy a menudo, me sorprendo a mí mismo pensando *¿Qué haría* **Dani***?*. Mis otros compañeros de oficina, **Daniel Kinzel** y **Hartmut Preuß** también han sido de ayuda estos años. Ha sido un placer discutir con ellos sobre ciencia, política, o idiomas. Si yo me voy, quién les preguntará el artículo de tal o cual palabra en alemán? Lo mismo es válido para el **Dr. Julien Guthmuller**, que hacía lo que podía con mi francés de bachillerato. A la **Dra. Marta Łabuda** le agradezco profundamente algo tan importante como su sentido del humor y su calidez. Es una suerte haberla tenido cerca para alegrar la vida del grupo. Mi compañera (y, ojalá dentro de poco, doctora) **Verónica Leyva** también hace que el trabajo en el grupo sea más agradable. Tanto en Berlín como en Jena, los cafés de media tarde valen la pena por su compañía (no porque el café sea tentador, eso seguro). He tenido la oportunidad de supervisar las tesis de fin de carrera de **Mariana Aßmann**, **Stephan Kupfer** (ahora miembros del grupo) y actualmente de **Caroline von Eiff**, quien seguro se alegrará de que vuelva a tener tiempo para sus preguntas. No sé si ellos se dan cuenta, pero ayudándoles también aprendo muchísimo, cosa que les agradezco. Los estudiantes visitantes **Cristian Buendía**, **André Santos**, y los doctores **Diniz Sena** y **Ricardo Matute** también aportaron sus buenas vibraciones al ambiente de la oficina.

Quiero darle las gracias especialmente al **Dr. Philipp Marquetand**, que, desde su llegada al grupo hace pocos meses, se ha convertido rápidamente en un tipo junto al que merece la pena estar. Ha sabido aconsejarme tanto en asuntos científicos como personales, aunque más importantes han sido los consejos cuando lo uno y lo otro eran el mismo asunto. Por si fuera poco, se tomó la molestia de corregirme y aconsejarme en la preparación de este manuscrito, aunque fuera hasta altas horas de la noche. Por ello le vuelvo a decir de nuevo, *merci, mon ami*!

Le agradezco también a **Melanie Grigsby** sus correcciones lingüísticas en parte de este manuscrito.

Este proyecto me ha dado la oportunindad única de trabajar con la profesora **Dª Tamar Seideman** y su grupo en la Northwestern University en Chicago. Le agradezco a ella y a los Drs. **Ramakrishna Sesha Shankar** y **Adam Pelzer** el haberme acogido y haber hecho de mi estancia allí una experiencia inolvidable.

Asímismo, le agradezco mucho al profesor **D. Luis Serrano-Andrés**, del Instituto de Ciencia Molecular de Valencia, su interés en mi proyecto. Lo que empezó timidamente como una consulta sobre el programa MOLCAS por correo electrónico acabó en una publicación de la que me siento muy orgulloso. En persona, por correo electrónico o a través de las páginas del manual de MOLCAS, sus ideas siempre resultan esclarecedoras. [*El profesor D. Luis Serrano-Andrés falleció inesperadamente el 15 de Septiembre, estando ya escritas las lineas anteriores. Siempre estará presente para los que tuvimos la suerte de conocerle.*]

Poder contar con los Drs. **Peter Tolstoy** e **Ingo Barth** entre mis amigos (ambos de la época de Berlín), es una suerte. Los dos son físicos, los dos son excelentes científicos. Conocí a **Peter** desde mis primeros días en Berlín. Siempre ha demostrado un interés genuino por cualquier tipo de ciencia que se cruce en su camino, algo de lo que yo me he aprovechado para aprender bastante física. Su aproximación a cualquier problema científico es única, provocativa a veces, y siempre con sentido del humor, lo que da lugar a discusiones que se resuelven felizmente después de algunas cervezas (o vodkas). Cuando a **Ingo** su nuevo compañero de oficina lo ametralló con preguntas sobre operadores Hamiltonianos, acomplamientos cinéticos y láseres, **Ingo** no sólo ofreció respuestas, sino también amistad y familia.

Antes de cerrar el párrafo berlinés, quiero agradecerle a los profesores **D. Jörn Manz** y **D. Hans-Heinrich Limbach** su apoyo en las primeras fases inciertas del doctorado, especialmente a través del colegio de graduados GK#788.

De vuelta en Jena, toca agradecer a mis amigos de la ya legendaria **Stammtisch Española** su amistad. Entre los muchos visitantes, el núcleo duro de la *Stammtisch* (**Catha**, **Dani**, **Jutta**, **Valentina**, **Raúl**, **Bea**, **Emilio**, **Eliseo**, **Katrin**, **Alejandro**, **Sergio**, **Fernando**, **Ana**...) es un grupo divertido y sólido del que pude formar parte. Chicos, muchas gracias.

Me despido con la ciudad que lo empezó todo. **Berlín** y mi gente de la época **Erasmus** (**Javi**, **Dani**, **Ale**, **Marga**, **Laura**, **Patri**...). Esa ciudad y esas personas cambiaron mi vida, y tienen mucho que ver con mi decisión de quedarme en Alemania. Gracias.

Selbständigkeitserklärung:

Ich erkläre, dass ich die vorliegende Arbeit selbständig und unter Verwendung der angegebenen Hilfsmittel, persönlichen Mitteilungen und Quellen angefertigt habe.

Jena, den .....

Guillermo Pérez Hernández

Appendix: Programs

- `mydiag.f90`

  This program diagonalizes a number `npot` of potential energy surfaces defined as arrays over a number `npoints` of equally spaced points, with `mass` and the potential energy array (from file) as inputs. The user can switch between the subroutines `tred2`+`tql2`[146] or `zheevd`[145] for matrix diagonalization. Particle-in-a-ring functions are used to construct the system's Hamiltonian, yielding the evaluation of the kinetic energy term trivial (cf. l. `257`). A switch to a *toy-model* harmonic potential is built within the code (cf. line `106`) for debugging and general checking. Two additional switches are provided for `verbose` and `veryverbose` printing levels. Other internal subroutines are included within the program: `doheadpsi` provides the wavefunction files with headers and `doheader` provides the standard output header.

```
 1  program mydiag !This program should diagonalize in the basis of
 2                 !linear combinations of
 3                 !the particle in a ring (free-rotor in the plane)
 4
 5  !INPUT in the main program are mass,gridpoints
 6
 7  !INPUT from s.i.
 8  !nb              basis functions. total nr. will be 2*nb+1
 9  !npot            potential to be diagonalized
10  !npoints         number of points
11  !harm            logical. For switching to a toy harmonic potential
12  !verbose         verbose ouput, for debugging and checking
13  !veryverbose     even more stuff on output, take your time...
14  !rut             character*6. Can be 'NR_F90' or 'LAPACK' to switch between d
    iag routines
15  !mass            mass in a.u.
16
17  !INPUT from files
18  !i3.3_i3.3.poten potential file, with i=npot
19
20  !OUTPUT to  files
21  !E_i3.3.dat              File with eigenenergies
22  !EIGEN/i6.6_j3.3.psi            Files with eigenfunctions, (i=wf index,j=pot
     index)
23
24  implicit none
25
26
27  INteger, Parameter :: DP= Kind(1.0D0)
28
29  integer i,j,k
30  integer error
31  integer points
32  integer nb
33  integer npot
34
35  real(KIND=DP) :: theta(:),x(:),thres
36  allocatable theta,x
37  real(KIND=DP) :: arg(:)
38  allocatable   arg
39  real(KIND=DP) :: pot(:)
40  allocatable pot
41  complex(KIND=DP) fi(:,:),fi2(:,:),faux(:)
42  allocatable fi,fi2,faux
43
44  complex(KIND=DP) integrand(:)
45  allocatable integrand
46  complex(KIND=DP) integral
47
48  logical harm
49  real(KIND=DP) :: kharm
50  real(KIND=DP) :: nu
51  real(KIND=DP) :: V0
52  real(KIND=DP) :: Eharm(:)
53  allocatable Eharm
54
55  complex(Kind=DP),parameter :: Im=dcmplx(0.d0,1.d0)
56  real(KIND=DP),parameter :: pi=dacos(-1.d0)
57  real(KIND=DP) :: mass
58  real(KIND=DP) :: high,low
59  real(KIND=DP) :: dtheta
60  real(KIND=DP) :: dummyreal
61
62  complex(Kind=DP) :: T(:,:),V(:,:),H(:,:)
63  real(KIND=DP) :: REH(:,:),REEVEC(:,:),REEVAL(:),REEVAL2(:),REEVEC2(:,:)
64  allocatable REH,REEVEC,REEVAL,REEVAL2,REEVEC2
65  complex(Kind=DP) EVEC(:,:)
66  real(KIND=DP) :: EVAL(:)
67  allocatable EVEC,EVAL
68  allocatable T,V,H
69
70  complex(Kind=DP) EIGEN(:,:),VC(:)
71  allocatable EIGEN,VC
72
73  character*21 fname
```

```
 74  character*21 filein
 75  logical verbose
 76  logical veryverbose
 77  character*6 rut
 78  !For jgv's
 79  real(KIND=DP),allocatable :: realH(:,:),imH(:,:),realE(:,:),imE(:,:),realEIG
     (:)
 80  real(kind=DP),allocatable :: fv1(:),fv2(:),fm1(:,:)
 81  !################################
 82
 83  !mass=1.218790D+06
 84
 85  !Definitions
 86  !nb=100
 87  !harm=.false.
 88  !verbose=.false.
 89  !verbose=.true.
 90  !veryverbose=.false.
 91  !veryverbose=.true.
 92
 93  !Input
 94  read(*,*) nb
 95  read (*,*) npot
 96  read (*,*) points
 97  read (*,*) harm
 98  read (*,*) verbose
 99  read (*,*) veryverbose
100  read (*,*) rut
101  read (*,*) mass
102  !##################
103
104
105  !Switch for harmonic oscillator
106  if (harm) mass=1.d0
107  kharm=1.d0
108  nu=sqrt(kharm/mass)
109  V0=4.d0
110  !################################
111
112
113  write(filein,'(i3.3,a1,i3.3,a6)') npot,'_',npot,'.poten'
114  allocate (fi(-nb:nb,1:points),fi2(-nb:nb,1:points),faux(1:points))
115  allocate (theta(1:points),pot(1:points),x(1:points))
116  allocate (arg(1:points))
117  allocate (T(-nb:nb,-nb:nb),V(-nb:nb,-nb:nb),H(-nb:nb,-nb:nb))
118  allocate (EVEC(-nb:nb,-nb:nb),EVAL(-nb:nb))
119  allocate (REEVEC(-nb:nb,-nb:nb),REEVAL(-nb:nb),REEVAL2(-nb:nb),REH(-nb:nb,-n
     b:nb),REEVEC2(-nb:nb,-nb:nb))
120  allocate (Eharm(-nb:nb))
121  allocate (integrand(1:points))
122  allocate (EIGEN(-nb:nb,1:points),VC(-nb:nb))
123  !For jgv's
124  allocate (realH(1:2*nb+1,1:2*nb+1),imH(1:2*nb+1,1:2*nb+1))
125  allocate (realE(1:2*nb+1,1:2*nb+1),imE(1:2*nb+1,1:2*nb+1))
126  allocate (realEIG(1:2*nb+1))
127  allocate (fv1(1:2*nb+1),fv2(1:2*nb+1),fm1(2,1:2*nb+1))
128
129
130  open(unit=51,file=filein,status='old')
131  read(51,*) (theta(i),pot(i),i=1,points)
132  close(51)
133  low=theta(1)
134  high=theta(points)
135  dtheta=(high-low)/(points-1)
136
137
138  !Optional
139  if (verbose) then
140     write(*,*) '# Following space array has been created'
141     write(*,'(i4.4,E20.10E3)') (i,theta(i),i=1,points)
142     write(*,*) '# End space array'
143  endif
144
145  !Write stuff on output
146  call doheader (mass,high,low,points,harm,nb,nu,kharm)
```

```
147  write(*,'(x,a25,x,a21)') 'Potential read from file:',filein
148  write(*,'(x,a25,x,a21)') 'Using routine           :',rut
149
150  !Create harmonic potential
151  if (harm) then
152     do i=1,points
153        pot(i)=V0+.5d0*kharm*((.5*pi-theta(i))**2)
154     enddo
155     do i=-nb,nb
156        Eharm(i)=(.5+(i+nb))*nu
157     enddo
158     write(*,*) 'Harmonic function has overwritten read potential'
159  endif
160
161  !call integratec(dcmplx(pot(:),0.d0),1,points,integral)
162  !write(*,*) integral
163  !pot(:)=pot(:)-real(integral)/(2.d0*pi)*dtheta
164  !call integratec(dcmplx(pot(:),0.d0),1,points,integral)
165  !write(*,*) integral
166
167  if (verbose) then
168     write(*,*) '# Following potential will be used'
169     write(*,'(2(E20.10E3,x))') (theta(i),pot(i),i=1,points)
170     write(*,*) '# End potential'
171  endif
172
173  !Create basis functions fi2 (primary)
174  !of the particle in the ring functions
175  do i=-nb,nb
176     do j=1,points
177         fi2(i,j)=cdexp(Im*real(i)*theta(j))
178         !fi2(i,j)=dcmplx(dcos(real(i)*theta(j)),dsin(real(i)*theta(j)))
179     enddo
180     fi2(i,:)=fi2(i,:)/dsqrt(2.d0*pi)
181     fi(i,:)=fi2(i,:)
182     if (dabs(cdabs(fi(i,1))-cdabs(fi(i,points))).gt.1.d-6) then
183        write(*,*) "basis functions not periodic",cdabs(fi(i,1))-cdabs(fi(i,po
     ints)),i
184        write(*,*) fi(i,1),fi(i,points)
185     endif
186  enddo
187  !Create basis functions as linear combinations
188  !sum and difference of primary basis. (sum=cos,dif=sin)
189  !Goal is to keep everything real
190  if (.true.) then
191     do i=-nb,-1
192        fi(i,:)=fi2(+i,:)+fi2(-i,:)
193        fi(i,:)=fi(i,:)/dsqrt(2.d0)
194     enddo
195     fi(0,:)=dcmplx(1.d0,0.d0)
196     fi(0,:)=fi(0,:)/dsqrt(2.d0*pi)
197     do i=1,nb
198        fi(i,:)=fi2(+i,:)-fi2(-i,:)
199        fi(i,:)=fi(i,:)/dsqrt(2.d0)
200        fi(i,:)=fi(i,:)*Im
201     enddo
202  endif
203
204  !Write stuff on ouput
205  write(*,*) 'Basis functions created and stored'
206
207  !Check wfs of base:orthonormal
208  if (verbose) then
209     write(*,*) '# Check orthonormal basis'
210     do i=-nb,nb
211        integral=0.d0
212        do j=-nb,nb
213           integrand(:)=dconjg(fi(j,:))*fi(i,:)
214           call integratec(integrand,1,points,integral)
215           write(*,100) i,j,integral*dtheta,cdabs(integral)*dtheta
216        enddo
217     write(*,*)
218     enddo
219     write(*,*) '# End orthonormal basis'
220
```

```
221      if (veryverbose) then
222         !Check basis functions
223         write(*,*) '# These are the functions of your basis'
224         do i=-nb,nb
225            do j=1,points
226               write(*,'(i4.3,10(E20.10E3,x))') i,theta(j),fi(i,j)
227            enddo
228            write(*,*)
229         enddo
230      write(*,*) '# End functions of basis'
231      endif
232
233   endif
234
235   !Evaluate kinetic operator
236   write(*,*) 'Evaluating kinetic energy operator...'
237   T(:,:)=0.0d0
238
239   !if (.false.) then
240   !do i=-nb,nb
241   !   do j=-nb,nb
242   !      !Operator on LHS
243   !      !Diferenciate 1st time
244   !      faux(:)=real(j)*fi(-j,:)
245   !      !Diferenciate the product mass(x)*faux(:)
246   !      faux(:)=0.d0+(1.d0/mass)*real(j**2)*fi(+j,:)
247   !      integrand=dconjg(fi(i,:))*faux(:)
248   !      call integratec (integrand,1,size(integrand),T(i,j))
249   !      T(i,j)=T(i,j)*dtheta/2.d0
250   !      write(*,'(10(E20.10E3,x))') real(i),real(j),T(i,j)
251   !   enddo
252   !   write(*,*)
253   !enddo
254   !endif
255
256   do i=-nb,nb
257      T(i,i)=real(i**2)
258   enddo
259   T(:,:)=T(:,:)/(2.0d0*mass)
260   !T(:,:)=T(:,:)/(2.0d0)
261
262   !Write stuff on output
263   write(*,*) '...done!'
264
265   !Evaluate potential operator
266   write(*,*) 'Evaluating potential energy operator...'
267   V(:,:)=dcmplx(0.0d0,0.d0)
268   do i=-nb,nb
269      do j=i,nb
270   !     if (i*j.gt.0.d0) then
271            integrand(:)=dconjg(fi(i,:))*pot(:)*fi(j,:)*dtheta
272            call integratec (integrand,1,points,integral)
273            V(i,j)=integral
274            V(j,i)=dconjg(V(i,j))
275   !       endif
276      enddo
277   enddo
278   do i=-nb,nb
279      fi2(i,:)=dcmplx(1.d0/(pi)*dsin(real(i)*theta(:)),0.d0)
280      integrand(:)=dconjg(fi2(i,:))*(pot(:))
281      call integratec (integrand,1,points,integral)
282      VC(i)=integral*dtheta
283   enddo
284   !Write stuff on output
285   write(*,*) '...done!'
286
287   !Build Hamiltonian
288   H(:,:)=0.0d0
289   H(:,:)=T(:,:)+V(:,:)
290
291   if (veryverbose) then
292
293      if (.false.) then
294      !Check potential array decomposition
295      write(*,*) '# Checking potential Fourier decomposition'
```

```
296      do i=1,points
297         integral=dcmplx(0.d0,0.d0)
298         do j=-nb,nb
299            integral=integral+VC(j)*fi2(j,i)
300         enddo
301         write(*,'(3(E20.10E3,x))') theta(i),integral!+minval(pot(:))
302      enddo
303      write(*,*) '# End       potential Fourier decomposition'
304      endif
305
306      !Check potential energy matrix
307      write(*,*) '# Checking potential energy matrix'
308      do i=-nb,nb
309         do j=-nb,nb
310            write (*,100) i,j,real(V(i,j)),dimag(V(i,j)),abs(V(i,j))
311         enddo
312         write(*,*)
313      enddo
314      write(*,*) '# End potential energy matrx'
315      !Check kinetic energy matrix
316      write(*,*) '# Checking kinetic energy matrix'
317      do i=-nb,nb
318         do j=-nb,nb
319            write (*,100) i,j,real(T(i,j)),dimag(T(i,j)),abs(T(i,j))
320         enddo
321         write(*,*)
322      enddo
323      write(*,*) '# End kinetic energy matrx'
324      !Check Hamiltonian matrix
325      write(*,*) '# Checking Hamiltonian matrix'
326      do i=-nb,nb
327         do j=-nb,nb
328            write (*,100) i,j,real(H(i,j)),dimag(H(i,j)),abs(H(i,j))
329         enddo
330         write(*,*)
331      enddo
332      write(*,*) '# End Hamiltonian matrx'
333   endif
334
335   !Write stuff on output
336   write(*,*) 'Diagonalizing total Hamiltonian...'
337
338   !diagonalize
339   if (rut.eq.'NR_F90') then
340      write(*,*) '...using tred2 + tql2 routines...'
341      REH(:,:)=real(H(:,:))
342
343      !Calling first subroutine to reduce with Householder algorithm
344      ! to a tridiagonal matrix
345      call tred2(2*nb+1,2*nb+1,REH,REEVAL,REEVAL2,REEVEC)
346
347      if (veryverbose) then
348         deallocate(integrand)
349         allocate  (integrand(-nb:nb))
350         write(*,*) '# Checking 1st Orthogonal transf matrix'
351         do i=-nb,nb
352            do j=-nb,nb
353               write (*,100) i,j,REEVEC(i,j)
354            enddo
355            write(*,*)
356         enddo
357         write(*,*) '# End 1st Orthogonal matrix'
358         write(*,*) '# Checking orthogonality of 1st Orthogonal transf matrix'
359         do i=-nb,nb
360            integral=0.d0
361            do j=-nb,nb
362               integrand(:)=REEVEC(j,:)*REEVEC(i,:)
363               call integratec(integrand,-nb,+nb,integral)
364               write(*,100) i,j,integral,abs(integral)
365            enddo
366         write(*,*)
367         enddo
368         write(*,*) '# End 1st orthogonality test'
369         write(*,*) '# Checking elements of main diagonal and and sub-diagonal'
370         do i=-nb,nb
```

```
371            write(*,400) i,REEVAL(i),REEVAL2(i)
372         enddo
373         write(*,*) '# End main diagonal and sub-diagonal'
374      endif
375
376      !Call second subroutine, to determine eigenvalues and eigenvectors
377      !tridiagonal matrix
378      call tql2(2*nb+1,2*nb+1,REEVAL,REEVAL2,REEVEC,error)
379
380      if (veryverbose) then
381         write(*,*) '# Checking 2nd Orthogonal transf matrix'
382         do i=-nb,nb
383            do j=-nb,nb
384               write (*,100) i,j,REEVEC(i,j),abs(REEVEC(i,j))
385            enddo
386            write(*,*)
387         enddo
388         write(*,*) '# End 2nd Orthogonal matrix'
389         write(*,*) '# Checking orthogonality of 2nd Orthogonal transf matrix'
390         do i=-nb,nb
391            integral=0.d0
392            do j=-nb,nb
393               integrand(:)=REEVEC(j,:)*REEVEC(i,:)
394               call integratec(integrand,-nb,+nb,integral)
395               write(*,100) i,j,integral,abs(integral)
396            enddo
397         write(*,*)
398         enddo
399         write(*,*) '# End 2nd orthogonality test'
400      endif
401   elseif (rut.eq.'LAPACK') then
402      write(*,*) '...using zheevd routine...'
403      call mydiagsubc (H,2*nb+1,EVEC,EVAL)
404   elseif (rut.eq.'rutjgv') then
405      write(*,*) '...using jgv    routine...'
406      do i=-nb,nb
407         do j=-nb,nb
408            realH(i+nb+1,j+nb+1)=real(H(i,j))
409            imH  (i+nb+1,j+nb+1)=dimag(H(i,j))
410   !         write(*,*) 'Doing ',i,' to ',i+nb+1,' and ',j,' to ',j+nb+1
411         enddo
412      enddo
413
414   !   call ch(2*nb+1,2*nb+1,realH,imH,realEIG,1,realE,imE,fv1,fv2,fm1,i)
415
416      write(*,*) "Start jgv's EVEC"
417      do i=1,2*nb+1
418         EVAL(i-nb-1)=realEIG(i)
419         do j=1,2*nb+1
420            EVEC(i-nb-1,j-nb-1)=dcmplx(realE(i,j),imE(i,j))
421            !write(*,*) 'Doing from',i,' to ',i-nb-1,' and ',j,' to ',j-nb-1
422            write(*,'(2(i3,3x),10(E20.10E3,x))') i,j,realE(i,j),imE(i,j)!,realH
   (i,j),imH(i,j)
423         enddo
424         write(*,*)
425      enddo
426      write(*,*) "End   jgv's EVEC"
427   else
428      write(*,*) 'Which subroutine do you want to use exactly?'
429      STOP
430   endif
431
432   !Write stuff on output
433   write(*,*) '...done!'
434
435   !Write eigenvalues
436   if (verbose) write(*,*) '# This are your eigenvalues'
437   if (verbose) write(*,'(i4.3,x,E20.10E3)') (i+nb,EVAL(i),i=-nb,nb)
438
439   if (rut.eq.'NR_F90') then
440      EVAL(:)=REEVAL(:)
441      EVEC(:,:)=REEVEC(:,:)
442   endif
443
444   if (verbose) then
```

```
445      !Write matrix of eigenvectors
446      write(*,*) '#This is the matrix of your eigenvectors'
447      do i=-nb,nb
448         do j=-nb,nb
449            write(*,100) i,j,real(EVEC(i,j)),dimag(EVEC(i,j)),cdabs(EVEC(i,j))
450         enddo
451      write(*,*)
452      enddo
453   endif
454
455   if (harm) then
456      open(unit=52,file='Eharm.dat',status='unknown')
457      open(unit=53,file='Vharm.dat',status='unknown')
458      write (53,200) (theta(j),pot(j),j=1,points)
459      close(52)
460      close(53)
461   endif
462
463   !Save energies
464   write(fname,'(a1,i2.2,a1,i4.4,a4)') 'E',npot,'.',points,'.dat'
465   open(unit=51,file=fname,status='unknown')
466   do i=-nb,nb
467      write(51,200) EVAL(i)
468      if (harm) write (52,200) Eharm(i)
469   enddo
470   close(51)
471
472   !Write stuff on output
473   write(*,*) 'Energies written to ',fname
474
475   !Write stuff on output
476   write(*,*) 'Rotating obtained eigenvectors to position space, storing and wr
      iting'
477
478   !Calculate eigenfunction in terms of spacial base
479   EIGEN(:,:)=dcmplx(0.d0,0.d0)
480   !Loop over eigenvectors columns of the Hamiltonian
481   do j=-nb,nb
482
483      !Loop over basis functions
484      do i=-nb,nb
485         EIGEN(j,:)=EIGEN(j,:)+EVEC(i,j)*fi(i,:)
486      enddo
487
488      !Storing the eigenvectors in positon space basis
489      write(fname,'(i3.3,a1,i3.3,a4)') j+nb+1,'_',npot,'.psi'
490      open(unit=57,file='EIGEN/'//fname,status='unknown')
491      call doheadpsi(EIGEN(j,:),theta(:),EVAL(j),j+nb+1,57)
492      !Loop over space points
493      do k=1,points
494         write(57,300) theta(k),EIGEN(j,k),cdabs(EIGEN(j,k))**2
495      enddo
496      close(57)
497
498   enddo
499   !Write stuff on output
500   write(*,*) '...done!'
501
502   !Write stuff on output
503   write(*,*) 'Mission acomplished.'
504
505   100 format (2(i4.3,x),3(E20.10E3,x))
506   200 format (2(E20.10E3,x))
507   300 format (10(E20.10E3,x))
508   400 format (1(i4.3,x),2(E20.10E3,x))
509   !################################
510   contains
511
512   subroutine mydiagsubc (matin,df,matvec,ev)
513   !This subroutine calls a LAPACK diagonalization zheevd
514   !For diagonalizing complex hermitian matrices
515   !Input
516   ! matin:          matrix to diagonalize
517   ! df:             dimension of the matrix
518   ! matvec:         matrix with eigenvectors as column vectors
```

```
519  ! ev:              vector with eigenvalues
520
521  implicit none
522  integer df
523  complex(KIND=DP) ::  matin(1:df,1:df),matvec(1:df,1:df)
524  real(KIND=DP) :: ev(1:df)
525  complex(Kind=DP) matarray(1:df*(df+1)/2)
526  integer i,j,k
527
528  complex(Kind=DP) work(1:df**2+2*df)
529  real(KIND=DP) :: rwork(:)
530  allocatable rwork
531  integer lrwork
532  integer iwork(1:5*df+3)
533  integer info
534
535  lrwork=int(log(df*1.d0)/log(2.d0))+1
536  lrwork=3*df**2+(4+2*lrwork)*df+1
537  allocate (rwork(1:lrwork))
538
539  !write(*,*) '# Matrix that enters mydiagsubc'
540  !do i=1,df
541  !   do j=1,df
542  !      !if (cdabs(matin(i,j)).le.1.d-3) matin(i,j)=dcmplx(0.d0,0.d0)
543  !      write(*,'(2(i3.3,x),4(E20.10E3))') i,j,matin(i,j)
544  !   enddo
545  !   write(*,*)
546  !enddo
547  !write(*,*) '# End matrix that enters mydiagsubc'
548
549  call zheevd('V','U',df,matin,df,ev,work,df**2+2*df,rwork,lrwork,iwork,5*df+3
     ,info)
550  if (info.ne.0) write (*,*) "something wrong with routine"
551  matvec(:,:)=matin(:,:)
552  end subroutine mydiagsubc
553  !###################################
554  subroutine doheadpsi(psi,space,E,n,ffi)
555  !Puts together a header for psi files
556  !ffi is integer determining fortran file on which
557  !stuff will be written
558  implicit none
559  INteger, Parameter :: DP= Kind(1.0D0)
560
561  integer points
562  integer n
563  integer ffi
564
565  complex(KIND=DP) psi(:)
566  real(KIND=DP) space(:)
567  real(KIND=DP) E
568  complex(KIND=DP) norm
569  complex(KIND=DP) center
570
571  call integratec(dconjg(psi(:))*psi(:),1,size(psi(:)),norm)
572  norm=norm*(space(2)-space(1))
573  call determine(psi(:),space(:),points,center)
574  write(ffi,'(a1,x,i3.3,a15)') '#',n,'-th eigenfunction'
575  write(ffi,'(a7,x,E20.10E3)')       '# norm=',real(norm)
576  write(ffi,'(a7,x,E20.10E3)')       '# E    =',E
577  if      (real(center).lt..5*dacos(-1.d0)-.2) then
578     write(ffi,'(a7,x,E20.10E3,x,a6)')       '# <q> =',real(center),'(anti)'
579  elseif (real(center).gt..5*dacos(-1.d0)+.2) then
580     write(ffi,'(a7,x,E20.10E3,x,a5)')       '# <q> =',real(center),'(syn)'
581  elseif ((real(center).le..5*dacos(-1.d0)+.2) .or. &
582           (real(center).ge..5*dacos(-1.d0)-.2)) then
583     write(ffi,'(a7,x,E20.10E3,x,a6)')       '# <q> =',real(center),'(twst)'
584  endif
585  write(ffi,'(a54)')             '# space         Re{psi}        Im{psi}
     abs{psi}^2'
586
587  end subroutine
588  !###################################
589  subroutine renorm(psi,space)
590  !Renormalizes a wf in a given space
591  !Variable psi is overwritten on output
```

```
592  implicit none
593  INteger, Parameter :: DP= Kind(1.0D0)
594
595  integer points
596  complex(KIND=DP) psi(:)
597  real(KIND=DP)    space(:)
598
599  complex(KIND=DP) area
600
601  call integratec(dconjg(psi(:))*psi(:),1,size(space(:)),area)
602  area=area*(space(2)-space(1))
603  psi(:)=psi(:)/sqrt(cdabs(area))
604  end subroutine renorm
605  !#######################
606  subroutine determine(f,space,points,value)
607  !Calculates center of of the 1st half of wf,
608  !to avoid periodicity problems
609  implicit none
610  INteger, Parameter :: DP= Kind(1.0D0)
611
612  integer i,j,k
613
614  integer points
615  complex(KIND=DP) f(1:points)
616  real(KIND=DP) space(1:points)
617  complex(KIND=DP) value
618
619  call integratec(dconjg(f(:))*space(:)*f(:),1,points/2,value)
620  value=value*2*(space(2)-space(1))
621  end subroutine
622  !#########################
623  subroutine doheader (mass,high,low,points,harm,nb,nu,kharm)
624  !Given the input parameters, this subroutine creates the
625  !header of the output. To avoid verbose on main program
626  implicit none
627
628  real*8 mass
629  real*8 high,low
630  real*8 nu,kharm
631  integer points
632  integer nb
633  logical harm
634
635  write(*,*) 'Starting diagonalization'
636  write(*,'(x,a5,10x,x,f13.5,x,a2)') 'mass:',mass,'au'
637  write(*,'(x,a9, 6x,x,f13.6,x,a2,x,f13.6,x,a2,x,i4.4,x,a6)') 'interval:',low,
     'to',high,'in',points,'points'
638  if (harm) then
639     write(*,*) 'Detected harmonic oscillator'
640     write(*,'(x,a2,13x,x,f13.5)') 'k:',kharm
641     write(*,'(x,a3,12x,x,f13.5)') 'nu:',nu
642  endif
643  write(*,'(x,a10,x,i4.4)') 'n basis f:',2*nb+1
644  end subroutine doheader
645  !#########################
646  subroutine getargL (r,argL)
647  !Gets the Local argument of each complex in a complex array
648  !I never finish to write this subroutine because it bores me to death
649  implicit none
650  integer, parameter :: DP=KIND(1.d0)
651  real(KIND=DP), parameter :: zero=1.d-6
652  complex(KIND=DP) r(:)
653  real(KIND=DP) argL
654
655  real(KIND=DP) a,b
656  integer i,j,k
657
658  do i=1,size(r)
659     a=dreal(r(i))
660     b=dimag(r(i))
661     argL=dacos(dabs(a/b))
662     if ((a.gt.zero) .and. (b.gt.zero)) then
663        argL=argL
664     elseif ((a.lt.zero) .and. (b.gt.zero)) then
665        argL=180.d0-argL
```

```
666      elseif ((a.lt.zero) .and. (b.lt.zero)) then
667      endif
668   enddo
669   end subroutine getargL
670   !#######################################
671   subroutine getargG (r,argG)
672   !Gets global phase (argG) of complex array.
673   !This routine is thought to substract from a complex array (usually
674   !wavefunction) its global phase, so it becomes a pure real number
675   !without lost of module or sign (important for wfs)
676   implicit none
677   integer, parameter :: DP=KIND(1.d0)
678   complex (KIND=DP) r(:)
679   real(KIND=DP) argG
680   real(KIND=DP) normR,normI,norm
681   complex(KIND=DP) dummycomp
682   complex(KIND=DP) integrand(1:size(r))
683   real(KIND=DP),parameter :: pi=dacos(-1.d0)
684   integer i
685
686   call integratec(dcmplx(dimag(r(:))**2,0.d0),1,size(r),dummycomp)
687   normI=cdabs(dummycomp)
688   norm=normR+normI
689
690   argG=dacos(normR/norm)
691   write(*,'(20(F13.4,x))') normR,normI,norm,argG*360.d0/(2.d0*pi)
692   end subroutine getargG
693   !######################
694   subroutine integratec(f,start,finish,area)
695   !Integration of a complex number
696   !
697   ! CAREFUL: dx is not taken into account here
698   !
699   implicit none
700   Integer, Parameter :: DP= Kind(1.0D0)
701   integer i,j,k
702   integer a,b
703   integer start,finish
704   complex(KIND=DP) f(start:finish)
705   complex(KIND=DP) area
706
707   area=dcmplx(0.d0,0.d0)
708   do i=start,finish-1
709   !do i=start+1,finish-1
710       a=i
711       b=i+1
712       area=area+real(b-a)/6.d0*(f(a)+4.d0*(f(a)+f(b))/2.d0+f(b))
713   enddo
714   !area=area+(f(start)+f(finish))/2.d0
715   end  subroutine integratec
716   !######################
717   end program mydiag
718
```

- `mypropa.f90`

  This program uses the Split-Operator-technique to propagate an `npot`-dimensional wavefunction on a grid of `np` evenly spaced points. The program is written for `npot` adiabatic potential energy surfaces. The subroutine `getlaser` (called at line `101`, provided also in this Appendix) can generate an arbitrary combination of `npu` laser sub-pulses as sum of oscillating functions$\times$ $\sin^2$-envelopes, where each sub-pulse can have different delays and overall lengths. `getlaser` can also read arbitrary pulses from files (most typically, OCT-pulses).

  The program `mypropa` itself constitutes a `do loop` which calls `nt` times the Split-Operator subroutine `propagSO` (cf. line `170`, also provided in this Appendix). Other used subroutines are `calcprop`, that can compute expectation values for position, momentum, kinetic energy or potential energy (see lines `137-140`) and `getdipoles`, that automatically reads available dipoles from the working directory and includes them in the computation.

```
 1  program mypropa !Guille's approach to numerical propagation
 2  !with split-operator method
 3  implicit none
 4  integer npot,np,nt
 5  integer npr,ipr
 6  integer npu
 7  character*2 itu                        !Input time units
 8  integer,parameter:: DP=kind(1.d0)
 9  complex(kind=DP),allocatable :: wff(:,:),wfb(:,:)
10  complex(kind=DP),allocatable :: psi_I(:,:),psi_F(:,:)
11  real(kind=DP),allocatable :: V(:,:),r(:)
12  real(kind=DP),allocatable :: norm(:),normF(:),normB(:)
13  complex(kind=DP) overlap
14  real(kind=DP),allocatable :: dx(:,:,:),dy(:,:,:),dz(:,:,:)
15  real(kind=DP),allocatable :: Ex(:,:),Ey(:,:),Ez(:,:)
16  real(kind=DP),allocatable :: fieldx(:),fieldy(:),fieldz(:)
17  real(kind=DP),allocatable :: t(:)
18  real(kind=DP) dr,dt
19  complex(kind=DP) mean,muEx,muEy,muEz
20  complex(kind=DP),allocatable :: expcR(:),expcK(:),expcT(:),expcV(:),expcF(:,
    :)
21  real(kind=DP) dummyreal
22  complex(kind=DP) dummycomp
23  real(kind=DP) mass,penv
24
25  complex(kind=DP) suma
26
27  character*50 fname
28  real(KIND=DP),parameter :: pi=dacos(-1.d0)
29  real(KIND=DP),parameter :: Im=dcmplx(0.d0,1.d0)
30  real(KIND=DP),parameter :: fs2au=41.341191
31  real(KIND=DP),parameter :: au2cm=219474.6313705
32  real(KIND=DP),parameter :: au2GVm=5.142216D+02
33  integer i,j,k
34
35  dt=0.d0
36
37  read(*,*) npot
38  read(*,*) np
39  read(*,*) nt
40  read(*,*) dt,itu
41  read(*,*) mass
42  read(*,*) npu
43  read(*,*) npr
44
45  allocate(r(1:np))
46  allocate(psi_I(1:npot,1:np),psi_F(1:npot,1:np))
47  allocate(wff(1:npot,1:np),wfb(1:npot,1:np),V(1:npot,1:np))
48  allocate(norm(1:npot),normF(1:npot),normB(1:npot))
49  allocate(t(0:nt))
50  if (npu.gt.0) allocate(Ex(1:npu,0:nt),Ey(1:npu,0:nt),Ez(1:npu,0:nt))
51  allocate(fieldx(0:nt),fieldy(0:nt),fieldz(0:nt))
52  allocate(expcR(1:npot),expcK(1:npot),expcT(1:npot),expcV(1:npot),expcF(1:npo
    t,1:npot))
53  allocate(dx(1:npot,1:npot,1:np),dy(1:npot,1:npot,1:np),dz(1:npot,1:npot,1:np
    ))
54
55  !Inform before starting propagation
56  write(*,'(a30,x,i2.2     )') ' Number of potentials: ',npot
57  write(*,'(a30,x,F10.2,x,a3)') ' Duration of the propagation ',(nt)*dt,itu
58
59  !Read potentials
60  do i=1,npot
61    write(fname,"(A1,I1.1,A4)") "V",i,".dat"
62    call readfr(fname,V(i,:),r,np)
63  enddo
64  dr=r(2)-r(1)
65
66  !Read psi_I
67  call readfc('psi_I.in',psi_I,r,np,npot)
68  do k=1,npot
69     norm(k)=cdabs(overlap(psi_I(k,:),psi_I(k,:),np,dr))
70  enddo
71
72  !Renormalize
```

```
 73  do k=1,npot
 74     psi_I(k,:)=psi_I(k,:)/sqrt(sum(norm(:)))
 75     normF(k)=cdabs(overlap(psi_I(k,:),psi_I(k,:),np,dr))
 76  enddo
 77  write(*,'(a20,3(E20.10E3,x))') "# Norm of initial wf (on each potential)",(n
     ormF(k),k=1,npot),sum(normF(:))
 78
 79  !Read dipoles
 80  dx(:,:,:)=0.d0
 81  dy(:,:,:)=0.d0
 82  dz(:,:,:)=0.d0
 83  call getdipoles(npot,np,dx,dy,dz)
 84
 85  !Convert timestep
 86  !Other time-dependent transformations (freq, lengths, delays...)
 87  !will be converted to au in the subroutine getlaser if needed.
 88  if (itu.eq.'fs') then
 89     dt=dt*fs2au
 90  elseif (itu.eq.'au') then
 91  else
 92     write(*,*) "I don't understand your time units"
 93     STOP
 94  endif
 95
 96  !Generate the field
 97  fieldx(:)=0.d0
 98  fieldy(:)=0.d0
 99  fieldz(:)=0.d0
100  if (npu.gt.0) then
101     call getlaser(nt,npu,dt,itu, &      !Input
102          t,fieldx,fieldy,fieldz)        !Output, don't worry with what getlase
     r gives you for t,
103                                         !it will be recalculated.
104  else
105     write(*,*) "This is a field free propagation."
106  endif
107
108  !Calculate some properties at the beginning
109  do i=1,npot
110     call calcprop(psi_I(i,:),r,V(i,:),mass,np,'r',mean)
111     write (*,'(a10,x,i2.2,a30,2(E20.10E3,x))') "On pot.",i,"mean position of
     psi_I is ",mean
112     call calcprop(psi_I(i,:),r,V(i,:),mass,np,'p',mean)
113     write (*,'(a10,x,i2.2,a30,2(E20.10E3,x))') "On pot.",i,"mean momentum of
     psi_I is ",mean
114  enddo
115
116  !Open all outputs
117  open(1,file="norm.dat", status='unknown')
118  open(2,file="r1.dat",   status='unknown')
119  open(3,file="k1.dat",   status='unknown')
120  open(5,file="ekin.dat", status='unknown')
121  open(6,file="epot.dat", status='unknown')
122  open(7,file="elas.dat", status='unknown')
123  open(8,file="esum.dat", status='unknown')
124
125  wfF(:,:)=psi_I(:,:)
126
127  !Propagation starts!
128  ipr=0 !Initialize printing counter
129  do i=0,nt,+1
130     ipr=ipr+1
131     t(i)=(i)*dt
132     if ((ipr.eq.npr+1) .or. (i.eq.0))then
133        ipr=1
134        suma=dcmplx(0.d0,0.d0)  !Initialize mu*E
135        do k=1,npot
136           normF(k)=cdabs(overlap(wff(k,:),wff(k,:),np,dr))
137           call calcprop(wff(k,:),r,V(k,:),mass,np,'r',expcR(k))
138           call calcprop(wff(k,:),r,V(k,:),mass,np,'p',expcK(k))
139           call calcprop(wff(k,:),r,V(k,:),mass,np,'T',expcT(k))
140           call calcprop(wff(k,:),r,V(k,:),mass,np,'V',expcV(k))
141           !If there is field,calculate its interaction energy
142           if (npu.gt.0) then
143              !The dipole-field interaction is a matrix, thus open a new loop
```

```
144               do j=1,npot
145                  suma=suma &
146  &                        +overlap(wff(k,:),-1.d0*dx(k,j,:)*fieldx(i)*wff(j,:
     ),np,dr) &!Calculate <wff(k)|muX_kj*Ex|wff(j)> (ATT NO NORM!)
147  &                        +overlap(wff(k,:),-1.d0*dy(k,j,:)*fieldy(i)*wff(j,:
     ),np,dr) &!Calculate <wff(k)|muY_kj*Ey|wff(j)> (ATT NO NORM!)
148  &                        +overlap(wff(k,:),-1.d0*dz(k,j,:)*fieldz(i)*wff(j,:
     ),np,dr)  !Calculate <wff(k)|muZ_kj*Ez|wff(j)> (ATT NO NORM!)
149               enddo
150            endif
151          suma=suma/sum(normF(:))
152          enddo
153          write (1,'(1000(E20.10E3,x))') t(i)/fs2au,(normF(k),k=1,npot),sum(norm
     F(:))
154          write (2,'(1000(E20.10E3,x))') t(i)/fs2au,(real(expcR(k)),k=1,npot)
155          write (3,'(1000(E20.10E3,x))') t(i)/fs2au,(real(expcK(k)),k=1,npot)
156          write (5,'(1000(E20.10E3,x))') t(i)/fs2au,(real(expcT(k)),k=1,npot)
157          write (6,'(1000(E20.10E3,x))') t(i)/fs2au,(real(expcV(k)),k=1,npot)
158          write (7,'(1000(E20.10E3,x))') t(i)/fs2au,real(suma)
159          write (8,'(1000(E20.10E3,x))') t(i)/fs2au,real((suma)+sum(expcT(:))+su
     m(expcV(:)))
160          write(fname,'(i6.6,a4)') i,'.dat'
161          open(11,file=fname,status='unknown')
162          write (11,'(a5,x,F13.6,x,i6.6)') '#Time',t(i)/fs2au,i
163          write (11,'(a5,x,1000(E20.10E3,x))') '# E  ',(cdabs(expcT(k)+expcV(k)+
     0.d0),k=1,npot)
164          do k=1,np
165             write (11,'(10000(E20.10E3,x))') r(k),(wff(j,k),cdabs(wff(j,k))**2,
     j=1,npot)
166          enddo
167          close(11)
168       endif
169
170       call propagSO(wfF,dt,dr,V,dx,dy,dz,fieldx(i),fieldy(i),fieldz(i),mass,+1,
     np,npot)
171    enddo
172    !Propagation terminated
173    close(1)
174    close(2)
175    close(3)
176    close(5)
177    close(6)
178    close(7)
179    close(8)
180
181    !Write stuff on output
182    do i=1,npot
183       call calcprop(wff(i,:),r,V(i,:),mass,np,'r',mean)
184       write (*,'(a10,x,i2.2,a30,2(F13.6,x))') "On pot.",i,"mean position of wff
          is ",mean
185       call calcprop(wff(i,:),r,V(i,:),mass,np,'p',mean)
186       write (*,'(a10,x,i2.2,a30,2(F13.6,x))') "On pot.",i,"mean momentum of wff
          is ",mean
187    enddo
188
189    end
190    !Functions
191    !###############################
192    function overlap(f1,f2,np,dr)
193    implicit none
194    integer,parameter :: DP=kind(1.d0)
195    integer i,j,k,np
196    complex(kind=DP) f1(1:np),f2(1:np)
197    real(kind=DP) dr
198    complex(kind=DP) overlap
199
200    overlap=(0.d0,0.d0)
201    do i=1,np-1
202       overlap=overlap+dconjg(f1(i))*f2(i)
203    enddo
204    overlap=overlap*dr
205    return
206    end function
207    !###############################
```

- `propagSO.f90`

  This subroutine reads an `npot`×`np`-dimensional wavefunction, the time-interval `dt`, the potential `V`, the dipoles `dx,dy,dz`, the field components `Ex,Ey,Ez`, the `mass`, and the direction of the propagation `dir` (forward or backward) as an input and performs the evaluation of the time-propagator upon the wavefunction as outlined in equations Eqs. (3.37) to (3.45). The process includes fast Fourier transforms for switching between position and momentum space (see lines `26,42,93,103`) for the evaluation of the kinetic energy term, and the required matrix diagonalization for the potential term (see line `66`). The subroutine `diag` is an alias for a simplified call of the `zheevd` subroutine.

```
 1  subroutine propagSO(wf,dt,dr,V,dx,dy,dz,Ex,Ey,Ez,mass,dir,np,npot)
 2  implicit none
 3  !What this subroutine has to get from the main program
 4  !wf              wavefunction(1:npot,1:np),complex
 5  !dt              timestep in atomic units
 6  integer,parameter :: DP=kind(1.d0)
 7  complex(kind=DP) wf(1:npot,1:np)
 8  real(kind=DP) Ex,Ey,Ez,dx(1:npot,1:npot,1:np),dy(1:npot,1:npot,1:np),dz(1:np
    ot,1:npot,1:np),V(1:npot,1:np)
 9  real(kind=DP) dr,mass,dt
10  integer dir
11
12  integer npot,np
13  integer i,j,ii,ij,ik
14  real(kind=DP) k,dk
15  real(kind=DP) VW(1:npot,1:npot)
16  real(kind=DP) VWd(1:npot)
17  complex(kind=DP) zsum(1:npot)
18  real(kind=DP),parameter :: pi=dacos(-1.d0)
19
20  dk=2.d0*pi/np/dr
21
22  !Apply exp(-Im*T*t/2) to the wavefunction.
23  !In phase space, it is equivalent to multply with momentum value
24  !Loop over potentials
25  do ii=1,npot
26     call tfft(wf(ii,:),np,np,1)
27
28     !Reorder k-vector in momentum space
29     do ij=1,np
30        if (ij.le.np/2) then
31            k=(ij-1)*dk
32        else
33            k=(ij-1-np)*dk
34        endif
35        !Calculate value of the momentum at each (reordered) point
36        k=-real(dir)*dt*k**2/2./mass
37        !Multiply times wf
38        wf(ii,ij)=cdexp(dcmplx(0.d0,k/2.))*wf(ii,ij) !Split is done (mult. x k
    /2)
39     enddo
40     !End reorder
41
42     call tfft(wf(ii,:),np,np,-1)
43  enddo
44  ! 1/2 Kinetic term done
45
46  !Evaluate potential term
47  !Loop over points
48  do ii=1,np
49     !Prepare a matrix V-muE (npot x npot) for every point to be diagonalized:
50
51     !Loop over potentials
52     do ij=1,npot
53        do ik=1,npot
54           if (ij.eq.ik) then
55              VW(ij,ik)=V(ij,ii)
56           else
57              VW(ij,ik)=0.d0
58           endif
59           VW(ij,ik)=VW(ij,ik) -dx(ij,ik,ii)*Ex    &
60  &                            -dy(ij,ik,ii)*Ey    &
61  &                            -dz(ij,ik,ii)*Ez
62        enddo
63     enddo
64
65     !Diagonalize
66     call diag(VW,npot,VWd)
67
68     !U(rotation matrix) * psi
69     do ij=1,npot
70        zsum(ij)=dcmplx(0.d0,0.d0)
71        do ik=1,npot
72           zsum(ij)=zsum(ij)+VW(ik,ij)*wf(ik,ii)
73        enddo
```

```
74       enddo
75       !Ud(diagonalized matrix) * U * psi
76       do ik=1,npot
77          k=-real(dir)*dt*VWd(ik)
78          zsum(ik)=cdexp(dcmplx(0.0d0,k))*zsum(ik)    !Nosplit
79       enddo
80       !Udagger(rotation matrix dagger) * Ud * U * psi
81       do ij=1,npot
82          wf(ij,ii)=dcmplx(0.0d0,0.d0)
83          do ik=1,npot
84             wf(ij,ii)=wf(ij,ii)+VW(ij,ik)*zsum(ik)
85          enddo
86       enddo
87       !End Loop over points
88
89    enddo
90    !Potential done
91
92    do ii=1,npot
93       call tfft(wf(ii,:),np,np,1)
94       do ij=1,np
95          if (ij.le.np/2) then
96             k=(ij-1)*dk
97          else
98             k=(ij-1-np)*dk
99          endif
100           k=-real(dir)*dt*k**2/2./mass
101         wf(ii,ij)=cdexp(dcmplx(0.d0,k/2.))*wf(ii,ij) !Split
102      enddo
103      call tfft(wf(ii,:),np,np,-1)
104   enddo
105   ! 1/2 Kinetic term done
106
107   end subroutine propagSO
```

- `getlaser.f90`

  This subroutine interfaces with other programs and provides them with the desired type of laser. It reads propagation parameters from the main program (number of timesteps `nt`, number of wanted laserpulses `npu`, timestep `dt`) as well as from the subroutine's input file `laser.para`, which contains one block of parameters per wanted sub-pulse. The header of the source is extensively documented.

```
subroutine getlaser(nt,npu,dt,itu, &
                    fieldx,fieldy,fieldz)
!With whole bunch of paramters read from input, this subroutine
!"fills" the laser array with whatever laser the user
!has chosen:

!INPUT from the main program
!nt             number of timesteps
!npu            number laser pulses
!dt             timestep
!itu            input time units, 'fs' or 'au'.

!INPUT from the file 'laser.para' (don't return to main program)
!Following lines per kth-laser pulse
!lt     'hc' for half-cycle laser pulses,'fr' for freq
!       if (lt.eq.hc) then read
!               nhc             number of half cycles
!               lhc             lenght of half-cycle
!       if (lt.eq.fr) then read
!               omega,ifu       frequency,input freq units
!       endif
!       Eox,Eoy,Eoz,iAu         Amplitudes in x,y,z,input Amp units
!       Ex,Ey,Ez                Oscillating amplitudes in x,y,z
!       phax,phay,phaz          Phases in x,y,z
!       env,delay,length        envelope function (.true. or .false.),delay,
length
!       dalpha                  angular velocity of polarization vector

!INPUT laser pulses throuhg laser_k.in
!The files have to have t,fieldx(k),fieldy(k),fieldz(k) as input
!The input time units of laser_k.in has to be specified through itu in laser
.para
!The input Amp  units of laser_k.in has to be specified through iAu in laser
.para

!OUTPUT to the main program
!fieldx,fieldy,fieldz   Oscillating amplitudes

!OUTPUT to the user
!laser.dat              containing time, fieldx,fieldy,fieldz
!If polarization(t) is given, following files for every k-th pulse
!polvc_k.dat            containig polarization vectors of each pulse

implicit none
integer,parameter :: DP=kind(1.d0)

!Input variables from the main program
integer nt,npu
real(kind=DP) dt
character*2   itu  !Input time units

!Input variables from file 'laser.para'
character*2   lt(1:npu)  !laser type 'hc' for half-cycle laser pulse,fr for
freq defined lasers

!Depending on lt, following variables for each kth-laser pulse
!Only if lt(k).eq. hc
integer       nhc(1:npu) !number of half-cycles
real(kind=DP) lhc(1:npu) !lenght of half-cycle
!Only if lt(k).eq. fr
real(kind=DP) omega(1:npu)
character*4   ifu(1:npu) !Input freq units

!For all lasertypes (lt.eq.fr.) or (lt.eq.hc)
real(kind=DP) Eox(1:npu),Eoy(1:npu),Eoz(1:npu)
real(kind=DP) phax(1:npu),phay(1:npu),phaz(1:npu)
character*4   iAu(1:npu) !Input amp  units
logical       env(1:npu)
real(kind=DP) delay(1:npu),length(1:npu)
real(kind=DP) dalpha(1:npu)

!Output variables
real(kind=DP) t
real(kind=DP) fieldx(0:nt),fieldy(0:nt),fieldz(0:nt)

```

```
 72  !Subroutine internal variables
 73  integer i,j,k
 74  real(kind=DP) Ex(1:npu),Ey(1:npu),Ez(1:npu)
 75  character*50  fname
 76  real(kind=DP) E2(0:nt)
 77  real(kind=DP) polvcx(1:npu),polvcy(1:npu),polvcz(1:npu)
 78  real(kind=DP) suma,dummyreal
 79  real(kind=DP) wu2otu      !working units (au) to ouput units of time
 80  real(kind=DP) wu2oAu      !working units (au) to ouput units of amplitude
 81
 82  !Numbers
 83  !real(kind=DP),parameter :: pi=dacos(-1.d0)
 84  real(kind=DP) pi
 85  real(kind=DP),parameter :: au2GVm=5.142216D+02
 86  real(kind=DP),parameter :: fs2au =41.341191
 87  real(KIND=DP),parameter :: au2cm=219474.6313705
 88
 89  pi=dacos(-1.d0) !To run in Evanston...
 90
 91  !Initialize fields
 92  Ex(:)=0.d0
 93  Ey(:)=0.d0
 94  Ez(:)=0.d0
 95  fieldx(:)=0.d0
 96  fieldy(:)=0.d0
 97  fieldz(:)=0.d0
 98  !Initialize polarization vector
 99  polvcx(:)=0.d0
100  polvcy(:)=0.d0
101  !Initialize conversion factors
102  wu2otu=1.d0
103  wu2oAu=1.d0
104
105  !Get parameters!
106  open(1,file='laser.para',status='old')
107  do k=1,npu
108     read(1,*) lt(k)
109     if (lt(k).eq.'hc') then
110        read(1,*) nhc(k)
111        read(1,*) lhc(k)
112     elseif (lt(k).eq.'fr') then
113        read(1,*) omega(k),ifu(k)
114     else
115        write(*,*) 'What type of laser do you want exactly ',lt(k),'?'
116        STOP
117     endif
118     read(1,*) Eox(k),Eoy(k),Eoz(k),iAu(k)
119     if ((iAu(k).ne.'au').and.(iAu(k).ne.'GV/m')) then
120         write(*,*) 'Eo units for pulse ',k,' are ',iAu(k),'?'
121         STOP
122     endif
123     read(1,*) phax(k),phay(k),phaz(k)
124     read(1,*) env(k),delay(k),length(k)
125     if (lt(k).eq.'hc') length(k)=nhc(k)*lhc(k)
126     read(1,*) dalpha(k)
127  enddo
128  close(1)
129
130  !Convert times
131  if (itu.eq.'fs') then
132     dt=dt*fs2au
133     delay(:)=delay(:)*fs2au
134     length(:)=length(:)*fs2au
135     lhc(:)=lhc(:)*fs2au
136     wu2otu=1.d0/fs2au
137  elseif (itu.eq.'au') then
138  else
139     write(*,*) "I don't understand your time units"
140     STOP
141  endif
142
143  !Convert omega and amplitudes
144  do k=1,npu
145     if (ifu(k).eq.'cm-1') omega(k)=omega(k)/au2cm
146     if (iAu(k).eq.'GV/m') then
```

```
147         Eox(k)=Eox(k)/au2GVm
148         Eoy(k)=Eoy(k)/au2GVm
149         Eoz(k)=Eoz(k)/au2GVm
150         wu2oAu=au2GVm
151      endif
152   enddo
153
154   !Convert revolutions of polarization vector to a differential of alpha
155   dalpha(:)=dalpha(:)*2.d0*pi/length(:)
156   !Convert phases
157   phax(:)=180.d0/pi*phax(:)
158   phay(:)=180.d0/pi*phay(:)
159   phaz(:)=180.d0/pi*phaz(:)
160
161   do k=1,npu
162      write(*,*) k,'-th pulse'
163      if (lt(k).eq.'hc') then
164         length(k)=nhc(k)*lhc(k)
165         omega(k)=pi/lhc(k)
166         write (*,'(a25,x,1(i3      ,x),a15,x,1(F13.6,x),a9)')'Half-cycle pulse
     :',nhc(k),'cycles of  ',lhc(k)/fs2au,'fs each.'
167      endif
168      if (omega(k).ge.0.d0) then
169         write (*,'(a25,x,1(E20.10E3,x),a15,x,1(F13.6,x),a9)')'Frequency of
      ',omega(k),'hartree and',omega(k)*au2cm,'cm-1.'
170         write (*,'(a25,x,L2                                  )')'Envelope functio
     n',env(k)
171         write (*,'(a25,x,1(F13.6,   x),a07,x,1(F13.6,x),a3)')'Delay
      ',delay(k)/fs2au,'fs and',delay(k),'au.'
172         write (*,'(a25,x,1(F13.6,   x),a07,x,1(F13.6,x),a3)')'Length
      ',length(k)/fs2au,'fs and',length(k),'au.'
173         write (*,'(a25,x,3(E20.10E3,x),a15                )')'Eox,Eoy,Eoz:
      ',Eox(k),Eoy(k),Eoz(k),'au and'
174         write (*,'(a25,x,3(F13.6,   x),a15                )')'Eox,Eoy,Eoz:
      ',Eox(k)*au2GVm,Eoy(k)*au2GVm,Eoz(k)*au2GVm,'GV/m.'
175         write (*,'(a25,x,3(F13.6,   x),a15                )')'phases (x,y,z)
      ',phax(k)*pi/180.d0,phay(k)*pi/180.d0,phaz(k)*pi/180.d0,'degree'
176         write (*,'(a25,x,1(F13.6,   x),a15                )')'alphadot
      ',dalpha(k)*180.d0/pi*fs2au,'degrees/fs'
177         write (*,'(a25,x,1(E20.10E3,x),a15                )')'alphadot
      ',dalpha(k)                 ,'radians/au'
178
179
180         write(fname,'(a6,i3.3,a4)') 'polvc_',k,'.dat'
181         if (dalpha(k).gt.(0.d0)) open(2,file=fname)
182
183         !Generate laser for every timestep
184         do i=0,nt
185            t=i*dt
186            !Ex(k), Ey(k),Ez(k) are 1D reals and need to be initialized
187            Ex(k)=0.d0
188            Ey(k)=0.d0
189            Ez(k)=0.d0
190            if ((t.ge.delay(k)).and.(t.le.delay(k)+length(k))) then
191                !Assure the laser is supossed to be on and make it oscillate
192                Ex(k)=dcos(omega(k)*(t-delay(k))+phax(k))
193                Ey(k)=dcos(omega(k)*(t-delay(k))+phay(k))
194                Ez(k)=dcos(omega(k)*(t-delay(k))+phaz(k))
195                !Correct for constant laser field
196                if (omega(k).eq.0.d0) then
197                   Ex(k)=1.d0
198                   Ey(k)=1.d0
199                   Ez(k)=1.d0
200                endif
201                if (env(k)) then
202                   !Multiply with envelope
203                   Ex(k)=Ex(k)*sin((t-delay(k))*pi/(length(k)))**2
204                   Ey(k)=Ey(k)*sin((t-delay(k))*pi/(length(k)))**2
205                   Ez(k)=Ez(k)*sin((t-delay(k))*pi/(length(k)))**2
206                endif
207                !Multiply with amplitude
208                Ex(k)=Ex(k)*Eox(k)
209                Ey(k)=Ey(k)*Eoy(k)
210                Ez(k)=Ez(k)*Eoz(k)
211                if ((dalpha(k).ne.0.d0) .and. (Eoy(k).eq.0.d0)) then
```

```
212                  !Add the polarization if dalpha=/zero
213                  polvcx(k)=dcos(0.0d0*pi+(t-delay(k))*dalpha(k))
214                  polvcy(k)=dsin(0.0d0*pi+(t-delay(k))*dalpha(k))
215                  E2(i)=Ex(k)
216                  Ex(k)=E2(i)*polvcx(k)
217                  Ey(k)=E2(i)*polvcy(k)
218               elseif ((dalpha(k).ne.0.d0) .and. (Eox(k).eq.0.d0)) then
219                  !Add the polarization if dalpha=/zero
220                  polvcx(k)=dcos(0.5d0*pi+(t-delay(k))*dalpha(k))
221                  polvcy(k)=dsin(0.5d0*pi+(t-delay(k))*dalpha(k))
222                  E2(i)=Ey(k)
223                  Ex(k)=E2(i)*polvcx(k)
224                  Ey(k)=E2(i)*polvcy(k)
225               endif
226            endif
227
228            if (dalpha(k).ne.(0.d0)) write(2,'(F13.6,x,6(E20.10E3,x))') t*wu2ot
     u,polvcx(k),polvcy(k)
229
230            !Before time-loop is over, add all components of the field
231            fieldx(i)=fieldx(i)+Ex(k)
232            fieldy(i)=fieldy(i)+Ey(k)
233            fieldz(i)=fieldz(i)+Ez(k)
234
235         enddo
236         !End timestep for this pulse
237         if (dalpha(k).ne.(0.d0)) close(2)
238
239      !Other posibilities for initial laser: READ LASER
240      elseif (omega(k).lt.0.d0) then
241         write(fname,'(a6,i3.3,a3)') 'laser_',k,'.in'
242         open (unit=11,file=fname,status='old')
243         write(*,*) 'Reading X,Y,and Z component of laser from',fname
244         do i=0,nt
245            read(11,*) t,Ex(k),Ey(k),Ez(k)
246            if (iAu(k).eq.'GV/m') then
247                Ex(k)=Ex(k)/au2GVm
248                Ey(k)=Ey(k)/au2GVm
249                Ez(k)=Ez(k)/au2GVm
250            endif
251            !Before time-loop is over, add all components of the field
252            fieldx(i)=fieldx(i)+Ex(k)
253            fieldy(i)=fieldy(i)+Ey(k)
254            fieldz(i)=fieldz(i)+Ez(k)
255         enddo
256         close(11)
257      endif
258   write (*,*)
259   enddo
260   !End loop over pulses
261
262   !Write out final field
263   open(4,file='laser.dat',status='unknown')
264   do i=0,nt
265      t=i*dt
266      write (4,'(1000(E20.10E3,x))') t*wu2otu,fieldx(i)*wu2oAu,fieldy(i)*wu2oAu
     ,fieldz(i)*wu2oAu
267   enddo
268   close(4)
269   !Important addendum: because I want my laser routine to leave my
270   !dt variable untouched, I need to transform it back in
271   !case it was transformed by the routine
272   dt=dt*wu2otu
273   end subroutine
```

- `oct.f90`

  This program implements the rapidly convergent algorithm of Zhu, Botina, and Rabitz[81] outlined in equations Eqs. (3.47) to (3.55). It makes use of `propagSO` for the needed time propagations, and as such, `oct` functions similarly to `mypropa` in the read-in of parameters, anduse as well the subroutines `getdipoles` and `calcprop`. The subroutine `getlaser` (also provided above) is also used to generate the initial, guessed laser field (Eq. (3.47)). See header of the source code for more details.

```
program oct !Trying to implement the OCT-algorithm of Zhu and Rabitz

!INPUT from standard input
!npot           number of potentials
!np             number of gridpoints
!nt             number of timesteps
!dt             timestep length,currently read only in femtoseconds
!env            logical, envelope true of false
!mass           mass
!pen            logical,penalty function
!penv           real, functional will be mutiplied with 1/penv. Only read if
 pen=true

!INPUT from files
!from the main program:
!V_XXX.dat      X-th potential, format i3.3 (read from main program)
!psi_I.in       initial wf. To be read with a loop read(*,*) r,(Re{Psi},Im{P
si},i=1,npot)
!psi_F.in       target wf. To be read with a loop read(*,*) r,(Re{Psi},Im{Ps
i},i=1,npot)
!from the subroutines
!laser.para     laser paramters
!getdipole      dipole momenta

implicit none
integer npot,np,nt
integer,parameter:: DP=kind(1.d0)
complex(kind=DP),allocatable :: wff(:,:),wfb(:,:)
complex(kind=DP),allocatable :: psi_I(:,:),psi_F(:,:)
real(kind=DP),allocatable :: V(:,:),r(:)
real(kind=DP),allocatable :: norm(:),normF(:),normB(:)
complex(kind=DP) overlap
real(kind=DP),allocatable :: dx(:,:,:),dy(:,:,:),dz(:,:,:)
real(kind=DP),allocatable :: d(:,:,:)
real(kind=DP),allocatable :: E1(:),E2(:)
real(kind=DP),allocatable :: Ex1(:),Ey1(:),Ez1(:)
real(kind=DP),allocatable :: Ex2(:),Ey2(:),Ez2(:)
real(kind=DP),allocatable :: t(:)
real(kind=DP) dr,dt
complex(kind=DP) mean
real(kind=DP) dummyreal
logical env,pen
real(kind=DP) mass,penv

complex(kind=DP) g1,g2,suma,ov1(:),ov2(:)
complex(kind=DP) gx2,gy2,gz2
allocatable ov1,ov2
real(kind=DP) eps
real(kind=DP) thres

character*50 fich
logical ex
real(KIND=DP),parameter :: pi=dacos(-1.d0)
real(KIND=DP),parameter :: Im=dcmplx(0.d0,1.d0)
real(KIND=DP),parameter :: fs2au=41.34
integer i,j,k,iter



read(*,*) npot
read(*,*) np
read(*,*) nt
read(*,*) dt
read(*,*) thres
read(*,*) env
read(*,*) mass
read(*,*) pen
if (pen) read(*,*) penv

dt=dt*fs2au
allocate(wff(1:npot,1:np),wfb(1:npot,1:np),V(1:npot,1:np))
allocate(norm(1:npot),normF(1:npot),normB(1:npot))
allocate(psi_I(1:npot,1:np),psi_F(1:npot,1:np))
allocate(r(1:np),d(1:npot,1:npot,1:np))
allocate(t(0:nt),E1(0:nt),E2(0:nt))
```

```
 73  allocate(ov1(1:npot),ov2(1:npot))
 74  allocate(dx(1:npot,1:npot,1:np),dy(1:npot,1:npot,1:np),dz(1:npot,1:npot,1:np
     ))
 75  allocate(Ex1(0:nt),Ey1(0:nt),Ez1(0:nt))
 76  allocate(Ex2(0:nt),Ey2(0:nt),Ez2(0:nt))
 77
 78  !Read potentials
 79  do i=1,npot
 80    write(fich,"(A1,I1.1,A4)") "V",i,".dat"
 81    call readfr(fich,V(i,:),r,np)
 82  enddo
 83  dr=r(2)-r(1)
 84
 85  !Read dipoles
 86  dx(:,:,:)=0.d0
 87  dy(:,:,:)=0.d0
 88  dz(:,:,:)=0.d0
 89  call getdipoles(npot,np,dx,dy,dz)
 90
 91  d(:,:,:)=dy(:,:,:)
 92
 93  !Read psi_I,psi_F
 94  call readfc('psi_I.in',psi_I,r,np,npot)
 95  do k=1,npot
 96     norm(k)=cdabs(overlap(psi_I(k,:),psi_I(k,:),np,dr))
 97  enddo
 98  do k=1,npot
 99     psi_I(k,:)=psi_I(k,:)/sqrt(sum(norm(:)))
100     normF(k)=cdabs(overlap(psi_I(k,:),psi_I(k,:),np,dr))
101  enddo
102  write(*,*) "# Norm of initial wf_I",(normF(k),k=1,npot),sum(normF(:))
103
104  call readfc('psi_F.in',psi_F,r,np,npot)
105  do k=1,npot
106     norm(k)=cdabs(overlap(psi_F(k,:),psi_F(k,:),np,dr))
107  enddo
108  do k=1,npot
109     psi_F(k,:)=psi_F(k,:)/sqrt(sum(norm(:)))
110     normB(k)=cdabs(overlap(psi_F(k,:),psi_F(k,:),np,dr))
111  enddo
112  write(*,*) "# Norm of initial wf_F",(normB(k),k=1,npot),sum(normB(:))
113
114  do i=1,npot
115     call calcprop(psi_I(i,:),r,V(i,:),mass,np,'r',mean)
116     write (*,'(a10,x,i2.2,a30,2(F13.6,x))') "On pot.",i,"mean position of psi
     _I is ",mean
117     call calcprop(psi_I(i,:),r,V(i,:),mass,np,'p',mean)
118     write (*,'(a10,x,i2.2,a30,2(F13.6,x))') "On pot.",i,"mean momentum of psi
     _I is ",mean
119     call calcprop(psi_F(i,:),r,V(i,:),mass,np,'r',mean)
120     write (*,'(a10,x,i2.2,a30,2(F13.6,x))') "On pot.",i,"mean position of psi
     _F is ",mean
121     call calcprop(psi_F(i,:),r,V(i,:),mass,np,'p',mean)
122     write (*,'(a10,x,i2.2,a30,2(F13.6,x))') "On pot.",i,"mean momentum of psi
     _F is ",mean
123  enddo
124
125  !Generate initial laser
126  call getlaser(nt,1,dt/fs2au,'fs', &     !Since getlaser will read fs, I have
     to send dt in fs
127  &              t,Ex1,Ey1,Ez1)
128
129  !Inform before starting propagations
130  write(*,'(a30,x,i2.2      )') ' Number of potentials: ',npot
131  write(*,'(a30,x,F10.2,x,a)') ' Duration of the pulse:',(nt-1)*dt/fs2au,'fs'
132  write(*,'(a30,x,L1        )') ' Use of sin2 envelope :',env
133  write(*,'(a30,x,L1        )') ' Use of penalty func. :',pen
134  if (pen) write(*,'(a30,x,a1,F10.2 )') ' Penalty function of    :',penv
135
136  E2(:)=E1(:)
137  Ex2(:)=Ex1(:)
138  Ey2(:)=Ey1(:)
139  Ez2(:)=Ez1(:)
140  open(1,file='field.in',status='unknown')
141  do i=0,nt-1
```

```
142      write(1,'(6(E20.10E3,x))') t(i)/fs2au,Ex1(i),Ey1(i),Ez1(i)
143   enddo
144   close(1)
145
146
147   open(1,file="normB.dat")
148   !First backward propagation
149   wfB(:,:)=psi_F(:,:)
150   !Open backward-time-loop
151   do i=nt-1,0,-1
152   !   call propag(wfB,dt,dr,V,d,E1(i),mass,-1,np,npot)
153      call propagSO(wfB,dt,dr,V,dx,dy,dz,Ex1(i),Ey1(i),Ez1(i),mass,-1,np,npot)
154      do k=1,npot
155         normB(k)=cdabs(overlap(wfb(k,:),wfb(k,:),np,dr))
156      enddo
157      write (1,'(1000(E20.10E3,x))') t(i)/fs2au,normB(:),sum(normB(:))
158   enddo !Close backward-time-loop
159   close(1)
160   !Terminated 1st backward propagation
161
162   !Check for the overlap wfB at time zero and psi_I
163   write(*,*) "Overlap between 1st wfB(t=0) and psi_I"
164   do k=1,npot
165      ov1(k)=overlap(psi_I(k,:),wfB(k,:),np,dr)
166      write(*,*) "Overlap in potential ",k,abs(ov1(k))!**2
167   enddo
168   !write(*,*) "total overlap",sum(abs(ov1(:))**2)
169   write(*,*) "total overlap",sum(abs(ov1(:)))
170
171   !First forward(double) propagation, the laser of psi_I prop. forward (E2)
172   !will be already changed with the information of psi_F prop. backward (with
      E1)
173   open(1,file="normF.dat")
174   wfF(:,:)=psi_I(:,:)
175   !write(*,*) "time k j     Re{<wfF(k)|wfB(k)>} Im{}   Re{<wfF(k)|d(k,j)|wfB(j
      )>} Im{} "
176   do i=0,nt-1,+1
177       g1=(0.d0,0.d0)  !Initialize first term
178       g2=(0.d0,0.d0)  !Initialize 2nd   term
179      gx2=(0.d0,0.d0)  !Initialize 2nd   term in x
180      gy2=(0.d0,0.d0)  !Initialize 2nd   term in y
181      gz2=(0.d0,0.d0)  !Initialize 2nd   term in z
182      !First term of overlap only on the diagonal of npot x npot matrix
183      do k=1,npot
184         g1=g1+overlap(wfF(k,:),wfB(k,:),np,dr)
185         !Second term of overlap over the WHOLE npot x npot dipole matrix
186         do j=1,npot
187            g2 =g2 +overlap(wfB(k,:), d(k,j,:)*wfF(j,:),np,dr)
188            gx2=gx2+overlap(wfB(k,:),dx(k,j,:)*wfF(j,:),np,dr)
189            gy2=gy2+overlap(wfB(k,:),dy(k,j,:)*wfF(j,:),np,dr)
190            gz2=gz2+overlap(wfB(k,:),dz(k,j,:)*wfF(j,:),np,dr)
191         !   write(*,'(F13.6,x,2(i7.7,x),20(E20.10e3,x))') t(i)/fs2au,k,j,overl
      ap(wfF(k,:),wfB(k,:),np,dr),overlap(wfF(k,:),d(k,j,:)*wfB(j,:),np,dr)
192         enddo
193         !write(*,*)
194      enddo
195      !Input of this info in the new laser (core of OCT)!!!!!
196      !if (cdabs(g1).lt.1.0d-5 ) g1=0.d0
197      !if (cdabs(g2).lt.1.0d-5 ) g2=0.d0
198      E2(i) =-dimag(g1* g2)
199      Ex2(i)=-dimag(g1*gx2)
200      Ey2(i)=-dimag(g1*gy2)
201      Ez2(i)=-dimag(g1*gz2)
202      if (pen) E2(i)=E2(i)/penv
203      if (env) then
204         E2(i) = E2(i)*sin(pi*t(i)/(nt*dt))**2
205         Ex2(i)=Ex2(i)*sin(pi*t(i)/(nt*dt))**2
206         Ey2(i)=Ey2(i)*sin(pi*t(i)/(nt*dt))**2
207         Ez2(i)=Ez2(i)*sin(pi*t(i)/(nt*dt))**2
208      endif
209      call propagSO(wfB,dt,dr,V,dx,dy,dz,Ex1(i),Ey1(i),Ez1(i),mass,+1,np,npot)
      !wfB props FWD with with E1 laser       <-
210      call propagSO(wfF,dt,dr,V,dx,dy,dz,Ex2(i),Ey2(i),Ez2(i),mass,+1,np,npot)
      !wfF props FWD with with E2 (new) laser _|
211   !   call propag(wfB,dt,dr,V,d,E1(i),mass,+1,np,npot)
```

```
212 !    call propag(wfF,dt,dr,V,d,E2(i),mass,+1,np,npot)
213     do k=1,npot
214        normB(k)=cdabs(overlap(wfb(k,:),wfb(k,:),np,dr))
215        normF(k)=cdabs(overlap(wff(k,:),wff(k,:),np,dr))
216     enddo
217 !    write(*,'(10000(F13.6,x))') r(k),t(i)/fs2au,(wfb(j,k),j=1,npot)
218     write (1,'(1000(E20.10E3,x))') t(i)/fs2au,normB(:),sum(normB(:)),normF,su
    m(normF(:))
219 !    write(*,*) 'End of iteration ',iter
220  enddo
221  close(1)
222  !First forward (double) propagation terminated
223
224  write(*,*) "Overlap between 1st wfF(t=tf) and psi_F"
225  do k=1,npot
226     ov1(k)=overlap(wff(k,:),psi_F(k,:),np,dr)
227     write(*,*) "Overlap in potential ",k,abs(ov1(k))!**2
228  enddo
229  !write(*,*) "total overlap",sum(abs(ov1(:))**2)
230  write(*,*) "total overlap",sum(abs(ov1(:)))
231
232  !Start counter of iterations for OCT-loop and save laser of wfF
233  iter=0
234  write(fich,'(a4,i4.4,a4)') 'las_',iter,'.dat'
235  open(unit=1,file=fich,status='unknown')
236  do i=0,nt-1
237     write (1,'(4(e20.10e3))') t(i)/fs2au,Ex2(i),Ey2(i),Ez2(i)
238  enddo
239  close(1)
240
241  !Begin OCT-loop
242  eps=1.d0
243  open(55,file='norms.dat',status='unknown')
244  do while (eps>thres)
245     iter = iter+1
246     E1(:) = E2(:)    !Improve the laser with the previous output of OCT-loop
247     Ex1(:)=Ex2(:)
248     Ey1(:)=Ey2(:)
249     Ez1(:)=Ez2(:)
250
251     !Backward propagation
252     wfB(:,:)=psi_F(:,:)
253     !Open backward-time-loop
254     do i=nt-1,0,-1
255 !       write(*,*) t(i)/fs2au,E1(i),Ey1(i)
256 !       call propag(wfB,dt,dr,V,d,E1(i),mass,-1,np,npot)
257        call propagSO(wfB,dt,dr,V,dx,dy,dz,Ex1(i),Ey1(i),Ez1(i),mass,-1,np,npo
    t)
258        do k=1,npot
259           normB(k)=cdabs(overlap(wfb(k,:),wfb(k,:),np,dr))
260        enddo
261 !      write(*,'(10000(F13.6,x))') r(k),t(i)/fs2au,(wfb(j,k),j=1,npot)
262     enddo !Close backward-time-loop
263     !Terminated backward propagation
264
265     !Forward(double) propagation, the laser of psi_I prop. forward (E2)
266     !will be already changed with the information of psi_F prop. backward
267     wfF(:,:)=psi_I(:,:)
268     do i=0,nt-1,+1
269        g1=(0.d0,0.d0)    !Initialize first term
270        g2=(0.d0,0.d0)    !Initialize 2nd   term
271        gx2=(0.d0,0.d0)   !Initialize 2nd   term in x
272        gy2=(0.d0,0.d0)   !Initialize 2nd   term in y
273        gz2=(0.d0,0.d0)   !Initialize 2nd   term in z
274
275        !First term of overlap only on the diagonal of npot x npot matrix
276        do k=1,npot
277           g1=g1+overlap(wfF(k,:),wfB(k,:),np,dr)
278           !Second term of overlap over the WHOLE npot x npot dipole matrix
279           do j=1,npot
280              g2 = g2+overlap(wfB(k,:),d(k,j,:) *wfF(j,:),np,dr)
281              gx2=gx2+overlap(wfB(k,:),dx(k,j,:)*wfF(j,:),np,dr)
282              gy2=gy2+overlap(wfB(k,:),dy(k,j,:)*wfF(j,:),np,dr)
283              gz2=gz2+overlap(wfB(k,:),dz(k,j,:)*wfF(j,:),np,dr)
284           enddo
```

```
285         enddo
286
287         !Input of this info in the new laser (core of OCT)!!!!!
288         E2(i) =-dimag(g1*g2)
289         Ex2(i)=-dimag(g1*gx2)
290         Ey2(i)=-dimag(g1*gy2)
291         Ez2(i)=-dimag(g1*gz2)
292         if (pen) E2(i)=E2(i)/penv
293         if (env) then
294            E2(i) = E2(i)*sin(pi*t(i)/(nt*dt))**2
295            Ex2(i)=Ex2(i)*sin(pi*t(i)/(nt*dt))**2
296            Ey2(i)=Ey2(i)*sin(pi*t(i)/(nt*dt))**2
297            Ez2(i)=Ez2(i)*sin(pi*t(i)/(nt*dt))**2
298         endif
299         call propagSO(wfB,dt,dr,V,dx,dy,dz,Ex1(i),Ey1(i),Ez1(i),mass,+1,np,npo
    t) !wfB props FWD with with E1 laser       <-
300         call propagSO(wfF,dt,dr,V,dx,dy,dz,Ex2(i),Ey2(i),Ez2(i),mass,+1,np,npo
    t) !wfF props FWD with with E2 (new) laser _|
301   !      call propag(wfB,dt,dr,V,d,E1(i),mass,+1,np,npot)
302   !      call propag(wfF,dt,dr,V,d,E2(i),mass,+1,np,npot)
303         do k=1,npot
304            normB(k)=cdabs(overlap(wfb(k,:),wfb(k,:),np,dr))
305            normF(k)=cdabs(overlap(wff(k,:),wff(k,:),np,dr))
306         enddo
307         write (55,'(1000(E20.10E3,x))') t(i)/fs2au,normB(:),sum(normB(:)),norm
    F,sum(normF(:)),iter*1.d0
308   !     write(*,'(10000(F13.6,x))') r(k),t(i)/fs2au,(wfb(j,k),j=1,npot)
309      enddo
310      write (55,*)
311      !First forward (double) propagation terminated
312
313      write(*,*) "For the forwardly propagated wavefunction, at t=T:"
314      do i=1,npot
315         call calcprop(wff(i,:),r,V(i,:),mass,np,'r',mean)
316         write (*,'(a10,x,i2.2,a30,2(F13.6,x))') "On pot.",i,"mean position wfF
     is ",mean
317         call calcprop(wff(i,:),r,V(i,:),mass,np,'p',mean)
318         write (*,'(a10,x,i2.2,a30,2(F13.6,x))') "On pot.",i,"mean momentum wfF
     is ",mean
319      enddo
320
321
322      write(*,*) "Overlap between wfF(t=tf) and psi_F"
323      do k=1,npot
324         ov2(k)=overlap(wff(k,:),psi_F(k,:),np,dr)
325         write(*,*) "Overlap in potential ",k,abs(ov2(k))!**2
326      enddo
327      write(*,*) "total overlap",sum(abs(ov2(:)))
328
329      eps=   abs(sum(abs(ov2(:)))-sum(abs(ov1(:))))/(sum(abs(ov1(:))))
330      write (*,*) 'Convergence ',eps,thres
331
332      ov1(:)=ov2(:)
333      write(fich,'(a4,i4.4,a4)') 'las_',iter,'.dat'
334      open(unit=1,file=fich,status='unknown')
335      do i=0,nt-1
336         write (1,'(4(e20.10e3))') t(i)/fs2au,Ex2(i),Ey2(i),Ez2(i)
337      enddo
338      close(1)
339      write(*,*) 'End of iteration ',iter
340
341      open(1,file='wfF.dat',status='unknown')
342      do i=1,np
343         write(1,'(2000(E20.10e3,x))') r(i),(wfF(j,i),j=1,npot)
344      enddo
345      close(1)
346
347   enddo !OCT-while loop converged
348
349   close(55)
350   !Write stuff on output
351   do i=1,npot
352      call calcprop(wff(i,:),r,V(i,:),mass,np,'r',mean)
353      write (*,'(a10,x,i2.2,a30,2(F13.6,x))') "On pot.",i,"mean position of wff
         is ",mean
```

```
354      call calcprop(wff(i,:),r,V(i,:),mass,np,'p',mean)
355      write (*,'(a10,x,i2.2,a30,2(F13.6,x))') "On pot.",i,"mean momentum of wff
         is ",mean
356   enddo
357
358   open(1,file='oct_field.dat')
359   do i=0,nt-1,+1
360      write (1,'(5(e20.10e3,x))') t(i)/fs2au,Ex2(i),Ey2(i),Ez2(i)
361   enddo
362   close(1)
363
364   open(1,file='oct_wfF',status='unknown')
365   do i=1,np
366      write(1,'(2000(E20.10e3,x))') r(i),(wfF(j,i),j=1,npot)
367   enddo
368   close(1)
369   end
370   !Functions
371   !################################
372   function overlap(f1,f2,np,dr)
373   implicit none
374   integer,parameter :: DP=kind(1.d0)
375   integer i,j,k,np
376   complex(kind=DP) f1(1:np),f2(1:np)
377   real(kind=DP) dr
378   complex(kind=DP) overlap
379
380   overlap=(0.d0,0.d0)
381   do i=1,np
382      overlap=overlap+dconjg(f1(i))*f2(i)
383   enddo
384   overlap=overlap*dr
385   return
386   end function
387   !################################
```

- `randomizeparallel.f90`

  This program performs a Monte-Carlo based pseudo-random conformational search, and the code is parallelized to n processors (line `102`). It reads from standard input the parameters `filein`, `tight`, `tipo`, and `seed`. `filein` is the name of the file with the molecular geometry in form of MOPAC[129] Z-matrix. The stepsize ω in Eq. (3.1) is `tight`. The type (`tipo`) of optimization can be minimum or TS, although TS has not been fully tested yet. The option `seed` informs the program if a new random table needs to be created or a previous one has to be used (in order to ensure reproducibility even in random conditions). The `filein` is scanned automatically by the subroutine `getzmatmopac` (line `32`, see end the source code), which automatically reads atom-labels and connectivities. Additionally, the MOPAC Z-matrix format allows each DOF to have another descriptor, an integer determining its status. This integer is used do differentiate the DOFs to be randomized from those to be left untouched.

  Before the optimization begins, separate files (line `59`) containing xyz-geometries of each randomized DOF are created for visualization purposes. Each of these files contains geometries spanning over the randomized interval, as to provide a quick visual impression of the impact of the `tight` parameter on the search. Only internal DOFs are randomized, thus the random perturbation is done in the more *chemical* Z-matrix-geometry, expressed in terms of bond-angles, bond-distances and dihedral angles. Transformation back to Cartesian is done by the subroutine `zmatcart` (line `74`).

  The search itself begins at line `102`, where the parallel segment of the code starts (`do`-loop opening in lines `101-106`). Each DOF undergoes the perturbation of Eq. (3.1) (lines `110-134`) and the full MOPAC-input is set up, including the optimization command-line for MOPAC (lines `136-146`). The program `randomizeparallel` is then interfaced with the MOPAC code via a script created in each iteration for each processor, which then executes MOPAC. (lines `140-160`). After the iteration has stopped, other scripts check for convergence (lines `182-191`). If the iteration has converged, a frequency calculation is automatically launched by the code (lines `214-232`). The outcome of that calculation is again checked (lines `234-260`) for negative frequencies. If none appear (line `262`), the converged geometry is a minimum, and the optimization is then stored and compressed (using the `bzip2`-compressor, see lines `282-285`). The name of the saved file is created with the obtained energy value in its filename. This allows for quick browsing of energy values while the program is running, and simplifies the manipulation by the program `alignMOPAC` further on (also in this Appendix).

  All the converged energy values are appended to a separate file `E.dat` *on the fly*, as they emerge from the algorithm (lines `297-300`). This file produces ultimately a histogram representing the distribution of energies for the whole search.

  The remaining parts of the code (lines `306-520`) correspond to the algorithm for random TS-search, which is not yet implemented fully. It bases on the same strategy as the minimum search, but combines searches for TSs with intermediate optimizations where parts of the molecule (specially CH_3-groups) are allowed to relax. In order for the algorithm to be efficient, fewer DOFs shold be randomized and smaller ω-values

should be used.

```
 1  program randomizeparallel !To randomly generate mopac inputs out of zmat and
 2                            !give them to mopac
 3  implicit none
 4  integer i,j,k
 5  integer ii,jj
 6  integer,parameter :: na=16
 7  integer,parameter :: DP=kind(1.d0)
 8  character*1    natomI(1:na)
 9  character*1    natom(1:na)
10  real(kind=DP) cnctvt_V(na,1:3)  !Conectivity value
11  real(kind=DP) cnctvt_VI(1:na,1:3)  !Conectivity value initial
12  integer       cnctvt_A(1:na,1:3)  !Conectivity atom
13  integer       cnctvt_AI(1:na,1:3)  !Conectivity atom  initial
14  integer       cnctvt_S(1:na,1:3)  !Conectivity status
15  integer       cnctvt_SI(1:na,1:3)  !Conectivity status initial
16  real(kind=DP) cart     (1:na,1:3)  !cartesian coords
17  integer       seed(1:2),succes,succesM,succesF,thread
18  real(kind=DP) ra,E,start,tight,amp(1:3),G
19  character*35 fname,dummychar,fname2,fname3,fname4
20  character*75 commandline
21  character*2  tipo
22  character*1  s
23  integer       signo,randcoords,counter
24  integer,allocatable :: listrandoms(:,:)
25  logical exi,corr
26  integer        omp_get_thread_num,fi
27  fname=''
28  read(*,*) fname
29  read(*,*) tight
30  read(*,*) tipo
31  read(*,*) s                   !read or create seed
32  call getzmatmopac(fname,na,natomI,cnctvt_AI,cnctvt_VI,cnctvt_SI)
33
34  cnctvt_V(:,:)=cnctvt_VI(:,:)
35  cnctvt_A(:,:)=cnctvt_AI(:,:)
36  cnctvt_S(:,:)=cnctvt_SI(:,:)
37  natom(:)=natomI(:)
38  if (s.eq.'c') call system ("echo $RANDOM > seed.dat")
39  open(51,file='seed.dat',status='old')
40  read(51,*) seed(1)
41  close(51)
42  write(*,*) "Seed  for this search was",seed
43  write(*,*) "Tight for this search was",tight
44  write(*,*) "Type of search",tipo
45  !call srand(seed)  !FOR RUNNING IN GFORTRAN
46  call random_seed(put=seed) !FOR RUNNING IN PGF90
47
48  !tight=.40
49  !tight=.50
50  !Choose amplitudes of motion
51  amp(1)=1.3d0
52  amp(2)=180.d0
53  amp(3)=360.d0
54  !Segment to randomize each coord separately
55  do i=1,na
56     do j=1,3
57        if (cnctvt_SI(i,j).eq.1) then
58           start=cnctvt_V(i,j)-tight*.5*amp(j) !(start at lowest value)
59           write(fname,'(a8,i2.2,a1,i1,a4)') "randoms.",i,".",j,".xyz"
60           open(60,file=fname,status='unknown')
61           write(fname,'(a8,i2.2,a1,i1,a9)') "randoms.",i,".",j,".zmat.mop"
62           write(*,'(a5,x,F9.4,x,a2,x,F9.4,x,a2,x,15a)') "From ",start,"to",cn
   ctvt_V(i,j)+tight*.5*amp(j),"in",fname
63           open(70,file=fname,status='unknown')
64           cnctvt_V(i,j)=start
65           do k=1,25
66              cnctvt_V(i,j)=start+tight*amp(j)/24.d0*k
67              if ((j.eq.2).and.(cnctvt_V(i,j).gt.179.99)) then
68                 cnctvt_V(i,j)=360.d0-cnctvt_V(i,j)
69                 cnctvt_V(i,3)=cnctvt_VI(i,3)+180.d0
70              elseif((j.eq.2).and.(cnctvt_V(i,j).lt.000.01)) then
71                 cnctvt_V(i,j)=360.d0-cnctvt_V(i,j)
72                 cnctvt_V(i,3)=cnctvt_VI(i,3)+180.d0
73              endif
74              call zmatcart(na,cnctvt_V(:,:),cnctvt_A(:,:),cart) !!!!
```

```
75              write(60,*) na
76              write(60,*) "Scf Done: ",cnctvt_V(i,j)
77              write(70,*)
78              write(70,*) "HEAT OF FORMATION:",cnctvt_V(i,j)
79              write(70,*)
80              do ii=1,na
81                 write(60,'(a1,x,3(F9.4,x))') natomI(ii),(cart(ii,jj),jj=1,3)
82                 write(70,'(a1,x,3(F9.4,x,i2,x),3(i2,x))') natomI(ii),(cnctvt_
   V(ii,jj),cnctvt_S(ii,jj),jj=1,3),&
83                       (cnctvt_A(ii,jj),jj=1,3)
84              enddo
85           enddo
86           close(60)
87           close(70)
88           cnctvt_V(:,:)=cnctvt_VI(:,:)
89        endif
90     enddo
91  enddo
92  inquire(file='E.dat',exist=exi)
93  if (exi) then
94     write(*,*) "E.dat already exists. Is this okay?"
95     STOP
96  else
97     open(50,file='E.dat',status='new')
98     close(50)
99  endif
100
101 counter=0
102 !Parallelizable part begins
103 !$OMP PARALLEL DO &
104 !$OMP PRIVATE(cnctvt_V,k,E,fname,fname2,fname3,fname4,commandline,ra,succesM
   ,succesF,thread,exi,fi,G   ) &
105 !$OMP SHARED(cnctvt_VI,tight,cnctvt_A,natomI,seed,counter)
106 do k=1,5000
107    cnctvt_V(:,:)=cnctvt_VI(:,:)
108    thread=omp_get_thread_num()
109    fi=thread
110    !Generating random
111    do i=1,na
112       do j=1,3
113          call random_number(harvest=ra)
114          corr=.false.
115          if(cnctvt_SI(i,1).eq.1) cnctvt_V(i,1)=cnctvt_VI(i,1)+(ra-.5d0)
116          if(cnctvt_SI(i,2).eq.1) then
117             cnctvt_V(i,2)=cnctvt_VI(i,2)+(ra-.5d0)*tight*180.d0
118             if ((cnctvt_V(i,2).gt.179.99)) then
119                cnctvt_V(i,2)=360.d0-cnctvt_V(i,j)
120                cnctvt_V(i,3)=cnctvt_VI(i,3)+180.d0
121                corr=.true.
122             elseif((cnctvt_V(i,2).lt.000.01)) then
123                cnctvt_V(i,2)=360.d0-cnctvt_V(i,j)
124                cnctvt_V(i,3)=cnctvt_VI(i,3)+180.d0
125                corr=.true.
126             endif
127          endif
128          if (corr) then
129             if(cnctvt_SI(i,3).eq.1) cnctvt_V(i,3)=cnctvt_V(i,3)+(ra-.5d0)*ti
   ght*360.d0
130          else
131             if(cnctvt_SI(i,3).eq.1) cnctvt_V(i,3)=cnctvt_VI(i,3)+(ra-.5d0)*t
   ight*360.d0
132          endif
133       enddo
134    enddo
135           if (tipo.eq.'MI') then
136              !Write the mopac input with an iteration dependent filename
137              fname=''
138              write(fname,'(a15,i4.4,4a)') 'PM6.random.opt.',k,'.mop'
139              open(100+fi,file=fname,status='new')
140              write(100+fi,'(99a)') 'PM6 CHARGE=-1 LET PRECISE GRAD=.01 NOXYZ
    GRAPH PRNT=2 COMPFG CYCLES=250 GEO-OK'
141              write(100+fi,'(a30)')
142              write(100+fi,'(a30)')
143              do i=1,na
144                 write(100+fi,'(a1,3x,3(F13.6,2x,i1,x),3(i2.2,x))') natomI(i)
```

```
     ,(cnctvt_V(i,j),1,j=1,3),(cnctvt_AI(i,j),j=1,3)
145                enddo
146                close(100+fi)
147
148                !Prepare command script (all filenames iteration dependent)
149                fname2=''
150                write(fname2,'(a12,i4.4,4a)') 'command.opt.',k,'.sht'
151                open(100+fi,file=fname2,status='unknown')
152                write(100+fi,*) "echo 'Full opt ...'"
153                write(100+fi,'(40a,x,23a)') '/user/guille/programs/MOPAC09/MOPA
     C2009.exe ',fname
154                write(100+fi,*) "echo '...done full opt'"
155                close(100+fi)
156
157                !Call MOPAC
158                commandline=''
159                write(commandline,'(a3,20a)') "sh ",fname2
160                call system (commandline)
161
162                !Prepare succes  script (all filenames iteration dependent)
163                fname=''
164                fname2=''
165                fname3=''
166                fname4=''
167                write(fname ,'(a11,i4.4,4a)') 'succes.opt.',k,'.sht'
168                write(fname2,'(a15,i4.4,4a)') 'PM6.random.opt.',k,'.out'
169                write(fname3,'(a11,i4.4,4a)') 'succes.opt.',k,'.dat'
170                write(fname4,'(a11,i4.4,4a)') 'succes.opt.',k,'.tmp'
171                inquire(file=fname2,exist=exi)
172                if (exi) then
173                   open(100+fi,file=fname,status='new')
174                   write(100+fi,'(40a,x,23a,a3,19a)') "grep 'SCF FIELD WAS ACHI
     EVED' ",fname2," > ", fname3
175                   write(100+fi,'(6a,x,19a,a3,19a)')  "wc -w ",fname3," > ",fna
     me4
176                   close(100+fi)
177                else
178                   write(*,*) fname2,"does not exist after minimizing?"
179                   STOP
180                endif
181
182                !Check success
183                commandline=''
184                write(commandline,'(a3,19a)') "sh ",fname
185                call system (commandline)
186                open(100+fi,file=fname4,status='old')
187                read(100+fi,*) succesM
188                close(100+fi)
189
190                !Converged minimization:
191                if(succesM.eq.4) then
192
193                   !Prepare geom-fish and mopac input for freqs (all filenames
     iteration dependent)
194                   fname=''
195                   fname2=''
196                   fname3=''
197                   write(fname ,'(a12,i4.4,a4)') 'get.mat.frq.',k,'.sht'
198                   write(fname2,'(a15,i4.4,4a)') 'PM6.random.frq.',k,'.mop'
199                   write(fname3,'(a15,i4.4,4a)') 'PM6.random.opt.',k,'.arc'
200                   write(fname4,'(a15,i4.4,4a)') 'PM6.random.opt.',k,'.out'
201                   inquire(file=fname4,exist=exi)
202                   if (exi) then
203                       open(100+fi,file=fname,status='new')
204                       write(100+fi,'(a25,x,a23)')" echo PM6 FORCE   > ",fname2
205                       write(100+fi,'(a10,x,a23)')" echo >> ",fname2
206                       write(100+fi,'(a10,x,a23)')" echo >> ",fname2
207                       write(100+fi,'(a50,x,a23)') "echo XX 0.0 0 0.0 0 0.0 0 0
      0 0 >> ", fname2
208                       write(100+fi,'(a6,i3,x,a23,a4,a23)') "tail ",-na,fname3,
     " >> ", fname2
209                       close(100+fi)
210                   else
211                      write(*,*) fname4,"does not exist when calc freqs?"
212                      STOP
```

```
213                   endif
214
215                   !Fish geometries and create mopac input
216                   commandline=''
217                   write(commandline,'(a3,20a)') "sh ",fname
218                   call system (commandline)
219
220                   !Prepare MOPAC script (filenames are iteration dependent)
221                   fname=''
222                   write(fname,'(a12,i4.4,4a)') 'command.frq.',k,'.sht'
223                   open(100+fi,file=fname,status='new')
224                   write(100+fi,*) "echo 'Freq calc...'"
225                   write(100+fi,'(40a,x,23a)') '/user/guille/programs/MOPAC09/M
    OPAC2009.exe ',fname2
226                   write(100+fi,*) "echo '...done freqs'"
227                   close(100+fi)
228
229                   !Call MOPAC
230                   commandline=''
231                   write(commandline,'(a3,20a)') "sh ",fname
232                   call system (commandline)
233
234                   !Prepare freq-fish script (filenames iteration dependent)
235                   fname=''
236                   fname2=''
237                   fname3=''
238                   fname4=''
239                   write(fname, '(a12,i4.4,4a)') 'get.neg.frq.',k,'.sht'
240                   write(fname2,'(a15,i4.4,4a)') 'PM6.random.frq.',k,'.out'
241                   write(fname3,'(a11,i4.4,4a)') 'succes.frq.',k,'.dat'
242                   write(fname4,'(a11,i4.4,4a)') 'succes.frq.',k,'.tmp'
243                   inquire(file=fname2,exist=exi)
244                   if (exi) then
245                      open(100+fi,file=fname,status='new')
246                      write(100+fi,'(a10,a23,a40,a23)') "grep FREQ ",fname2," |
     awk '{print $2}' | grep '\-' > ",fname3
247                      write(100+fi,'(a10,a23,a3, a23)') "wc -w ",fname3," > ",f
    name4
248                      close(100+fi)
249                   else
250                      write(*,*) fname2,"does not exist after calc freqs?"
251                      STOP
252                   endif
253
254                   !Get freqs
255                   commandline=''
256                   write(commandline,'(a3,20a)') "sh ",fname
257                   call system (commandline)
258                   open(100+fi,file=fname4,status='old')
259                   read(100+fi,*) succesF
260                   close(100+fi)
261
262                   !Loop of only positive frequencies
263                   if (succesF.eq.0) then
264                      !Get energy (just one commandline, no script)
265                      commandline=''
266                      fname3=''
267                      write(fname3,'(a15,i4.4,4a)') 'PM6.random.opt.',k,'.arc'
268                      write(commandline,'(a26,x,a23,a5,i4.4,4a)') "grep 'HEAT O
    F FORMATION' ",fname3," > E.",k,".tmp"
269                      call system (commandline)
270                      fname=''
271                      write(fname,'(a2,i4.4,a4)') "E.",k,".tmp"
272                      open(100+fi,file=fname,status='old')
273                      read(100+fi,*) (dummychar,i=1,4),E
274                      close(100+fi)
275                      write(*,*) "Minimization succesfully converged at ",E
276                      fname3=''
277                      write(fname3,'(a1,i4.4,F3.2,a,i4.4,a8)') 'E',int(E),(E-re
    al(int(E)))-0.005d0,'_',k,'.opt.out'
278                      if (E.le.-1d0) write(fname3,'(a1,i4.3,F3.2,a,i4.4,a8)') '
    E',int(E),-(E-real(int(E))+0.005d0),'_',k,'.opt.out'
279                      if ((E.gt.-1d0).and.(E.lt.0.d0)) write(fname3,'(a2,i3.3,F
    3.2,a,i4.4,a8)')&
280                                                'E-',int(E),-(E-real(int(E))+0.005d0),
```

```
     '_',k,'.opt.out'
281
282                      !Preparing script for saving geometry of checked-minimum
283                      fname=''
284                      fname2=''
285                      write(fname, '(a8,i4.4,a4)') 'do.save.',k,'.sht'
286                      write(fname2,'(a15,i4.4,4a)') 'PM6.random.opt.',k,'.out'
287                      open(100+fi,file=fname,status='new')
288                      write(100+fi,'(a3,a23,x,a24)') "cp ",fname2,fname3
289                      write(100+fi,*) "bzip2 ",fname3
290                      write(100+fi,'(a20,a24,a15,i2)') "echo done saving ",fnam
     e3," in thread ",thread
291                      close(100+fi)
292
293                      !Save geometry
294                      write(commandline,'(a3,a16)') "sh ",fname
295                      call system (commandline)
296
297                      !Append energy
298                      open(100+fi,file='E.dat',status='old',position='append')
299                      write(100+fi,'(E20.10E3)') E
300                      close(100+fi)
301                   endif
302                   !End loop positive frequencies
303                endif
304                !End loop of converged point
305
306             !For TS search
307             elseif((tipo.eq.'TS')) then
308                !Prepare input mopac file
309                write(fname,'(a18,i4.4,4a)') 'PM6.random.opt.H1.',k,'.mop'
310                open(100+fi,file=fname,status='new')
311                write(100+fi,'(99a)') 'PM6 LET NOXYZ GRAPH PRNT=2 COMPFG  GEO-O
     K '
312                write(100+fi,'(a30)')
313                write(100+fi,'(a30)')
314                do i=1,na
315                   if (natomI(i).ne.'H') write(100+fi,'(a1,3x,3(F13.6,2x,i1,x),
     3(i2.2,x))') natomI(i),&
316                                                          (cnctvt_V(i,j),0,j=1,3
     ),(cnctvt_AI(i,j),j=1,3)
317                   if (natomI(i).eq.'H') write(100+fi,'(a1,3x,3(F13.6,2x,i1,x),
     3(i2.2,x))') natomI(i),&
318                                                          (cnctvt_V(i,j),1,j=1,3
     ),(cnctvt_AI(i,j),j=1,3)
319                enddo
320                write(100+fi,*)
321                write(100+fi,*) "oldgeo PM6 1SCF  NOXYZ"  !This is to force the
      production of an .arc file!!!
322                write(100+fi,*)
323                close(100+fi)
324
325                !Call mopac on opt H1 (all filenames iteration dependent)
326                commandline=''
327                call system ("echo 'Hs opt....'")
328                write(commandline,'(15a,x,26a)') './MOPAC2009.exe ',fname
329                call system (commandline)
330                call system ("echo '...done Hs opt'")
331
332                !Check for succesfull opt of H1
333                fname3=''
334                write(fname3,'(a18,i4.4,4a)') 'PM6.random.opt.H1.',k,'.arc'
335                inquire(file=fname3,exist=exi)
336                !Fish geom
337                if (exi) then
338                   fname2=''
339                   write(fname2,'(a17,i4.4,4a)') 'PM6.random.TS.Cs.',k,'.mop'
340                   commandline=''
341                   write(commandline,'(a40,x,a25)') "echo XX 0.0 0 0.0 0 0.0 0 0
      0 0 > ", fname2
342                   call system (commandline)
343                   commandline=''
344                   write(commandline,'(a6,i3,x,a26,a4,a25)') "tail ",-na,fname3,
     " >> ", fname2
345                   call system(commandline)
```

```
346                 !Check for succesfull tailing for H1.arc
347                 inquire(file=fname2,exist=exi)
348                 if (exi) then
349                    !Extract geometry
350                    call getzmatmopac (fname2,na,natom,cnctvt_A,cnctvt_V,cnctv
    t_S)
351                    !Prepare mop file for optimizing TS all not TS carbon (all
     filenames iteration dependent)
352                    open(100+fi,file=fname2,status='old')
353                    write(100+fi,*) "PM6 RECALC=5 TS LET  NOXYZ GRAPH PRNT=2 C
    OMPFG  GNORM=.10 GEO-OK "
354                    write(100+fi,*)
355                    write(100+fi,*)
356                    do i=1,na
357                       if (natomI(i).eq.'H') write(100+fi,'(a1,3x,3(F13.6,2x,i
    1,x),3(i2.2,x))')&
358                                             natomI(i),(cnctvt_V(i,j),0,j=1,3)
    ,(cnctvt_AI(i,j),j=1,3)
359                       if (natomI(i).ne.'H') write(100+fi,'(a1,3x,3(F13.6,2x,i
    1,x),3(i2.2,x))')&
360                                             natomI(i),(cnctvt_V(i,j),1,j=1,3)
    ,(cnctvt_AI(i,j),j=1,3)
361                    enddo
362                    write(100+fi,*)
363                    write(100+fi,*) "oldgeo PM6 1SCF  NOXYZ"  !This is to forc
    e the production of an .arc file!!!
364                    write(100+fi,*)
365                    close(100+fi)
366                    !Call mopac on opt TS C only (all filenames iteration depe
    ndent)
367                    commandline=''
368                    call system ("echo 'Cs opt TS...'")
369                    write(commandline,'(15a,x,25a)') './MOPAC2009.exe ',fname2
370                    call system (commandline)
371                    call system ("echo '...done TS Cs opt'")
372                    !Check for succesfull opt TS of C only
373                    fname3=''
374                    write(fname3,'(a17,i4.4,4a)') 'PM6.random.TS.Cs.',k,'.arc'
375                    inquire(file=fname3,exist=exi)
376                    if (exi) then
377                       !Fish geom
378                       fname2=''
379                       write(fname2,'(a18,i4.4,4a)') 'PM6.random.opt.H2.',k,'.
    mop'
380                       commandline=''
381                       write(commandline,'(a40,x,a26)') "echo XX 0.0 0 0.0 0 0
    .0 0 0 0 0 > ", fname2
382                       call system (commandline)
383                       commandline=''
384                       write(commandline,'(a6,i3,x,a25,a4,a26)') "tail ",-na,f
    name3," >> ", fname2
385                       call system (commandline)
386                       !Check for succesfull tailing for TS.Cs.arc
387                       inquire(file=fname2,exist=exi)
388                       if (exi) then
389                          !Extract geometry
390                          call getzmatmopac (fname2,na,natom,cnctvt_A,cnctvt_V
    ,cnctvt_S)
391                          ! Prepare mop file for reoptimizing only HS (all fil
    enames iteration dependent)
392                          open(100+fi,file=fname2,status='old')
393                          write(100+fi,*) "PM6 LET NOXYZ GRAPH PRNT=2 COMPFG
    GEO-OK"
394                          write(100+fi,*)
395                          write(100+fi,*)
396                          do i=1,na
397                             if (natomI(i).ne.'H')write(100+fi,'(a1,3x,3(F13.6
    ,2x,i1,x),3(i2.2,x))') natomI(i),(cnctvt_V(i,j),0,j=1,3),(cnctvt_AI(i,j),j=1
    ,3)
398                             if (natomI(i).eq.'H')write(100+fi,'(a1,3x,3(F13.6
    ,2x,i1,x),3(i2.2,x))') natomI(i),(cnctvt_V(i,j),1,j=1,3),(cnctvt_AI(i,j),j=1
    ,3)
399                          enddo
400                          write(100+fi,*)
401                          write(100+fi,*) "oldgeo PM6 1SCF  NOXYZ"  !This is t
```

```
      o force the production of an .arc file!!!
  402                          write(100+fi,*)
  403                          close(100+fi)
  404                          !Call mopac reoptimizing H only (all filenames itera
      tion dependent)
  405                          commandline=''
  406                          call system ("echo 'Hs reopt...'")
  407                          write(commandline,'(15a,x,26a)') './MOPAC2009.exe ',
      fname2
  408                          call system (commandline)
  409                          call system ("echo '...done Hs reopt'")
  410                          !Check for succesfull reop of H2
  411                          fname3=''
  412                          write(fname3,'(a18,i4.4,4a)') 'PM6.random.opt.H2.',k
      ,'.arc'
  413                          inquire(file=fname3,exist=exi)
  414                          if (exi) then
  415                             !Fish geom
  416                             fname2=''
  417                             write(fname2,'(a18,i4.4,4a)') 'PM6.random.opt.TS.
      ',k,'.mop'
  418                             commandline=''
  419                             write(commandline,'(a40,x,a26)') "echo XX 0.0 0 0
      .0 0 0.0 0 0 0 0 > ", fname2
  420                             call system (commandline)
  421                             commandline=''
  422                             write(commandline,'(a6,i3,x,a26,a4,a26)') "tail "
      ,-na,fname3," >> ", fname2
  423                             call system (commandline)
  424                             !Check for succesfull tailing for opt.H2s.arc
  425                             inquire(file=fname2,exist=exi)
  426                             if (exi) then
  427                                !Extract geometry
  428                                call getzmatmopac (fname2,na,natom,cnctvt_A,cn
      ctvt_V,cnctvt_S)
  429                                !Prepare mop file for optimizing FULL TS HS (a
      ll filenames iteration dependent)
  430                                open(100+fi,file=fname2,status='old')
  431                                write(100+fi,*) "PM6 TS LET NOXYZ GRAPH PRNT=2
       COMPFG  GNORM=.1 GEO-OK "
  432                                write(100+fi,*)
  433                                write(100+fi,*)
  434                                do i=1,na
  435                                   write(100+fi,'(a1,3x,3(F13.6,2x,i1,x),3(i2.
      2,x))') natomI(i),&
  436                                                          (cnctvt_V(i,j),1,j=1,3),(c
      nctvt_AI(i,j),j=1,3)
  437                                enddo
  438                                write(100+fi,*)
  439                                write(100+fi,*) "oldgeo PM6 1SCF NOXYZ GRAD"
      !This is to force the production of an .arc file!!!
  440                                write(100+fi,*)
  441                                close(100+fi)
  442                                !Call mopac FULL TS OPTIMIZING (all filenames
      iteration dependent)
  443                                commandline=''
  444                                call system ("echo 'FULL TS opt...'")
  445                                write(commandline,'(15a,x,26a)') './MOPAC2009.
      exe ',fname2
  446                                call system (commandline)
  447                                call system ("echo '...done FULL TS opt'")
  448                             else
  449                                write(*,*) fname2,"does not exist after tailin
      g H2.arc?"
  450                                STOP
  451                             endif
  452                          else
  453                              write(*,*) fname3,"does not exist after reopting
       H2?"
  454                              STOP
  455                          endif
  456
  457                       else
  458                          write(*,*) fname2,"does not exist after tailing TS.C
      S.arc?"
```

```
459                         STOP
460                      endif
461
462                   else
463                      write(*,*) fname3,"does not exist after opting TS C?"
464                      STOP
465                   endif
466                else
467                   write(*,*) fname2,"does not exist after tailing H1.arc?"
468                   STOP
469                endif
470             else
471                write(*,*) fname3,"does not after opt H1?"
472                STOP
473             endif
474
475             !Get energy (just one commandline, no script)
476             commandline=''
477             fname2=''
478             write(fname2,'(a18,i4.4,4a)') 'PM6.random.opt.TS.',k,'.arc'
479             write(commandline,'(a26,x,a26,a5,i4.4,4a)') "grep 'HEAT OF FORMA
    TION' ",fname2," > E.",k,".tmp"
480             call system (commandline)
481             commandline=''
482             write(commandline,'(a26,x,a26,a6,i4.4,4a)') "grep 'GRADIENT NORM
     '    ",fname2," >>E.",k,".tmp"
483             call system (commandline)
484             fname=''
485             write(fname,'(a2,i4.4,a4)') "E.",k,".tmp"
486             open(100+fi,file=fname,status='old')
487             read(100+fi,*) (dummychar,i=1,4),E
488             read(100+fi,*) (dummychar,i=1,3),G
489             close(100+fi)
490             write(*,*) "Last energy is ",E
491             write(*,*) "Last gradient  ",G
492             fname3=''
493             write(fname3,'(a1,i4.4,F3.2,a,a,i3.3,F3.2,a,i4.4,a8)') 'E',int(E
    ),(E-real(int(E)))-0.005d0,'_',&
494                                                                    'G',int(G
    ),(G-real(int(G)))-0.005d0,'_',k,'.opt.out'
495             if (E.le.-1d0) &
496             write(fname3,'(a1,i4.3,F3.2,a,a,i3.3,F3.2,a,i4.4,a8)') &
497                                                                    'E',int(E
    ),-(E-real(int(E))+0.005d0),'_',&
498                                                                    'G',int(G
    ), (G-real(int(G))-0.005d0),'_',k,'.opt.out'
499             if ((E.gt.-1d0).and.(E.lt.0.d0)) &
500             write(fname3,'(a2,i3.3,F3.2,a,a,i3.3,F3.2,a,i4.4,a8)') &
501                                                                   'E-',int(E
    ),-(E-real(int(E))+0.005d0),'_',&
502                                                                    'G',int(G
    ), (G-real(int(G))-0.005d0),'_',k,'.opt.out'
503
504             !Preparing script for saving geometry of checked-minimum
505             fname=''
506             write(fname, '(a6,i4.4,a4)') 'do.cp.',k,'.sht'
507             open(100+fi,file=fname,status='new')
508             write(100+fi,'(a3,a26,x,a35)')"cp ",fname2,fname3
509             write(100+fi,*) "bzip2 ",fname3
510             write(100+fi,'(a20,a24,a15,i2)') "echo done saving ",fname3," in
     thread ",thread
511             close(100+fi)
512
513             !Save geometry
514             write(commandline,'(a3,a16)') "sh ",fname
515             call system (commandline)
516
517             !Append energy
518             open(100+fi,file='E.dat',status='old',position='append')
519             write(100+fi,'(E20.10E3)') E
520             close(100+fi)
521
522
523          endif
524
```

```
525
526      !Clean files
527      counter=counter+1
528      fname=''
529      write(fname,'(a12,i4.4,4a)') 'clean.after.',k,'.sht'
530      open(100+fi,file=fname,status='new')
531      write(100+fi,'(a4,i4.4,a5)') "rm *",k,"*.mop"
532      write(100+fi,'(a4,i4.4,a5)') "rm *",k,"*.arc"
533      write(100+fi,'(a4,i4.4,a5)') "rm *",k,"*.gpt"
534      write(100+fi,'(a4,i4.4,a5)') "rm *",k,"*.sht"
535      write(100+fi,'(a4,i4.4,a5)') "rm *",k,"*.tmp"
536      write(100+fi,'(a4,i4.4,a5)') "rm *",k,"*.out"
537      write(100+fi,'(a4,i4.4,a5)') "rm *",k,"*.dat"
538      write(100+fi,'(a4,i4.4,a5)') "rm *",k,"*.res"
539      write(100+fi,'(a4,i4.4,a5)') "rm *",k,"*.den"
540      write(100+fi,'(a21,x,i4.4,x,a15)') "echo Already tried",counter,"geometri
     es"
541      close(100+fi)
542      write(commandline,'(a3,a25,x,a19,x,a18)') "sh ",fname
543      call system (commandline)
544
545   enddo
546   !$OMP END PARALLEL DO
547   end
548   !######################
549   function signo(arg)
550   implicit none
551   integer signo,arg
552
553   if (arg.lt.0.d0) signo=-1
554   if (arg.ge.0.d0) signo=+1
555   end function
556   !########################
557   subroutine getzmatmopac(fname,na,natom,cnctvt_A,cnctvt_V,cnctvt_S)
558   implicit none
559   integer,parameter :: DP=kind(1.d0)
560   !coming from the main program
561   character*35,intent(IN) :: fname
562   character*1   natom(1:na)
563   integer na
564   real(kind=DP) cnctvt_V(1:na,1:3)  !Conectivity value
565   integer       cnctvt_A(1:na,1:3)  !Conectivity atom
566   integer       cnctvt_S(1:na,1:3)  !Conectivity status
567
568   !subroutine internal
569   integer i,j,k
570   cnctvt_A(:,:)=0
571   cnctvt_S(:,:)=0
572   cnctvt_V(:,:)=0.d0
573   open(200,file=fname,status='old')
574
575   i=1
576   read(200,*)    natom(i),(cnctvt_V(i,j),cnctvt_S(i,j),j=1,3)
577   !write(*,'(a1,x,3(F10.3,x,i2),x,3(i2,x))') natom(i),(cnctvt_V(i,j),cnctvt_S(
     i,j),j=1,3),(cnctvt_A(i,j),j=1,3)
578   do i=2,na
579      read(200,*) natom(i),(cnctvt_V(i,j),cnctvt_S(i,j),j=1,3),(cnctvt_A(i,j),j
     =1,3)
580   !   write(*,'(a1,x,3(F10.3,x,i2),x,3(i2,x))') natom(i),(cnctvt_V(i,j),cnctvt
     _S(i,j),j=1,3),(cnctvt_A(i,j),j=1,3)
581   enddo
582   close(200)
583
584   end subroutine
```

- `alignMOPAC.f90`

  This program complements the main conformer search-algorithm, since the only output of `randomizeparallel` consists only of the master energy-file `E.dat` and and the compressed `bz2`-files. The task lying ahead is that of sorting the randomly generated population of geometries into meaningful groups of similar (energetically and structurally) individuals. `alignMOPAC` performs that first step by selecting an energy range out of the original distribution, sorting the geometries within that range by relative stabilities, and re-aligning them in Cartesian coordinates with the same orientation.

  `alignMOPAC` starts by creating a list of converged `bz2`-files that is sorted by energy values (line `37`). This task is straightforward because the zipped `bz2`-files contain their respective energy values directly in their filenames, and so there is no need to unzip and open each separate file to retrieve the energy values. Bearing in mind that up to 5000 geometries were computed at once while testing the program, this is a valuable time saving. With the energy information made available, the program prompts the user for a given energy range (see lines `78-81`). Then, the algorithm advances the list of `bz2`-files until the energy range has been reached and extracts each geometry within that range (lines `97-100`). For the first geometry, the code calls the molecular visualization software MOLDEN[130] and displays the first optimization in full (lines `102-113`). This way, a the user can select four atoms that will determine the orientation of the retrieved geometries (`na1,na2,na3,na4`).

  The rest of geometries are retrieved, converted to Cartesian and oriented (lines `136` and `137`) accordingly. The subroutine `orientate` handles the orientation (see bottom of the source code). For completeness, the code also tries to reorient pairs of enantiomers, too (lines `139-185`). The sorted, oriented population of geometries are finally stored in the file `aligned.mld`. Visualization of this file with MOLDEN provides a quick overview of all obtained geometries and energies. Further handling of the geometries is done by the program `isocheck.f90`, explained in the following.

```
program alginMOPAC!This program reads .xyz geometries from a bunch
                  !of randomly generated isomers through MOPAC's semiempiric
al
implicit none
integer,parameter :: DP=kind(1.d0)
integer i,j,k
integer n,na,counter
integer na1,na2,na3,na4
character*40 dummychar
character*35 filename
character*150 command
character*1 answer
real(kind=DP) EL,EH                          !E_high,E_low,E_rough
real(kind=DP),allocatable:: E(:),Er(:)
real(kind=DP),allocatable:: cart    (:,:)  !cartesian coords
real(kind=DP),allocatable:: cartp   (:,:)  !cartesian coords of previous ite
r
real(kind=DP),allocatable:: cartn   (:,:)  !cartesian coords after correctio
n
real(kind=DP),allocatable:: cnctvt_V(:,:)  !Conectivity value
integer,allocatable ::      cnctvt_A(:,:)  !Conectivity atom
integer,allocatable ::      cnctvt_S(:,:)  !Conectivity status
character*1,allocatable::   natom(:)
character*5                 operation
real(kind=DP)               diff,thres
character*75 commandline
logical exi

inquire(file='align.in',exist=exi)
if (exi) then
else
   write(*,*) "Need align.in to work!"
   STOP
endif
filename=''
open(10,file='align.in',status='old')
read(10,*) filename
close(10)
call system ("ls -1 *.bz2 > files.tmp")
call system ("ls -1 *.bz2 | sed 's/_/ /' | sed 's/E//' > files_seg.tmp")
!ATTENTION. IN THIS PROGRAM THE RANDOM ORDER IN WHICH GEOMS WERE GENERATED I
S
!NOT CONSIDERED. INDEED, MAIN GOAL IS TO ORDER GEOMETRIES ACCORDING TO HEATS
 OF FORMATION
call system ("paste files_seg.tmp files.tmp | awk '{print $1,$3}' | sort -n
 > info.tmp")
call system ("wc -l info.tmp  > n.tmp")
open(50,file='grep.na.sh',status='new')
write(50,'(15a,35a,25a)') "grep '\.' ",filename," | wc -l > na.tmp"
close(50)
!write(commandline,'(15a,35a,25a)') "grep '\.' ",filename," | wc -l > na.tmp
"
call system ("sh grep.na.sh")
call system ("rm grep.na.sh")
open(50,file='n.tmp',status='old')
read (50,*) n
close(50)

open(50,file='na.tmp',status='old')
read (50,*) na
close(50)

allocate(cnctvt_V(1:na,1:3),cnctvt_A(1:na,1:3),cnctvt_S(1:na,1:3))
allocate(cart(1:na,1:3),cartp(1:na,1:3),cartn(1:na,1:3))
allocate(natom(1:na))

!Threshold for difference of geometries
thres=5.d0
!Initialize
cnctvt_V(:,:)=0.d0
cnctvt_A(:,:)=0
cart    (:,:)=0.d0
cartp    (:,:)=0.d0
cartn    (:,:)=0.d0
write(*,*) "Can read up to ",n,"geometries with ",na," atoms."
```

```
 69  allocate(Er(1:n),E(1:n))
 70  write(*,*) "Making an estimate of energies..."
 71  open(80,file='info.tmp',status='old')
 72  do i=1,n
 73     read(80,*) Er(i)
 74  enddo
 75  close(80)
 76  EL=minval(Er(:))-.5
 77  EH=maxval(Er(:))+.5
 78  write(*,'(a10,i6,a20,i2,a20,F20.10,a10,F20.10,a)') "Found ",n," geometries o
     f ",na," atoms between ",EL," and ",EH,"."
 79  write(*,*) "Do you want to lower that number to a particular range of energi
     es?(y/n)"
 80  read(*,*)  answer
 81  if (answer.eq.'y') read(*,*) EL,EH
 82
 83  open(60,file='info.tmp',status='old')
 84  open(70,file='aligned.mld',status='unknown')
 85  counter=1
 86  do i=1,n
 87
 88     !Initialize the marker for the ev. mirroring operation
 89     operation='none'
 90
 91     !Get the filenames and energy values
 92     !read(60,*) Er(i),dummychar,filename
 93     read(60,*) Er(i),filename
 94
 95     !Once you are in the energy range you want
 96  !   if (answer.eq.'n') read(*,*) EL,EH
 97     if ((Er(i).ge.EL).and.(Er(i).le.EH)) then
 98        write(commandline,'(a11,a35,a17)') "bunzip2 -c ",filename," > align_wo
     rk.tmp"
 99        !write(command,'(a11,a40,a25)') "cp         ",filename,"   align_work.
     tmp"
100        call system (commandline)
101
102        !Perform one first molden viewing to choose atoms of orientaton
103        if (counter.eq.1) then
104           write(*,*) "Choose the atoms for orientation NA1,NA2,NA3 and NA4"
105           call system ("molden align_work.tmp")
106           write(*,*) "Center of mass(CM) of NA1 and NA2 in the origin"
107           write(*,*) "CM--NA3 on the z-axis"
108           write(*,*) "CM-NA3-NA4   on the y=0 plane"
109           write(*,*) "if origin needs to be one atom, then NA1=NA2"
110           write(*,*) "Please type NA1,NA2,NA3,NA4................."
111           read(*,*) na1,na2,na3,na4
112           write(*,*) "Centering in  ",na1,na2,na3,na4
113        endif
114
115        call system (" grep 'FINAL HEAT' align_work.tmp | awk '{print $6}' > E
     .align.tmp")
116        open(66,file='E.align.tmp',status='old')
117        read(66,*) E(i)
118        close(66)
119        call system ("sed -n '/FINAL HEAT/,/Empirical/p' align_work.tmp | sed
     -n '/NC:NB:NA:I/,/Empirical/p' | grep -v NC > zmat.align.tmp1 ")
120        call system ("sed  's/XX/X/'  zmat.align.tmp1 > zmat.align.tmp")
121
122        !Get geometry as zmatrix
123        open(67,file='zmat.align.tmp',status='old')
124        read(67,*) dummychar,natom(1),(cnctvt_V(1,k),dummychar,k=1,3)
125        read(67,*) dummychar,natom(2),(cnctvt_V(2,k),dummychar,k=1,3),(cnctvt_
     A(2,k),k=1,1)
126        read(67,*) dummychar,natom(3),(cnctvt_V(3,k),dummychar,k=1,3),(cnctvt_
     A(3,k),k=1,2)
127        do j=4,na
128           read(67,*) dummychar,natom(j),(cnctvt_V(j,k),dummychar,k=1,3),(cnct
     vt_A(j,k),k=1,3)
129        enddo
130        close(67)
131  !      do j=1,na
132  !         write(*,'(a1,2x,3(F13.6,2x,i2,2x))') natom(j),(cnctvt_V(j,k),cnctv
     t_A(j,k),k=1,3)
133  !      enddo
```

```
134
135         !Orient
136         call zmatcart (na,cnctvt_V(:,:),cnctvt_A(:,:),cart(:,:))
137         call orientate (na,cart(:,1),cart(:,2),cart(:,3),na1,na2,na3,na4)
138
139         !Calculate difference with previous geometry
140         if (i.gt.1) then
141            diff=0.d0
142            !Sum differences in coordinates
143            do j=1,na
144               do k=1,3
145                  diff=diff+(cartp(j,k)-cart(j,k))**2
146               enddo
147            enddo
148            write(700,'(a25,2(F13.6,x),i3,a4,i3)') filename,E(i),diff,counter,"
    <-->",counter-1
149
150            !If found different geometries
151            if    (dabs(diff).gt.thres) then
152               write(*,*) "Found different geometries, diff=",diff
153
154               !Mirror geometry and reorient
155               cartn(:,:)= cart(:,:)
156               cartn(:,3)=-cart(:,3)
157               call orientate (na,cartn(:,1),cartn(:,2),cartn(:,3),na1,na2,na3,
    na4)
158               operation='mirror'
159
160               !Recalculate differences after mirroring and orientation (check
    if succesful)
161               diff=0.d0
162               do k=1,3
163                  do j=1,na
164                     diff=diff+(cartn(j,k)-cartp(j,k))**2
165                  enddo
166               enddo
167               write(*,'(a40,F13.6,x,i6,a4,i6)') 'After mirror on xy and reorie
    nt, diff=',diff,counter,"<-->",counter-1
168
169   !             write(* ,*) na+4
170   !             write(* ,*) 'SCF Done',E(i)
171   !             do j=1,na
172   !                if ((j.eq.2).or.(j.eq.10).or.(j.eq.11)) then
173   !                   write(* ,'(a1,2x,3(F13.6,2x))') 'B'     ,(cartn(j,k),k=1,
    3)
174   !                else
175   !                   write(* ,'(a1,2x,3(F13.6,2x))') natom(j),(cartn(j,k),k=1,
    3)
176   !                endif
177   !             enddo
178   !             write(* ,*) "X 0.0 0.0 0.0"
179   !             write(* ,*) "X 1.0 0.0 0.0"
180   !             write(* ,*) "X 0.0 2.0 0.0"
181   !             write(* ,*) "X 0.0 0.0 3.0"
182
183               cart(:,:)=cartn(:,:)
184            endif
185         endif
186         write(*,*) filename,E(i),diff
187         write(70,*) na+4
188         write(70,*) 'SCF Done',E(i)
189         do j=1,na
190            if ((j.eq.2).or.(j.eq.10).or.(j.eq.11)) then
191               !write(70,'(a1,2x,3(F13.6,2x))') 'B'     ,(cart(j,k),k=1,3)
192               write(70,'(a1,2x,3(F13.6,2x))') natom(j),(cart(j,k),k=1,3)
193            else
194               write(70,'(a1,2x,3(F13.6,2x))') natom(j),(cart(j,k),k=1,3)
195            endif
196         enddo
197         write(70,*) "X 0.0 0.0 0.0"
198         write(70,*) "X 1.0 0.0 0.0"
199         write(70,*) "X 0.0 2.0 0.0"
200         write(70,*) "X 0.0 0.0 3.0"
201         counter=counter+1
202         cartp(:,:)=cart(:,:)
```

```
203      else
204   !       write(*,*) filename," not read."
205      endif
206   enddo
207   write(*,*) "aligned.mld has",counter-1," geoms."
208   close(60)
209   close(70)
210   !call system ("rm *.tmp")
211   end
212   !################################
213   subroutine orientate  (na,x,y,z,na1,na2,na3,na4)
214   ! Orients n atoms with respect to 4 of them: NA1,NA2,NA3,NA4 resulting in
215   ! Center of mass(CM) of NA1 and NA2 in the origin
216   ! CM--NA3 on the z-axis
217   ! CM-NA3-NA4   on the y=0 plane
218   ! if origin needs to be one atom, then NA1=NA2
219   implicit none
220
221   integer na,na1,na2,na3,na4
222   integer,parameter :: DP=kind(1.d0)
223   integer i,j,k
224
225   real(kind=DP)  x(1:na),y(1:na),z(1:na)
226   real*8 xd(1:na),yd(1:na),zd(1:na)
227
228   real*8 rho(1:na),theta(1:na),h(1:na)
229
230   !Center the geometry in CM(NA1,NA2)
231   x=x-(x(na1)+x(na2))/2.d0
232   y=y-(y(na1)+y(na2))/2.d0
233   z=z-(z(na1)+z(na2))/2.d0
234
235   !CM-na3 on the z-axis:
236   !First, Bond CM-na3 on the zx-plane
237   call cart2cyl (na,x,y,z,rho,theta,h) !Transform to cylindrical coordinates
238   theta=theta-theta(na3)
239   call cyl2cart (na,rho,theta,h,x,y,z) !Transform back to cartesian
240
241   !Second, Bond CM-na3 on the z-axis,careful:theta defined with this axis
242   call cart2cyl (na,z,x,y,rho,theta,h)
243   theta=theta-theta(na3)
244   call cyl2cart (na,rho,theta,h,z,x,y)
245
246   !Plane CM-na3-na4 is on the xz-plane
247   call cart2cyl (na,x,y,z,rho,theta,h)
248   theta=theta-theta(na4)
249   call cyl2cart (na,rho,theta,h,x,y,z)
250   !Molecule is oriented!
251   end subroutine
252   !#####################################
253   SUBROUTINE cart2cyl (n,x,y,z,rho,theta,h)
254   implicit none
255   integer i
256   integer n
257   !real*8,parameter :: pi=dacos(-1.d0)
258   real*8           :: pi
259   real*8,parameter :: zero=1.d-8
260   real*8 x(1:n),y(1:n),z(1:n)
261   real*8 rho(1:n),theta(1:n),h(1:n)
262   logical debug
263
264   pi=dacos(-1.d0)
265   debug=.false.
266
267   !Defintion of cylindrical coordinates in I. quadrant
268   !Rho
269   rho=dsqrt(x**2+y**2)
270   !Make sure theta=90° is defined
271   do i=1,n
272      if (dabs(x(i)).lt.zero) then
273         theta(i)=dacos(-1.d0)/2
274      else
275         theta(i)=datan(dabs(y(i)/x(i)))
276      endif
277   enddo
```

```
278   h=z
279   !Correct theta for the appropiate quadrant
280   do i=1,n
281      if(debug) write(*,*) i
282      if     (x(i).gt.+zero)         then
283
284            if     (y(i).gt.+zero)        then
285                  theta(i)=theta(i)
286                  if(debug) write(*,*)"+ +"
287            elseif(dabs(y(i)).le.+10.d-5) then
288                  theta(i)=0.d0
289                  if(debug) write(*,*)"+ 0"
290            elseif(y(i).lt.-zero)        then
291                  theta(i)=2.d0*pi-theta(i)
292                  if(debug) write(*,*)"+ -"
293            endif
294
295      elseif(dabs(x(i)).le.+zero)  then
296
297            if     (y(i).gt.+zero)        then
298                  theta(i)=pi/2.d0
299                  if(debug) write(*,*)"0 +"
300            elseif(dabs(y(i)).le.+zero) then
301                   theta(i)=0.d0
302                   if(debug) write(*,*)"0 0"
303            elseif(y(i).lt.zero)         then
304                  theta(i)=1.5*pi/2.d0
305                  if(debug) write(*,*)"0 -"
306            endif
307
308      elseif((x(i).lt.-zero))       then
309
310            if     (y(i).gt.+zero)       then
311                  theta(i)=pi-theta(i)
312                  if(debug) write(*,*)"- +"
313            elseif(dabs(y(i)).lt.+zero) then
314                  theta(i)=pi
315                  if(debug) write(*,*)"- 0"
316            elseif(y(i).lt.-zero)       then
317                  theta(i)=pi+theta(i)
318                  if(debug) write(*,*)"- -"
319            endif
320      endif
321   if(debug) then
322      write (*,'(3(F13.6,x))') x(i),y(i),z(i)
323      write (*,'(3(F13.6,x))') rho(i),(180.0d0/pi)*theta(i),h(i)
324      write (*,*)
325   endif
326   enddo
327
328   !Re-transform and return to main program, just for test
329   x=rho*dcos(theta)
330   y=rho*dsin(theta)
331   z=h
332
333   end subroutine
334   !################################
335   SUBROUTINE cyl2cart (n,rho,theta,h,x,y,z)
336   implicit none
337   integer i
338   integer n
339   real*8 x(1:n),y(1:n),z(1:n)
340   real*8 rho(1:n),theta(1:n),h(1:n)
341
342   x=rho*dcos(theta)
343   y=rho*dsin(theta)
344   z=h
345
346   end subroutine
```

- `isocheck.f90`

  This program further complements the random search program `randomizeparallel` and the geometry-extractor program `alignMOPAC`. `isocheck` takes the file `aligned.mld` as an input, which in turn is the output of `alignMOPAC` (see above). All the geometries of interest are sorted by stability and oriented in `aligned.mld`. Operated on that file, `isocheck` reduces the whole sample of geometries to a set of unique individuals and groups the redundant geometries into separate files. Operated on any other input that is not preoriented, `isocheck` cannot function, because it relies upon superposition of the molecules' Cartesian coordinates to decide whether two geometries are the same or not. The threshold for difference in Cartesian coordinates, `thres`, is read from standard input, together with the `filename` with the sample of geometries (lines `27-28`).

  In a recurring scheme, `isocheck` defines a structure as unique if it is not identical (`diff>thres`) to another previously defined (and thus stored) unique structure (lines `71-91`). The code is written so that the check-`loop` is escaped as soon as a match between the current geometry and a unique geometry occurs (`diff<thres`), see line `80`, the `if-else`-conditions in lines `92`, and `109-110`. For example, if the 457-th structure is a duplicate of the 4-th (out of 12) individuals, the checks 5 to 12 are escaped.

  At the end of this process, a sample of distinct, individual geometries are obtained. These have been written in the file `singles.mld`. The duplicates of these geometries are stored in separate files (see line `95`) to check if the `thres`-value is adequate or it can be further refined.

```
1   program isocheck  !This program reads .xyz geometries from a *.mld file
2                     !If two of them are identical (compared through a threshol
    d)
3                     !it will group them in one file.
4                     !If the *.mld is not aligned, this program  is useless.
5                     !The program also eliminates dummy atoms for checking
6   implicit none
7   integer,parameter :: DP=kind(1.d0)
8   integer i,j,k,ii
9   integer n,na,counter,ngeomax
10  integer na1,na2,na3,na4
11  character*40 dummychar,filename,filename2
12  character*150 command
13  character*1 answer
14  real(kind=DP) EL,EH                          !E_high,E_low,E_rough
15  real(kind=DP),allocatable:: E(:),Er(:)
16  real(kind=DP),allocatable:: cart    (:,:)  !cartesian coords
17  real(kind=DP),allocatable:: cartS   (:,:,:)!cartesian coords Saved as unique
18  real(kind=DP),allocatable:: cartn   (:,:)  !cartesian coords after correctio
    n
19  real(kind=DP),allocatable:: cnctvt_V(:,:)  !Conectivity value
20  integer,allocatable ::      cnctvt_A(:,:)  !Conectivity atom
21  integer,allocatable ::      cnctvt_S(:,:)  !Conectivity status
22  character*1,allocatable::   natom(:)
23  logical                     operation,notsaved,saved
24  real(kind=DP)               diff,thres
25  integer,allocatable::       listsaved(:)
26
27  read(*,*) filename
28  read(*,*) thres
29  open(20,file=filename,status='old')
30  read(20,*) na
31  close(20)
32
33  write(command,'(9a,35a,30a)') "grep SCF ",filename," | wc -l > n.tmp"
34  open(30,file='dogrep.sh',status='unknown')
35  write(30,*) command
36  close(30)
37
38  call system ("sh dogrep.sh")
39
40  ngeomax=1000
41  open(50,file='n.tmp',status='old')
42  read (50,*) n
43  close(50)
44  !if (n.gt.ngeomax) STOP
45  allocate(cnctvt_V(1:na,1:3),cnctvt_A(1:na,1:3),cnctvt_S(1:na,1:3))
46  !allocate(cart(1:na,1:3),cartS(1:ngeomax,1:na,1:3),cartn(1:na,1:3))
47  allocate(cart(1:na,1:3),cartS(1:n,1:na,1:3),cartn(1:na,1:3))
48  allocate(listsaved(1:n))
49  allocate(natom(1:na))
50  allocate(Er(1:n),E(1:n))
51
52  !Initialize
53  !Once aligned.mld has the ALL geometries, we "skimm" it to eliminate and gro
    up succesive
54  !identical structures
55  write(*,*) "Starting the reagrupation of duplicates"
56  open(90,file=filename,status='old')
57  open(150,file='singles.mld',status='unknown')
58  E(:)=0.d0
59  counter=0
60  do i=1,n
61
62     read(90,*)
63     read(90,*) dummychar,dummychar,E(i)
64     do j=1,na
65        read(90,*) natom(j),(cart(j,k),k=1,3)
66     enddo
67
68     saved=.true.
69     do ii=1,counter
70        diff=0.d0
71        write(*,*) "Cheking ",i,"-th against ",ii,"-th saved..."
72        do j=1,na
```

```
 73           if ((natom(j).ne.'X').or.(natom(j).ne.'x')) then
 74              do k=1,3
 75                 diff=diff+(cartS(ii,j,k)-cart(j,k))**2
 76              enddo
 77           endif
 78        enddo
 79        if (dsqrt(diff).lt.thres) then
 80           saved=.false.
 81           write(filename2,'(i3.3,a10)') ii,'.group.mld'
 82           write(*,*) "saving in ",filename2
 83           open(1,file=filename2,status='old',position='append')
 84           write(1,*) na
 85           write(1,*) 'SCF Done',E(i)
 86           do j=1,na
 87              write(1,'(a1,2x,3(F13.6,2x))') natom(j),(cart(j,k),k=1,3)
 88           enddo
 89           close(1)
 90        endif
 91     enddo
 92     if (saved) then
 93         counter=counter+1
 94         write(*,'(a20,x,i3.3,a4,i3.3,30a,45a)') ".. and saving geom",i," as "
    ,counter,"-th geom. in file",filename2
 95         write(filename2,'(i3.3,a10)') counter,'.group.mld'
 96          open(1,file=filename2,status='unknown')
 97         listsaved(counter)=i
 98         cartS(counter,:,:)=cart(:,:)
 99         write(150,*) na
100         write(1,*) na
101         write(150,*) 'SCF Done',E(i)
102         write(1,*) 'SCF Done',E(i)
103         do j=1,na
104            write(150,'(a1,2x,3(F13.6,2x))') natom(j),(cart(j,k),k=1,3)
105            write(1,'(a1,2x,3(F13.6,2x))') natom(j),(cart(j,k),k=1,3)
106         enddo
107         close(1)
108     else
109        write(*,*) "... I've seen this before!"
110     endif
111
112  enddo
113  close(90)
114  close(150)
115  call system ("rm n.tmp dogrep.sh")
116  end
```